ISSN 2518-7198 (Print)
ISSN 2663-5089 (Online)

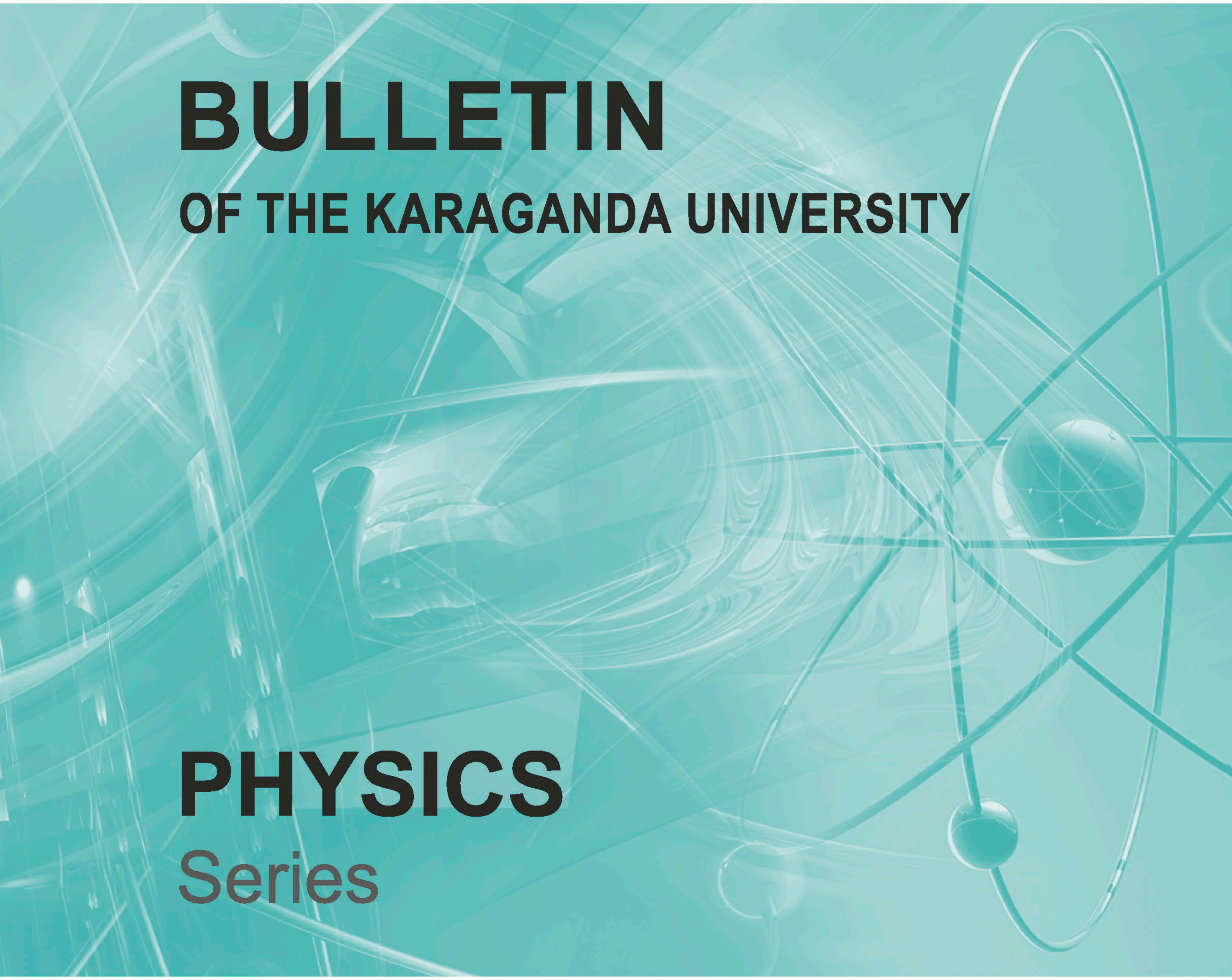

BULLETIN
OF THE KARAGANDA UNIVERSITY

PHYSICS
Series

2024 • Volume 29 • Issue 1(113)

ISSN 2663-5089 (Online)
ISSN-L 2518-7198 (Print)
Индексі 74616
Индекс 74616

ҚАРАҒАНДЫ УНИВЕРСИТЕТІНІҢ ХАБАРШЫСЫ

ВЕСТНИК КАРАГАНДИНСКОГО УНИВЕРСИТЕТА

BULLETIN OF THE KARAGANDA UNIVERSITY

ФИЗИКА сериясы

Серия ФИЗИКА

PHYSICS Series

2024

29-том • 1(113)-шығарылым
Том 29 • Выпуск 1(113)
Volume 29 • Issue 1(113)

1996 жылдан бастап шығады
Издается с 1996 года
Founded in 1996

Жылына 4 рет шығады
Выходит 4 раза в год
Published 4 times a year

Қарағанды / Караганда / Karaganda
2024

Бас редакторы

физ.-мат. ғыл. канд., проф. **А.К. Аймуханов**

Жауапты хатшы

PhD д-ры, қауымд. проф. **Д.Ж. Қарабекова**

Редакция алқасы

Н.Х. Ибраев,	физ.-мат. ғыл. д-ры, проф., акад. Е.А. Бөкетов атындағы Қарағанды университеті (Қазақстан);
Т.Ә. Көкетайтегі,	физ.-мат. ғыл. д-ры, проф., акад. Е.А. Бөкетов атындағы Қарағанды университеті (Қазақстан);
Б.Р. Нүсіпбеков,	техн. ғыл. канд., проф., акад. Е.А. Бөкетов атындағы Қарағанды университеті (Қазақстан);
А.О. Сәулебеков,	физ.-мат. ғыл. д-ры, проф., М.В. Ломоносов атындағы Мәскеу мемлекеттік университетінің Қазақстан филиалы, Астана (Қазақстан);
Б.Р. Ильясов,	PhD д-ры, қауымд. проф., Astana IT University, Астана (Қазақстан);
А.Д. Погребняк,	физ.-мат. ғыл. д-ры, проф., Сумы мемлекеттік университеті (Украина);
А.П. Суржиков,	физ.-мат. ғыл. д-ры, проф., Томск политехникалық университеті (Ресей);
И.П. Курытник,	техн. ғыл. д-ры, проф., Освенцимдегі В. Пилецкий атындағы Мемлекеттік жоғары кәсіптік мектебі (Польша);
М. Стоев,	PhD д-ры, инженерия д-ры, «Неофит Рильский» Оңтүстік-Батыс университеті, Благоевград (Болгария);
В.Ю. Кучерук,	техн. ғыл. д-ры, проф., Винница ұлттық техникалық университеті (Украина);
В.А. Кульбачинский,	физ.-мат. ғыл. д-ры, проф., М.В. Ломоносов атындағы Мәскеу мемлекеттік университеті (Ресей);
Bisquert Juan,	проф., физика проф., Хайме I университеті, Кастельо-де-ла-Плана (Испания);
Chun Li,	PhD д-ры, Чанчунь ғылым және технология университеті (Қытай);
Д.Т. Валиев,	физ.-мат. ғыл. канд., доц., Томск ұлттық политехникалық зерттеу университеті (Ресей)

Редакцияның мекенжайы: 100024, Қазақстан, Қарағанды қ., Университет к-сі, 28
Тел.: +7 701 531 4758; факс: (7212) 35-63-98.
E-mail: vestnikku@gmail.com; karabekova71@mail.ru
Сайты: physics-vestnik.ksu.kz

Атқарушы редактор

PhD д-ры **Г.Б. Саржанова**

Редакторлары

Ж.Т. Нурмуханова, С.С. Балкеева, И.Н. Муртазина

Компьютерде беттеген

М.С. Бабатаева

Қарағанды университетінің хабаршысы. «Физика» сериясы. — 2024. — 29-т., 1(113)-шығ. — 105 б. — ISSN-L 2518-7198 (Print). ISSN 2663-5089 (Online).

Меншік иесі: «Академик Е.А. Бөкетов атындағы Қарағанды университеті» КЕАҚ.

Қазақстан Республикасы Ақпарат және қоғамдық даму министрлігімен тіркелген. 30.09.2020 ж. № KZ38VPY00027378 қайта есепке қою туралы куәлігі.

Басуға 29.03.2024 ж. қол қойылды. Пішімі 60×84 1/8. Қағазы офсеттік. Көлемі 13,13 б.т. Таралымы 200 дана. Бағасы келісім бойынша. Тапсырыс № 20.

«Акад. Е.А. Бөкетов ат. Қарағанды ун-ті» КЕАҚ баспасының баспаханасында басылып шықты.
100024, Қазақстан, Қарағанды қ., Университет к-сі, 28. Тел. (7212) 35-63-16. E-mail: izd_kargu@mail.ru

© Академик Е.А. Бөкетов атындағы Қарағанды университеті, 2024

Главный редактор

канд. физ.-мат. наук, проф. **А.К. Аймуханов**

Ответственный секретарь

д-р PhD, ассоц. проф. **Д.Ж. Карабекова**

Редакционная коллегия

Н.Х. Ибраев,	д-р физ.-мат. наук, проф., Карагандинский университет им. акад. Е.А. Букетова (Казахстан);
Т.А. Кокетайтеги,	д-р физ.-мат. наук, проф., Карагандинский университет им. акад. Е.А. Букетова (Казахстан);
Б.Р. Нусупбеков,	канд. техн. наук, проф., Карагандинский университет им. акад. Е.А. Букетова (Казахстан);
А.О. Саулебеков,	д-р физ.-мат. наук, проф., Казахстанский филиал Московского государственного университета им. М.В. Ломоносова, Астана (Казахстан);
Б.Р. Ильясов,	д-р PhD, ассоц. проф., Astana IT University, Астана (Казахстан);
А.Д. Погребняк,	д-р физ.-мат. наук, проф., Сумской государственный университет (Украина);
А.П. Суржиков,	д-р физ.-мат. наук, проф., Томский политехнический университет (Россия);
И.П. Курытник,	д-р техн. наук, проф., Государственная высшая профессиональная школа им. В. Пилецкого в Освенциме (Польша);
М. Стоев,	д-р PhD, д-р инженерии, Юго-Западный университет «Неофит Рильский», Благоевград (Болгария);
В.Ю. Кучерук,	д-р техн. наук, проф., Винницкий национальный технический университет (Украина);
В.А. Кульбачинский,	д-р физ.-мат. наук, проф., Московский государственный университет им. М.В. Ломоносова (Россия);
Bisquert Juan,	проф., проф. физики, Университет Хайме I, Кастельо-де-ла-Плана (Испания);
Chun Li,	д-р PhD, Чанчуньский университет науки и технологии (Китай);
Д.Т. Валиев,	канд. физ.-мат. наук, доц., Национальный исследовательский Томский политехнический университет (Россия)

Адрес редакции: 100024, Казахстан, г. Караганда, ул. Университетская, 28
Тел.: +7 701 531 4758. Факс: (7212) 35–63–98.
E-mail: vestnikku@gmail.com; karabekova71@mail.ru
Сайт: physics-vestnik.ksu.kz

Исполнительный редактор

д-р PhD **Г.Б. Саржанова**

Редакторы

Ж.Т. Нурмуханова, С.С. Балкеева, И.Н. Муртазина

Компьютерная верстка

М.С. Бабатаева

Вестник Карагандинского университета. Серия «Физика». — 2024. — Т. 29, вып. 1(113). — 105 с. — ISSN-L 2518-7198 (Print). ISSN 2663-5089 (Online).

Собственник: НАО «Карагандинский университет имени академика Е.А. Букетова».

Зарегистрирован Министерством информации и общественного развития Республики Казахстан. Свидетельство о постановке на переучет № KZ38VPY00027378 от 30.09.2020 г.

Подписано в печать 29.03.2024 г. Формат 60×84 1/8. Бумага офсетная. Объем 13,13 п.л. Тираж 200 экз. Цена договорная. Заказ № 20.

Отпечатано в типографии издательства НАО «Карагандинский университет им. акад. Е.А. Букетова».
100024, Казахстан, г. Караганда, ул. Университетская, 28. Тел.(7212) 35-63-16. E-mail:izd_kargu@mail.ru

© Карагандинский университет им. акад. Е.А. Букетова, 2024

Chief Editor

Professor, Cand. of Phys. and Math. Sci. **A.K. Aimukhanova**

Responsible secretary

Associate Professor, PhD **D.Zh. Karabekova**

Editorial board

N.Kh. Ibrayev,	Prof., Doctor of phys.-math. sciences, Karagandy University of the name of acad. E.A. Buketov (Kazakhstan);
T.A. Koketaitegi,	Prof., Doctor of phys.-math. sciences, Karagandy University of the name of acad. E.A. Buketov (Kazakhstan);
B.R. Nussupbekov,	Prof., Cand. of techn. sciences, Karagandy University of the name of acad. E.A. Buketov (Kazakhstan);
A.O. Saulebekov,	Prof., Doctor of phys.-math. sciences, Kazakhstan branch of Lomonosov Moscow State University, Astana (Kazakhstan);
B.R. Ilyassov,	PhD, Assoc. Prof., Astana IT University (Kazakhstan);
A.D. Pogrebnjak,	Prof., Doctor of phys.-math. sciences, Sumy State University (Ukraine);
A.P. Surzhikov,	Prof., Doctor of phys.-math. sciences, Tomsk Polytechnic University (Russia);
I.P. Kurytnik,	Prof., Doctor of techn. sciences, The State School of Higher Education in Oświęcim (Auschwitz) (Poland);
M. Stoev,	PhD, Doctor of engineering, South-West University “Neofit Rilski”, Blagoevgrad (Bulgaria);
V.Yu. Kucheruk,	Prof., Doctor of techn. sciences, Vinnytsia National Technical University, Vinnitsia (Ukraine);
V.A. Kulbachinskii,	Prof., Doctor of phys.-math. sciences, Lomonosov Moscow State University (Russia);
Bisquert Juan,	Prof. of phys., Prof. (Full), Universitat Jaume I, Castellon de la Plana (Spain);
Chun Li,	PhD, Changchun University of Science and Technology (China);
D.T. Valiev	Assoc. Prof., Cand. of phys.-math. sciences, National Research Tomsk Polytechnic University (Russia)

Postal address: 28, University Str., 100024, Karaganda, Kazakhstan
Tel.: +7 701 531 4758; Fax: (7212) 35-63-98.
E-mail: vestnikku@gmail.com; karabekova71@mail.ru
Web-site: physics-vestnik.ksu.kz

Executive Editor

PhD **G.B. Sarzhanova**

Editors

Zh.T. Nurmukhanova, S.S. Balkeyeva, I.N. Murtazina

Computer layout

M.S. Babatayeva

Bulletin of the Karaganda University. “Physics” Series. — 2024. — Vol. 29, Iss. 1(113). — 105 p. — ISSN-L 2518-7198 (Print). ISSN 2663-5089 (Online).

Proprietary: NLC “Karagandy University of the name of academician E.A. Buketov”.

Registered by the Ministry of Information and Social Development of the Republic of Kazakhstan. Rediscount certificate No. KZ38VPY00027378 dated 30.09.2020.

Signed in print 29.03.2024. Format 60×84 1/8. Offset paper. Volume 13,13 p.sh. Circulation 200 copies. Price upon request. Order № 20.

Printed in the Publishing house of NLC “Karagandy University of the name of acad. E.A. Buketov”.
28, University Str., Karaganda, 100024, Kazakhstan. Tel. (7212) 35-63-16. E-mail: izd_kargu@mail.ru

© Karagandy University of the name of academician E.A. Buketov, 2024

МАЗМҰНЫ – СОДЕРЖАНИЕ – CONTENTS

КОНДЕНСАЦИЯЛАНҒАН КҮЙДІҢ ФИЗИКАСЫ
ФИЗИКА КОНДЕНСИРОВАННОГО СОСТОЯНИЯ
PHYSICS OF THE CONDENSED MATTER

ТЕХНИКАЛЫҚ ФИЗИКА
ТЕХНИЧЕСКАЯ ФИЗИКА
TECHNICAL PHYSICS

ЖЫЛУФИЗИКАСЫ ЖӘНЕ ТЕОРИЯЛЫҚ ЖЫЛУТЕХНИКАСЫ
ТЕПЛОФИЗИКА И ТЕОРЕТИЧЕСКАЯ ТЕПЛОТЕХНИКА
THERMOPHYSICS AND THEORETICAL THERMOENGINEERING

Article

Received: 20.09.2023
Accepted: 01.12.2023

UDC 538.958

https://doi.org/10.31489/2024PH1/6-12

A. Zhumabekov*, A. Kassanova, N. Ispulov, K. Dossumbekov,
Zh. Ospanova, T. Dossanov, A. Kurmanov

Toraighyrov University, Pavlodar, Kazakhstan
**Corresponding author's e-mail: almar89-89@mail.ru*

High responsivity UV detector based on TiO_2-rGO nanocomposite material

The influence of reduced graphene oxide and the optoelectronic characterictics of a nanocomposites based on rGO and TiO_2 were studied. Surface morphology and Raman spectra of nanocomposite materials indicate the presence of initial components. It has been illustrated that during hydrothermal synthesis further reduction of rGO occurs, i.e. the variety of oxygen-containing groups decreases. Studies of current-voltage characteristics have displayed the availability of rGO in the nanocomposite leads to an increase in the photo induced current to more than 40 μA. Next, the photoresponsivity of the samples was determined, which is three orders of value higher than pure titanium dioxide for nano-composite material. And the detectivity also increased 9 times. This parameter allows you to identify the performance of the device. In this regard, the UV detector based on nanocomposite has a higher performance. Studies also show a decrease in reaction time to light irradiation. When irradiated, the nanocomposite material reacts to light three orders of magnitude faster than TiO_2.

Keywords: graphene oxide, titanium dioxide, Raman spectra, optoelectronic properties, UV detectors.

Introduction

Photodetectors originated as incident light sensors, which were mainly used to convert the energy of a falling photon into an electrical signal. Typically, the sensing capacity of incident radiation can be significantly assessed by measuring the current or voltage signal generated in the device. Therefore, there is great interest in developing various photodetectors. So far, many researchers have reported various photodetector mechanisms included in the ultraviolet, visible and infrared regions. Therefore, it is necessary to develop a strategic device architecture using various composite materials to improve the perception of incident light. Therefore, achieving excellent photoresponsibility and photoresponsivity mechanism of a photodetector is primarily due to photoconductive, photoreflective and photoelectric effects.

Due to their improved physical and chemical properties, nanostructures have become attractive materials in the area of nanoelectronics, energy, optoelectronics, photocatalysis, sensors, drug delivery, biomedicine, lasers, and flexible technologies [1–3]. In particular, photodetector technology is practically applied in the ultraviolet region for ozone detection, pollution detection, gas sensors and flame detection; in the visible region for energy, fiber optic communications, video imaging and artificial vision, and infrared (IR) for biomedical imaging, defence, space telescopes and meteorology.

Wide bandgap metal oxide materials (ZnO, SnO_2, Ga_2O_3, WO_3 and TiO_2) provide outstanding processing approaches such as ease of fabrication, scalability, crystal orientation control, uniformity and reproducibility in the UV detector community. Thus, all the above features demonstrate that metal oxide semiconductors can be widely used in high-responsivity UV photodetectors.

In the last decade, works have been appeared where multicomponent and hybrid materials based on graphene and TiO_2 nanoparticles [4–6]. Materials received in these works mostly focus on creating TiO_2 nanocrystals with the desired size and morphology, followed by their modification and applying on the surface of graphene sheets. However, these hybrid materials have disadvantages. Their size is too small to be easily agglomerated. Moreover, during the process of photodecomposition of organic compounds, the effective surface area of TiO_2 and graphene of such a hybrid material can considerably decrease.

Titanium dioxide (TiO_2) is one of the most researched semiconductors due to its high potential of application in photocatalysis, photovoltaic cells and gas sensors. Titanium dioxide, with a bandgap of 3.2 eV, is responsivity to light with wavelengths below 380 nm. This allows it to be used for the manufacture of photodetectors for the UV-A range. TiO_2 with a Schottky barrier have high-speed UV detection, but have low photoresponsivity. This limits its use in UV detection. At the same time, oxygen vacancies in TiO_2 can lead to strong tunneling of carriers, this can increase the dark current. Thus, the properties of TiO_2 with excellent structural transformation and non-stoichiometric phase transitions ensure its importance in optoelectronic sensors and imaging systems [7–11].

Recently, graphene based photo-electric devices have drawn the attentions because of its superior optical and electrical properties [12]. Graphene has an almost flat absorption to the specific optical spectrum, and has ballistic electronic transport and ultrahigh carrier mobility, which may lower the recombination possibility of electrons and holes [13, 14]. Those properties make graphene an ideal material for photodetecting devices when combining it with other photoresponsivity responsivity materials.

One of the most important graphene derivatives is graphene oxide, an excellent carbon material with a high specific surface area, good dispersion and a surface rich in functional groups. Go contains a large number of oxygen-containing functional groups (hydroxyl, epoxy, carbonyl and carboxyl) on its basal plane and edges; these groups allow combining GO with other modified nanomaterials and provide ample opportunities for creating hybrid nanocomposites based on GO [15–17].

In addition, it is believed that the combination of TiO_2 and graphene oxide GO has synergistic effects and improves the photodegradation of organic compounds in both gaseous and aqueous media. Meanwhile, in [18] it was shown that the reduced graphene oxide (rGO) has a higher photocatalytic activity and electrical conductivity compared to graphene oxide.

In this work, an ultraviolet detector of a nanocomposite material based on rGO and TiO_2 was obtained. It is expected that the addition of rGO and TiO_2 in a complex will improve the optoelectronic characteristics of the detector, since their use has led to an increase in the effectiveness of photocatalytic properties [19].

Experimental

Preparation of nanocomposite materials was synthesized by the hydrothermal method according to the methods of work [19, 20]. The preparation were carried out on the basis of rGO (Cheaptubes, USA), TiO_2 (Sigma Aldrich), deionized water and ethanol. The concentration of rGO in the resulting nanocomposite material is 10%, since studies have shown that at this concentration the materials have highly efficient catalytic activity [19].

All reagents were analytically pure and used without further purification.

The surface morphology of the resulting composite materials was examined using a JEM-2100F transmission electron microscope with an accelerating voltage of 120 kV. To record Raman spectra, a Confotec MR520 microscope (Sol Instruments) with laser excitation at a wavelength of 632.8 nm was used. TiO_2 or TiO_2-rGO nanocomposite films were prepared from a paste obtained by constantly mixing $TiO_2$of 150 mg and TiO_2-rGO with 1 mL of ethanol for 24 hours.

The finished paste was applied to the surface of the substrates using the “spin-coating” method at a rotation speed of 2000 rpm. After application, the film was annealed in an argon atmosphere for 2 hours at a temperature of 450 ℃.

The photodetector was assembled on glass with a conducting layer of fluorinated tin oxide (FTO, Sigma Aldrich). Interdigitated tracks were cut on the surface substrates using a laser scriber BLS0503MM (Bodor) [21].

Measurements of the current-voltage characteristics (CVC) of the prepared samples were carried out using a potentiostat-galvanostat Elins P-40X (Elins) when the samples were irradiated with light from a xenon lamp with a power of 35 mW/ cm^2.

To study the response time of the samples, we used a setup and a pulsed laser LQ215 (Solar) with a third harmonic generator with 355 nm and a pulse duration of 7 ns [21].

Results and Discussion

A TEM study of the structure of prepared films showed that when rGO is applied, an island film is formed (Fig. 1).

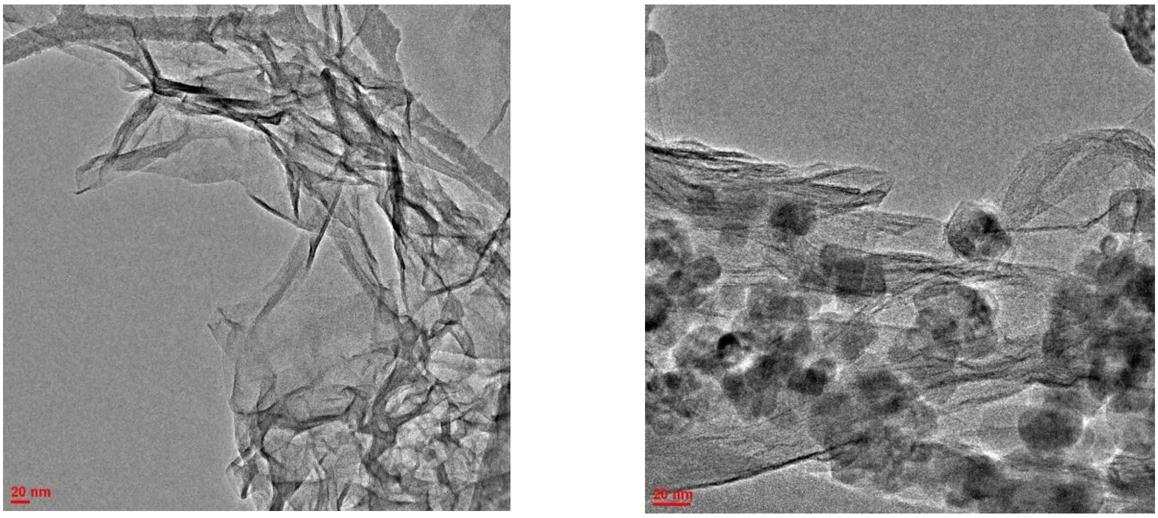

a)

b)

Figure 1. TEM images of rGO (*a*) and TiO_2-rGO (*b*) powders

TEM images (Fig. 1) show rGO sheets and TiO_2 particles dispersed on a surface of individual rGO sheets. In this case, a slight agglomeration of TiO_2 particles is also observed. Figure 1b shows larger flakes of thin translucent rGO enveloping TiO_2 particles.

TEM studies demonstrate that reduced graphene oxide sheets are dispersed throughout the synthesized composites. This can promote the formation of a conductive network between TiO_2 particles and more efficient injection of photogenerated electrons into graphene sheets, ensuring their further transfer to FTO layer and recording.

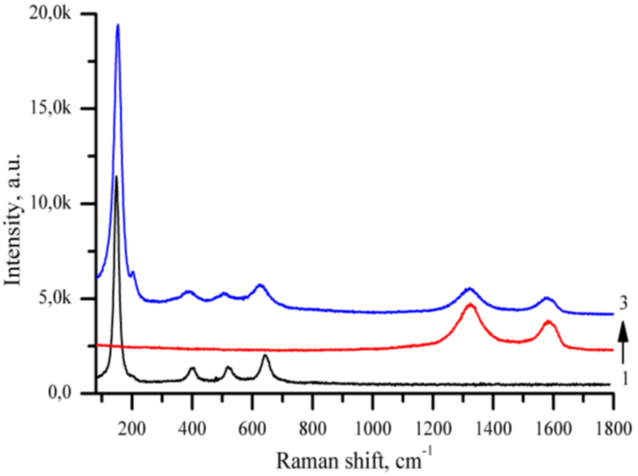

1 — TiO_2; *2* — rGO; *3* — TiO_2–rGO

Figure 2. Raman shift of samples

Raman spectra were recorded to identify the materials. According to the Raman spectra, the nanocomposite material contains TiO_2 and rGO peaks. Titanium dioxide of the anatase structure has six Raman-active peaks in the vibrational spectrum [19, 22]. The spectrum of reduced graphene oxide contains two characteristic bands: D- and G-bands (Table 1).

Table 1

Position and intensity of the RC shift

Sample	D, cm^{-1}	I, o.e.	G, cm^{-1}	I, o.e.	I_D/I_G
rGO	1326,83	2708	1582,79	1789	1,51
TiO_2-rGO	1321,22	1584	1571,97	1079	1,47

A decrease in the I_D/I_G intensity ratio in the nanocomposite material indicates the process of further reduction of graphene oxide during synthesis, where the formation of sp^2 carbon domains and a decrease in the amount of oxygen-containing groups can occur [23].

The main parameters for determining an ultraviolet detector are current-voltage characteristics (volt-ampere characteristics), with the help of which light and dark photocurrents are found, as well as responsivity and detectability. Figure 3 shows the CVC of light and dark photo-induced current for TiO_2 and TiO_2-rGO. The CVC of the samples were measured at a voltage of +30 V and at –30 V. The dependence of current on voltage has a nonlinear form. At the same time, even without illumination of the samples, so-called dark currents are recorded. The values of the generated photocurrent I_{ph} of the detector, shown in Table 2, were assessed from the difference in light and dark values.

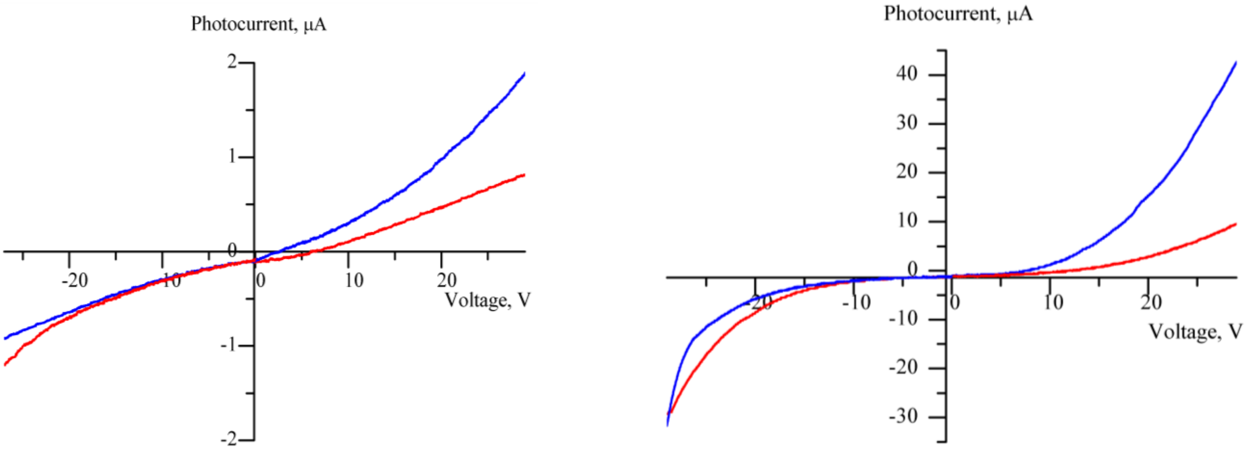

TiO_2 TiO_2-rGO

Figure 3. CVC of samples: blue — light, red — dark

The maximum photocurrent value was recorded in the TiO_2-rGO nanocomposite material, which is 46.83 µA (at +30 V), and the current is 29.76 µA at –30 V. It is also clear from Figure 3 that at +8V there is an intense increase photocurrent compared to dark current. This shows the response of the samples to irradiation. The difference between light and dark current is equal to the background photocurrent. The figure shows the current-voltage characteristics for pure TiO_2, where upon irradiation the photocurrent is only 1.9 µA, and the dark current is only 0.8 µA. Table 2 shows that the background current at +30V voltage in TiO_2-rGO is 36 times higher than in TiO_2. And at –30V this value only increases by almost 2 times.

The photoresponsivity of the detector is determined by the formula:

$$R = \frac{I_{ph}}{P}, \tag{1}$$

where P is the incident radiation power.

Table 2 shows, it is clear that the responsivity of TiO_2-rGO nanocomposite films has increased by almost three orders of magnitude. Next, the specific detection ability of the prepared samples D* was estimated, which determines the ability of the device to detect weak light signals and can be determined from expression (1) [24, 25]:

$$D^* = \frac{R\sqrt{A}}{\sqrt{2 \cdot e \cdot I_{dark}}}, \tag{2}$$

where R is the responsivity of the films, A is the illuminated area of the sample, e is the electron charge modulo, I_{dark} is the value of the dark current at +30 V.

Table 2

Optoelectronic characteristics UV detectors based on TiO_2 and nanocomposite TiO_2-rGO

Sample	I_{ph}, μA+30 V	I_{ph}, μA–30 V	R, A/W	D^*, Jones	τ_1, s	τ_2, s
TiO_2	1.10	2,98	$31.4\cdot10^{-6}$	$6.03\cdot10^{7}$	$17\cdot10^{-3}$	3,3
TiO_2-rGO	36.1	4,03	$1.03\cdot10^{-3}$	$55{,}9\cdot10^{7}$	$7\cdot10^{-6}$	$0{,}31\cdot10^{-3}$

According to the calculations that the specific detection ability of TiO_2 films is $6.03\cdot10^7$ Jones, while in the presence of rGO D* increased to $55.9\cdot10^7$ Jones. This can be explained by the fact that the responsivity of pure TiO2 films has a very low value. Table 2 shows the rise and fall times of the samples. The rise time for TiO_2-rGO is three orders of magnitude longer than that for TiO_2. Thus, the nanocomposite material reacts faster to the incident light. However, the decay time in the nanocomposite material also passes faster and is equal to 0.31 ms.

Thus, the optoelectronic characteristics of a UV detector based on a nanocomposite material are improved by the addition of reduced graphene oxide.

Conclusions

Thus, a nanocomposite material based on rGO and TiO_2 was obtained using a hydrothermal synthesis method. The surface morphology of the nanocomposite is shown and the rGO sheets and TiO_2 nanoparticles are clearly visible. The Raman spectrum also confirms the presence of initial components in the nanocomposite material. The intensity ratio shows that further reduction of rGO occurs in the nanocomposite material. Studies of current-voltage characteristics have shown that in the nanocomposite material the background photocurrent is 36 μA, and in pure TiO_2 it is only 1.1 μA. Accordingly, the responsivity of the nanocomposite UV detector is three orders of magnitude greater and is equal to 1 mA, whereas for TiO_2 it is 31 μA. The detectability also shows the best results for TiO_2-rGO. Studies of the timing characteristics of the nanocomposite material show rise and fall reaction times of 7 μs and 0.31 ms, respectively.

Thus, the results obtained show that the optoelectronic characteristics of the UV detector of the TiO_2-rGO nanocomposite material are much higher than those of pure TiO_2.

Acknowledgements

This research is funded by the Science Committee of the Ministry of Science and Higher Education of the Republic of Kazakhstan (Grant No. AP19576361).

References

1 Wang, Z.L. (2007). Novel nanostructures of ZnO for nanoscale photonics, optoelectronics, piezoelectricity, and sensing. *Appl. Phys. Mater. Sci. Process*, 88, 7–15.

2 Laurenti, M., Lamberti, A., Genchi, G.G., Roppolo, I., Canavese, G., Vitale-Brovarone, C., Ciofani, G., & Cauda, V. (2019). Graphene oxide finely tunes the bioactivity and drug delivery of mesoporous ZnO scaffolds. *ACS Appl. Mater. Interfaces,* 11, 449–456.

3 Cheng, R., Wen, Y., Yin, L., Wang, F., Liu, K., Shifa, T.A., Li, J., Jiang, C., Wang, Z., & He, J. (2017). Ultrathin single-crystalline CdTe nanosheets realized via Van der Waals epitaxy. *Adv. Mater.*, 29, 1703122.

4 Wang, T. Tang, T., Gao, Y., Chen, Q., Zhang, Zh., & Bian, H. (2019). Hydrothermal preparation of Ag-TiO_2-reduced graphene oxide ternary microspheres structure composite for enhancing photocatalytic activity. *Physica E*, 112, 128–136.

5 Maiti, R., Sinha, T.K., & Mukherjee, S. (2016). Enhanced and selective photodetection using graphene–stabilized hybrid plasmonic silver nanoparticles. *Plasmonics,* 11, 1297-1–8.

6 Liu, Y., Cheng, R., & Liao, L. (2011). Plasmon resonance enhanced multicolour photodetection by graphene. *Nat. Commun, 2*(1), 1–7.

7 Cho, H., Joo, H., Kim, H., Kim, J.E., Kang, K.S., & Yoon, J. (2021). Improved photo-electrochemical properties of TiO_2 nanotubes doped with Er and effects on hydrogen production from water splitting. *Chemosphere*, 267, 129289.

8 Yan, L., Yu, J., & Luo, H. (2017). Ultrafine TiO_2 nanoparticles on reduced graphene oxide as anode materials for lithium ion batteries. *Appl. Mater. Today*, 8, 31–34.

9 Kment, S., Krysova, H., Hubicka, Z., Kmentova, H., Kavan, L., & Zboril, R. (2017). Very thin thermally stable TiO_2 blocking layers with enhanced electron transfer for solar cells. *Appl. Mater. Today*, 9, 122–129.

10 Phukan, P., & Sahu, P.P. (2020). High performance UV photodetector based on metal-semiconductor-metal structure using TiO_2-rGO composite. *Optical Materials*, 109, 110330-110339.

11 Ahmad, H., Tajdidzadeh, M., & Thambiratnam, K. (2018). Infrared photodetectors based on reduced graphene oxide nanoparticles and graphene oxide. *Laser Phys*, 28, 066204-1–8.

12 Kamat, P.V. (2011). Graphene-based nanoassemblies for energy conversion. *J. Phys. Chem. Lett.*, 2, 242–251.

13 Serikov, T.M., Kayumova, A.S., Baltabekov, A.S., Ilyina, L.F., & Zhanbirbayeva, P.A. (2022). Photocatalytic Activity of Nanocomposites Based on Titania Nanorods and Nanotubes Doped with Ag and Reduced Graphene Oxide Nanoparticles. *Nanobiotechnology Reports*, *18*(2), 207–215.

14 Wang, X., Zhi, L., & Muellen, K. (2008). Transparent, Conductive graphene electrodes for dye-sensitized solar cells. *Nano Lett.*, 8, 323–327.

15 Ng, Y.H., Lightcap, I.V., Goodwin, K., Matsumura, M., & Kamat, P.V. (2010). To what extent do graphene scaffolds improve the photovoltaic and photocatalytic response of TiO_2 nanostructured films. *J. Phys. Chem. Lett*, 15, 2222–2227.

16 Li, Q., Guo, B.D., Yu, J.G., Ran, J.R., Zhang, B.H., Yan, H.J., & Gong, J.R. (2011). Highly efficient visible-light-driven photocatalytic hydrogen production of CdS-cluster-decorated graphene nanosheets. *J. Am. Chem. Soc*, 133, 10878–10884.

17 Nguyen-Phan, T-D., Pham, V.H., Shin, E.W., Pham, H-D., Kim, S., & Chung, J.S. (2011). The role of graphene oxide content on the adsorption-enhanced photocatalysis of titanium dioxide/graphene oxide composites. *Chem Eng J.*, *170*(1), 226–32.

18 Ibrayev, N., Seliverstova, E., & Zhumabekov, A. (2018). Preparation of graphene nanostructured films for photovoltaics. *IOP Conf. Series: Materials Science and Engineering*, 447.

19 Ibrayev, N., Zhumabekov, A., Ghyngazov, S., & Lysenko, E. (2019). Synthesis and study of the properties of nanocomposite materials TiO_2-GO and TiO_2-rGO. *Material Research Express*, *6*(11), 1–11.

20 Zhumabekov, A.Z., Ibrayev, N.K., & Seliverstova, E.V. (2020). Photoelectric properties of a nanocomposite derived from reduced graphene oxide and TiO_2. *Theor. Exp. Chem.*, *55*(6), 398–406.

21 Seliverstova, E., Zhumabekov, A., & Ibrayev, N. (2020). The Effect of Silver Nanoparticles on the Photodetecting Properties of the TiO_2/Graphene Oxide Nanocomposite. *Optics and Spectroscopy*, *128*(9), 1337–1345

22 Swamy, V., Kuznetsov, A., Dubrovinsky, L.S., Caruso, R.A., Shchukin, D.G., & Muddle, B.C. (2005). Finite-size and pressure effects on the Raman spectrum of nanocrystalline anatase TiO_2. *Phys. Rev. B*, 71, 184302–12.

23 Jorio, A., Dresselhans, M., Saito, R., & Dresselhaus, G.F. (2011). Raman spectroscopy in graphene related system. *Wiley–VCH*, 356 p.

24 Li, Sh., Tao, D., Zhang, Ya., Yuning, L., Weijie, Y., Chen Q., & Zewen L. (2019). Solar–blind ultraviolet detection based on TiO_2 nanoparticles decorated graphene field–effect transistors. *Nanophotonics*, *8*(5), 899–908.

25 De Sanctis, A., Mehew, J.D., Craciun, M.F., & Russo S. (2018). Graphene–based light sensing: fabrication, characterization, physical properties and performance. *Materials*, *11*(9), 1762–1791.

А. Жумабеков, А. Қасанова, Н. Испулов, К. Досумбеков,
Ж. Оспанова, Т. Досанов, А. Құрманов

TiO_2-rGO нанокомпозиті негізіндегі жоғарысезімтал ультракүлгін детектор

Мақалада титан диоксиді мен rGO негізіндегі нанокомпозиттік материалдың оптоэлектрондық қасиеттеріне қайта құрылған графен оксидінің әсері зерттелген. Нанокомпозиттік материалдардың бетінің морфологиясы және рамандық спектрлері бастапқы компоненттердің болуын көрсетеді. Гидротермалдық синтез кезінде rGO одан әрі қайта құрылады, яғни оттегі бар топтардың саны азаятындығы көрсетілген. Вольт-ампер сипаттамаларының зерттеуі бойынша нанокомпозитте rGO-ның болуы фотоиндукцияланған токтың 40 мкА-дан жоғары мәнге әкелетінін көрсетті. Осыдан нанокомпозиттік материал үшін таза титан диоксидімен салыстырғанда үш ондықтан артық асатын үлгілердің сезімталдығы анықталды. Ал детекторлау қабілеті де 9 есе өсті. Бұл параметр құрылғының өнімділігін анықтауға мүмкіндік береді. Осыған байланысты нанокомпозит негізіндегі ультракүлгін детектордың өнімділігі жоғары. Сондай-ақ, зерттеулер жарық сәулеленуінде реакция уақытының азаюын көрсетеді. Сәулеленген кезде нанокомпозиттік материал TiO_2-ге қарағанда үш реттік шамадағы жарыққа тез әрекет етеді. Алынған нәтижелерді оптоэлектрондық және фотокаталитикалық қосымшаларға арналған жарыққа сезімтал жаңа құрылғыларды жасауда қолдануға болады.

Кілт сөздер: графен оксиді, титан диоксиді, КШ спектрі, оптоэлектрондық қасиеттері, ультракүлгін детекторы.

А. Жумабеков, А. Касанова, Н. Испулов, К. Досумбеков,
Ж. Оспанова, Т. Досанов, А. Курманов

Высокочувствительный УФ детектор на основе нанокомпозита TiO_2–rGO

Изучено влияние восстановленного оксида графена на оптоэлектронные свойства нанокомпозитного материала на основе диоксида титана и rGO. Морфология поверхности и Раман-спектры нанокомпозитных материалов показывают наличие исходных компонентов. Показано, что при гидротермальном синтезе происходит дальнейшее восстановление rGO, то есть уменьшается количество кислородсодержащих групп. Исследования вольт-амперных характеристик показали, что наличие rGO в нанокомпозите приводит к увеличению фотоиндуцированного тока к более 40 мкА. Отсюда была определена чувствительность образцов, которая для нанокомпозитного материала превысила уровень на три порядка по сравнению с чистым диоксидом титана. А детектирующая способность также увеличилась в 9 раз. Данный параметр позволяет выявить производительность устройства. В связи с этим УФ детектор на основе нанокомпозита обладает более высокой производительностью. Также исследования показывают уменьшение времени реакции на облучение светом. При облучении нанокомпозитный материал реагирует на свет на три порядка быстрее, чем TiO_2. Полученные результаты могут быть использованы при разработке новых светочувствительных устройств для оптоэлектронных и фотокаталитических приложений.

Ключевые слова: оксид графена, диоксид титана, спектр КР, оптоэлектронные характеристики, УФ детектор.

Information about authors

Zhumabekov, Almar — PhD, Associate Professor, Computer Science Faculty, Toraighyrov University, Pavlodar, Kazakhstan; e-mail: almar89-89@mail.ru; ORCID ID https://orcid.org/0000-0003-2360-3747

Kassanova, Assiya — PhD, Assoc. Professor, Department of Chemistry and Chemical Technologies, Toraighyrov University, Pavlodar, Kazakhstan; asiyakass@mail.ru; ORCID ID https://orcid.org/0000-0002-9563-5521

Ispulov, Nurlybek — Candidate of physical and mathematical sciences, Professor, Computer Science Faculty, Toraighyrov University, Pavlodar, Kazakhstan; nurlybek_79@mail.ru, https://orcid.org/0000-0003-4703-1413

Dossumbekov, Kairat — Master, Senior teacher, Computer Science Faculty, Toraighyrov University, Pavlodar, Kazakhstan; kairat_83@inbox.ru; ORCID ID https://orcid.org/0000-0002-9695-8154

Ospanova, Zhulduz — PhD student, Toraighyrov University, Pavlodar, Kazakhstan; zhulduz-ospan@mail.ru

Dossanov, Talgat — Candidate of physical and mathematical sciences, Computer Science Faculty, Toraighyrov University, Pavlodar, Kazakhstan; dosts81@mail.ru

Kurmanov, Almas — Senior teacher, Master, Computer Science Faculty, Toraighyrov University, Pavlodar, Kazakhstan; almaskurmanov@mail.ru

Article

Received: 03.11.2023
Accepted: 12.12.2023

UDC 538.971

https://doi.org/10.31489/2024PH1/13-22

M.M. Kubenova[1*], K.A. Kuterbekov[1], M.Kh. Balapanov[2], R.Kh. Ishembetov[2],
G.D. Kabdrakhimova[1], R.A. Alina[1], M. Tatay[1], R. Ildos[1]

[1]L.N. Gumilyov Eurasian National University, 2 Satpayev str., 010008 Astana, Kazakhstan;
[2]Ufa University of Science and Technology, 32 Zaki Validi str., 450076 Ufa, Bashkortostan, Russia
[*]Corresponding author's e-mail: kubenova.m@yandex.kz

Thermal properties of Cu_2S binary copper sulfides

Copper chalcogenides have a complex electronic structure due to the interaction of hybridized s- and p-states of chalcogen forming a valence band with 3d states of copper, which greatly complicates the interpretation of temperature dependences of kinetic parameters having a nonmonotonic character. Cu_2S copper sulfide is an effective thermoelectric material, so it is interesting to study its kinetic parameters of solid solutions that it forms with alkali metals. The nonstoichiometry of chalcogenides can be easily controlled electrochemically, therefore, the task of selecting the optimal composition according to the cationic sublattice is quite feasible. The paper presents experimental studies of the properties of Cu_2S binary copper sulfide. Copper chalcogenides have a complex electronic structure due to the interaction of hybridized s- and p-states of chalcogen forming a valence band with 3d states of copper, which greatly complicates the interpretation of temperature dependences of kinetic parameters having a nonmonotonic character. For the Cu_2S sample, rather low values of the electron thermal EMF coefficient of the sample from 0.05 mV/K to 0.25 mV/K were found, which are more typical for metals than for semiconductors. The thermal conductivity of the Cu_2S sample is quite low, it rises to 0.3 W/m*K at a phase transition of about 380 K and does not fall below 0.2 W/m*K. Thus, the nonstoichiometry of chalcogenides can be easily controlled electrochemically, therefore, the task of selecting the optimal composition according to the cationic sublattice is quite feasible. In addition, to improve the thermoelectric properties of Cu_2S, it can be achieved by alloying alkali metals into a binary copper sulfide matrix.

Keywords: thermoelectric materials, copper sulfide, crystal structure, conductivity, thermal conductivity, Seebeck coefficient, superionic conductors.

Introduction

Copper sulfide has proven to be a more efficient material in solar cells [1]. CES with Cu_2S–CDs heterojunction attract attention due to the real possibility of their wide application as ground-based photovoltaic energy converters; in addition, the study of the properties of the heterojunction is of considerable scientific interest.

One of the first methods for producing a thin Cu_2S film in a Cu_2S–CDs solar cell consists in dipping a substrate with a deposited CDs layer with a solution heated to 90 °C containing copper ions, in which 2 g of NaCl and 6 g of CuCl per 1 liter of H_2O (pH ~3...4). As a result of the substitution reaction, a Cu_2S film with a thickness of 30 nm is formed on the surface of CDs. The efficiency of such a solar cell reaches 10 % [1].

Copper selenide has also performed well in the composition of solar cells. $Cu_{2-x}Se$-*n*-Si hetero junction elements with an efficiency of 8.8 % were manufactured on monocrystalline *n*-Si substrates by $Cu_{2-x}Se$ thermal sputtering [2, 3]. During spraying, a pre-synthesized material is used, which is evaporated either from the liquid phase or from a red-hot rod. With such a technology for manufacturing solar cells, nonstoichiometric copper selenide can be used, obtained according to the methods developed in this project.

Modern silicon solar cells have achieved very high efficiency — about 25 %. One of the interesting directions is the use of quantum dots, which makes it possible to obtain layers with different band gap widths from the same material, for example, silver sulfide. It is in optical devices that nanotechnology products are used, including in SE.

Experimental part

The technique of synthesis of $Cu_{2-x}S$ nanodiscs. The following chemicals are used for the synthesis of nanodiscs: copper (I) chloride (CuCl, 99.995 %), oleylamine (OAm, 70 %), sulfur (S) powder (99.98 %) and trioctylphosphine oxide (TOPO, technical grade 90 %).

The synthesis of Cu_2S nanoplates is carried out in one stage. The diameter of the resulting discs is about 20–30 nm, the thickness is 3–5 nm.

The required amount of CuCl (0.25–0.5 mmol — depending on the desired nonstoichiometry *x*) is mixed with 1 mmol of sulfur powder, 4 g of trioctylphosphinoxide (TOPO) and 10 ml of oleylamine (OAm). The solution is degassed at room temperature in a nitrogen atmosphere, then heated to 85 °C and maintained at this temperature for 1 hour. After that, the heating jacket is Cu_2S removed and 20–30 ml of ethanol is injected, the temperature decreases to ~ 40 °C. The resulting Cu_2S powder is collected by centrifugation at 9000 rpm for 1 min. The collected Cu_2S samples are re-dispersed in chloroform. This procedure is repeated twice to clean the prepared Cu_2S. Then the obtained samples are dried at a temperature of 40–50 °C.

An X-ray phase analysis of the obtained compacted nanocrystalline and powder samples was performed at room temperature (Tables 1–3). The identification of X-ray reflexes was carried out.

Table 1

Results of RFA $Cu_{1.85}S$

No.	2 θ, (deg)	d, (ang.)	Height (cps)	FWHM (deg)	Size (ang.)	Phase name	Chemical formula
1	24.705(7)	3.6008(11)	163(26)	0.10(2)	830(172)	Unknown	
2	26.533(11)	3.3567(14)	479(45)	0.121(16)	706(95)	Roxbyite(2,-3,2),chalcocite, high, copper(I) sulfide(1,0,0)	$Cu_{29}S_{16}$, Cu_2S
3	29.783(11)	2.9974(11)	460(44)	0.15(2)	566(93)	Roxbyite(2,-4,0),chalcocite, high, copper(I) sulfide(1,0,1)	$Cu_{29}S_{16}$, Cu_2S
4	31.209(8)	2.8636(8)	763(57)	0.121(10)	714(59)	Roxbyite(1,3,-4)	$Cu_{29}S_{16}$
5	34.059(4)	2.6302(3)	866(60)	0.096(8)	904(76)	Roxbyite(5,1,0)	$Cu_{29}S_{16}$
6	35.392(3)	2.5341(2)	1627(83)	0.071(6)	1233(97)	Roxbyite(0,4,-4)	$Cu_{29}S_{16}$
7	36.377(3)	2.4678(2)	2243(97)	0.122(5)	717(32)	Unknown	
8	37.920(10)	2.3708(6)	940(63)	0.232(10)	378(17)	Roxbyite(3,-2,5),chalcocite, high, copper(I) sulfide(1,0,2)	$Cu_{29}S_{16}$, Cu_2S
9	38.55(5)	2.333(3)	225(31)	0.71(6)	123(11)	Roxbyite(1,-5,-3)	$Cu_{29}S_{16}$
10	42.244(12)	2.1376(6)	460(44)	0.19(3)	478(72)	Unknown	
11	43.296(3)	2.08806(13)	389(40)	0.066(10)	1352(198)	Sulfur-III(1,0,-1)	S
12	46.309(13)	1.9590(5)	294(35)	0.30(7)	304(73)	Roxbyite(6,2,3)	$Cu_{29}S_{16}$
13	46.909(9)	1.9353(4)	1098(68)	0.257(14)	352(19)	Roxbyite(0,6,-4),chalcocite, high, copper(I) sulfide(1,1,0)	$Cu_{29}S_{16}$, Cu_2S
14	47.99(3)	1.8942(13)	147(25)	0.17(7)	522(216)	Roxbyite(5,-5,0)	$Cu_{29}S_{16}$
15	48.942(6)	1.8596(2)	1424(77)	0.196(12)	464(28)	Roxbyite(6,4,0),chalcocite, high, copper(I) sulfide(1,0,3)	$Cu_{29}S_{16}$, Cu_2S
16	54.71(3)	1.6763(8)	340(38)	0.24(3)	391(50)	Chalcocite, high, copper(I) sulfide(1,1,2)	Cu_2S
17	56.437(9)	1.6291(2)	190(28)	0.17(2)	570(83)	Chalcocite, high, copper(I) sulfide(2,0,1)	Cu_2S
18	61.32(3)	1.5107(6)	346(38)	0.37(5)	262(32)	Unknown	
19	73.45(2)	1.2882(3)	192(28)	0.13(4)	793(252)	Unknown	
20	74.92(9)	1.2665(13)	78(18)	0.34(17)	312(157)	Chalcocite, high, copper(I) sulfide(2,1,0)	Cu_2S

Name: **Roxbyite**	Name: **chalcocite**, high, copper(I) sulfide
Chemical Formula: $Cu_{29}S_{16}$	Chemical Formula: Cu_2S
Z value: 4	Z value: 2
Space Group: P-1(2)	Space Group: P63/mmc(194)
Cell: 13.4090 13.4051 15.4852 90.022 90.021 90.020	Cell: 3.9590 3.9590 6.7840 90.000 90.000 120.000
Volume: 2783.448	Volume: 92.085
Crystal System: Triclinic	Crystal System: Hexagonal
Reference: Mumme, W.G., Gable, R.W., Petricek, V. Can. Mineral. 50 (2012) 423.	Reference: Cava, R.J., Reidinger, F., Wuensch, B.J. Solid State Ionics 5 (1981) 501.

Table 2

Results of RFA $Cu_{1.80}S$

2-theta (deg)	d (ang.)	Height (cps)	FWHM (deg)	Size (ang.)	Phase name	Chemical formula
12.261(11)	7.213(7)	199(12)	0.115(17)	727(109)	Unknown	Unknown
20.929(5)	4.2411(10)	144(10)	0.06(9)	1445(2251)	Roxbyite(3,1,0)	$Cu_{29}S_{16}$
24.741(9)	3.5956(13)	141(10)	0.15(3)	563(123)	Roxbyite(2,3,-1), Copper Sulfide(1,1,0)	$Cu_{29}S_{16}$,CuS_2
26.55(3)	3.355(4)	374(16)	0.15(2)	559(79)	Roxbyite(2,-3,2), ?-Cu_2S(1,0,0)	$Cu_{29}S_{16}$,Cu_2S
27.79(3)	3.207(4)	80(7)	0.47(10)	182(40)	Roxbyite(2,-1,4)	$Cu_{29}S_{16}$
29.798(8)	2.9959(8)	274(14)	0.30(3)	289(25)	Roxbyite(2,-3,3),?-Cu_2S(1,0,1)	$Cu_{29}S_{16}$, Cu_2S
31.217(14)	2.8629(13)	482(18)	0.152(16)	566(60)	Roxbyite(1,3,-4)	$Cu_{29}S_{16}$
34.09(2)	2.6279(15)	568(20)	0.16(5)	552(187)	Roxbyite(5,1,0)	$Cu_{29}S_{16}$
35.435(7)	2.5312(5)	4395(54)	0.10(3)	859(220)	Roxbyite(0,4,-4), Copper Sulfide(1,1,1)	$Cu_{29}S_{16}$, CuS_2
36.366(4)	2.4685(3)	2765(43)	0.094(16)	932(160)	Unknown	Unknown
36.54(5)	2.457(3)	388(16)	0.26(4)	330(46)	Roxbyite(2,-5,-1), Copper Sulfide(1,2,0)	$Cu_{29}S_{16}$, CuS_2
37.882(13)	2.3731(8)	844(24)	0.22(4)	399(64)	Roxbyite(3,-2,5),?-Cu_2S(1,0,2)	$Cu_{29}S_{16}$, CuS_2
38.704(14)	2.3246(8)	471(18)	0.27(2)	320(24)	Unknown	Unknown
42.219(16)	2.1388(8)	267(13)	0.30(5)	300(49)	Copper Sulfide(2,1,0)	CuS_2
46.38(2)	1.9562(10)	275(14)	0.34(5)	267(43)	Roxbyite(6,2,3)	$Cu_{29}S_{16}$
46.910(5)	1.93527(18)	848(24)	0.26(2)	345(27)	Roxbyite(0,6,-4),?-Cu_2S(1,1,0)	$Cu_{29}S_{16}$, CuS_2
47.981(7)	1.8946(3)	155(10)	0.14(3)	627(116)	Roxbyite(5,-5,0)	$Cu_{29}S_{16}$
48.670(6)	1.8693(2)	604(20)	0.115(12)	794(86)	Unknown	Unknown
48.925(8)	1.8602(3)	1110(27)	0.213(13)	428(27)	Roxbyite(6,4,0),?-Cu_2S(1,0,3)	$Cu_{29}S_{16}$, Cu_2S
54.738(12)	1.6756(3)	274(14)	0.23(4)	403(63)	?-Cu_2S(1,1,2)	Cu_2S
56.496(17)	1.6275(4)	110(9)	0.26(5)	367(73)	?-Cu_2S(2,0,1)	Cu_2S
61.31(2)	1.5109(5)	394(16)	0.28(4)	349(49)	Copper Sulfide(0,2,2)	CuS_2
65.73(7)	1.4194(14)	95(8)	0.80(11)	123(17)	Copper Sulfide(3,0,1)	CuS_2
68.09(4)	1.3759(8)	119(9)	0.30(8)	335(91)	Unknown	Unknown
73.40(6)	1.2889(9)	137(10)	0.29(7)	360(86)	Copper Sulfide(1,4,1)	CuS_2
74.996(9)	1.26541(13)	956(25)	0.083(8)	1264(123)	Copper Sulfide(3,2,1)	CuS_2

Name: **Roxbyite**	Name: **Copper disulfide**
Chemical Formula: $Cu_{29}S_{16}$	Chemical Formula: CuS_2
Z value: 4	Z value: 2
Space Group: P-1(2)	Space Group: Pnnm(58)
Cell: 13.4090 13.4051 15.4852 90.022 90.021 90.020	Cell: 4.6510 5.7930 3.5320 90.000 90.000 90.000
Volume: 2783.448	Volume: 95.164
Crystal System: Triclinic	Crystal System: Orthorhombic
Reference: Mumme, W.G., Gable, R.W., Petricek, V. Can. Mineral. 50 (2012) 423.	Reference: Kjekshus, A., Rakke, T. Acta Chem. Scand., Ser. A33(1979)617.

Table 3

Results of RFA $Cu_{1.75}S$

2-theta (deg)	d (ang.)	Height (cps)	FWHM (deg)	Size (ang.)	Phase name	Chemical formula
20.931(11)	4.241(2)	117(9)	0.11(5)	772(368)	Roxbyite(3,-1,0)	$Cu_{58}S_{32}$
24.70(2)	3.601(3)	135(10)	0.15(4)	575(150)	Roxbyite(1,-1,-4),Djurleite, syn(7,1,1)	$Cu_{58}S_{32}$, $Cu_{31}S_{16}$
26.55(3)	3.355(3)	313(15)	0.18(3)	486(93)	Roxbyite(2,-3,2),Djurleite, syn(8,0,0)	$Cu_{58}S_{32}$, $Cu_{31}S_{16}$
29.802(8)	2.9955(8)	272(14)	0.34(3)	253(20)	Roxbyite(2,-2,-4),Djurleite, syn(4,0,-4)	$Cu_{58}S_{32}$, $Cu_{31}S_{16}$
31.181(7)	2.8661(6)	621(20)	0.104(13)	829(107)	Roxbyite(1,-3,-4),Djurleite, syn(9,1,-1)	$Cu_{58}S_{32}$, $Cu_{31}S_{16}$
34.09(2)	2.6278(19)	461(18)	0.18(2)	474(55)	Roxbyite(5,-1,0),Djurleite, syn(4,5,-2)	$Cu_{58}S_{32}$, $Cu_{31}S_{16}$
35.39(2)	2.5342(17)	415(17)	0.20(5)	432(116)	Roxbyite(5,0,2),Djurleite, syn(2,6,-1)	$Cu_{58}S_{32}$, $Cu_{31}S_{16}$
36.399(6)	2.4663(4)	2192(38)	0.160(7)	545(24)	Djurleite, syn(3,5,3)	$Cu_{31}S_{16}$
37.571(11)	2.3920(7)	374(16)	0.58(5)	152(14)	Djurleite, syn(11,1,0)	$Cu_{31}S_{16}$
37.928(3)	2.37030(17)	653(21)	0.135(18)	648(88)	Roxbyite(1,-2,-6)	$Cu_{58}S_{32}$
42.24(4)	2.1380(19)	380(16)	0.34(5)	263(37)	Roxbyite(2,-3,-6),Djurleite, syn(9,2,4)	$Cu_{58}S_{32}$, $Cu_{31}S_{16}$
43.296(3)	2.08809(13)	550(19)	0.064(11)	1399(248)	Copper, syn(1,1,1)	Cu
46.403(10)	1.9552(4)	515(19)	0.26(2)	343(27)	Djurleite, syn(3,7,-3)	$Cu_{31}S_{16}$
46.90(2)	1.9356(8)	795(23)	0.26(2)	344(28)	Roxbyite(0,0,8),Djurleite, syn(5,6,-4)	$Cu_{58}S_{32}$, $Cu_{31}S_{16}$
48.630(11)	1.8708(4)	704(22)	0.129(15)	705(80)	Djurleite, syn(2,8,-2)	$Cu_{31}S_{16}$
48.925(15)	1.8602(5)	1015(26)	0.24(3)	383(42)	Roxbyite(4,-3,-6)	$Cu_{58}S_{32}$
54.75(4)	1.6753(13)	256(13)	0.32(7)	292(65)	Roxbyite(8,0,0)	$Cu_{58}S_{32}$
56.46(7)	1.6284(18)	141(10)	0.24(8)	400(129)	Roxbyite(2,-4,-8)	$Cu_{58}S_{32}$
61.30(4)	1.5110(9)	280(14)	0.36(7)	265(48)	Unknown	Unknown
73.39(12)	1.2891(17)	111(9)	0.72(15)	144(31)	Copper, syn(2,2,0)	Cu

Name: **Roxbyite**	Name: **Djurleite**, syn
Chemical Formula: $Cu_{29}S_{16}$	Chemical Formula: $Cu_{31}S_{16}$
Z value: 4	Z value: 8
Space Group: P-1(2)	Space Group: P21/n(14)
Cell: 13.4090 13.4051 15.4852 90.022 90.021 90.020	Cell: 26.8970 15.7450 13.4650 90.000 90.130 90.000
Volume: 2783.448	Volume: 5702.322
Crystal System: Triclinic	Crystal System: Monoclinic
Reference: Mumme, W.G., Gable, R.W., Petricek, V. Can. Mineral. 50 (2012) 423.	Reference: Potter, II, R., Evans, Jr. J. Research U. S. Geol. Surv.4 (1976) 205.

X-ray phase analysis was performed on a Bruker diffractometer (Germany) using radiation from a CuKa X-ray tube and a graphite monochromator on a diffracted beam. Diffractograms were recorded in the range of angles 2θ from 20 to 110, with a step of 2θ = 0.02. The BrukerAXSDIFFRAC.EVAv software was used to identify the phases.4.2 and the international database ICDD PDF-2.

$Cu_{1.75}S$ samples at room temperature contain the rhombic phase of anilite with parameters a = 7.8902 and 7.8938 Å, b = 7.8408 and 7.8433 Å, c = 11.011 and 11.012 Å, respectively, and the hexagonal phase of digenite with the spatial group R-3m (166) and parameters a = 3.94310 Å and 3.94437 Å, c = 48.43262 Å and 48.43325 Å respectively.

The difference in the parameters of the crystal lattice due to changes in the interplane distances of samples with different sodium content, as well as the broadening of diffraction lines on diffractograms, may be due to microstresses in the structure, which are associated with the accumulation of dislocations, as well as the fragmentation of crystallites associated with crystallization processes. The analysis of the angular dependence of the physical broadening makes it possible to assess the influence of both factors. The Williamson-Hall method was used to assess the impact.

The size of the crystallites was estimated based on the width of the X-ray lines. The crystallite sizes in all samples range from 30 to 90 nm, which is due to the method of synthesis of sodium and potassium hydroxides in the melt.

Phase transitions and thermal effects in the Cu_2S sample were studied using the DSC 404 F1 Pegasus device (NETZSCH, Germany) in an argon atmosphere in the temperature range (300–600) K. The heating rate was 10 K/min.

To calculate the heat capacity, three different measurements were carried out: baseline, standard (sapphire) and the test sample. The following parameters remained identical in all measurements: argon flow, argon flow rate, initial temperature, heating rate, mass of the crucible and lid, the crucibles on the sensor were oriented, maintaining their position on the sensor. During the measurement, a program was used that includes holding the sample at a constant temperature (at least half an hour) in an argon current, after which heating was carried out at a constant rate of 5 K/min. Measurements of the baseline and standard were carried out in the same mode. The DSC 404 F1 Pegasus allows for a calorimetric experiment with a small sample quantity, we used sample weights from 40 to 150 mg.

Figure 1 shows the curves of the Cu_2S DSC. There is an acute endothermic peak of DSC, the temperature of which lies within 381.5 K, depending on the composition. Heat capacity peaks are observed at the same temperatures.

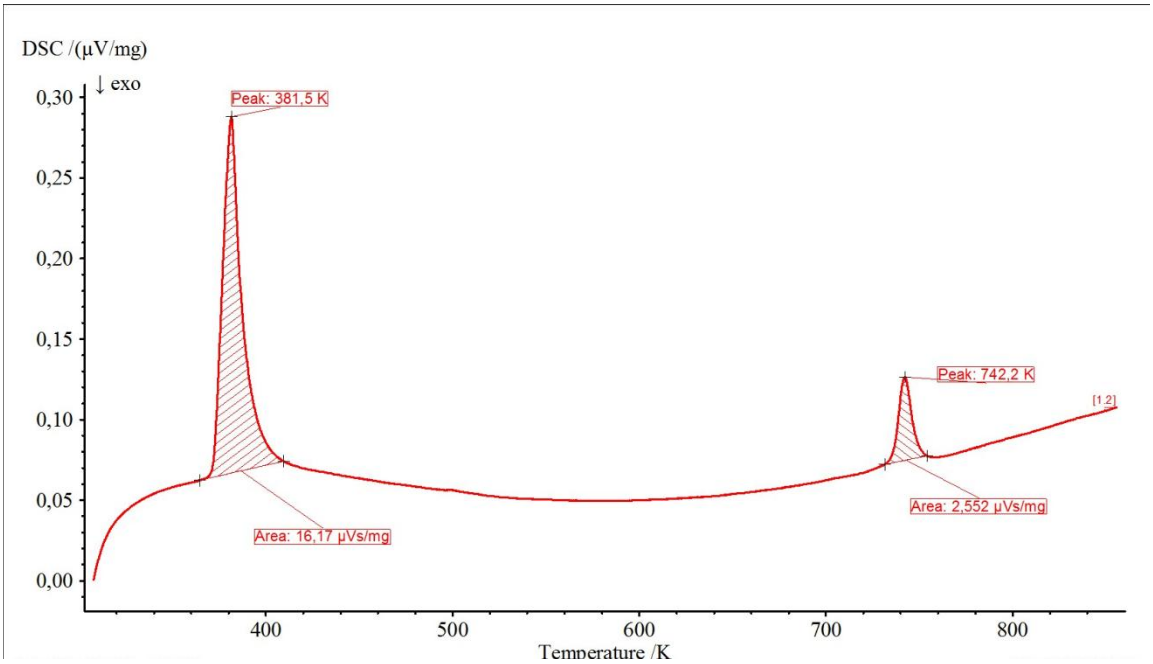

Figure 1. DSC curves of the sampleCu_2S

The structure of Cu_2S copper sulfide ((chalcosine), close to stoichiometric, according to Abrikosov N.H. [4]) has three modifications: orthorhombic below 105 °C, hexagonal below (420–450) °C and high-temperature cubic (phase). Figure 2 shows an image taken with a scanning electron microscope from the surface of Cu_2S powder obtained by electrohydrodynamic impact. It can be seen that the particles have the shape of ribbons and wires ranging in size from fractions of a micron to tens of microns.

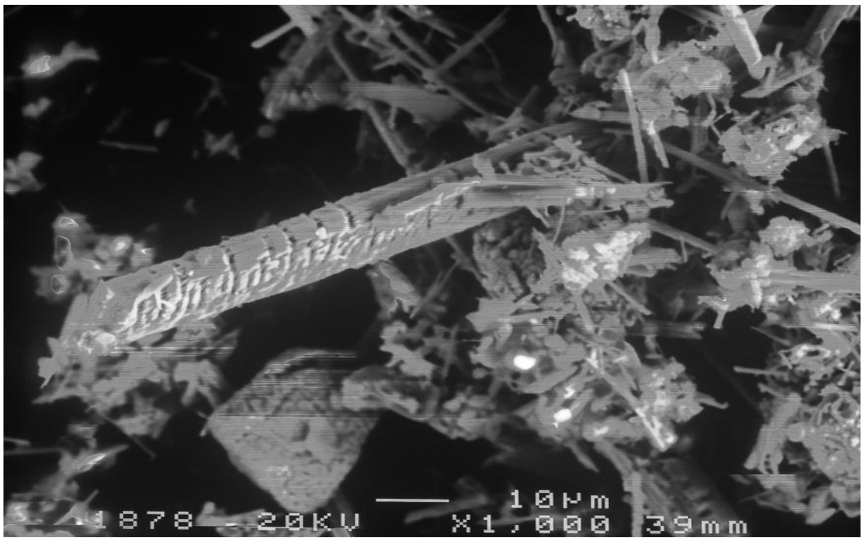

Figure 2. A snapshot of Cu_2S powder on a scanning electron microscope

Thermal conductivity measurements were carried out using the flash method on the LFA 467 HT HyperFlash device (NETZSCH, Germany). Thermal conductivity (k) was found from three measurements:

$$k(T)=a(T)*\rho(T)*c_p(T),$$

where T is temperature, k is thermal conductivity, a is thermal conductivity, ρ is bulk density, c_p is specific heat capacity.

The thermal conductivity a was determined using the LFA 467 HT installation according to the Parker formula from the analysis of the time dependence of the temperature of the opposite side of the sample after short-term heating of one side of the sample by a powerful light pulse. The values of the c_p heat capacity were measured on a DSC 404 F1 Pegasus DSC calorimeter (NETZSCH, Germany) in an argon atmosphere. The density of the sample was found from measurements of weight and volume. Figure 2 shows the temperature dependences of the thermal conductivity, heat capacity and thermal conductivity of Cu_2S.

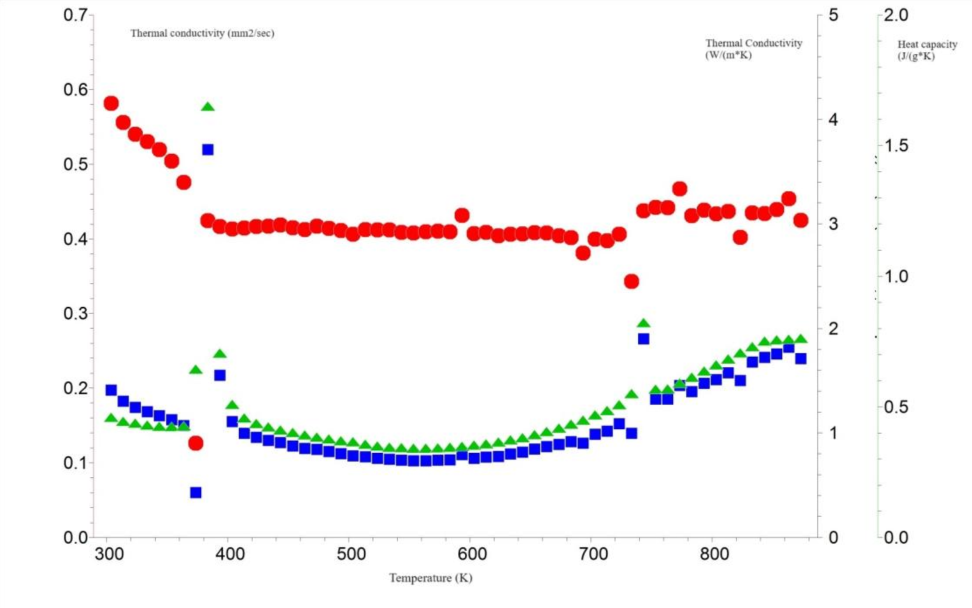

Figure 3. Temperature dependence of thermal conductivity Cu_2S

The thermal conductivity of the Cu_2S sample is quite low, it rises to 0.3 W/m*K at a phase transition of about 380 K and does not fall below 0.2 W/m*K.

In the semiconductor under consideration, the concentration of impurity carriers of electrons in the conduction band and holes in the valence band is usually much higher than the concentration of uncontrolled impurities and equilibrium point defects. The concentration of n_i native carriers is determined by the temperature and the width of the band gap. In most cases, n_i is also significantly less than n_t. In this case, the temperature dependence of the electronic conductivity is determined by the temperature dependence of the mobility and has a metallic character [5, 6]. Figure 4 shows the temperature dependence of the electron thermo-emf coefficient of the Cu_2S sample.

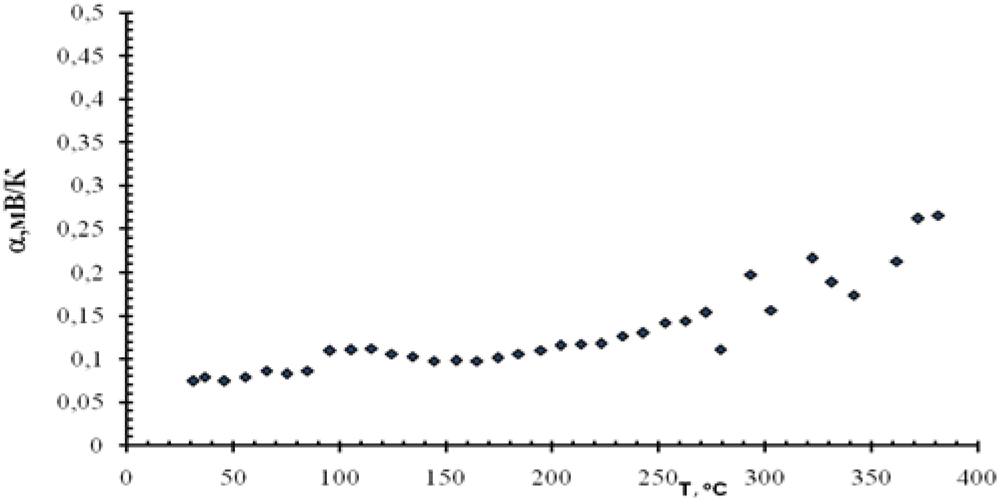

Figure 4. Temperature dependence of the coefficient of electronic thermo-emf of a coarse-grained sample Cu_2S

The coefficient of thermal EMF strongly depends on the nonstoichiometry of the sample and is maximum for a composition close to saturation with copper. The temperature dependence of the electron thermal emf coefficient of the Cu_2S sample has rather low values here from 0.05 mV/K to 0.25 mV/K, which are more typical for metals than for semiconductors.

Figure 5 shows the temperature dependence of the electron conductivity of coarse-grained Cu_2S. It can be seen from the figure that the semiconductor temperature dependence of about 185 °C changes to a metallic type of dependence.

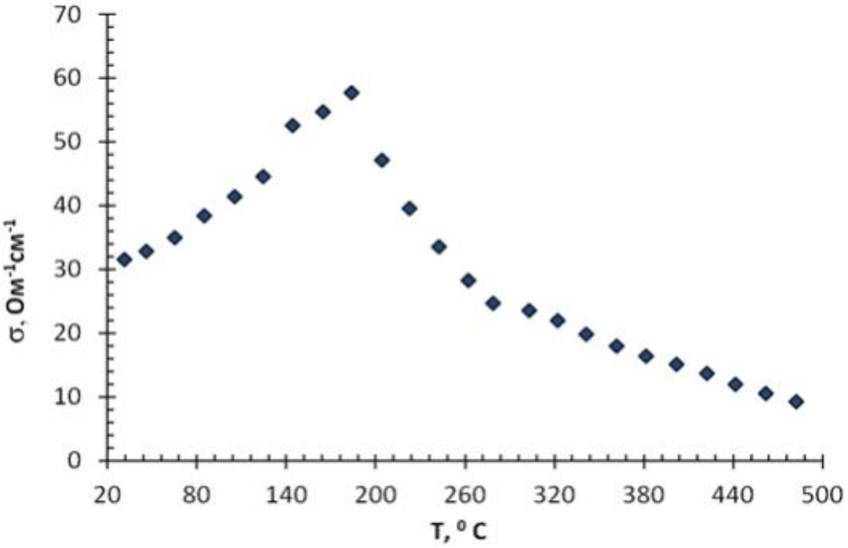

Figure 5. Temperature dependence of the conductivity of a large-crystal Cu_2S

During annealing, the conductivity of polycrystalline samples usually increases with grain growth, and a similar dependence is observed here. The reasons for this behavior of kinetic coefficients are changes in the specific gravity in the total volume of grain boundary layers, which increase the concentration of defects — scattering centers for current carriers.

For the Cu_2S sample, a phase transition of about 400 K is clearly visible on the temperature dependence of the conductivity (according to the literature data — 403 K), corresponding peaks are also present on the temperature dependence of the DSC.

Conclusion

Copper chalcogenides have a complex electronic structure due to the interaction of hybridized *s*- and *p*-states of chalcogen forming a valence band with 3*d* states of copper [7, 8], which greatly complicates the interpretation of temperature dependences of kinetic parameters having a nonmonotonic character.

Cu_2S copper sulfide is an effective thermoelectric material, so it is interesting to study its kinetic parameters of solid solutions that it forms with alkali metals. The nonstoichiometry of chalcogenides can be easily controlled electrochemically, therefore, the task of selecting the optimal composition according to the cationic sublattice is quite feasible. In addition, to improve the thermoelectric properties, it can be achieved by alloying lithium into a binary copper sulfide matrix, we obtained a high ZT with local maxima that reaches up to 2 [9]. When doped with sodium, this indicator reached up to 1 [10, 11]. Thus, the work on the synthesis of copper sulfides of different composition and morphology is in the current trend of searching for new thermoelectric materials and allows us to hope for practical application of the obtained materials in the near future.

Acknowledgments

The Science Committee of the Republic of Kazakhstan, which is part of the Ministry of Science and Higher Education, provided funding for this research (No. AP14871197).

References

1 Chopra, K. & Das, S. (1986). Thin−film solar cells. Moscow: Mir, 435 p.

2 Scheer, R. & Schock, H.-W. (2011). *Chalcogenide Photovoltaics: Physics, Technologies, and Thin Film Devices*. Ed. 2011 WILEY-VCH Verlag & Co. KGaA, Germany, 386.

3 Okimura, H., Matsumae, T., & Makabe, R.J.T.S.F. (1980). Electrical properties of $Cu_{2-x}Se$ thin films and their application for solar cells. *Thin Solid Films, 71*(1), 53–59.

4 Abrikosov, N.H., Bankina, V.F., Poretskaya, L.V., Skudnova, E.V., & Chizhevskaya, S.N. (1975). Semiconductor chalcogenides and alloys based on them. Moscow: Nauka, 220 p.

5 Berezin, V.M. & Vyatkin, G.P. (2001). Superionic semiconductor chalcogenides. Chelyabinsk: Publishing house of South Ural State University, 135 p.

6 Khassenov, A.K., Karabekova, D.Zh., Nussupbekov, B.R., G.A. Bulkairova, A.S. Kudusov, Alpysova, G.K., & Bolatbekova, M.M. (2023). Investigation of the influences of pulsed electrical discharges on the grinding of quartz raw materials. *Bulletin of the University of Karaganda – Physics, 2*(110), 93–99.

7 Domashevskaya, E.P., Terekhov, V.A., Kashkarov, V.M., Panfilova, E.P., Gorbachev, V.V., & Shchukarev, A.V. (2000). *d-p* resonance in some copper chalcogenides according to X-ray ultra-soft emission and X-ray photoelectron spectroscopy data. *Condensed media and interphase boundaries, 2*(4), 353–357.

8 Lavrentiev, A.A., Nikiforov, I.Ya., Dubeyko, V.A., Gabrelyan, B.V., Domashevskaya, E.P., Rehr, J.J., & Ankudinov, A.L. (2001). *d-p*-resonance effect in copper compounds with various crystalline structures. *Condensed media and interphase boundaries, 3*(4), 107–121.

9 Balapanov, M.H., Kuterbekov, K.A., Ishembetov, R.H., Kurbanova, M.M., Kabyshev, A.M., Bekmyrza, K., & Yakshibaev, R.A. New thermoelectric material $Li_{0.15}Cu_{1.85}S$ Eurasian patent No.030605, 08/31/2018.

10 Balapanov, M.Kh., Ishembetov, R.Kh., Kuterbekov, K.A., Almukhametov, R.F., & Yakshibaev, R.A. (2018). Transport phenomena in superionic $Na_xCu_{2-x}S$ (x = 0,05; 0,1; 0,15; 0,2) compounds. *Ionics, 24*(5), 1349–1356. DOI:10.1007/s11581-017-2299-z

11 Kuterbekov, K.A., Balapanov, M.K., Kubenova, M.M., Ishembetov, R.Kh., Zeleev, M.Kh., Yakshibaev, R.A., Kabyshev, A.M., Alina, R.A., Bekmyrza, K.Zh., Baikhozhaeva, B.U., Abseitov, E.T., & Taimuratova, L.U. (2022). Chemical diffusion and ionic conductivity in nonstoichiometric nanocrystalline superionic $Na_xCu_{1.75}S$ (x = 0.1, 0.15, 0.2, 0.25) materials. *Ionics, 28,* 4311–4319. https://doi.org/10.1007/s11581-022-04651-y

М.М. Кубенова, К.А. Кутербеков, М.Х. Балапанов, Р.Х. Ишембетов,
Г.Д. Кабдрахимова, Р.А. Алина, М. Татай, Р. Ильдос

Cu_2S бинарлы мыс сульфидінің жылулық қасиеттері

Мыс халькогенидтері валенттік аймақты құрайтын гибридтелген *s*- және *p*- халькоген күйлерінің 3*d* мыс күйлерімен өзара әрекеттесуіне байланысты күрделі электрондық құрылымға ие, бұл қасиеттер монотонды емес сипаттағы кинетикалық параметрлердің температураға тәуелділігін интерпретациялауды қиындатады. Cu_2S мыс сульфиді тиімді термоэлектрлік материал болып табылады, сондықтан оның сілтілі металдарды құрайтын қатты ерітінділерінің кинетикалық параметрлерін зерттеу өте қызықты. Мақалада Cu_2S бинарлы мыс сульфидінің қасиеттерінің эксперименттік зерттеулер нәтижелері ұсынылған. Cu_2S үлгісі үшін жартылай өткізгіштерге қарағанда металдарға тән 0,05 мВ/К-ден 0,25 мВ/К-ге дейінгі үлгінің электронды термо-эқк өте төмен мәндері анықталды. Cu_2S үлгісінің жылу өткізгіштігі өте төмен, ол шамамен 380 К фазалық ауысу кезінде 0,3 Вт/м*К-ге дейін көтеріледі және 0,2 Вт/м*К-ден төмен түспейді. Сонымен қатар халькогенидтерді стехиометриясыз электрхимиялық оңай басқаруға болады, сондықтан катиондық қосалқы тор негізінде оңтайлы құрамды таңдау әбден мүмкін. Сондай-ақ Cu_2S термоэлектрлік қасиеттерін жақсарту үшін мыс сульфидінің бинарлы матрицасына сілтілі металдарды легирлеу кезінде қол жеткізуге болады.

Кілт сөздер: термоэлектрлік материалдар, мыс сульфиді, кристалдық құрылым, өткізгіштік, жылу өткізгіштік, Зеебек коэффициенті, суперионды өткізгіштер.

М.М. Кубенова, К.А. Кутербеков, М.Х. Балапанов, Р.Х. Ишембетов,
Г.Д. Кабдрахимова, Р.А. Алина, М. Татай, Р. Ильдос

Тепловые свойства бинарного сульфида меди Cu_2S

Халькогениды меди обладают сложной электронной структурой из-за взаимодействия гибридизованных *s*- и *p*- состояний халькогена, образующих валентную зону, с 3*d*-состояниями меди, что сильно затрудняет интерпретацию температурных зависимостей кинетических параметров, имеющих немонотонный характер. Сульфид меди Cu_2S является эффективным термоэлектрическим материалом, поэтому интересно исследовать его кинетические параметры твердых растворов, которые он образует с щелочными металлами. Нестехиометрией халькогенидов можно легко управлять электрохимически, поэтому задача подбора оптимального состава по катионной подрешетке является вполне осуществимой. В статье представлены экспериментальные исследования свойств бинарного сульфида меди Cu_2S. Для образца Cu_2S обнаружены довольно низкие значения коэффициента электронной термо-эдс образца от 0,05 мВ/К до 0,25 мВ/К, характерные более для металлов, чем для полупроводников. Теплопроводность образца Cu_2S является достаточно низкой, она поднимается до 0,3 Вт/м*К при фазовом переходе около 380 К и не опускается ниже 0,2 Вт/м*К. Таким образом, нестехиометрией халькогенидов можно легко управлять электрохимически, поэтому задача подбора оптимального состава по катионной подрешетке является вполне осуществимой. Кроме того, улучшения термоэлектрических свойств Cu_2S можно достичь при легировании щелочных металлов в матрицу бинарного сульфида меди.

Ключевые слова: термоэлектрические материалы, сульфид меди, кристаллическая структура, проводимость, теплопроводность, коэффициент Зеебека, суперионные проводники.

Information about authors

Kubenova, M.M. — PhD, Research teacher, Department of Standardization and Certification, L.N. Gumilyov Eurasian National University, Astana, Kazakhstan. ORCID: https://orcid.org/0000-0003-2012-2702

Kuterbekov, K.A. — Doctor of physical and mathematical sciences, Professor of the International Department of Nuclear Physics, new materials and technologies, L.N. Gumilyov Eurasian National University, Astana, Kazakhstan. ORCID: https://orcid.org/0000-0001-7116-1520

Balapanov, M.Kh. — Doctor of physical and mathematical sciences, Professor of the Department of General Physics, Ufa University of Science and Technology, Ufa, Russia. ORCID: https://orcid.org/0000-0001-788 5-9462

Ishembetov, R.Kh. — Candidate of physical and mathematical sciences, Docent of the Department of General Physics, Ufa University of Science and Technology, Ufa, Russia. ORCID: https://orcid.org/0000-0002-0938-3998

Kabdrakhimova, G.D. — PhD, Associate professor of the International Department of Nuclear Physics, new materials and technologies, L.N. Gumilyov Eurasian National University, Astana, Kazakhstan. ORCID: https://orcid.org/0000-0003-2453-1028

Alina, R.A. — Doctoral student, L.N. Gumilyov Eurasian National University, Astana, Kazakhstan.

Tatay, M. — Student, L.N. Gumilyov Eurasian National University, Astana, Kazakhstan.

Ildos, R. — Student, L.N. Gumilyov Eurasian National University, Astana, Kazakhstan.

Article

Received: 25.09.2023
Accepted: 08.12.2023

UDC 533.9.07

https://doi.org/10.31489/2024PH1/23-33

L.G. Sulyubayeva[1, 2], B.K. Rakhadilov[1], Y. Naimankumaruly[1],
M.B. Bayandinova[1], N. Muktanova[1], N.E. Berdimuratov[2*]

[1]PlasmaScience LLP, Ust-Kamenogorsk, 070000, Kazakhstan;
[2]Research Center Surface Engineering and Tribology, Sarsen Amanzholov East Kazakhstan University, Ust-Kamenogorsk, 070000, Kazakhstan
[*]Corresponding author's e-mail: nurbol.ber@gmail.com)

Study of changes in the surface structure of tungsten irradiated by helium plasma

One of the important aspects is the interaction of plasma with the surface of a material, especially in the conditions of a fusion facility. The current work presents the preliminary results of the study of tungsten surface structure modification under helium plasma irradiation. A small-sized linear simulator KAZ-PSI with a plasma-beam setup was designed and assembled, where helium was used as a working gas. The main elements of the linear plasma simulator are an electron beam gun with a LaB6 cathode, a plasma-beam discharge chamber, an interaction chamber, a target device, and an electromagnetic system consisting of electromagnetic coils. It was revealed that under irradiation on the surface of the samples there is a relief with defective structure consisting of chaotically arranged ledges and pits of various shapes with average size (100–600) nm and pore sizes (0.1–1.5) μm with visible areas of flaking and sputtering. It was found that when the negative potential on the target is varied by –500V/–1000V/–1500V, the formation of dislocation with chaotic and cellular structure of tungsten with an average grain size of (1–25) μm is observed; it was revealed that the total values of elastic and plastic components of deformation across the tungsten grain differ from each other by about 2.5 times.

Keywords: tungsten, helium plasma, structure, surface modification, quantitative parameters of fine structure, plasma generator, surface.

Introduction

As it is known, to the present day, the successful implementation of the International Thermonuclear Experimental Reactor (ITER) project and new advances in next-generation nuclear fusion reactors such as ITER and China Fusion Engineering Test Reactor (CFETR), Demonstration Fusion Power Plant (DEMO) contribute to the development of nuclear energy and fusion and bring them to a new frontier [1–3]. Materials in fusion devices withstand severe exposure to high-temperature plasma, which promotes the development of radiation defects and subsequently leads to material damage. Therefore, the problem of improving the properties and performance characteristics of materials remains one of the important tasks for fusion energy [4]. According to the authors of the review paper [5] in the ITER facility [1], protective materials must withstand three conditions simultaneously: first, the effects of surface sputtering, blistering, and erosion during the interaction of the particles flying out of the plasma without excessive contamination of the core plasma; second, due to the rapid release of energy during plasma rupture, a relatively high steady-state surface heat load of ~10 $MW \cdot m^{-2}$ and a transient heat load of ~20 $MW \cdot m^{-2}$ are released; third, resistance to damage from neutron radiation with energy 14.1 MeV, embrittlement from hydrogen (H) isotope (deuterium (D) and tritium (T))/helium (He) and gas swelling.

Along with other energy sources, nuclear fusion is seen as the most promising alternative to fossil fuels for a future carbon-free energy system. ITER, currently the largest fusion device under construction, is expected to provide a high thermal output of ~150 MW [6]. However, the extreme conditions created during ITER operation pose significant challenges for the plasma facing materials (PFM) in the divertor of the fusion device; e.g., high heat flux deposition and particle bombardment. In the background of nuclear fusion reactor devices such as ITER and DEMO, tungsten (W) is considered as a potential and one of the most promising candidate PFM materials for plasma facing components (PFC) due to its high melting point, good thermal conductivity, low sputtering yield and low hydrogen solubility [7–8].

Helium atoms, which have low solubility in metals, can lead to undesirable changes in material properties, such as the formation of nanopores and bubbles [9, 12–13], blisters, etc. Experiments to determine the influence of helium performed in reactor experiments are very challenging due to the requirement for prolonged material irradiation. However, for a quick assessment of the influence of helium (hydrogen, deuterium) on material properties, valuable information is provided by simulation experiments on plasma generator stands, where atoms of the plasma-forming gas are introduced into the material through bombardment by helium ions in accelerators. In recent years, a series of experiments have been conducted on such linear simulation setups (NAGDIS-II, JULE-PSI, PISCES-A, LENTA, etc.), which have allowed important conclusions to be drawn about the nature of defects and the embrittlement and erosion mechanisms.

In the divertor, the tungsten material will face not only extreme heat fluxes but also high fluxes of low-energy particles such as deuterium, tritium, and helium. In many studies, it has been observed that exposure to helium plasma can induce the formation of nanobubbles under the tungsten surface [10, 11]. Their formation is due to the diffusion and clustering of helium atoms in the tungsten matrix [12], and the subsequent size of the nanobubbles increases as the temperature of tungsten increases during exposure [13, 14]. He atoms diffuse so rapidly and are deposited into He bubbles, causing embrittlement and curing problems in W. The rapid accumulation of He atoms also leads to microstructure evolution such as nucleation of He bubbles and subsequent formation of nano- and microscale “fluff” on the W surface at elevated temperatures, which significantly reduces the W properties themselves and affects the stability of the core plasma [15]. In the bulk of plasma facing components, He atoms can be formed by tritium decay and as a product of nuclear reactions induced by neutron irradiation. Due to the high defect binding energy, a high concentration of He can be rapidly achieved in the subsurface of PFC. This can sharply change the surface morphology and affect the erosion rate and the transfer of hydrogen isotopes into the bulk of PFC [16, 17].

Simulation facilities are very effective tools for testing candidate fusion reactor materials, to fill up the database on various aspects of plasma-surface interaction. Interest in modeling the interaction of plasma with fusion reactor material on simulation benches with gas-discharge plasma generators arose in the early eighties of the last century. With the help of ion-beam facilities, basic understanding of the elementary processes occurring under the action of ions on the surface of a solid body, such as sputtering of the material, capture and reflection of particles from it, has already been obtained. When the full-scale tokamak-reactor ITER is launched, where all damaging factors will be fully combined, one should expect the manifestation of new synergetic phenomena and effects, the study of which can rely to a large extent on the database and physical models developed in simulation experiments. At present, the Kazakhstan Materials Testing Tokamak with materials is used to test parameter measurement techniques in plasma interaction studies, and a plasma-beam facility was developed at the National Nuclear Center of the Republic of Kazakhstan in cooperation with foreign scientists to test Tokamak KTM diagnostic equipment. This plasma beam installation PBI-1 is located in the laboratory “Testing of materials under fusion reactor conditions”. With the use of this unit earlier authors [18–20] carried out works on the study of plasma interaction with stainless steel, tantalum, beryllium, tungsten and molybdenum samples, where systematized results of the effect of hydrogen and deuterium plasma on the microstructure, morphology and erosion of the surface of tungsten and molybdenum were obtained [21, 22]. The results showed that the degree of surface erosion increases with increasing target temperature and ion energy. It was found that during irradiation of tungsten and molybdenum with hydrogen plasma the main relief-forming mechanism is surface sputtering and erosion is characterized by thermal etching of the surface. After irradiation with hydrogen plasma, small cracks are observed on the samples, and the size and number of cracks increase with increasing temperature. It is revealed that after irradiation the structure of tungsten is more fragmented and characterized by a more developed defect substructure. The reason for the appearance of these structural disorders seems to be mechanical stresses in the tungsten lattice caused by implanted ions. Based on the obtained results, an in-depth study of the fine structure of plasma-irradiated tungsten is proposed, and the relationship between dislocation structure and erosion processes in tungsten is also established. In this regard, the aim of the present work is to investigate the changes in the fine structure of the surface of tungsten irradiated with low-temperature helium plasma on a newly developed small-size linear divertor plasma simulator.

Materials and methods

To test materials for plasma impact, a small-size linear plasma simulator KAZ-PSI was developed and assembled in PlasmaScience LLP (Republic of Kazakhstan, Ust-Kamenogorsk), which allows simulating the operation of thermonuclear facilities, in particular Tokamak KTM. The developed linear plasma simulator KAZ-PSI is universal and allows testing of materials under conditions of complex influence on them both plasma flow and powerful thermal load created with the help of electron beam.

The main elements of the plasma unit are an electron beam gun (EBG), a plasma-beam discharge chamber, a vacuum interaction chamber, a cooling target device, and an electromagnetic system consisting of electromagnetic coils [8]. The electron beam gun consists of a heated thermoemissive cylindrical cathode made of LaB_6 and a holed anode. The cathode is heated by resistive method and a 50 kW DC power supply is used for heating. The electron beam gun is cooling by compressed air flow.

The operating principle of the KAZ-PSI plasma SLS unit is as follows: the electron gun forms an electron beam of axially symmetric character, the gun cathode is heated by electron bombardment from the heater filament, which helps to adjust the gun power. The vacuum drop between the gun and the discharge chamber is realized by autonomous pumping of the gun. The plasma cord is formed in the discharge chamber by the interaction of the electron beam with the working gas (helium). In the discharge chamber, the electromagnetic system (a system of coils), which creates a longitudinal magnetic field, focuses the electron and plasma beams. By changing the value of electric current flowing through the electromagnetic coils, it is possible to manipulate the value of magnetic field strength in the plasma beam discharge chamber, thus controlling the beam diameter. The plasma discharge hits a sample of the material under test, which is placed on a target device in the interaction chamber. General view (Fig. 1a) and schematic (1b) images of the setup are shown in Figure 1 *a–b*, where the main components of the small-size linear simulator (SLS) are indicated: electron gun, vacuum sensor, electromagnetic coils, Langmuir probe, interaction chamber, target cooling, negative potential, residual gas analyzer, turbomolecular pump, forevacuum pump, personal computer for controlling the KAZ-PSI plasma SLS.

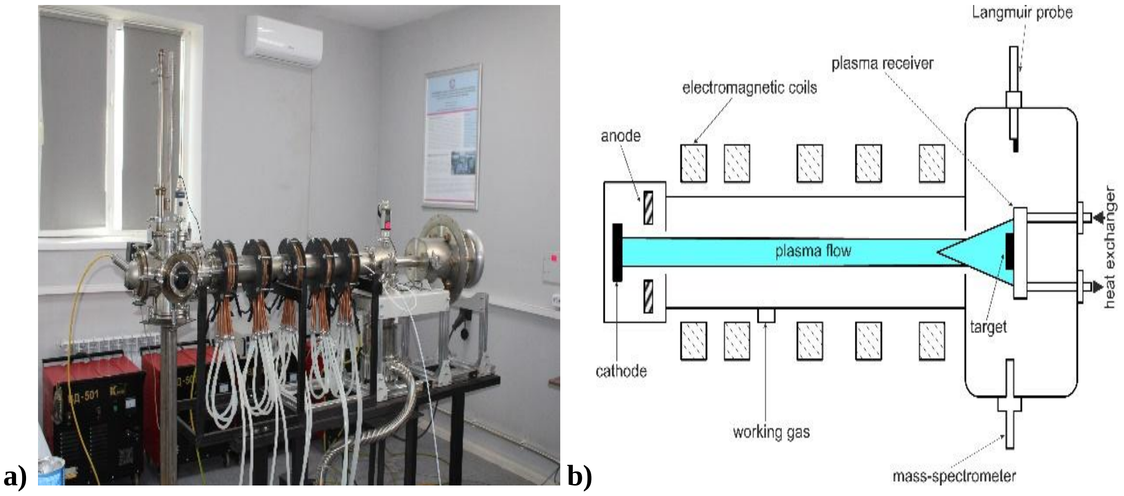

Figure 1. General view and schematic representation of KAZ-PSI plasma SLS and its main parts

Experiments in the KAZ-PSI plasma SLS were carried out in plasma-beam discharge regimes according to the previously worked out technological regimes. The samples were irradiated with helium plasma with ion energy of 1.5–2.5 keV for 3 hours, with the primary beam power of 250 W, the average value of total ion current at the target was 200–300 mA and the total ion current saturation had a value in the range of 4–8 mA. The regimes were varied according to the negative potential on the target: Regime 1 –500 V, Regime 2 –1000 V and Regime 3 –1500 V. During irradiation, the pressure in the chamber was $\sim 1.8\times10^{-3}$ Torr. Helium of special purity was used as the working gas.

In the present work, tungsten of 99.95 % purity was chosen as the research materials. Blanks of samples for research in the form of a cylinder with a diameter of 6.3 mm were made from tungsten rods. Cutting of samples was performed on a cooled cutting machine model DTQ-5 using a diamond disk with a thickness of 0.3 mm. The specimen is not subjected to thermal stress. After cutting, the specimen cuts were ground to a depth of 0.5 mm. The specimens were polished before irradiation.

Optical metallography was used to study the structure of the materials under study [7]. For metallographic analysis we used an optical light microscope “ALTAMI-MET-1M” of the Research Center “Surface Engineering and Tribology” of Sarsen Amanzholov East-Kazakhstan University and PlasmaScience LLP. The samples for research were prepared according to the standard technique, including mechanical grinding and mechanical polishing. Polishing was carried out on a grinding disk covered with felt, pre-washed and soaked in water for 1–2 hr. Chemical etching in a solution containing 50 % hydrofluoric acid and 50 % nitric acid was used to reveal the microstructure of tungsten. To study the fine structure of the surface layer, a Philips CM30 transmission electron microscope at an accelerating voltage of 125–300 kV with an energy-dispersive micro (nano) analysis system was used [10]. The studies were carried out by diffraction electron microscopy of thin foils at an accelerating voltage of 125 kV. The working magnification in the microscope column was chosen from 10000 to 80000 magnification. Roughness was measured using the Confocal 3D profilometer Leica DCM8 SR.

Results and discussion

Figure 2 shows the microstructure of the tungsten surface before (Fig. 2*a*) and after helium plasma irradiation (Fig. 2*b*) at a potential difference of –1000 V. It is possible to observe the surface change as a relief development with defective structure as a result of inhomogeneous helium saturation of the surface. The resulting relief consists of chaotically arranged ledges and pits of various shapes with an average size of (100–600) nm, and pores (0.1–1.5) μm with visible areas of flaking and sputtering, which is most likely associated with different erosion coefficients.

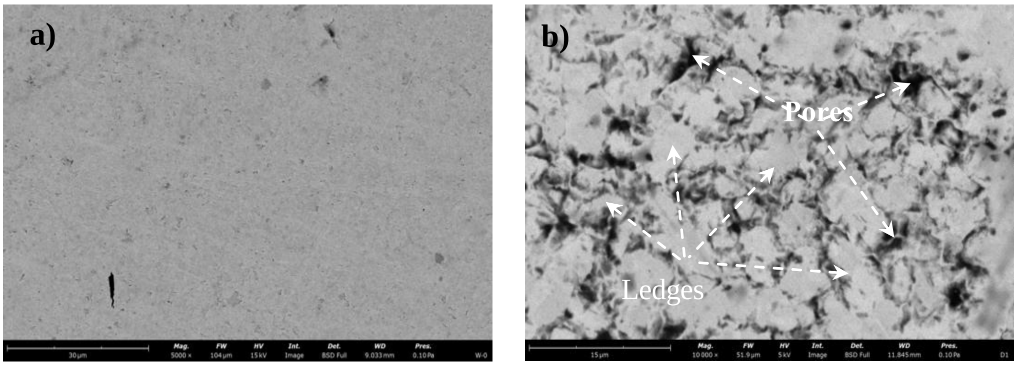

Figure 2. Tungsten surface microstructure before and after irradiation

The surface roughness of tungsten samples before and after helium plasma irradiation was evaluated using a precision tester with a diamond probe. Figure 3 *a–b* presents the forms and profiles of surface roughness along with the distribution graph of the mean arithmetic deviation of the profile across the tungsten surface before and after (–1000V) helium plasma irradiation. From Figure 3*b*, it is shown that the roughness of the surface increases by approximately 2 times after irradiation. The increase in roughness is attributed to the sputtering of the surface by helium ions, as well as the formation of blisters. According to microstructural analysis of the tungsten surface after helium plasma irradiation, defects in the form of etching pits are observed, which are confirmed by the results of roughness assessment and the conclusions of the authors [23, 24]. It is worth noting that in this process, the primary role in changing the relief is played by the sputtering of the surface by helium ions, achieved by transferring kinetic energy to the surface W atom through a cascade of successive collisions between W atoms.

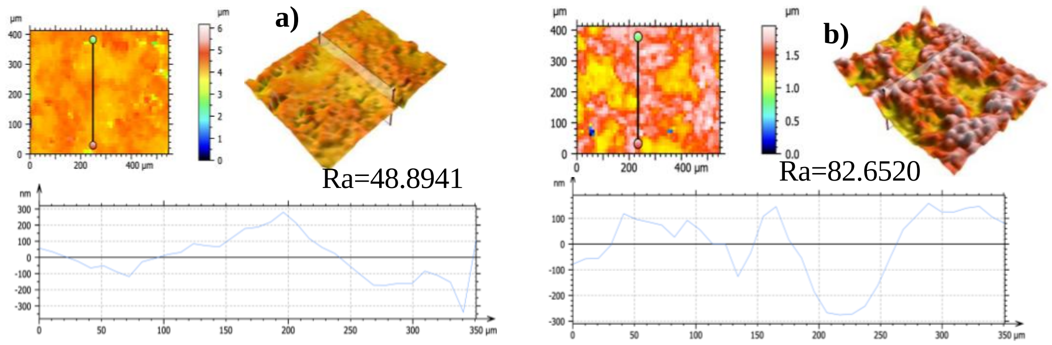

Figure 3. Tungsten surface roughness results before (*a*) and after (*b*) helium plasma irradiation

On the transmission electron microscope the fine structure of the surface (10–20 μm) of tungsten after irradiation with helium plasma was analyzed. Thus, Figure 4 shows the electron image of the fine structure of tungsten, before and after irradiation with helium plasma. It is evident from the figure that under helium plasma irradiation a developed relief with dislocation structure is observed as a result of inhomogeneous etching of the surface, which is markedly different from the structure of the initial state of tungsten (Fig. 4*a*). The morphological component of the structure of samples after helium modification as in the initial state is tungsten, but after irradiation tungsten have defective structure (Fig. 4*b*).

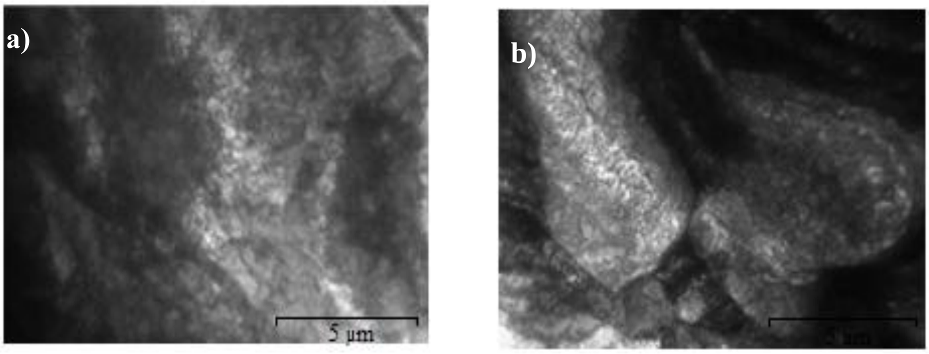

Figure 4. Electron microscopic images of the fine structure of the tungsten surface before (*a*) and after helium plasma irradiation (*b*)

When varying the negative potential on the target at –500V/–1000V/–1500V, the formation of dislocation with chaotic (Fig. 5 *b*) and cellular structure (Fig. 5 *a*, *c*) of tungsten with average grain size (1–25) µm is observed. Figure 5 shows micrographs of fine structure of tungsten surface samples irradiated by helium plasma at different target potentials (*a*) –500 V, (*b*) –1000 V, (*c*) –1500 V. According to the analysis of microphotographs of irradiated samples, it is established that in tungsten material there are intrinsic stress fields (σ) due to deformation of grains, which are localized on the grain body (Fig. 5 *d*), grain boundaries and joints (Fig. 5 *e*), ledges on intergrain boundaries (Fig. 5 *f*).

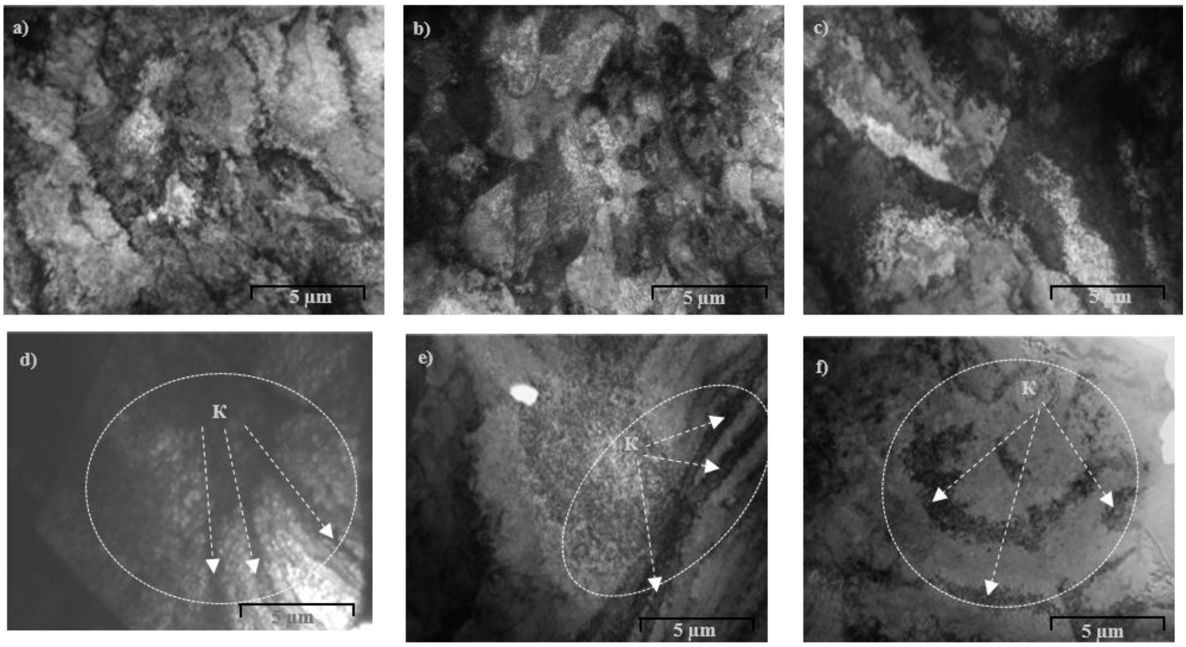

Figure 5. Micrographs of fine structure of tungsten samples irradiated by helium plasma at different target potentials

Also on electron-microscopic images Fig. 5 *d*–*f* it is possible to see how the internal stress fields lead to the appearance of bending extrinsic contours (denoted by the letter K) by which it is possible to determine the nature of deformation of local areas of the tungsten sample. From the available theoretical literature, it is known that the deformation is distinguished locally into elastic and plastic, mixed, as well as three types of deformation of the crystal lattice — bending, torsion and mixed type (χ). According to the method described in [25–27], the extinction contours can be determined by the mutual orientation of the vector of the acting reflection and the extinction line, and the value of internal stresses by the elastic and plastic components of deformation. The tensor quantities were applied to the calculation as follows.

The internal bending-torsion stresses of the crystal lattice are determined as follows:

$$\begin{gathered} \sigma = \sigma_{11\text{-plas}} + \sigma_{12\text{-elas}}, \\ \sigma_{11} = \sigma_{11\text{-plas}} + \sigma_{11\text{-elas}}, \\ \sigma_{12} = \sigma_{12\text{-plas}} + \sigma_{12\text{-elas}}, \end{gathered} \tag{1}$$

where $\sigma_{11\text{-plas}}$, $\sigma_{11\text{-elas}}$ and $\sigma_{12\text{-plas}}$, $\sigma_{12\text{-elas}}$ are tensors of internal bending and torsion stresses respectively [27].

Plastic and elastic components of internal stress amplitude in bending and torsion:

$$\begin{gathered} \sigma_{11\text{-plas}} = \mu\,(b\,\chi_{11\text{-plas}})^{1/2},\ \sigma_{11\text{-elas}} = \mu\, t\, \chi_{11\text{-elas}}; \\ \sigma_{12\text{-plas}} = \mu\,(b\,\chi_{12\text{-},\text{plas}})^{1/2},\ \sigma_{12\text{-elas}} = \mu\, t\, \chi_{12\text{-elas}}, \end{gathered} \tag{2}$$

where μ is the elasticity modulus, b is the Burgers vector, t is the foil thickness, χ_{11} and χ_{12} are the components of the curvature-torsion amplitude tensor of the crystal lattice [27].

Thus, according to calculations, the values of stress σ belong in the range of 0–850 MPa and 1100–1980 MPa and they are localized over a larger area inside the tungsten grain. Thus, the average value of internal stress across the grain was calculated and was equal to 1560 MPa, with the tungsten strength limit of 500–1400 MPa according to the reference book. Also the components of the tensor of internal stresses of the elastic component of deformation were calculated, they are on average on the grain are equal to: bending stress σ_{11} = 620 MPa and torsion σ_{12} = 1470 MPa of the crystal lattice; the average values of the components of the tensor of internal stresses of the plastic component of deformation on the grain are equal to: bending stress σ_{11} = 350 MPa and torsion σ_{12} = 480 MPa of the crystal lattice. The total values of the components of elastic and plastic strains across the grain differ from each other by approximately 2.5 times.

Figure 6 shows electron microscopic images of the fine structure of tungsten in the initial state (*a* — light-field image, *b* — microdiffraction pattern, *c* — its indexed scheme) and after irradiation (*d* — light-field image, *e* — microdiffraction pattern, *f* — indexed scheme) where there are embedding reflections in the form of carbide. According to microdiffraction studies, grain boundary etching is observed, the internal structure of tungsten and carbide grains are clearly expressed. Grain boundaries are clearly revealed, inside the grains there is already well enough expressed modified substructure and defective microstructure.

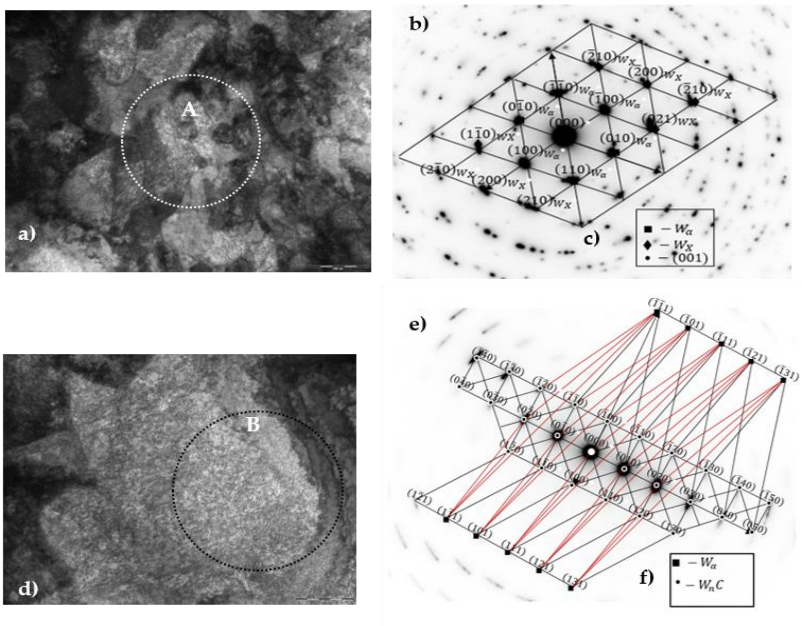

Figure 6. Electron microscopic images of the fine structure of tungsten and their microdiffraction patterns

Thus, modification of tungsten with helium leads to defectively that apparently approaches the defectively of matrix grain boundaries. The possibility of formation of such substructure of grains at helium plasma irradiation is provided by the increased energy state of the surface and subsurface layers exposed throughout the irradiation and neutral atoms of low-temperature plasma. Tungsten carbide particles, which were apparently a residual product inside the chamber, can be located in different morphological components of the matrix. In fact, carbide can localize at matrix grain boundaries and in the grain body, as in (Fig. 5 *d*). According to the studies, carbide was not bound to the boundaries but is a product of matrix delamination in α-WC or β-WC. These localizations are mostly related to crystal structure defects [28].

Conclusions

Thus, summarizing the above results we can draw the following main conclusions of this paper:

– the simulation stand of the small-size linear plasma simulator KAZ-PSI with a plasma-beam unit opens the possibility to test and justify the choice of candidate fusion reactor materials under different operating conditions, as well as significantly expands the available results on various aspects of plasma-surface interaction and helps to reliably harmonize computational models and work out diagnostic methodologies under sufficiently well-programmed conditions;

– conducted preliminary experiments to investigate changes in the structure of tungsten under helium plasma irradiation, showed that after irradiation on the surface is formed relief with defective structure, consisting of chaotically located ledges and pits of various shapes with an average size of (100–600) nm, and pores with sizes (0.1–1.5) μm with visible areas of flaking and sputtering;

– it is found that by varying the negative potential on the target by –500 V/–1000 V/–1500 V, the formation of dislocation with chaotic and cellular structure of tungsten with an average grain size of (1–25) μm was observed;

– determined that the values of internal stress σ lie in the range 0–850 MPa and 1100–1980 MPa;

– it is revealed that the total values of elastic and plastic components of deformations across the tungsten grain differ from each other approximately 2.5 times;

– it is found that modification of tungsten with helium leads to defectively, which is apparently close to the defectively of the grain boundaries of the matrix, not leading to the destruction of the material.

Acknowledgments

This research is funded by the Science Committee of the Ministry of Science and Higher Education of the Republic of Kazakhstan (Grant No.BR21882370).

References

1 Neilson G.H Summary of the international workshop on magnetic fusion energy (MFE) roadmapping in the ITER era / G.H. Neilson, G. Federici, J. Li, D. Maisonnier, R. Wolf // Nuclear Fusion. — 2012. — 52(4). — 047001. https://doi.org/10.1088/0029-5515/52/4/047001.

2 Wan Y. Overview of the present progress and activities on the CFETR / Y. Wan, J. Li, Y. Liu, X. Wang, V. Chan, C. Chen, X. Duan, P. Fu, X. Gao, K. Feng, S. Liu, Y. Song, P. Weng, B. Wan, F. Wan, H. Wang, S. Wu, M. Ye, Q. Yang, G. Zheng, G. Zhuang, Q. Li // Nuclear Fusion. — 2017. — 57(10). — 102009. https://doi.org/10.1088/1741-4326/aa686a.

3 Zohm H. On the physics guidelines for a tokamak DEMO / H. Zohm, C. Angioni, E. Fable, G. Federici, G. Gantenbein, T. Hartmann, K. Lackner, E. Poli, L. Porte, O. Sauter, G. Tardini, D. Ward, M. Wischmeier // Nuclear Fusion. — 2013. — 53(7). — 073019. https://doi.org/10.1088/0029-5515/53/7/073019.

4 Zinkle S.J. Fusion materials science and technology research opportunities now and during the ITER era / S.J. Zinkle, J.P. Blanchard, R.W. Callis, C.E. Kessel, R.J. Kurtz, P.J. Lee, K.A. McCarthy, N.B. Morley, F. Najmabadi, R.E. Nygren, G.R. Tynan, D.G. Whyte, R.S. Willms, B.D. Wirth // Fusion Engineering and Design. — 2014. — 89(7–8). — 1579. https://doi.org/10.1016/j.fusengdes.2014.02.048.

5 Li Y.G. A review of surface damage/microstructures and their effects on hydrogen/helium retention in tungsten / Y.G. Li, Q.R. Zheng, L.M. Wei, C.G. Zhang, Z. Zeng // Tungsten. — 2020. — 2. — P. 34–71. https://doi.org/10.1007/s42864-020-00042-w.

6 Kallenbach A. The ASDEX Upgrade Team. Impurity seeding for tokamak power exhaust: from present devices via ITER to DEMO / A. Kallenbach, M. Bernert, R. Dux, L. Casali, T. Eich, L. Giannone, A. Herrmann, R. McDermott, A. Mlynek, H. Müller, F. Reimold, J. Schweinzer, M. Sertoli, G. Tardini, W. Treutterer, E. Viezzer, R. Wenninger, M. Wischmeier // Plasma Physics and Controlled Fusion. — 2013. — 55(12). — 124041. https://doi.org/10.1088/0741-3335/55/12/124041.

7 Салтыков С.А. Стереометрическая металлография / С.А. Салтыков. — М.: Металлургия, 1976. — С. 190.

8 Pitts R.A. Physics basis for the first ITER tungsten divertor / R.A. Pitts, X. Bonnin, F. Escourbiac, H. Frerichs, J.P. Gunn, T. Hirai, A.S. Kukuushkin, E. Kakeeva, M.A. Miller, D. Moulton, V. Rozhansky, I. Senichenkov, E. Sytova, O. Schmitz // Nuclear Materials and Energy. — 2019. — P. 20. — 100696. https://doi.org/10.1016/j.nme.2019.100696.

9 Balooch M. Mechanical and structural transformations of tungsten implanted with helium ions / M. Balooch, F.I. Allen, M.P. Popovic, P. Hosemann // Journal of Nuclear Materials. — 2022. — Vol. 559. — 153436. https://doi.org/10.1016/j.jnucmat.2021.153436.

10 Эндрюс К. Электронограммы и их интерпретация / К. Эндрюс, Д. Дайсон, С. Киоун. — М.: Мир, 1971. — 256 с.

11 Perez D. Diffusion and transformation kinetics of small helium clusters in bulk tungsten / D. Perez, T. Vogel, B.P. Uberuaga // *Phys. Rev. B.* – 2014. — 90. — 14102. https://doi.org/10.1103/PhysRevB.90.014102.

12 Miyamoto M. Systematic investigation of the formation behavior of helium bubbles in tungsten / M. Miyamoto, S. Mikami, H. Nagashima, N. Iijima, D. Nishijima, R. Doerner, N. Yoshida, H. Watanabe, Y. Ueda, A. Sagara // Nuclear Materials. — 2015. — P. 463. — 333–6. https://doi.org/10.1016/j.jnucmat.2014.10.098.

13 Thompson M. Measuring temperature effects on nano-bubble growth in tungsten with grazing incidence small angle x-ray scattering / M. Thompson, R. Doerner, N. Ohno, N. Kirby, P. Kluth, D. Riley, C. Corr // Nuclear Materials and Energy. — 2017. — P. 121294–1297. https://doi.org/10.1016/j.nme.2016.11.025.

14 Qin W. Nanochannel structures in W enhance radiation tolerance / W. Qin, F. Ren, R.P. Doerner, G. Wei, Y. Lv, S. Chang, M. Tang, H. Deng, C. Jiang, Y. Wang // ActaMaterialia. — 2018. — 153. — P. 147–155. https://doi.org/10.1016/j.actamat.2018.04.048.

15 Tulenbergenov T. Interaction between nitrogen plasma and tungsten / T. Tulenbergenov, M. Skakov, A. Kolodeshnikov, V. Zuev, B.K. Rakhadilov, I. Sokolov, D. Ganovichev, A. Miniyazov, O. Bukina // Nuclear Materials and Energy. — 2017. — 13. — P. 63–67. https://doi.org/10.1016/j.nme.2017.07.005.

16 Tulenbergenov T.R. Formation of “Fuzz” on the Pre-Nitrided Tungsten Surface / T.R. Tulenbergenov, M.K. Skakov, I.A. Sokolov, D.A. Ganovichev // Physics of Atomic Nuclei. — 2019. — 82(11). — 1454–1459. https://doi.org/10.1134/S1063778819120299.

17 Sokolov I.A. Study of the Interaction of Plasma with Berylli um That Is a Candidate Material for the First Wall of a Fusion Reactor / I.A. Sokolov, M.K. Skakov, V.A. Zuev, D.A. Ganovichev, T.R. Tulenbergenov, A.Z. Miniyazov // Technical Physics. — 2018. — P. 63. — 506–510. https://doi.org/10.1134/S1063784218040230.

18 Tulenbergenov T.R. Studies on gas release from pre-saturated samples on a plasma beam installation / T.R. Tulenbergenov, T.V. Kulsartov, I.A. Sokolov, B.K. Rakhadilov, D.A. Ganovichev, A.J. Miniyazov, A.A. Sitnikov // Physical Sciences and Technology. — 2017. — 4(2). — P. 15–28. https://doi.org/10.26577/phst-2017-2-130.

19 Rakhadilov B.K. Tungsten Surface Erosion by Hydrogen Plasma Irradiation / B.K. Rakhadilov, M.K. Skakov, T.R. Tulenbergenov // Key Engineering Materials. — 2017. — 736, 46–51. https://doi.org/10.4028/www.scientific.net/KEM.736.46.

20 Рахадилов Б.К. Патент РК № 22: Установка для моделирования взаимодействия плазмы с кандидатными материалами термоядерного реактора / Б.К. Рахадилов, М.К. Скаков, Т.Р. Туленбергенов. — 2017. — Бюл. — № 2.

21 Rakhadilov B.K. Plasma installation for research of plasma-surface interaction / B.K. Rakhadilov, M. Skakov, T. Tulenbergenov, L. Zhurerova, Sh. Kurbanbekov // Eurasian Physical Technical Journal. — 2019. — 16. — P. 36–42. https://doi.org/10.31489/2019No2/36-42.

22 Rakhadilov B. Hydrogen and deuterium storage in tungsten when irradiation with plasma beam / B. Rakhadilov, M. Skakov, A. Miniyzov, A. Kengesbekov // Conference Proceedings. — 2018. — P. 1216–1221.

23 Xuechun Li In-situ measurements of low energy D plasma-driven permeation through He pre-damaged W / Li Xuechun, Zhoua Hai-Shan, Liua Hao-Dong, Wanga Lu, Luo Guang-Nan // Nuclear Fusion. — 2021. — P. 1–15. https://doi.org/10.1088/1741-4326/ac4716.

24 You Sung Phase-Field Study of Microstructure Evolution in Tungsten Polycrystalline under He/D Irradiation / Sung You, A. Han // Materials. — 2021. — 14(23). — 7433. https://doi.org/10.3390/ma14237433.

25 Уманский Я.С. Физическое металловедение / Я.С. Уманский, Б.Н. Финкельштейн, М.Е. Блантер и др. — М.: Гос. науч.-тех. изд-во литературы по чёрной и цветной металлургии, 1955. — С. 721.

26 Koneva N.A. Determination of the energy density stored during plastic deformation of an isotropic body, according to curvature-torsion of the crystal lattice / N.A. Koneva, S.F. Kiseleva, N.A. Popova, E.V. Kozlov // Fundamental Problems and Modern Technologies of Material Science. — 2011. — 3. — 34.

27 Киселева С.Ф. Распределение внутренних напряжений и плотности запасенной энергии внутри отдельного зерна деформированного поликристалла / С.Ф. Киселева, Н.А. Попова, Н.А. Конева, Э.В. Козлов // Письма о материалах. — 2012. — Т. 2. — С. 84–89. https://doi.org/10.22226/2410-3535-2012-2-84-89.

28 Рахадилов Б.К. Изменение поверхности вольфрама при облучении плазменным пучком / Б.К. Рахадилов, М.К. Скаков, Т.Р. Туленбергенов, В.К. Виелеба // Вестн. Караганд. ун-та. Сер. Физика. — 2016. — № 3(83).

Л.Г. Сулюбаева, Б.К. Рахадилов, Е. Найманқұмарұлы,
М.Б. Баяндинова, Н. Мұқтанова, Н.Е. Бердимуратов

Төментемпературалы гелий плазмасымен сәулеленген вольфрам бетінің құрылымының өзгеруін зерттеу

Термоядролық қондырғы жағдайындағы ең маңызды аспектілердің бірі плазманың материалдың бетімен әрекеттесуі. Мақалада гелий плазмасымен сәулелену кезіндегі вольфрам бетінің құрылымын өзгертуді зерттеудің алдын-ала нәтижелері келтірілген. Гелий жұмыс газы ретінде пайдаланылған плазмалық-сәулелік қондырғысы бар шағын көлемді сызықтық Каз-ПСИ симуляторы әзірленді және құрастырылды. Сызықтық плазмалық имитатордың негізгі элементтері LaB_6 катодты электронды сәулелік зеңбірек, плазмалық сәулелік разряд камерасы, өзара әрекеттесу камерасы, нысаналық құрылғы және электромагниттік катушкалардан тұратын электромагниттік жүйе. Сәулелену кезінде үлгілердің бетінде орташа мөлшері (100–600) нм және кеуек өлшемдері (0,1–1,5) мкм, қабыршықтану мен тозаңданудың көрінетін жерлері бар, әр түрлі пішіндегі ретсіз орналасқан дөңестер мен шұңқырлардан тұратын ақаулы құрылымы бар рельеф пайда болатыны анықталды. Нысанаға теріс потенциал -500В/-1000В/-1500В өзгерген кезде орташа түйіршік мөлшері (1–25) мкм болатын ретсіз және ұяшықты вольфрам құрылымы бар дислокациялардың пайда болуы байқалады; вольфрам түйіршігі бойынша деформацияның серпімді және пластикалық компоненттерінің жиынтық мәндері бір-бірінен шамамен 2,5 есе ерекшеленетіні анықталды.

Кілт сөздер: вольфрам, гелий плазмасы, құрылымы, беттің модификациясы, жұқа құрылымның сандық параметрлері, плазмалық генератор, беті.

Л.Г. Сулюбаева, Б.К. Рахадилов, Е. Найманқұмарұлы,
М.Б. Баяндинова, Н. Мұқтанова, Н.Е. Бердімуратов

Исследование изменения структуры поверхности вольфрама, облученного низкотемпературной гелиевой плазмой

Одним из важных аспектов является взаимодействие плазмы с поверхностью материала, особенно в условиях термоядерной установки. В статье представлены предварительные результаты исследования модификации структуры поверхности вольфрама при облучении гелиевой плазмой. Был разработан и смонтирован малогабаритный линейный симулятор КАЗ-ПСИ с плазменно-пучковой установкой, где в качестве рабочего газа использовался гелий. Основными элементами линейного плазменного имитатора являются электронно-пучковая пушка с катодом из LaB6, камера плазменно-пучкового разряда, камера взаимодействия, мишенное устройство и электромагнитная система, состоящая из электромагнитных катушек. Обнаружено, что при облучении на поверхности образцов образуется рельеф с дефектной структурой, состоящей из хаотично расположенных выступов и ямок различной формы со средним размером (100–600) нм и размерами пор (0,1–1,5) мкм с видимыми участками шелушения и напыления. Установлено, что при изменении отрицательного потенциала на мишени на –500 В/–1000 В/–1500 В наблюдается образование дислокаций с хаотической и ячеистой структурой вольфрама со средним размером зерна (1–25) мкм; выявлено, что суммарные значения упругой и пластической составляющих деформации по зерну вольфрама отличаются друг от друга примерно в 2,5 раза.

Ключевые слова: вольфрам, гелиевая плазма, структура, модификация поверхности, количественные параметры тонкой структуры, плазменный генератор, поверхность.

References

1 Neilson, G.H., Federici, G., Li, J., Maisonnier, D., & Wolf, R. (2012). Summary of the international workshop on magnetic fusion energy (MFE) roadmapping in the ITER era. *Nuclear Fusion, 52*(4), 047001. https://doi.org/10.1088/0029-5515/52/4/047001.

2 Wan, Y., Li, J., Liu, Y., Wang, X., Chan, V., Chen, C., Duan, X., Fu, P., Gao, X., Feng, K., Liu, S., Song, Y., Weng, P., Wan, B., Wan, F., Wang, H., Wu, S.,Ye, M., Yang, Q., Zheng, G., Zhuang, G., & Li, Q. (2017). Overview of the present progress and activities on the CFETR. *Nuclear Fusion, 57*(10), 102009. https://doi.org/10.1088/1741-4326/aa686a.

3 Zohm, H., Angioni, C., Fable, E., Federici, G., Gantenbein, G., Hartmann, T., Lackner, K., Poli, E., Porte, L., Sauter, O., Tardini, G., Ward, D., & Wischmeier, M. (2013). On the physics guidelines for a tokamak DEMO. *Nuclear Fusion, 53*(7), 073019. https://doi.org/10.1088/0029-5515/53/7/073019.

4 Zinkle, S.J., Blanchard, J.P., Callis, R.W., Kessel, C.E., Kurtz, R.J., Lee, P.J., McCarthy, K.A., Morley, N.B., Najmabadi, F., Nygren, R.E., Tynan, G.R., Whyte, D.G., Willms, R.S., & Wirth, B.D. (2014). Fusion materials science and technology research opportunities now and during the ITER era. *Fusion Engineering and Design, 89*(7–8), 1579. https://doi.org/10.1016/j.fusengdes.2014.02.048

5 Li, Y.G., Zheng, Q.R., Wei, L.M., Zhang, C.G., & Zeng, Z. (2020). A review of surface damage/microstructures and their effects on hydrogen/helium retention in tungsten. *Tungsten, 2,* 34–71. https://doi.org/10.1007/s42864-020-00042-w.

6 Kallenbach, A., Bernert, M., Dux, R., Casali, L., Eich, T., Giannone, L., Herrmann, A., McDermott, R., Mlynek, A., Müller, H., Reimold, F., Schweinzer, J., Sertoli, M., Tardini, G., Treutterer, W., Viezzer, E., Wenninger, R., & Wischmeier, M. (2013). The ASDEX Upgrade Team. Impurity seeding for tokamak power exhaust: from present devices via ITER to DEMO. *Plasma Physics and Controlled Fusion, 55*(12), 124041. https://doi.org/10.1088/0741-3335/55/12/124041.

7 Saltykov, S.A. (1976). *Stereometricheskaia metallografiia [Metallografia stereometrica]*. Moscow: Metallurgiia [in Russian].

8 Pitts, R.A., Bonnin, X., Escourbiac, F., Frerichs, H., Gunn, J.P., Hirai, T., Kukuushkin, A.S., Kakeeva, E., Miller, M.A., Moulton, D., Rozhansky, V., Senichenkov, I., Sytova, E., & Schmitz, O. (2019). Physics basis for the first ITER tungsten divertor. *Nuclear Materials and Energy,* 20, 100696. https://doi.org/10.1016/j.nme.2019.100696.

9 Balooch, M., Allen, F.I., Popovic, M.P., & Hosemann, P. (2022). Mechanical and structural transformations of tungsten implanted with helium ions. *Journal of Nuclear Materials, 559,* 153436. https://doi.org/10.1016/j.jnucmat.2021.153436.

10 Endryus, K., Dajson, D., & Kioun, S. (1971). Elektronogrammy i ikh interpretatsiia [Electronograms and their interpretation]. Moscow: Mir [in Russian].

11 Perez, D., Vogel, T., & Uberuaga, B.P. (2014). Diffusion and transformation kinetics of small helium clusters in bulk tungsten. *Phys. Rev. B., 90,* 14102. https://doi.org/10.1103/PhysRevB.90.014102.

12 Miyamoto, M., Mikami, S., Nagashima, H., Iijima, N., Nishijima, D., Doerner, R., Yoshida, N., Watanabe, H., Ueda, Y., & Sagara, A. (2015). Systematic investigation of the formation behavior of helium bubbles in tungsten. *Nuclear Materials,* 463, 333–6. https://doi.org/10.1016/j.jnucmat.2014.10.098.

13 Thompson, M., Doerner, R., Ohno, N., Kirby, N., Kluth, P., Riley, D., & Corr, C. (2017). Measuring temperature effects on nano-bubble growth in tungsten with grazing incidence small angle x-ray scattering. *Nuclear Materials and Energy,* 121294–1297. https://doi.org/10.1016/j.nme.2016.11.025.

14 Qin, W., Ren, F., Doerner, R.P., Wei, G., Lv, Y., Chang, S., Tang, M., Deng, H., Jiang, C., & Wang, Y. (2018). Nanochannel structures in W enhance radiation tolerance. *ActaMaterialia, 153,* 147–155. https://doi.org/10.1016/j.actamat.2018.04.048.

15 Tulenbergenov, T., Skakov, M., Kolodeshnikov, A., Zuev, V., Rakhadilov, B.K., Sokolov, I., Ganovichev, D., Miniyazov, A., & Bukina, O. (2017). Interaction between nitrogen plasma and tungsten. *Nuclear Materials and Energy, 13,* 63-67. https://doi.org/10.1016/j.nme.2017.07.005.

16 Tulenbergenov, T.R., Skakov, M.K., Sokolov, I.A., & Ganovichev, D.A. (2019). Formation of “Fuzz” on the Pre-Nitrided Tungsten Surface. *Physics of Atomic Nuclei, 82*(11), 1454–1459. https://doi.org/10.1134/S1063778819120299.

17 Sokolov, I.A., Skakov, M.K., Zuev, V.A., Ganovichev, D.A., Tulenbergenov, T.R., & Miniyazov, A.Z. (2018). Study of the Interaction of Plasma with Beryllium That Is a Candidate Material for the First Wall of a Fusion Reactor. *Technical Physics, 63,* 506-510. https://doi.org/10.1134/S1063784218040230.

18 Tulenbergenov, T.R., Kulsartov, T.V., Sokolov, I.A., Rakhadilov, B.K., Ganovichev, D.A., Miniyazov, A.J., & Sitnikov, A.A. (2017). Studies on gas release from pre-saturated samples on a plasma beam installation. *Physical Sciences and Technology, 4*(2), 15–28. https://doi.org/10.26577/phst-2017-2-130.

19 Rakhadilov, B.K., Skakov, M.K. & Tulenbergenov, T.R. (2017). Tungsten Surface Erosion by Hydrogen Plasma Irradiation. *Key Engineering Materials, 736,* 46–51. https://doi.org/10.4028/www.scientific.net/KEM.736.46.

20 Rahadilov, B.K., Skakov, M.K., & Tulenbergenov, T.R. (2017). Patent RK № 22: Ustanovka dlia modelirovaniia vzaimodeistviia plazmy s kandidatnymi materialami termoiadernogo reaktora [Patent of the Republic of Kazakhstan No. 22 Installation for modeling plasma interaction with candidate materials of a thermonuclear reactor]. Biulleten, 2 [in Russian].

21 Rakhadilov, B.K., Skakov, M., Tulenbergenov, T., Zhurerova, L., & Kurbanbekov, Sh. (2019). Plasma installation for research of plasma-surface interaction. *Eurasian Physical Technical Journal, 16,* 36-42. https://doi.org/10.31489/2019No2/36-42.

22 Rakhadilov, B., Skakov, M., Miniyzov, A., & Kengesbekov, A. (2018). Hydrogen and deuterium storage in tungsten when irradiation with plasma beam. *Conference Proceedings,* 1216–1221.

23 Xuechun, Li, Hai-Shan, Zhoua, Hao-Dong, Liua, Lu, Wanga, & Guang-Nan, Luo. (2021). In-situ measurements of low energy D plasma-driven permeation through He pre-damaged W. *Nuclear Fusion,* 1–15. https://doi.org/10.1088/1741-4326/ac4716

24 You, Sung & Han, A. (2021). Phase-Field Study of Microstructure Evolution in Tungsten Polycrystalline under He/D Irradiation. *Materials, 14*(23), 7433. https://doi.org/10.3390/ma14237433

25 Umanskij, Ya.S., Finkel'shtejn, B.N., & Blanter, M.E. et al. (1955). Fizicheskoe metallovedenie [Physical metallurgy]. Moscow: Gosudarstvennoe nauchno-tekhnicheskoe izdatelstvo literatury po chernoi i tsvetnoi metallurgii [in Russian].

26 Koneva, N.A., Kiseleva, S.F., Popova, N.A., & Kozlov, E.V. Determination of the energy density stored during plastic deformation of an isotropic body, according to curvature-torsion of the crystal lattice. *Fundamental Problems and Modern Technologies of Material Science, 3,* 34.

27 Kiseleva, S.F., Popova, N.A., Koneva, N.A., & Kozlov, E.V. (2012). Raspredelenie vnutrennikh napriazhenii plotnosti zapasennoi energii vnutri otdelnogo zerna deformirovannogo polikristalla [Distribution of internal stresses and stored energy density inside a single grain of deformed polycrystal]. *Pisma o materialakh — Letters about materials, 2,* 84–89. https://doi.org/10.22226/2410-3535-2012-2-84-89 [in Russian].

28 Rakhadilov, B.K., Skakov, M.K., Tulenbergenov, T.R., & Wieleba, W.K. (2016). Izmenenie poverkhnosti volframa pri obluchenii plazmennym puchkom [Change the tungsten surface when irradiated by plasma beam]. *Bulletin of the University of Karaganda-Physics, 3*(83) [in Russian].

Information about authors

Sulyubayeva, L.G. — PhD, Associate professor, Senior Researcher of Scientific Research Center “Surface Engineering and Tribology”, S. Amanzholov East Kazakhstan University, Ust-Kamenogorsk, Kazakhstan; e-mail: lsulyubayeva@gmail.com, https://orcid.org/0000-0002-1924-1459

Rakhadilov, B.K. — PhD, Associate professor, Director of “PlasmaScience” LLP, Ust-Kamenogorsk, Kazakhstan; e-mail: rakhadilovb@mail.ru, ORCID iD: https://orcid.org/0000-0001-5990-7123

Naimankumaruly, Y. — PhD student of Shakarim University, Semey; Researcher of “PlasmaScience” LLP, Ust-Kamenogorsk, Kazakhstan; e-mail: naimankumarylu@gmail.com, https://orcid.org/0009-0005-1953-316X

Bayandinova, M.B. — PhD student of Sarsen Amanzholov EKU, researcher of “PlasmaScience” LLP, Ust-Kamenogorsk, Kazakhstan, e-mail: shohmanovamb@gmail.com

Muktanova, N. — PhD student of D. Serikbayev East Kazakhstan Technical University, Researcher of “PlasmaScience” LLP. E-mail: muktanovan@gmail.com, https://orcid.org/0000-0002-4823-6640

Berdimuratov, N.E. — Junior researcher of scientific research center “Surface engineering and tribology”, Sarsen Amanzholov East Kazakhstan University, Ust-Kamenogorsk, Kazakhstan; e-mail: nurbol.ber@gmail.com. ORCID ID: https://orcid.org/0009-0000-6880-6439

Article

Received: 02.10.2023
Accepted: 10.12.2023

UDC 691.5

https://doi.org/10.31489/2024PH1/34-42

B.K. Rakhadilov[1], L.B. Bayatanova[1, 2], A.B. Kengesbekov[1, 2,*], S.A. Abdulina[2, 4],
M.K. Kylyshkanov[3], M.A. Podoinikov[2], G.S. Moldabaeva[3]

[1]*PlasmaScience LLP, Ust-Kamenogorsk, Kazakhstan;*
[2]*Institute of composite materials, Ust-Kamenogorsk, Kazakhstan;*
[3]*Ulba Metallurgical Plant JSC, Ust-Kamenogorsk, Kazakhstan;*
[4]*D. Serikbayev East Kazakhstan Technical University, Ust-Kamenogorsk, Kazakhstan*
[*]*Corresponding author's e-mail: aidar.94.01@mail.ru*

Activation of fluoranhydrite with various chemical additives for the production of gypsum fiberboards

Preliminary studies of fluoranhydrite as a binder showed that on its own it almost does not harden, intervention in the technological process of basic production is almost impossible, so in order to obtain materials it is necessary to develop ways of modifying it to initiate the binder properties or use “acidic” fluoranhydrite before the neutralization stage. In this work the influence of various additives (sodium sulfate and sodium sulfite, potassium sulfate, copper sulfate, iron sulfate crystallohydrate, alumina aluminate, sodium carbonate) on the properties of fluorine hydrite binders produced by neutralization of sour waste from hydrofluoric acid production with an excess of limestone was studied. In this work to obtain dependences of anhydrite binder technological properties on the number of introduced additives and determine the optimal composition of the binder, as well as create mathematical models of the processes under study and their statistical analysis used mathematical planning of the experiment. As the conducted studies showed the speed of setting of products based on anhydrite binder and their strength mainly depend on the temperature of water and its amount for mixing at the optimum dispersity of the binder. The strength of the samples made from the neutralized waste was found to be in the range of 0.5–1.2 MPa, and the strength of the samples based on the activated anhydrite binder — in the range of 5.3–10.7 MPa that corresponds to the parameters of the material suitable for the production of boards.

Keywords: fluorine gypsum, anhydrite, hydrofluoric acid, anhydrite binder, activator.

Introduction

Increase of construction rates is impossible without orientation of building complex to the most effective low-cost and non-deficit materials, allowing to improve the comfort of housing. One of the ways to solve this problem is the expansion of production and introduction of new highly effective products and structures on the basis of gypsum binder which has a number of advantages in comparison with other building materials — low cost with high consumer properties (hygiene, fire resistance, bio resistance, providing a favorable climate indoors). In addition, the rapid hardening of gypsum eliminates the need for significant energy consumption for heat treatment to obtain products for different purposes, which helps to reduce energy costs for the manufacture of products. To obtain a fluorine hydrite-based binder suitable for the production of partition walls, it is necessary to solve the problem of accelerating the time of setting and hardening of the material. It is known that insoluble anhydrite (AII), a component of fluoranhydrite, does not hydrate and does not harden under normal conditions. For its activation it is necessary to change the coordination of

Ca^{2+} ions in the crystal lattice of calcium sulfate, which is achieved by the introduction of hardening activators [1, 2]. As a rule, substances that increase the solubility of AII and are centers of crystallization are used as hardening activators [3].

The primary challenges in producing various construction materials based on fluoroaranhydrite stem from the sulfuric acid present within it, residing in the grains' pores and adsorbed on the surface. Neutralizing this acid with alkaline components (such as lime, lime flour, carbide silt, Portland cement, nepheline slime, etc.) is necessary [4, 5]. To enhance fluoroaranhydrite's activity and its suitability for construction product manufacturing, it is suggested to employ complex additives and techniques. However, this approach results in increased complexity and cost in the overall production processes and final products [6].

The purpose of this article is to select the optimal chemical and quantitative composition of activating additives and to study the effect of composition modification on the strength of anhydrite binder.

Materials and methods of research

The raw material for the production of anhydrite binder is gypsum-containing waste products of hydrofluoric acid. An anhydrite binder, also known as anhydrite cement, is a substance produced through the grinding of naturally occurring or artificially prepared anhydrite (achieved by heating at 600–700 °C) with activators. The primary source materials for anhydrite binder include natural two-water gypsum and anhydrite, with their quality specifications outlined in GOST 4013-82.

Immediately out of the furnace waste is granulated material of gray color, granule size of which is 0.3 mm to 60-70 mm. Physico-chemical characteristics of this waste and the possibility of obtaining binder material from it have been previously studied, the results of research are described in [2, 7] and [8]. According to the above-mentioned sources, the properties of the waste obtained at different times are close to each other, which indicate a fairly homogeneous composition of the waste output and the stability of their production regime [9]. The chemical composition of the waste is as follows (wt.%): CaO — 28–39; SO_3 — 38–56; SiO_2 — 0.2; Al_2O_3 — 0.5; Fe_2O_3 — 0.3; Cr_2O_3 — 0.01; TiO_2 — 0.012; Na — 0.015; K — 0.01; H_2SO_4 — 10–15; CaF_2 — 3, HF — 0.3.

The crystal structure consists of finely dispersed translucent idiomorphic anhydrite crystals 5–10 μm in size. The average refractive index N = 1.57. HF, fluorite CaF_2 and iron hydroxides were observed as impurities. The total anhydrite content is about 95%. The phase composition of the gypsiferous waste was determined by the X-ray phase method. Acidic waste is identified as $CaSO_4$ — calcium sulfate. The neutralized waste is an anhydride of orthorhombic structure [2, 10–12].

Interference in the main production process to regulate the properties of the by-product is undesirable, so we studied the properties of the initial fluorine hydride binder obtained by: 1) the method of co-milling with a neutralizing component in the form of limestone in the enterprise (JSC “Ulba Metallurgical Plant”); 2) in the laboratory of the “Institute of Composite Materials” [13].

When performing this work as activating additives were used: (K_2SO_4), copper sulfate ($CuSO_4$), crystalline hydrate of iron sulfate ($FeSO_4 \cdot 7H_2O$), alumina aluminate, Na_2CO_3, NaCl. By analysis of literature data the content of additives was accepted (0.5–3 %) from weight of dry matter with a step of 0.5%. All additives were introduced with mixing water both separately and in combination of the two components. The additives used, in addition to activating hardening, also affect the other physical and mechanical properties of the binder. Mathematical planning of the experiment was used to accelerate the selection of hardening activators.

A fractional three-factor experiment was used to select the modifier additives. Calculations were carried out on a computer program “STATISTICA”.

Results and discussion

According to the ideas of most modern researchers, the process of hardening of anhydrite binder proceeds mainly as a result of hydration when dissolving anhydrite in water and subsequent crystallization of the resulting gypsum. Acceleration of hydration and hardening of anhydrite to technically acceptable terms is achieved by the introduction of additives — curing activators, formula 1:

$$m\mathrm{CaSO_4} + (\mathrm{salt})\, n\mathrm{H_2O} = (\mathrm{salt})\, m\mathrm{CaSO_4} \cdot n\mathrm{H_2O} \tag{1}$$

which then disintegrates to form two-water gypsum equation 2:

$$(\mathrm{salt})\, m\mathrm{CaSO_4} \cdot n\mathrm{H_2O} \rightarrow (\mathrm{salt})\, \mathrm{H_2O} + \mathrm{CaSO_4} \cdot 2\mathrm{H_2O} \tag{2}$$

Two-water gypsum is released first in a colloidal state and then crystallizes. The period when a significant amount of colloidal $CaSO_4\cdot 2H_2O$ is formed is accompanied by heat release. During this period, the setting process takes place, and recrystallization processes contribute to the solidification. In the initial hours, the strength of the anhydrite binder rises, followed by a subsequent decrease in strength. This decline can be attributed to the disintegration of the unstable complex hydrate during this phase. Subsequently, the strength undergoes a prolonged increase. As the hardening progresses, there is a gradual augmentation in the quantity of bound water within the products [14].

According to research conducted by other scholars, there is no formation of intermediate compounds between sulfates and anhydrite. The accelerating impact of additives is attributed to factors other than the formation of such compounds. Some researchers posit that the activating influence of lime, caustic dolomite, and other low-soluble compounds, which share crystallochemical similarities with gypsum, lies in their ability to act as centers of crystallization. In this view, the particles of additives serve as nuclei for crystallization, facilitating the rapid removal of a supersaturated dihydrate solution formed during the hydration of anhydrite. This process leads to the equilibrium state with the separation of $CaSO_4\cdot 2H_2O$ in the sediment, thereby reducing supersaturation and creating conditions for the dissolution of new portions of anhydrite [15].

Additionally, some researchers propose that activators, such as acidic anhydrite hardening agents, enhance its solubility and chemical potential in the early stages of hardening [16]. The types of activation utilized are determined based on the chemical composition of the introduced additives.

Despite a significant amount of research on the activation of anhydrite binders (including those from man-made waste) and the selection of optimal chemical and quantitative composition of activating additives, this process also requires an individual approach.

Using the statistical package, we analyzed the experimental data for the mixture in terms of strength, the beginning and the end of setting.

The results of the processing of the experimental data on the strength index are presented below.

In order to identify statistically significant effects a variance analysis of these models was performed, the results of which are presented in Table 1.

Table 1

Results of the analysis of variance on the strength index

	SS	df	MS	SS	df	MS	F	p	R-Sqr	R-Sqr
Linear	235.6788	3	78.55961	236.8854	15	15.79236	4.974533	0.013618	0.498723	0.398468
Quadratic	127.6587	6	21.27646	109.2266	9	12.13629	1.753126	0.215443	0.768864	0.537728
Special Cubic	9.2003	4	2.30008	100.0263	5	20.00526	0.114974	0.971532	0.788333	0.237998
Total Adjusted	472.5642	18	26.25357							

Table 1 shows that statistically significant effects are observed in the linear model (p-value criterion less than 0.05). For other models this criterion has a higher value. Therefore, we will further consider the linear model.

Regression equation will have the following form

$$Y_{\text{пр}} = 0.67\cdot A + 12.35\cdot B - 1.99\cdot C + 7.39\cdot D. \tag{3}$$

For the selected model statistics were calculated, the values of which are presented in Table 2.

Table 2

Value of statistics for the selected model

	Coeff.	Std.Err.	t(15)	p	–95, %	+95, %
(A)Var1	0.66734	2.682398	0.248784	0.806902	-5.05006	6.38473
(B)Var2	12.34584	2.682398	4.602539	0.000345	6.62845	18.06324
(C)Var3	-1.98789	2.682398	-0.741086	0.470085	-7.70528	3.72951
(D)Var4	7.38734	2.682398	2.754004	0.014767	1.66994	13.10473

However, only B and D are significant factors in this model.

The table of variance analysis shows good results for the fitted linear model, which are presented in Table 3.

Table 3

Analysis of variance in the linear model

	SS	df	MS	F	p
Model	235.6788	3	78.55961	4.974533	0.013618
Total Error	236.8854	15	15.79236		
Total Adjusted	472.5642	18	26.25357		

Below are the results of processing the experimental data on the beginning of the setting of the mixture.

As a mathematical model the followings were tried: linear, quadratic and special cubic.

In order to identify statistically significant effects, a variance analysis of these models was performed, the results of which are presented in Table 4.

Table 4

Results of the analysis of variance on the beginning of setting

	SS	Df	MS	SS	df	MS	F	p	R-Sqr	R-Sqr
Linear	671.938	3	223.9792	376.6788	15	25.11192	8.919238	0.001239	0.640785	0.568942
Quadratic	223.116	6	37.1860	153.5625	9	17.06250	2.179401	0.141220	0.853557	0.707114
Special Cubic	116.034	4	29.0084	37.5290	5	7.50579	3.864800	0.085301	0.964211	0.871159
Total Adjusted	1048.616	18	58.2565							

Table 4 shows that statistically significant effects are observed in the linear model (p-value criterion less than 0.05). For other models this criterion has a higher value. Therefore, we will further consider the linear model.

The regression equation will have the following form

$$Y_n = 23.52 \cdot A + 6.06 \cdot B + 26.73 \cdot C + 6.46 \cdot D. \quad (4)$$

For the selected model statistics were calculated, the values of which are presented in Table 5.

Table 5

Value of statistics for the selected model

	Coeff.	Std.Err.	t(15)	p	–95, %	+95, %
(A)Var1	23.52158	3.382515	6.953874	0.000005	16.31192	30.73124
(B)Var2	6.06337	3.382515	1.792564	0.093230	-1.14629	13.27303
(C)Var3	26.72606	3.382515	7.901239	0.000001	19.51640	33.93572
(D)Var4	6.45740	3.382515	1.909054	0.075575	-0.75226	13.66706

As follows from Table 5, factors *A* and *C* are significant for the selected model (p-value is much less than 0.05).

The table of variance analysis shows good results for the selected linear model, which are presented in Table 6.

Table 6

Analysis of variance in the linear model

	SS	df	MS	F	p
Model	671.938	3	223.9792	8.919238	0.001239
Total Error	376.679	15	25.1119		
Total Adjusted	1048.616	18	58.2565		

Processing of the results on the indicator of the end of setting.

Below there are the results of dispersion analysis of experimental data at the end of setting of the mixture.

As a mathematical model the following models were tried: linear, quadratic and special cubic. The results of the analysis of variance on these models are shown in Table 7.

Table 7

Results of analysis of variance

	SS	df	MS	SS	df	MS	F	p	R-Sqr	R-Sqr adjusted
Linear	328.107	2	164.0533	820.2934	7	117.1848	1.399954	0.308011	0.285708	0.081624
Quadratic	370.594	3	123.5314	449.6994	4	112.4248	1.098791	0.446624	0.608412	0.118928
Special Cubic	208.983	1	208.9826	240.7168	3	80.2389	2.604504	0.204965	0.790389	0.371168
Total Adjusted	1148.400	9	127.6000							

Table 7 shows that statistically significant effects are not observed for any model (p-values for all models are greater than 0.05). However, this index is the smallest for the special cubic model, which has the smallest mean square error (MS = 80.2) and the largest Fisher index (F = 2.6).

The quality of this model is estimated by such indicator as the coefficient of determination Rsqr, which is 0.79 for this model. This indicates a high quality of the model. We can say that 80 % of the observed effect is explained by the selected factors.

The regression equation will be as follows:

$$\begin{aligned} Y_{regressio} = {} & +59.267319210644 \cdot A + 26.812866336268 \cdot B + 33.44914754712 \cdot C - \\ & - 51.840010145936 \cdot A \cdot B - 78.566741356355 \cdot A \cdot C + \\ & + 6.524344955884 \cdot B \cdot C + 463.76702491378 \cdot A \cdot B \cdot C. \end{aligned} \quad (5)$$

Next, the statistics for the selected model were calculated. These values are presented in Table 8.

Table 8

Value of statistics for the selected model

	Coeff.	Std.Err.	t(3)	p	–95, %	+95, %
(A)Var1	59.2673	8.6593	6.84438	0.006384	31.710	86.825
(B)Var2	26.8129	8.6592	3.09644	0.053444	–0.745	54.370
(C)Var3	33.4491	8.6592	3.86283	0.030675	5.892	61.007
AB	–51.8400	43.5889	–1.18929	0.319876	–190.559	86.879
AC	–78.5667	43.5889	–1.80245	0.169264	–217.286	60.153
BC	36.5243	43.5888	0.83793	0.463575	–102.195	175.243
ABC	463.7670	287.3673	1.61385	0.204965	–450.764	1378.298

As it follows from Table 8, factors A and C are the most significant for the chosen model (p-value is much less than 0.05).

Using the obtained regression equation we calculated parameter values for different points of the plan, which are shown in Table 9.

Table 9

Experimental and theoretical parameter values

	Observed	Predictd	Resids
1	57.00000	59.26732	–2.26732
2	25.00000	26.81287	–1.81287
3	35.00000	33.44915	1.55085
4	26.00000	30.08009	–4.08009
5	26.00000	26.71655	–0.71655
6	39.00000	39.26209	–0.26209
7	39.00000	46.58826	–7.58826
8	54.00000	44.66838	9.33162
9	46.00000	38.03215	7.96785
10	37.00000	39.12314	–2.12314

The calculated theoretical values were compared with the experimental values and a divergence histogram was plotted in Figure 1.

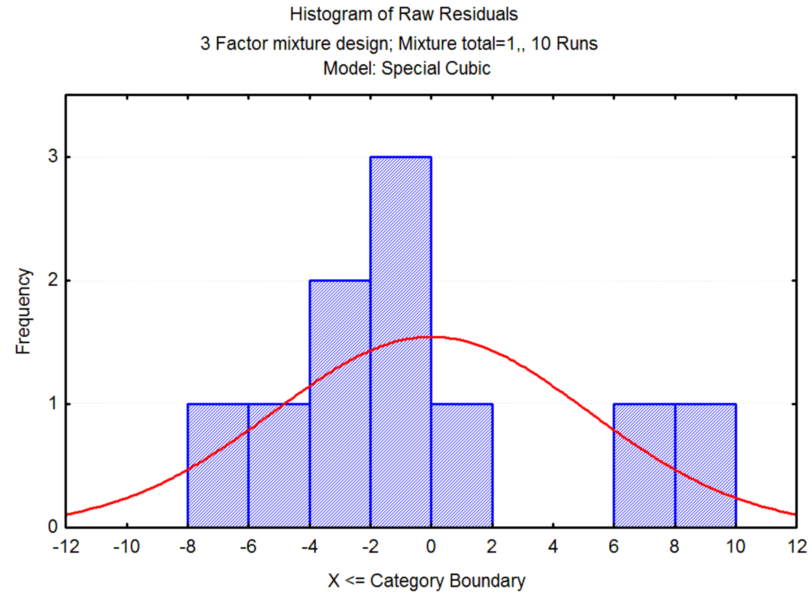

Figure 1. Histogram of the difference between the theoretical and experimental values

This histogram obeys the normal law of distribution, which is a prerequisite for the construction of regression models.

Figure 2 shows the response surface of the setting time depending on the selected factors.

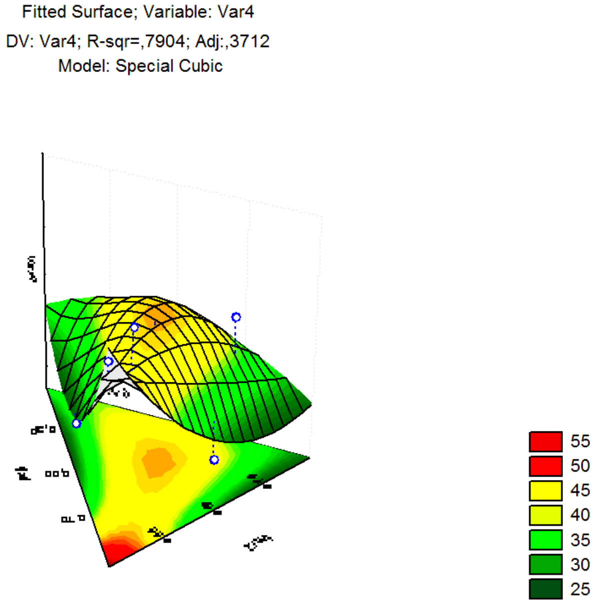

Figure 2. Response surface of the setting time

The contour plot of the studied dependence is shown in Figure 3.

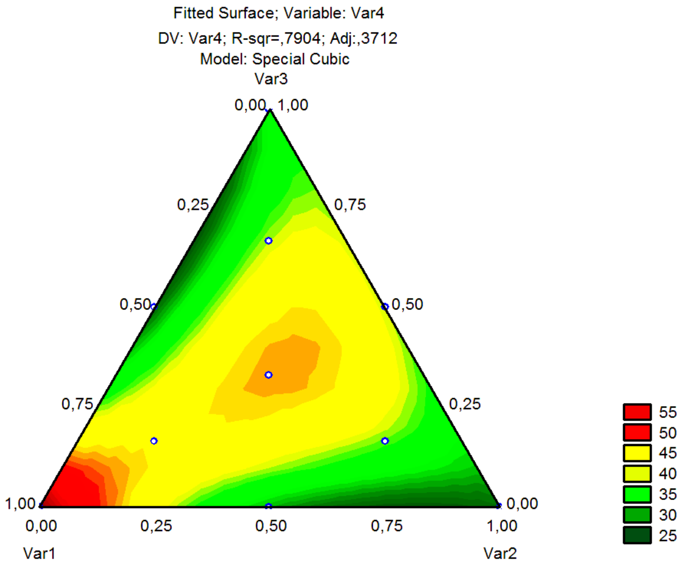

Figure 3. Contour plot of the studied dependence

According to the model obtained, using the contour plot of the studied dependence by varying the percentage of components anhydrite binder with the necessary setting time was obtained.

The greatest effect was obtained by using potassium sulfate in an amount of 1.5 %. The results of the experiment are shown in Figure 4.

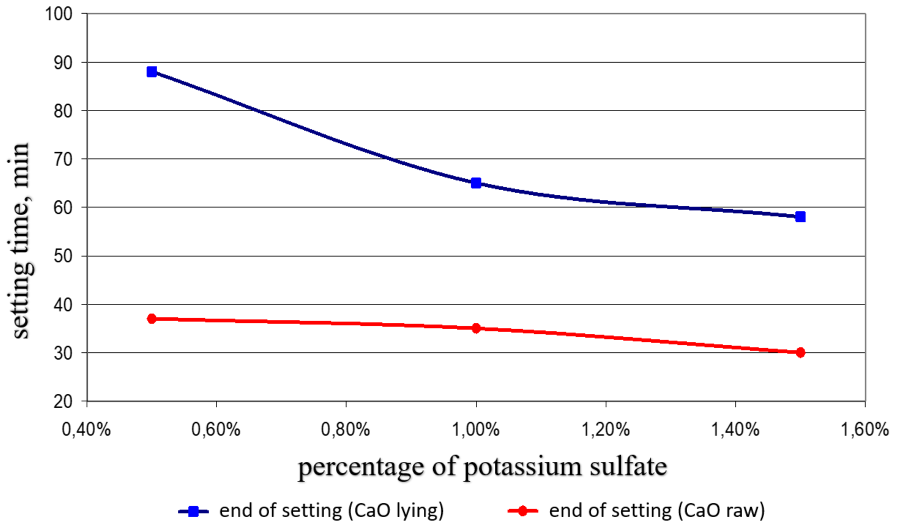

Figure 4. Dependence of setting time on the amount of potassium sulfate and lime quality.

As the studies have shown the rate of setting of products based on anhydrite binder and their strength mainly depend on the temperature of water and its amount for mixing at the optimum dispersity of the binder.

Experimental data showed that the strength of samples made from neutralized waste is in the range of 0.5–1.2 MPa, and the strength of samples based on activated anhydrite binder is in the range of 5.3–10.7 MPa, which corresponds to the parameters of the material suitable for the production of slabs.

Acknowledgments

The work was carried out within the framework of the Ministry of Science and Higher Education of the Republic of Kazakhstan grant AP14871496 “Development of technology for obtaining anhydrite binder from industrial waste for use in the production of building material”.

References

1 Budnikov, P.P. & Zorin, S.P. (1954). *Anhydrite cement*. Moscow: State Publishing House of Literature on Building Materials, 93.

2 Bayatanova, L., Rakhadilov, B., Kengesbekov, A., Kylyshkanov, M., Abdulina, S., Adilkanova, M., & Sagdoldina, Z. (2023). Production of Anhydrite Binder from Waste Fluoranhydrite. *ChemEngineering, 7*, 28.

3 Schulze, W., Tischer, W., & Ettel, V.P. (1990). *Mortars and concretes on non-cemental binders*. Moscow: Stroyizdat, 240.

4 Rudnov, V.S., Vladimirova, E.V., Domanskaya, I.K., & Gerasimova, E.S. (2018). *Construction materials and products*. Ekaterinburg: Publishing house of Ural. Univ, 203.

5 Kuzmenkov, M.I., & Kunitskaya, T.S. (2003). *Binders and the production technology of products based on them*. Minsk.

6 Kudyakov, A., & Anikanowa, L. (2011). *PoröseWandbaumaterialien auf Basis des saurenFluoranhydrids*. WeimarerGipstagung. Bauhaus-Universität, 245–249.

7 Rodin, A.N. (1987). Testing gypsum binder and determine its suitability in construction. *Collection of articles. Building materials on the basis of various industrial wastes of Kazakhstan.* Alma-Ata: NIISTROMPROEKT.

8 Rodin, A.N. et al. (1989). Phthoranhydrite binder from hydrofluoric acid production wastes. *Collection of articles. Building materials on the basis of various industrial wastes of Kazakhstan.* Alma-Ata: NIISTROMPROEKT, 121–128.

9 Petrova, L.V. (2009). *Chemistry of binding building materials.* Ulyanovsk: UlGTU, 64.

10 Kudyakov, A.I., Anikanova, L.A., & Redlikh, V.V. (2013). Materials for enclosing structures made of composite fluoroanhydrite binders. *Dry building mixtures*, 12–14.

11 Anikanova, L.A., Volkova, O.V., Kurmangalieva, A.I., & Volkov, K.S. (2015). Study of acid fluoride raw materials for the production of composite binders. *Bulletin of Tomsk State University of Architecture and Civil Engineering,* 160–170.

12 Anikanova, L.A. (2015). Efficiency of using acid fluoride in the production of wall and finishing materials. *Bulletin of Tomsk State University of Architecture and Civil Engineering*, 163–171.

13 Kengesbekov, A.B., Sagdoldina, Zh.B., Buitkenov, D.B., Ocheredko, I.A., Abdulina, S.A., & Torebek, K. (2022). Investigation of the characteristics of an indirect plasma torch. *Bulletin of the University of Karaganda-Physics,* 3(107), 80–88.

14 Derevyanko, V.N., Kondratieva, N.V., & Hryshko, A.N. (2018). Hydration of gypsum systems. *Bulletin of the Prydniprovska State Academy of Civil Engineering and Architecture,* 3 (241-242), 43–53.

15 Ushakov, V.V. (2003). The choice of chemical additives in the composition of dry building mixtures. *Industrial and Civil Engineering, 12*, 41-42.

16 Korovyakov, V.F. (2003). Gypsum binders and their use in construction. *Russian Chemical Journal*, *XLVII*, 4, 18–25.

Б.К. Рахадилов, Л.Б. Баятанова, А.Б. Кенесбеков, С.А. Абдулина,
М.К. Кылышканов, М.А. Подойников, Г.С. Молдабаева

Ойықтақталарды өндіру үшін әртүрлі химиялық қоспалармен фторангидритті белсендіру

Фторангидриттің тұтқырлық сапасын алдын-ала зерттеуде оның өздігінен қатып қалмайтындығын, негізгі өндіріс процесіне араласу іс жүзінде мүмкін еместігін көрсетті, сондықтан материалдарды алу үшін оның тұтқырлық қасиеттерін қоздырып, түрлену тәсілдерін жасау қажет немесе бейтараптандыру сатысына дейін «қышқыл» фторангидритті қолдану керек. Бұл жұмыста әртүрлі қоспалардың (натрий сульфаты мен сульфиті, калий сульфаты, мыс сульфаты, темір сульфатының кристаллогидраты, калий-алюминий ашудастары, натрий карбонаты) фторангидрит тұтқырлығының заттардың қасиеттеріне әсері зерттелді, олар балқытқыш қышқылын өндіруде қышқыл қалдықтарын артық әктаспен бейтараптандырудан алынған. Сонымен қатар ангидрит тұтқырлығыың технологиялық қасиеттеріне енгізілген қоспалар санына тәуелділігін алуда және тұтқыр заттың оңтайлы құрамын анықтауда, сондай-ақ зерттелетін процестердің математикалық модельдерін құру және олардың статистикалық талдауына эксперименттің математикалық жоспарлауы қолданылды. Зерттеулер көрсеткендей, ангидриттің тұтқырлығына негізделген өнімдердің қату жылдамдығы және олардың беріктігі негізінен судың температурасына және тұтқырдың оңтайлы дисперсияға айналу кезіндегі оның мөлшеріне байланысты. Бейтараптандырылған қалдықтардан жасалған үлгілердің беріктігі 0,5–1,2 МПа шегінде, ал белсендірілген ангидрит тұтқырлығы негізіндегі үлгілердің беріктігі 5,3–10,7 МПа шегінде екені анықталды, бұл плиталарды өндіруге жарамды материалдың параметрлеріне сәйкес келеді.

*Кілт сөздер:*фторгипс, ангидрит, балқытқыш қышқыл, ангидритті тұтқырлық, активатор.

Б.К. Рахадилов, Л.Б. Баятанова, А.Б. Кенесбеков, С.А. Абдулина,
М.К. Кылышканов, М.А. Подойников, Г.С. Молдабаева

Активация фторангидрита различными химическими добавками для производства пазогребневых плит

Предварительные исследования фторангидрита в качестве вяжущего показали, что самостоятельно он практически не твердеет, вмешательство в технологический процесс основного производства практически невозможно, поэтому с целью получения материалов необходимо разрабатывать способы модифицирования его для инициирования вяжущих свойств или использовать «кислый» фторангидрит до стадии нейтрализации. В статье исследовано влияние различных добавок (сульфата и сульфита натрия, сульфата калия, сульфата меди, кристаллогидрата сульфата железа, алюмокалиевых квасцов, карбоната натрия) на свойства фторангидритовых вяжущих, полученных нейтрализацией «кислого» отхода производства плавиковой кислоты избытком известняка. Для получения зависимостей технологических свойств ангидритовых вяжущих от количества введенных добавок и определения оптимального состава вяжущего, а также создания математических моделей исследуемых процессов и их статистического анализа авторами применено математическое планирование эксперимента. Как показали проведенные исследования, скорость схватывания изделий на основе ангидритового вяжущего и их прочность в основном зависят от температуры воды и ее количества для затвердения при оптимальной дисперсности вяжущего. Выявлено, что прочность образцов, изготовленных из нейтрализованного отхода, находится в пределах 0,5–1,2 МПа, а прочность образцов на основе активированного ангидритового вяжущего — в пределах 5,3–10,7 МПа, что соответствует параметрам материала, пригодного для производства плит.

Ключевые слова: фторгипс, ангидрит, плавиковая кислота, ангидритовое вяжущее, активатор, оптимальная дисперсность.

Information about authors

Rakhadilov, B.K. — PhD, Associate professor, Director of “PlasmaScience” LLP, Ust-Kamenogorsk, Kazakhstan; e-mail: rakhadilovb@mail.ru, ORCID iD: https://orcid.org/0000-0001-5990-7123

Bayatanova, L.B. — PhD, Senior researcher of “Institute of composite materials”, Ust-Kamenogorsk, Kazakhstan; e-mail: leila_1809@mail.ru, ORCID iD: https://orcid.org/0000-0002-5630-4746

Kengesbekov, A.B. — PhD, Researcher “PlasmaScience” LLP, Director of “Institute of composite materials”, Ust-Kamenogorsk, Kazakhstan; e-mail: aidar.94.01@mail.ru, ORCID iD: https://orcid.org/0000-0002-5630-9467

Abdulina, S.A. — PhD, Associate professor, senior researcher of “Institute of composite materials”, Associate professor, D. Serikbayev East Kazakhstan Technical University, Ust-Kamenogorsk, Kazakhstan; e-mail: abdulina.saule@mail.ru, ORCID iD: https://orcid.org/0000-0001-6328-8652

Kylyshkanov, M.K. — D.Ph.-M.Sc., Professor, Head of the research center “Ulba Metallurgical Plant” JSC Ust-Kamenogorsk, Kazakhstan; e-mail: kylyshkanov@mail.ru, ORCID iD: https://orcid.org/0000-0002-8304-7124

Podoynikov, M.A. — Deputy head of research center “Ulba Metallurgical Plant” JSC, Ust-Kamenogorsk, Kazakhstan; e-mail: shestakovka@ulba.kz, ORCID iD: https://orcid.org/0000-0001-6598-9305

Moldabayeva, G.S. — Teacher, Ulba Metallurgical Plant JSC, Ust-Kamenogorsk, Kazakhstan; e-mail: gulzhaz_83@mail.ru, ORCID iD: https://orcid.org/0000-0001-9192-7087

Article

Received: 01.10.2023
Accepted: 19.12.2023

UDC 62.59

https://doi.org/10.31489/2024PH1/43-58

N. Sklyarov[1], A. Shapovalov[1], P. Chernenko[1], A. Korniev[1],
A. Kashkanov[2*], V. Kashkanov[2], V. Kucheruk[3]

[1]*National Academy of the National Guard of Ukraine, Kharkiv, Ukraine;*
[2]*Vinnytsia National Technical University, Vinnytsia, Ukraine;*
[3]*Uman National University of Horticulture, Uman, Ukraine*
[*]*Corresponding author's e-mail: a.kashkanov@vntu.edu.ua*

Research of the vacuum brake booster working process

The creation of a laboratory installation was carried out with an aim to ensure the study of the working processes and characteristics of vacuum boosters as a part of hydraulic brake drives for vehicles with a gross weight of up to 3.5 tons for civilian usage, and armored vehicles with a gross weight of up to 8.5 tons designated for service and combat missions. Theoretical researches in this direction have been previously carried out by a number of scientists of the Department of "Automobiles" named after prof. Gredeskul A.B. in Kharkiv National Automobile and Road University, the results of which have been highlighted in a number of scientific papers. Comparison of the results of theoretical studies with the experimental ones, received on the laboratory setup and suggested in this paper, according to the experimental method described in the article, using the created electronic signal processing complex and sensor unit, made it possible to establish a discrepancy between theoretical and experimental studies within 6%. This complex for experimental research was created for the first time, thus allowing to obtain the results that confirm the theoretical studies of the vacuum boosters of the brake drive of cars, as well as revealed a number of dependencies between the weight and overall parameters of the under research unit, along with the number of functional relationships between the structural components of the vacuum boosters, which enables to significantly optimize its design.

Keywords: vehicles, active safety, brake system, vacuum brake booster, static and dynamic characteristics, experimental research, technique, equipment.

Introduction

An analysis of the state of traffic safety in the world in general [1] and in Ukraine in particular [2] indicates the need for an urgent solution to the problems of accidents. A significant number of road traffic accidents occur due to insufficient active safety of vehicles, which is significantly determined by the efficiency of the vehicle braking system [3–5].

The vacuum brake booster is the most common service device for the brake systems of cars and light-duty vehicles [6, 7], the operation of which is provided both in the sectors of the national economy and in the automotive equipment of the National Guard of Ukraine. The efficiency and quality of its work largely determine the ergonomic conditions and the effectiveness of the brake control [8, 9] and, ultimately, the active safety of the car [6, 10]. Recently, the vacuum booster is increasingly not only a device for reducing the force on the brake pedal, but also an automatic device that corrects the actions of the driver (anti-lock braking system (ABS) and a motion stabilization system (ESP) [11], an emergency braking system Brake Assist (BAS) [12], etc.), which simplifies driving (preventive safety systems [13], energy recovery systems in hybrid and electric vehicles [14, 15], etc.). Therefore, improving the working process of the vacuum brake booster is the most important task to improve the active safety of the car.

The relevance of the topic lies in the fact that in order to reduce the accident rate of vehicles in the process of braking, it is necessary to implement a number of measures in the field of research support to improve brake drives [16–18]. One of these areas is the development of methods for the development of efficient vacuum brake boosters, which are produced in Ukraine. Currently, this is hampered by insufficient knowledge about their operational processes, as well as the lack of scientifically based generalized criteria for evaluating effectiveness [19–23].

Research objectives:
– study of working processes in a two-chamber vacuum amplifier;
– determination of static and dynamic characteristics of a two-chamber vacuum amplifier;
– comparison of theoretical and experimental results.

To achieve the goals set, the following tasks were solved:

– development of experimental research methodology;
– creation of an experimental facility;
– development and preparation of a measuring and recording complex based on a modern element base;
– implementation of a complex of experimental studies provided for by the program;
– processing the results of experiments and performing their analysis.

Object of the research — the working process of the vacuum brake booster.

The subject of the research is the increase in the efficiency of vacuum boosters of the brake drive.

Research methods. Methods of generation, selection and analysis of information were used to determine the state of the problem and to set the research objectives. In experimental studies of the working processes of vacuum boosters of the brake drive, the method of full-scale experiment was used.

The scientific novelty of the results obtained is that: for the first time, a structural analysis was carried out and the relationships between the elements of a vacuum amplifier were determined, which made it possible, using the proposed criteria, to determine its rational structure; regularities of interaction of structural elements and their influence on the working process, as well as the efficiency of vacuum boosters of the brake drive have been clarified.

A number of scientists of the Department of “Automobiles” named after A.I. d.t.s., prof. Gredeskula A.B., at Kharkiv National Automobile and Road University, have made a range of researches which are reflected in a number of scientific papers [8, 24–28]. Comparison of the results of theoretical studies obtained in these works with the experimental ones obtained on the laboratory setup suggested in this work, according to the experimental method described in the article, using the created electronic signal processing complex and a sensor unit, made it possible to establish a discrepancy between theoretical and experimental research within 6 %. To study the working process of the vacuum brake booster, a special installation was developed and created. The installation contains a system for supplying energy to a vacuum amplifier (vacuum) and an input signal formation mechanism (compressed air), an amplifier load and a measuring complex.

The energy supply system allows you to create, control and maintain the required level of vacuum in the vacuum cavities of the amplifier. The input signal generation mechanism provides the necessary level and nature of the force change on the amplifier pusher. This mechanism is a pneumatic chamber with an adjustable throttle at the inlet. To study the static characteristics, the pneumatic chamber is replaced by a lead screw. The main brake cylinder connected to the brake mechanisms is used as a booster load.

Improving the design, as well as the working processes of the units and apparatus of the hydraulic brake drive of a car, is based on the results of theoretical and experimental studies. The reliability of theoretical provisions fully depends on the level of experimental research. Theoretical studies carried out by the authors in [8, 24–28] required experimental confirmation, as a result of which it became necessary to create a special installation for studying the working process of a vacuum brake booster.

The developed mathematical model is based on the results of analysis and synthesis of the constituent elements of the Vacuum brake booster, using a gas dynamic model. Features of the working process are considered taking into account the gas-dynamic model shown in Figure 1. In accordance with the scheme of Figure 1. Vacuum brake booster has a body divided by a partition into two chambers. The chambers are divided by pistons into cavities 4, 5, 8 and 9. The cavities 9 and 5 are permanently connected to a vacuum source.

The connection of cavities 4 and 8 depends on the mode of operation. The air resistance between the cavities depends on the cross section of the throttles $Д_a$, $Д_b$ and $Д_к$.

The mathematical model of the dynamic state of the pusher has the form

$$F_T + F_{KH} - M_T \cdot \ddot{X}_T - k_T \cdot (\dot{X}_T - \dot{X}_1) - F_A - F_B - F_{TP} - F_H = 0. \tag{1}$$

During the movement of the pusher, the force from the FKH valve remains unchanged. The friction force of the pusher relative to the piston is non-linear

$$F_{TP1} = \begin{cases} F_{TP1} \cdot sign(\dot{X}_T - \dot{X}_1) \; if \; \dot{X}_T \neq \dot{X}_1, \\ F_{TP1} = 0 \; if \; \dot{X}_T = \dot{X}_1. \end{cases} \tag{2}$$

The relative displacement of the pusher and piston leads to the actuation of the switchgear and the mass flow of air into the atmospheric cavities has dependence

$$G_a = f_a \cdot p_a \cdot V_{кр} \cdot \varphi(\sigma). \tag{3}$$

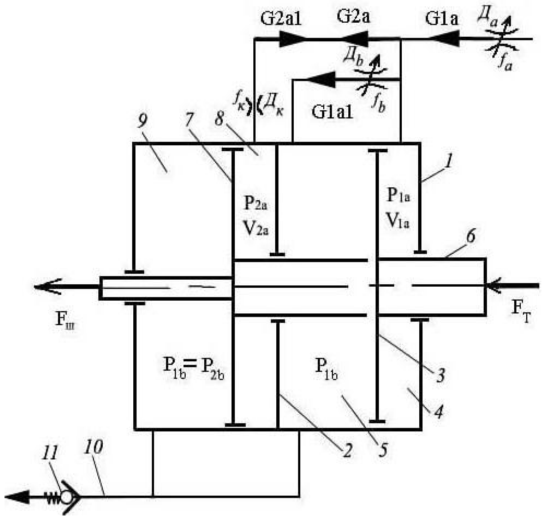

Figure 1. Scheme of the gas-dynamic model of a two-chamber Vacuum brake booster

The expenditure function $\varphi(\sigma)$ is taken in the following form

$$\varphi(\sigma)=\sqrt{\frac{1-\sigma_a^2}{2\cdot k\cdot(\xi_a-\ln\sigma_a)}}\,, \tag{4}$$

and the resistance coefficient of the atmospheric valve

$$\xi_a=0{,}55+4\cdot\left(\frac{b_T}{d_a}-0{,}1\right)+0{,}176\cdot\left(\frac{d_a}{h_{кл}}\right)^2. \tag{5}$$

The following assumptions are made in the model: rarefaction in vacuum cavities is constant, and the temperature regime is also unchanged.

A change in pressure in atmospheric cavities leads to the formation of additional forces on the booster pistons. Since the pistons in the investigated Vacuum brake booster do not have a rigid connection, when developing the model, it became necessary to confirm the hypothesis about the movement of the pistons without separation from each other during the working process.

To theoretically confirm this hypothesis, the equations of the dynamic state of the piston of the first chamber

$$M_1\cdot\ddot{X}_1+f_1\cdot\dot{X}_1+R=S_1\cdot\Delta P+f_{T1}\cdot\left(\dot{X}_T-\dot{X}_1\right)+R_1+S_У\cdot\left(P_0-P_{b1}\right), \tag{6}$$

replaced by an equation for the reaction of the dynamic component of the force of the second piston. The condition for the absence of contact break is the value for the reaction between the pistons $R>0$. This condition is met by the following relations:

$$S_1\cdot\left(P_{1a}-P_{1b}\right)+f_{T1}\cdot\left(\dot{X}_T-\dot{X}_1\right)+F_{ПР}-\left(S_У-S_Ш\right)\cdot\left(P_0-P_b\right)+S_У\cdot\left(P_0-P_{1b}\right)-f_1\cdot\dot{X}_1-M_1\cdot\ddot{X}_1\le 0\,, \tag{7}$$

$$\ddot{X}_1\le\frac{S_1\cdot\left(p_{1a}-p_{1b}\right)+f_{T1}\cdot\left(\dot{X}_T-\dot{X}_1\right)+F_{пр}-\left(S_у-S_ш\right)\cdot\left(p_0-p_b\right)+S_у\left(p_0-p_{1b}\right)-f_1\cdot\dot{X}_1}{M_1}. \tag{8}$$

The results of the calculation of expressions (6), (7), (8) using the Simulink application of the MATLAB environment [29] in the form of a graphical dependence of the reaction between the pistons during braking are shown in Figure 2.

The above dependence theoretically confirms the hypothesis of the movement of pistons without separation from each other in a two-chamber vacuum booster.

Given the confirmation received, the mathematical model of the two-chamber Vacuum brake booster is simplified. The model, which takes into account the masses of individual pistons, has been converted to a single-mass model.

The force on the pistons is formed due to the pressure difference. The value of pressure in atmospheric cavities varies depending on the mass flow of air, as well as changes in the volume of cavities in accordance with the equations:

$$\frac{dP_{1a}}{dt}=\frac{G_{1a}-S_1\cdot P_{1a}\cdot \dot{X}_1}{V_{1a}+S_1\cdot X_1}\cdot k, \tag{9}$$

$$\frac{dP_{2a}}{dt}=\frac{G_{2a}-S_2\cdot P_{2a}\cdot \dot{X}_1}{V_{2a}+S_2\cdot X_1}\cdot k. \tag{10}$$

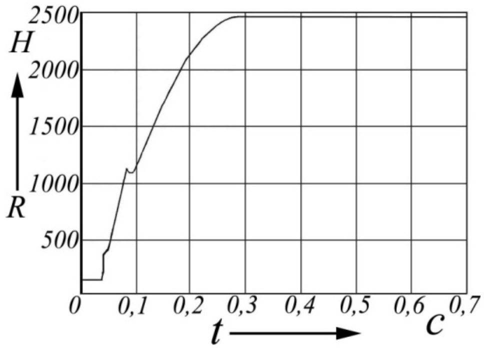

Figure 2. Dependence $R = f(t)$

The connection between the distribution and actuating devices is performed by the tracking device. The scheme of the most common tracking device is shown in Figure 3.

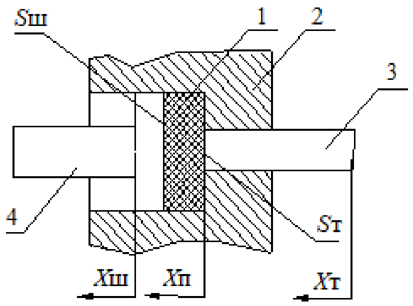

Figure 3. Scheme of the studied tracking device: *X*т, *X*п, *X*ш — displacement of the pusher, piston and rod, respectively; *S*т, *S*ш are the areas of reactive washer 1 interacting with the pusher and rod, respectively

During operation of the Vacuum brake booster, pressure builds up in reaction disc 1. The change in pressure depends on the relative position of the pusher 3, piston 2 and rod 4 and can be described by the following mathematical expression:

$$\frac{dP}{dt}=\frac{\left[\dot{X}_{П}\cdot\left(S_{Ш}-S_{Т}\right)+\dot{X}_{Т}\cdot S_{Т}-\dot{X}_{Ш}\cdot S_{Ш}\right]\cdot E}{V_{РШ}}, \tag{11}$$

on the other side

$$\frac{dP}{dt}=\frac{\dot{F}_S}{S_{Ш}}, \tag{12}$$

where $\dot{F}_S$ — the rate of change of force on the rod according to the dependence $\dot{F}_S = f\left(X_{Ш}\right)$.

In this case, the speed of movement of the rod has the form

$$\dot{X}_{Ш}=\frac{\dot{X}_{П}\cdot\left(S_{Ш}-S_{Т}\right)+\dot{X}_{Т}\cdot S_{Т}-\frac{dP}{dt}\cdot\frac{V_{РШ}}{E}}{S_{Ш}}. \tag{13}$$

The developed mathematical model is implemented in the Simulink application of the MATLAB environment. The mathematical model and the method of its implementation make it possible to expand the possibilities of choosing and optimizing the parameters of promising Vacuum brake boosters.

Special installation for studying the working process of the vacuum brake booster

This article suggests the development of a modern measuring and recording complex designed for experimental studies of an automobile hydraulic brake drive with a vacuum booster.

Equipment for research of working processes and characteristics of vacuum amplifiers.

To study the working processes and characteristics of vacuum amplifiers, a laboratory setup was developed, the block diagram of which is shown in Figure 4.

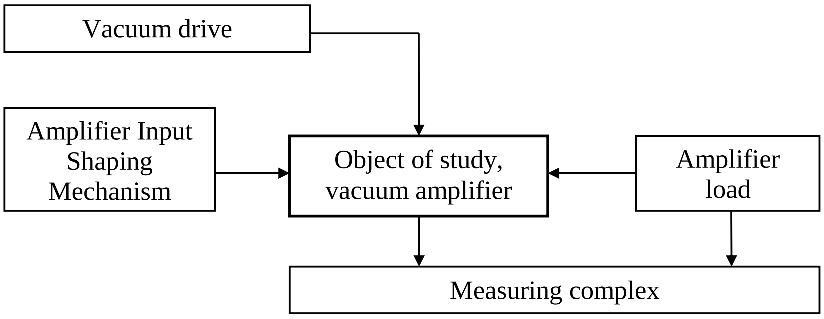

Figure 4. Structure of the laboratory setup

To provide vacuum, a vacuum drive was used, made according to the scheme shown in Figure 5.

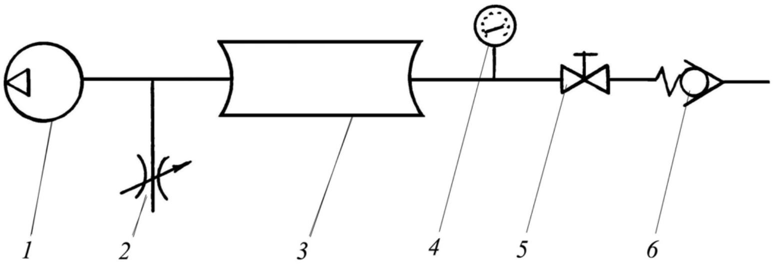

1 — vacuum pump; *2* — choke of variable cross section;
3 — vacuum receiver; *4* — vacuum gauge; *5* — uncoupling valve; *6* — check valve

Figure 5. Diagram of the vacuum drive

As a vacuum pump pos. 1 in Figure 5, a SO 7B reciprocating compressor unit with an air flow rate of at least 0.5 m3/min is used. To maintain the vacuum level, a variable cross-section throttle 2 was used in the line between pump 1 and vacuum receiver 3. Receiver 3, with a volume of 20 liters, is designed to smooth out the rarefaction pulsations and provide a vacuum reserve. To control the vacuum in the system, VP4-UU2 vacuum gauge is installed. Vacuum installation allows to obtain a stable level of vacuum up to 20 kPa absolute pressure.

The load of the investigated vacuum booster is a hydraulic drive, consisting of a main brake cylinder of the “Tandem” type with an inner diameter of 28 mm. Separate cavities of the master cylinder are connected by flexible hoses to the working cylinders of two drum brake mechanisms. The main brake cylinder and brake mechanisms are serial components of the brake system of a UAZ-3151 car in civilian design or KrAZ Cougar for the needs of the National Guard of Ukraine. Visual control of pressure in the hydraulic drive circuits is carried out by MP4-UU2 manometers with a pressure range of 0-16 MPa, a division value of 0.2 MPa and an accuracy class of 1.5. To register the pressure in the hydraulic drive, a KRT-7 sensor is installed. The location of the equipment on the experimental setup is shown in Figure 6.

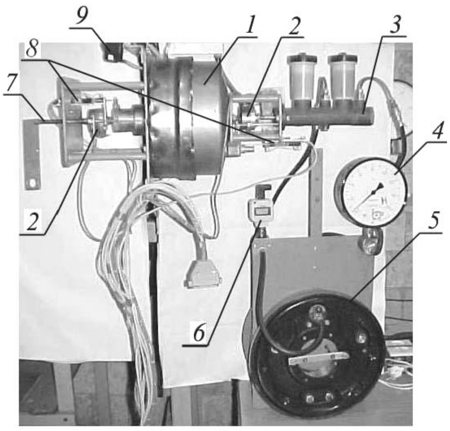

1 — vacuum brake booster under research; *2* — force sensors; *3* — the main brake cylinder; *4* — manometer;
5 — brake mechanisms with active and passive brake shoes (2 brake mechanisms); *6* — pressure sensor;
7 — screw device for forming the input signal; *8* — movement sensors; *9* — vacuum sensors

Figure 6. Location of equipment in the laboratory setup

On the input side of the vacuum booster, a bracket of increased rigidity is installed, made in the form of a straight parallelepiped. The amplifier under study is installed on one of the bases. On the opposite base, the installation of loading devices of the amplifier is provided. The bases are connected with pins. A force sensor is installed between the loading device and the pusher of the amplifier. A bracket for mounting displacement sensors is fixed on parallel studs. The bases of the pusher and piston displacement sensors are mounted on the bracket, and the movable sensor rods are connected to the booster pusher and piston. A smaller bracket, similar in design, is located between the vacuum booster outlet and the main brake cylinder of the load. There are also sensors for force and movement of the amplifier rod. To form the input signal of the amplifier under study, two variants of devices are provided. The first option is mechanical, screw (pos. 7, Fig. 6). It allows you to consistently set a stable rigid position of the booster pusher. The thread pitch of the screw pusher is 1 mm. The second variant of the device for forming the input signal of the amplifier is pneumatic.

The characteristic of the load is the dependence of the force on the piston of the main brake cylinder on its movement. The load characteristic obtained on the experimental setup is shown in Figure 7.

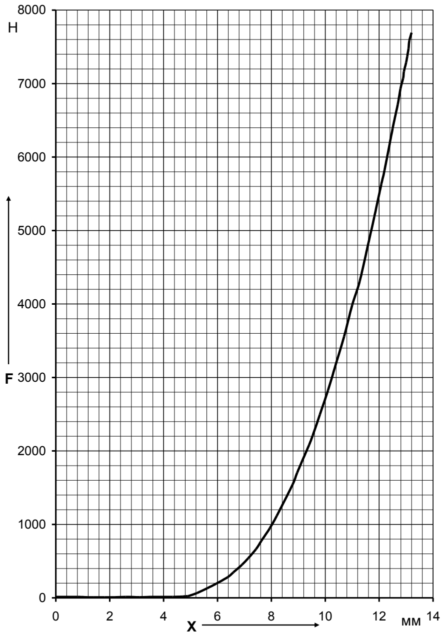

F — force at the entrance of the main brake cylinder; X — movement of the piston of the main brake cylinder

Figure 7. Load characteristic of the vacuum booster

The general scheme of a pneumatic drive with an input signal conditioning device is shown in Figure 8.

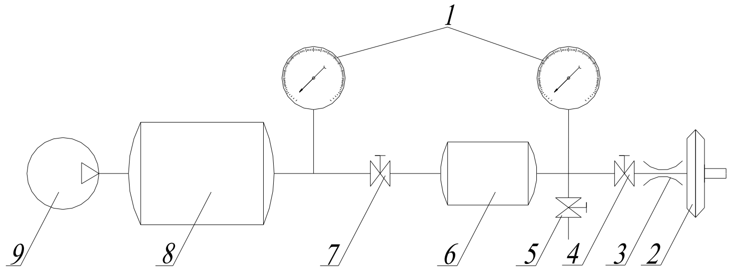

1 — pressure gauges; *2* — pneumatic chamber type 9; *3* — throttle; *4* — valve for flowing the receiver into the pneumatic chamber; *5* — valve for setting the pressure in the receiver; *6* — working receiver; *7* — valve for filling receiver 6; *8* — storage tank; *9* — stationary compressor

Figure 8. Scheme of the pneumatic drive of the experimental setup

The composition of the pneumatic actuator Figure 8 includes a stationary compressor *9* with a storage capacity of 200 l, a working receiver *6* of a laboratory unit with a capacity of 20 l, pressure gauges *1* for controlling the pressure in the pneumatic drive and the working receiver, as well as filling valves *7* and flow *4*, *5* of the working receiver *6*. Pneumatic chamber *2* is installed coaxial to the pusher of the studied amplifier. Air is supplied from the working receiver to the pneumatic chamber by a manual push-button valve *4*. The filling rate of the pneumatic chamber is provided by a constant-section throttle *3* installed at the inlet of the pneumatic chamber.

The placement of the elements of the investigated vacuum amplifier relative to the load and the device for forming the input signal is shown in Figure 9.

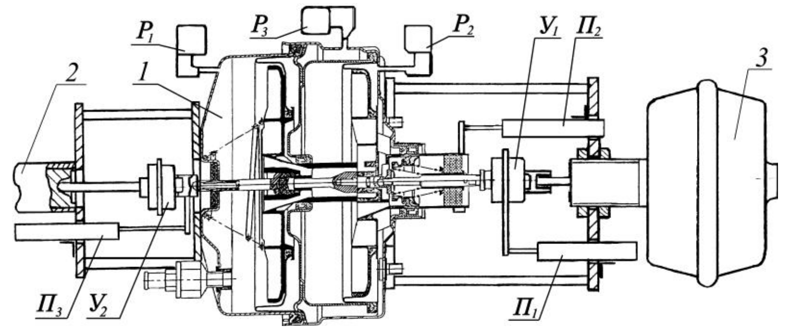

1 — vacuum booster under research; *2* — load; *3* — pneumatic chamber;
P_1, P_2, P_3 — displacement sensors; $П_1$, $П_2$, $П_3$ — vacuum sensors; $У_1$, $У_2$ — force sensors

Figure 9. Layout of the vacuum amplifier on the experimental setup

Technique of performing research on the experimental facility

When performing research on the experimental setup, the following parameters of the vacuum amplifier were measured and recorded:

- force on the pusher;
- force on the rod;
- pusher movement;
- piston movement;
- rod movement;
- pressure (vacuum) in the cavities of the amplifier.

The investigated physical processes require the use of high-precision and high-speed measuring instruments. Processing and analysis of the results is most expediently performed using modern digital computers (PC). Thus, the narrow specialization of the performed research led to the creation of a special measuring and recording complex.

Automated system for measuring and recording complex of working processes of vacuum brake boosters

Structural measuring and recording complex consist of three parts. The first part includes sensors for measuring the physical quantities of the studied parameters. The second part consists of pre-processing equipment, recording and issuing information about the parameters under study. The third part of the complex provides the necessary levels of power supply for sensors and equipment for processing and issuing information.

Taking into account the technical requirements for the implementation of the experiment and the results of the analysis of the products of the world's leading manufacturers of measuring equipment, the necessary measuring instruments were determined and purchased.

Strain gauges model LPX manufactured by Precision Transducers Ltd are used for force measurement. The experimental setup uses LPX sensors with force measurement ranges F = 0–2500 N and 0–10000 N.

With the help of this complex, you can solve the following tasks:

a) determination of the static characteristics of the dual-circuit master brake cylinder, single-chamber and double-chamber vacuum brake boosters;

b) determination of the dynamic characteristics of the hydraulic drive and the vacuum brake booster;

c) determination of the static and dynamic parameters of the working process of the vacuum brake booster.

To solve these problems in the process of research, it is necessary to obtain information on measuring the forces and displacements of the pusher, the booster rod, the degree of valve opening, the level of rarefaction in the working cavities of the booster, and the fluid pressure in the hydraulic brake drive circuits [8, 24, 27]. Based on the analysis of the designs of hydraulic brake drives of cars [6], the ranges of measured values were determined:

– force on the pedals: 0...500 N;

– force on the pusher: 0...2500N;

– force on the rod: 0...10000 N;

– movement of the rod and pusher: 0...50 mm;

– rarefaction in the working cavities of the amplifier: 0...0.09 MPa;

– pressure in the hydraulic drive of the brakes: 0...15 MPa.

Analysis of the products of the world's leading manufacturers of measuring equipment [9, 20, 22, 23, 30–32] was carried out taking into account the ratio of functional properties — price. As a result of this analysis, the following measuring devices were identified:

– for force measurement, LPX model sensors manufactured by Precision Transducers Ltd (New Zealand) with force measurement ratings up to 500 N, 2500 N and 10000 N;

– for measuring displacements, precision potentiometric sensors model CLP–13-50 manufactured by Megatron (Germany);

– for measuring pressure in the cavities of the vacuum booster BOSCH sensors series 0261230004 (Germany);

– to measure pressure in the hydraulic drive, the following sensors: strain gauges of the D, MD and KRT-7 series and the DM 5001, DM 5007 series.

During the development of the measuring and recording complex, the problem of providing various levels of power supply to sensors and stabilization, different in type (current and voltage) and the level of output signals, was solved. In addition, the peculiarity of the studied work processes was taken into account — the measurement and registration of fast and slow processes [33, 34]. For the rational use of the amount of memory, automatic measurement of the data recording interval was applied depending on the speed of the process. As a result, a circuit of a special electronic signal processing unit (SPU) was developed. Designed by SPU, designed for simultaneous use of 12 channels and has the following functionalities:

– ensuring stable power supply of channels;

– noise filtering and signal stabilization;

– calibration of sensors;

– determination and setting of the initial value of the measured parameter;

– testing and control of serviceability of channels;

– automatic mode of measurement and registration of parameters;

– accumulation, reading of parameters and cleaning of the system.

The structure of one SPU channel and the algorithm of operation of the electronic unit are presented respectively in Figure 10 and Figure 11.

According to the SPU channel structure shown in Figure 10, first, the sensor signal is amplified, stabilized, and digitized. Digital signals are fixed and accumulated. Each channel has the ability to calibrate the signal using an external keyboard and display the accumulated information.

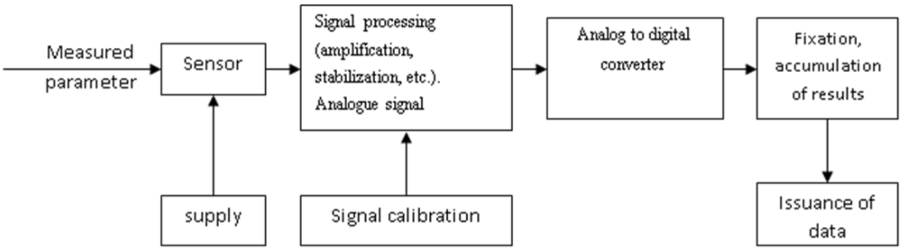

Figure 10. SPU channel structure

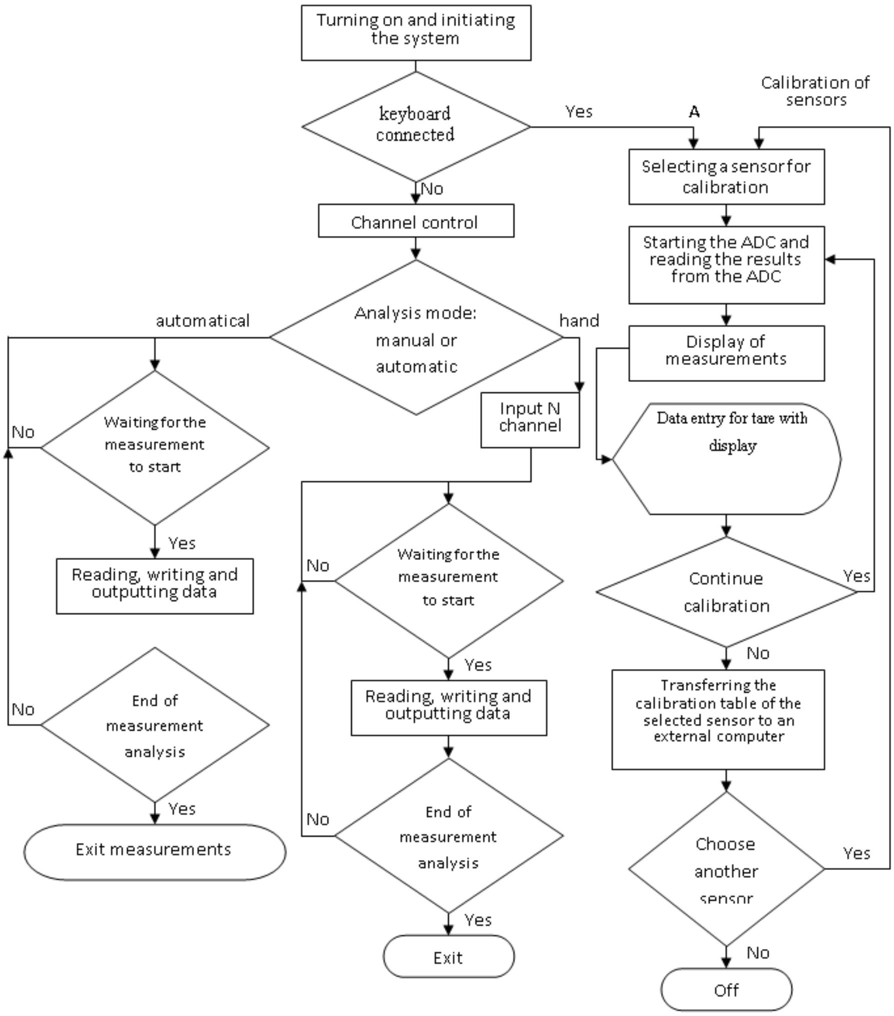

Figure 11. Algorithm of operation of the electronic unit SPU

According to the algorithm (Fig. 11), the SPU works as follows. When the measuring complex is turned on, the entire SPU periphery is initiated.

After initiation, the sign of connecting an external keyboard is checked. Based on the connection, the mode of further operation is selected:

– with the connected keyboard the tare mode;

– without keyboard connection – measurement mode.

In the calibration mode, the system displays information about the calibration with the number of the sensor and the corresponding channel of the analog-to-digital converter (ADC) on the graphic display.

After starting ADC, the measured value is displayed on the display. The equivalent calibrated value of the parameter and the command to fix this value by the system are set from the keyboard. Then, the following values are fixed similarly until the sign of the end of the calibration process is entered.

After calibration is completed, the measurement mode is set: manual or automatic, and the system proceeds to control the ADC channels. Then the connection and serviceability of sensors is checked with visual control of information on the display. After testing the sensors, the system analyses the operating mode: manual or automatic. Manual mode provides for viewing the measurement result on the display. ADC channels are triggered by a process start signal. Information is read from them and written to the random access memory (RAM) of the controller. The measurement results are displayed if necessary.

Measurements in automatic mode are performed similarly to manual ones, but the results are accumulated in blocks in the form of numerical arrays in RAM for further use for processing on an external PC. The SPU electronic element base is combined on three boards, as shown in the block diagram of Figure 12.

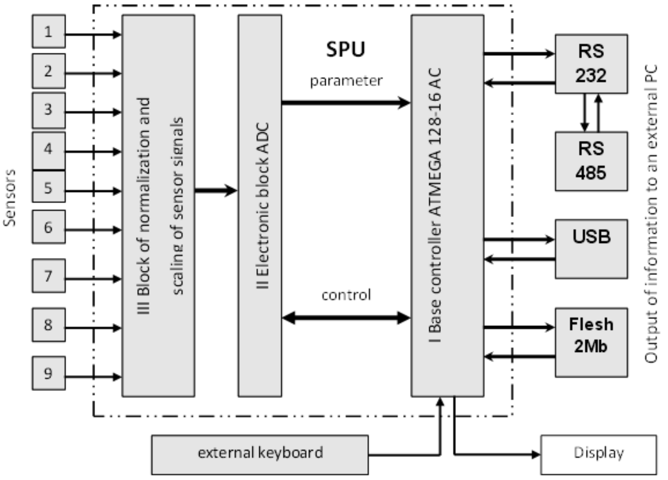

Figure 12. Block diagram of the measuring complex

The measuring complex, the block diagram of which is shown in Figure 3 has nine channels with sensors, signal processing unit (SPU) with keyboard, display via PC interface. To study the working process of a vacuum amplifier, it is necessary to know the change in the level of rarefaction in the cavities, the change in the forces on the pusher and rod, the coordinates of the movement of the pusher, piston, rod.

The board I of the controller is designed to control the entire measuring complex and has an interface connection with a PC. The controller is based on the ATMEGA 128-16 AC microprocessor.

For communication with external devices, I/O and storage of temporary data, a rewritable Flash program memory module is used.

The measuring system for communication with PC has three interfaces RS-232, RS-485 and USB. The RS-232 interface scheme is based on the ADM 202 EAN chip. The RS-485 interface is based on the MAX 487E CPA chip. For USB communication, the FT 245 BM-FTDI chip is used.

The measurement results are displayed on the BG12864A GPLW graphic display.

Board II ADC contains 12 independent analog-to-digital channels. Each channel is based on AD 7492 AR-5 chips.

The signals from the sensors are pre-processed on the electronic unit III. The sensor signal normalization and scaling unit contains LM 358 operational amplifiers. The pre-processed signals from the sensors enter the switch, are processed at the voltage limiter, and then go directly to the ADC. All ADC channels are launched simultaneously, then each of them is selected using decoders and read into the controller's RAM.

The complex is powered by DC voltage 12V. Power supply of the sensors is from the signal processing unit with a voltage of 5V.

The non-linearity of the output signals of pressure, vacuum and force ±0.2 %. Non-linearity of motion signals ±0.3 % and resolution <0.01 mm.

The overall dimensions of the signal processing unit are 140×120×60 mm. Weight is 0.38 kg.

To measure the force, LPX Precision Transducers with measurement limits of 2500 N and 10000 N are used. The combined error of the sensors is 0.1% and the allowable overload is 150 %.

The movement of the pusher, piston and booster rod is measured by CLP-13-50 sensors. These sensors have a resolution of less than 0.01 mm with a linearity tolerance of up to 0.7–1.3 % at a travel speed not exceeding 5 m/s. Such accuracy is sufficient to estimate the relative movement of the pusher and piston, rod and piston.

The installation of force and displacement sensors does not require changes in the design of the vacuum booster.

The research facility is equipped with three vacuum sensors BOSCH series 0261230004 with absolute pressure measurement limits from 20 to 100 kPa. When studying the working process of two-chamber vacuum amplifiers, rarefaction sensors are connected to both atmospheric cavities and the vacuum cavity. In the case of a single-chamber amplifier study, only two vacuum sensors are used. Connecting the measuring cavities of the vacuum sensors to the corresponding cavities requires a change in the design of the amplifier housing. It is quite simple to do this by making axial holes in the corresponding bolts for fastening the amplifier and the main brake cylinder.

The layout of the sensors on the installation is shown in Figure 9, and a general view of the setup and sensors is shown in Figure 13.

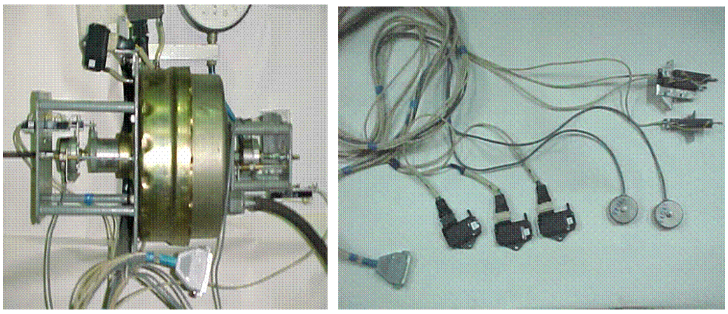

Figure 13. Automated system for measuring and complex recording of working processes of vacuum brake boosters

Results of experimental researches

Before the experiment, the sensors are calibrated, the elements and parameters are set, which determine the initial conditions and characteristics of the input action in accordance with the research program. After starting the control program on the PC, the input signal conditioning device is activated. Registration of changes in effort, rarefaction, and displacements is automatically recorded in the memory of a personal computer in the form of a matrix with a quantization of 0.1–100 mls. The quantization level is set before the experiment, depending on the speed of the process.

After the experiment, the result is presented on the computer monitor as a graph $Fi = f\ (t)$, which can be used to evaluate its quality. An example of an "electronic oscillogram" is shown in Figure 14 *a*. Processing of the matrix of experimental data is carried out in the EXCEL software. In this case, it is possible to construct graphical dependences of the function under study on time or any other process parameter (Figure 14 *b*).

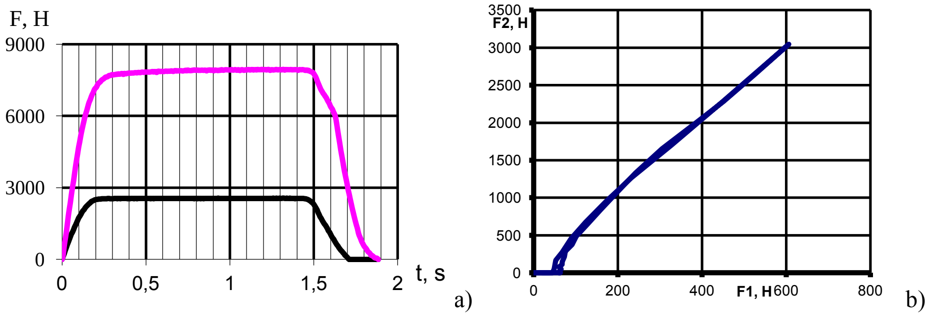

a)

b)

a) "electronic oscillogram"; *b*) dependence of the force at the output of the amplifier on the input force

Figure 14. The results of processing the results of the study

The name of the data matrix file is assigned automatically and represents the time of the experiment.

To obtain information about the operation of the vacuum amplifier, a dosed force was applied to its input (pusher). The dosing of the force in terms of magnitude and speed was provided by changing the pressure in the pneumatic chamber *3* (Fig. 9). In the processes of imitation of braking and releasing, the following were measured: the movement of the pusher, piston and rod; force on the pusher and rod; pressure in vacuum and atmospheric cavities. As a result of the created processing technique, absolute and relative data on the parameters of the workflow were obtained.

The study of the dynamics of the working process was carried out with a consistent study of the influence: liquefaction in a vacuum cavity; force on the pusher; the rate of force application to the pusher.

The general view of the experimental dynamic characteristics is shown in Figure 15.

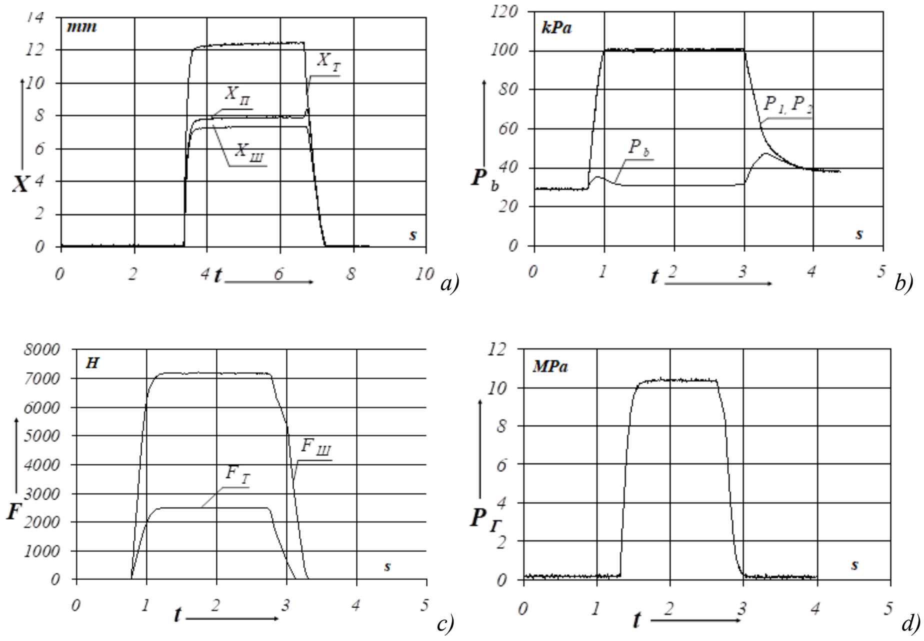

a) displacement $X = f(t)$; *b*) rarefaction $Pb = f(t)$; c) efforts $F = f(t)$; d) pressure in the load drive $RG = f(t)$;
Xт, Xп, Xш — displacement of the pusher, piston and rod, respectively; Pb, P1, P2 — change in pressure in the vacuum cavity and atmospheric cavities; Fт, Fш — force on the pusher and rod, respectively

Figure 15. General view of the obtained experimental dynamic characteristics

As a result of the experiments performed, it turned out that:

– the vacuum level practically does not affect the time of the braking process;

– the pressure equalization time in the vacuum and atmospheric cavities increases with an increase in the initial rarefaction;

– the braking process reduces the rarefaction in the vacuum cavity by an average of 6 kPa;

– with a decrease in the rate of effort on the pusher from 0.04 s to 0.3 s, the time for changing pressure in atmospheric cavities decreases by 0.2–0.24 s.

The theoretical position on the joint movement of the pistons without separation from each other is confirmed by the ratios of the movement of the pusher and the rod Xт>Xш. The influence of the rate of braking on the parameters of the working process Vacuum brake booster is shown in Table.

Also previously unknown data on the relative motion of the pusher, piston and rod, depending on the deformation of the follower element was obtained.

Subsequent experimental studies were carried out with the location of the brake system in full on the stand with the inclusion of the Vacuum brake booster created by it. The developed measuring and recording complex were used at the stand. The following parameters were measured: the force on the brake pedal and its movement; pressure in the hydraulic brake drive and pressure in the vacuum and atmospheric cavities Vacuum brake booster. The results obtained indicate minor deviations in performance due to the influence of the braking system. The errors of the static characteristics do not go beyond the recommended limits, and the dynamic characteristics confirm the high level of tracking action. The difference between the experimental and theoretical results when compared does not go beyond 6%. Comparison of the experimental dynamic and static characteristics of the Vacuum brake booster with the theoretical ones is shown in Figure 16.

Table

The results of the study of the influence of the rate of input action on the working process of the vacuum amplifier

Process parameters	Parameter value									
t_{T3} – time of change of force on the pusher from “0” to F_{Tmax}, s	0.04	0.08	0.09	0.09	0.10	0.26	0.28	0.29	0.30	0.32
t_{31} – time of pressure change in atmospheric cavities during braking, s	0.75	0.64	0.75	0.76	0.68	0.35	0.20	0.48	0.30	0.46
$t_{Ш3}$ – time of change of force on the rod from “0” to $F_{Шmax}$, s	0.82	0.72	0.80	1.00	0.80	0.48	0.40	0.52	0.50	0.46
Δt – release delay, s	0.18	0.12	0.20	0.17	0.15	0.16	0.15	0.12	0.18	0.09
$t_{Ш3} - t_{31}$, s	0.07	0.08	0.05	0.24	0.12	0.13	0.20	0.04	0.20	0
P_{BH} – initial vacuum level, kPa	28	54	22	32	36	24	32	56	44	67
F_{Tmax} – maximum force on the pusher, kN	2.4	2.5	2.4	2.5	2.4	2.4	2.5	2.5	2.4	2.5
$F_{Шmax}$ – maximum, force on the rod, kN	7.2	5.4	7.6	6.9	6.4	7.5	6.8	5.2	6.0	4.4

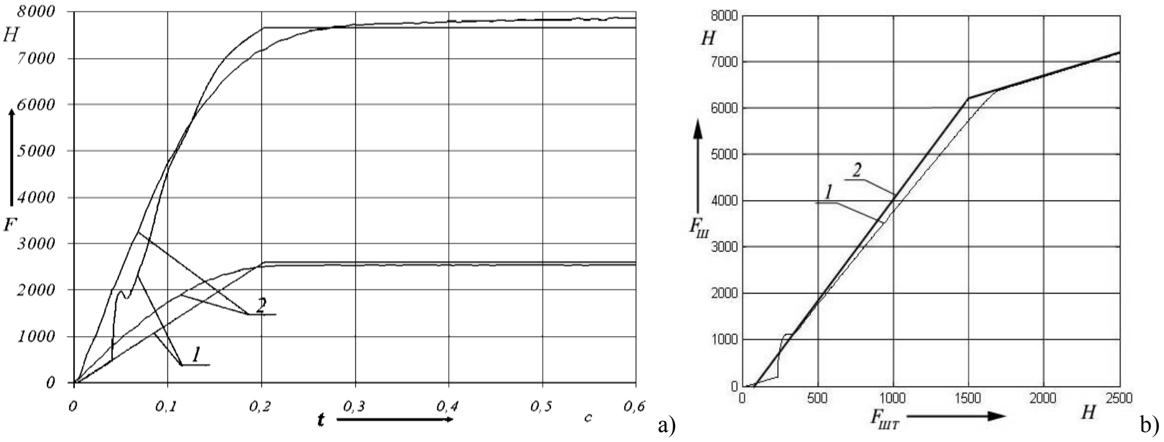

a) dynamic response; *b*) static characteristic;
1 — results of mathematical modeling; *2* — results of the experimental study

Figure 16. Comparison of experimental and theoretical characteristics

The developed setup can be used not only to study the characteristics of the working process of vacuum amplifiers, but also to certify each manufactured amplifier. At the same time, each manufactured unit will have a serial number, a real characteristic, a release date, etc., which will make it easy to identify the product and detect fakes.

Conclusions

1. The existing assessment of the efficiency of amplifiers is carried out according to one parameter — the gain, which is understood as the ratio of the output force to the input force. This approach is logical, mainly when there is no energy supply from an additional source, that is, the amplifier is considered as an energy converter. This approach does not allow us to evaluate the efficiency of amplifiers on vehicles with different masses. The developed set of criteria for evaluating the efficiency of vacuum boosters of the brake drive made it possible to comprehensively evaluate the effectiveness of vacuum boosters.

2. As criteria for evaluating the effectiveness, it is proposed to use:

– criteria for evaluating the work of a unit of mass and unit of volume, which is the ratio of the work at the output of the amplifier, respectively, to its mass and building volume;

– criteria for evaluating the power of a unit of volume and unit of mass, which allow us to evaluate not only the compactness of the amplifier, but also its speed;

– coefficient of compliance and specific idling of the booster pusher, characterizing the layout volume of the pedal drive.

3. The use of the proposed set of criteria made it possible to find ways to reduce the volume and mass in the amplifier design by 30–40% compared to analogues.

4. The created measuring and recording complex is used for bench studies of the characteristics of vacuum amplifiers.

5. Work continues to improve it, aimed at using it to obtain output passport data in the production of brake system units, in particular, vacuum boosters.

6. In the future, with appropriate modifications, the created complex is supposed to be included in the automation system for managing the work processes of vehicle units.

7. The practical use of the results obtained is aimed at achieving a social effect on improving the working conditions of drivers and increasing the active safety of cars.

Acknowledgements

The authors express their gratitude to the lecturers of the Department of Automobiles named after A. B. Gredeskula at Kharkiv National Automobile and Road University, who assisted in the research.

References

1 Road traffic injuries. World Health Organization. Retrieved from http://www.who.int/mediacentre/factsheets/fs358/en/

2 Kashkanov, A. & Palchevskyi, O. (2022). Problems of transport systems functioning of Ukraine large cities in modern conditions. Advances in Mechanical Engineering and Transport, *18*(1), 97–102. https://doi.org/10.36910/automash.v1i18.764.

3 Kashkanov, A.A., Diorditsa, V.M., Kucheruk, V.Yu., Karabekova, D.Zh., Khassenov, A.K., & Sharzadin, A.M. (2019). Inertial evaluation of the tyre-road interaction during emergency braking. *Bulletin of the University of Karaganda-Physics, 2*(94), 82–91. https://doi.org/10.31489/2019Ph2/82-91.

4 Lengyel, H., Maral, S., Kerebekov, S., Szalay, Z., & Török, Á. (2023). Modelling and Simulating Automated Vehicular Functions in Critical Situations — Application of a Novel Accident Reconstruction Concept. Vehicles, *5*, 266–285. https://doi.org/10.3390/vehicles5010015.

5 Bogomolov, V., Klimenko, V., Leontiev, D., Ponikarovska, S., Kashkanov, A., & Kucheruk, V. (2021). Plotting the adhesion utilization curves for multi-axle vehicles. *Bulletin of the University of Karaganda-Physics, 1*(101), 35–45. https://doi.org/10.31489/2021Ph1/35-45.

6 Robert, Bosch GmbH (2022). Automotive Handbook. 11th ed. Karlsruhe: Wiley.

7 Walker, J., Rucoba, R., Barnes, D., & Kent, S. (2019). Brake Vacuum Booster Characterization, SAE Technical Paper 2019-01-0412. https://doi.org/10.4271/2019-01-0412.

8 Volkov, V.P., Sklyarov, V.N., Schuklinov, S.N., & Sklyarov, N.V. (2008). Brake drives of passenger cars. Publishing House of Khnadu, 542 p.

9 Aleksandrowicz, P. (2019). The Impact of a Vehicle Braking System State on Safe Driving. Part Two. *AIP Conference Proceedings, 2077*(1). https://doi.org/10.1063/1.5091862.

10 Pacejka, H.B. (2012). Tyre and vehicle dynamics. 3rd Ed. Butterworth-Heinemann, Elsevier. https://doi.org/10.1016/C2010-0-68548-8

11 Kashkanov, A.A., Rotshtein, A.P., Kucheruk, V.Yu., & Kashkanov, V.A. (2020). Tyre-Road friction Coefficient: Estimation Adaptive System. *Bulletin of the University of Karaganda-Physics, 2*(98), 50–59. https://doi.org/10.31489/2020Ph2/50-59.

12 Breuer, J., Faulhaber, A., Frank, P., & Gleissner, S. (2015). Real world safety benefits of brake assistance systems. *Proceedings of the 20th International Technical Conference on the Enhanced Safety of Vehicles*, 07-0103. Washington, DC: National Highway Traffic Safety Admin-istration. Retrieved from https://www-esv.nhtsa.dot.gov/Proceedings/20/07-0103-O.pdf.

13 Harald, K. et al. (2016). Prospective Evaluation of the Collision Severity L7e Vehicles Considering a Collision Mitigation System. *Transportation Research Procedia, 14,* 3877–3885. https://doi.org/10.1016/j.trpro.2016.05.474.

14 Zhang, X., Lu, Z., Yuan, X., Wang, Y., & Shen, X. (2021). L2-Gain Adaptive Robust Control for Hybrid Energy Storage System in Electric Vehicles. *IEEE Transactions on Power Electronics, 36,* 7319–7332. https://doi.org/10.1109/TPEL.2020.3041653.

15 Szumska, E., Skuza, A., & Jurecki, R. (2023). The analysis of energy recovered by an electric vehicle during selected braking manoeuvres. *The Archives of Automotive Engineering – Archiwum Motoryzacji, 99*, 18–29. https://doi.org/10.14669/AM/162079.

16 Prasetya, S., Budiono, H.D.S., Baskoro, A.S., Shamsuddin, A., Sumarsono, D.A., Adhitya, M., Zainuri, F., Nazaruddin, Heryana, G., & Siregar, R. (2020). Smart Braking Actuator Control for a Heavy Weighted Electric Vehicle. *Journal of Mechanical Engineering Research and Developments*, (1), 8–16.

17 Siregar, R., Adhitya, M., Sumarsono, D.A., Nazaruddin, Heryana, G., & Zainuri, F. (2020). Study the Brake Performance of a Passenger Car Based on the Temperature That Occurs in Each Brake Unit. Recent Progress on: Mechanical, Infrastructure and Industrial Engineering. In: *Proceedings of International Symposium on Advances in Mechanical Engineering (ISAME): Quality in Research 2019 2227*, 020013

18 Zhao, J., Xi, X., Na, Q., Wang, S., Kadry, S.N., & Kumar, P.M. (2021). The Technological Innovation of Hybrid and Plug-in Electric Vehicles for Environment Carbon Pollution Control. *Environmental Impact Assessment Review, 86*, https://doi.org/10.1016/j.eiar.2020.106506.

19 Ko, S., Song, C., & Kim, H. (2016). Cooperative Control of The Motor and Electric Booster Brake to Improve the Stability of An In-Wheel Electric Vehicle. *International Journal of Automotive Technology, 17*(3), 447–456.

20 Yu, L., Liu, X., & Liu, X. (2016). Analysis of Energy Consumption on Typical Main Cylinder Booster Based Brake-by-Wire System. *SAE Technical Paper* 2016-01-1955. https://doi.org/10.4271/2016-01-1955.

21 LSP (2023). The Future of Braking-Integrated Braking System. Retrieved from https://www.lsp-ias.de/en/products-services/own-innovations/integratedmodular-braking-system.

22 Chen, Z., Zhu, B., Zhao, J., Wu, J., Song, D., & Du, J. (2022). Electro-Hydraulic Distribution Control Strategy for Regenerative Braking Based on Adjustable Cylinder Reservoir. *Qiche Gongcheng/Automotive Engineering, 44*(2), 239–246. https://doi.org/10.19562/j.chinasae.qcgc.2022.02.011.

23 Mei, M., Cheng, S., Li, L., & Yan, B. (2022). Precise Position Adjustment of Automotive Electrohydraulic Coupling System With Parameter Perturbations. *Journal of Dynamic Systems, Measurement and Control, Transactions of the ASME, 144*(5), 051008. https://doi.org/10.1115/1.4053430.

24 Leontiev, D., Klimenko, V., Mykhalevych, M., Don, Y., & Frolov, A. (2020). Simulation of Working Process of the Electronic Brake System of the Heavy Vehicle. In: Palagin, A., Anisimov, A., Morozov, A., Shkarlet, S. (Ed.) *Mathematical Modeling and Simulation of Systems. MODS 2019. Advances in Intelligent Systems and Computing, 1019*. Springer, Cham. https://doi.org/10.1007/978-3-030-25741-5_6.

25 Schuklinov, S.N. & Sklyarov, N.V. (2005). Criteria for evaluating the effectiveness of the design of vacuum amplifiers, Automobile transport. *Sat. scientific tr.*, 16: 159-161.

26 Schuklinov, S.M., Sklyarov, V.M., & Sklyarov, M.V. (2008). Improvement of the dynamic characteristics of the vacuum substation of the galmium drive. Autoshlyahovik of Ukraine, 5: 19–22.

27 Shuklynov, S., Kholodov, M., Verbitskiy, V., Makarov, V. et al. (2020). Simulation of the Combined Braking Control System for Hybrid Electric Vehicles. *SAE Technical Paper* 2020-01-0217. https://doi.org/10.4271/2020-01-0217.

28 Sklyarov, V.N. & Sklyarov, M.V. (2011). Technique for modeling the hydraulic galvanic drive, Automobile transport. *Sat. scientific tr.*, 29: 105–111.

29 MathWorks (2023). Use Object-Oriented Programming to Model Real-World Objects. Retrieved from https://ch.mathworks.com/products/matlab/object-oriented-programming.html.

30 Chen, P., Wu, J., Zhao, J., & He, Rui. (2018). Design and Position Control of a Novel Electric Brake Booster. *SAE International Journal of Passenger Cars — Mechanical Systems, 11*(5), 1–11.

31 Lu, M., Huang, R., Yin, W., Zhao, Q., & Peyton, A. (2019). Measurement of Permeability for Ferrous Metallic Plates using a Novel Lift-off Compensation Technique on Phase Signature. *IEEE Sensors Journal, 19*(17), 440–446.

32 Lyu, D. & Jing, L. (2019). EBooster: A Technology That Improves the Efficiency of Brake Recuperation in Electric Vehicle. In: *Proceedings — 2019 Chinese Automation Congress, CAC 2019*, 5712–5716.

33 Golnaraghi, Farid & Benjamin, C. Kuo (2017). Automatic Control Systems. 10th ed. New York: McGraw-Hill Education. Retrieved from https://www.accessengineeringlibrary.com/content/book/9781259643835.

34 Sokolov, Y.N., Iliushko, V.M., Emad, A.R. (2005). Automatic Control Systems: Fundamentals, Theory and Application. Edited by Y.N. Sokolov. JAI – Amman.

Н. Скляров, А. Шаповалов, П. Черненко, А. Корнев,
А. Кашканов, В. Кашканов, В. Кучерук

Вакуумдық тежегіш күшейткіштің жұмыс процесін зерттеу

Зертханалық қондырғыны жасау толық массасы 3,5 тоннаға дейінгі азаматтық мақсаттағы автомобильдердің гидравликалық тежегіш жетектерінің және қызметтік-жауынгерлік міндеттерді орындауға арналған толық массасы 8,5 тоннаға дейінгі автобронетанк техникасының құрамындағы вакуумдық күшейткіштердің жұмыс процестері мен сипаттамаларын зерттеуді қамтамасыз ету мақсатында жүргізілді. Бұған дейін Харьков ұлттық автомобиль-жолдары университетінің т.ғ.д., проф. А.Б. Гредескул атындағы Автомобиль кафедрасының бірқатар ғалымдары осы бағытта теориялық зерттеулер жүргізумен айналысқан, олардың біразы ғылыми жұмыстарда көрініс тапқан. Теориялық зерттеулердің нәтижелерін осы жұмыста ұсынылған зертханалық қондырғыда орнатылған эксперименттік қондырғылармен, мақалада сипатталған эксперименттік әдістеме бойынша, сигналдарды өңдеудің электронды кешені мен датчиктер блогының көмегімен салыстыру теориялық және эксперименттік зерттеулердің сәйкессіздігін 6% шегінде анықтауға мүмкіндік берді. Эксперименттік зерттеулерді жүргізуге арналған бұл кешен алғаш рет жасалды және автомобильдердің тежегіш жетегінің вакуумдық күшейткіштерінің теориялық зерттеулерін растап қана қоймай, сонымен қатар зерттелетін тораптың салмақ пен габариттік параметрлері арасындағы бірқатар тәуелділіктерді, сондай-ақ вакуумдық күшейткіштердің құрылымдық компоненттері арасындағы бірқатар функционалдық қатынастарды анықтады, бұл оның дизайнын айтарлықтай оңтайландыруға мүмкіндік береді.

Кілт сөздер: көлік құралдары, белсенді қауіпсіздік, тежеу жүйесі, вакуумдық тежегіш күшейткіш, статикалық және динамикалық сипаттамалар, тәжірибелік зерттеулер, технология, жабдық.

Н. Скляров, А. Шаповалов, П. Черненко, А. Корнев,
А. Кашканов, В. Кашканов, В. Кучерук

Исследование рабочего процесса вакуумного усилителя тормозов

Создание лабораторной установки проводилось с целью обеспечения исследования рабочих процессов и характеристик вакуумных усилителей в составе гидравлических тормозных приводов автомобилей с полной массой до 3,5 т гражданского назначения и автобронетанковой техники с полной массой до 8,5 т, предназначенной для выполнения служебно-боевых задач. Проведением теоретических исследований в этом направлении ранее занимался ряд учёных кафедры автомобилей им. д-ра техн. наук, проф. А.Б. Гредескула Харьковского национального автомобильно-дорожного университета, которые отражены в их научных работах. Сравнение результатов теоретических исследований с экспериментальными, полученными на предлагаемой в настоящей работе лабораторной установке по экспериментальной методике, описанной в статье, с помощью созданного электронного комплекса обработки сигналов и блока датчиков, позволило установить расхождение теоретических и экспериментальных исследований в пределах 6 %. Данный комплекс для проведения экспериментальных исследований создан впервые и позволил получить результаты, которые не только подтвердили теоретические исследования вакуумных усилителей тормозного привода автомобилей, но и выявили ряд зависимостей между весовыми и габаритными параметрами исследуемого узла, а также функциональные взаимосвязи между структурными компонентами вакуумных усилителей, что позволяет значительно оптимизировать его конструкцию.

Ключевые слова: транспортные средства, активная безопасность, тормозная система, вакуумный усилитель тормозов, статические и динамические характеристики, экспериментальные исследования, техника, оборудование.

Information about authors

Sklyarov, N.V. — Associate professor, Candidate of technical sciences, Associate professor of the Department of Armored Vehicles, National Academy of the National Guard of Ukraine, e-mail: nikotinonikos@gmail.com, https://orcid.org/0000-0001-7785-6059

Shapovalov, A.I. — Associate professor, Candidate of technical sciences, Deputy head of the Department of Armored Vehicles, National Academy of the National Guard of Ukraine, e-mail: halex1702@gmail.com, https://orcid.org/0000-0001-8518-4336

Chernenko, P.V. — Senior teacher of the Department of Armored Vehicles, National Academy of the National Guard of Ukraine, e-mail: Pav.chernenko@ukr.net, https://orcid.org/0000-0003-0351-3111

Korniev, A.V — Teacher of the Department of Armored Vehicles, National Academy of the National Guard of Ukraine; e-mail: ssv4055@ukr.net, https://orcid.org/0000-0003-4808-4410

Kashkanov, A.A. — Professor, Doctor of science (Engineering), Professor of the Department of Automobiles and Transport Management, Vinnytsia National Technical University, Ukraine, e-mail: a.kashkanov@gmail.com, https://orcid.org/0000-0003-3294-6135

Kashkanov, V.A. — Candidate of technical sciences, Associate professor of the Department of Automobiles and Transport Management, Vinnytsia National Technical University, Ukraine, e-mail: kash_2004@ukr.net, https://orcid.org/0000-0002-3897-6792

Kucheruk, V.Yu. — Professor, Doctor of science (Engineering), Professor of the Department of Information Technologies, Uman National University of Horticulture, Ukraine, e-mail: vladimir.kucheruk@gmail.com, https://orcid.org/0000-0002-6422-7779

Article

Received: 27.09.2023
Accepted: 05.12.2023

UDC 538.971

https://doi.org/10.31489/2024PH1/59-65

M.M. Kubenova[1*], K.A. Kuterbekov[1], M.Kh. Balapanov[2], R.Kh. Ishembetov[2],
G.D. Kabdrakhimova[1], R.A. Alina[1], D. Bulatova[1], M. Tatay[1], O. Yelibayev[1]

[1]*L.N. Gumilyov Eurasian National University, 2 Satpayev str., 010008 Astana, Kazakhstan;*
[2]*Ufa University of Science and Technology, 32 Zaki Validi str., 450076 Ufa, Bashkortostan, Russia*
[*]*Corresponding author's e-mail: kubenova.m@yandex.kz*

Investigation of thermoelectric properties of nanocrystalline copper chalcogenides

Modern research efforts are aimed at developing fuel cells characterized by high efficiency, low cost and environmental friendliness, which largely depend on the properties of the corresponding catalyst materials — the most important components of the fuel cell. Catalysts based on metal chalcogenides, predominantly S based, have activity in accelerating the oxygen reduction reaction comparable to the activity of Pt in H_2SO_4. The work uses the technique of compacting powder materials and obtained volumetric samples. Nanodisperse powder fractions with an average particle size of (50–100) nm were obtained. The values of the thermo-emf coefficient (about 0.08 mV/K) were obtained for the studied alloy with low defects in the cation sublattice of the $Cu_2S_{0.5}Te_{0.5}$ type. It was found that a decrease in grain size leads to a significant decrease in electronic conductivity for all studied samples. The paper presents the results of a study of the thermoelectric properties of the $Cu_2S_{0.5}Te_{0.5}$ triple alloy. For the studied composition, a decrease in thermal conductivity by (25–30)% and a slight increase in the thermal emf coefficient compared with large–crystal samples were obtained. Low thermal conductivity was found in the range (0.3–1.1) W m^{-1} K^{-1} with a conductivity above 1000 ohms-1cm-1. For the studied sample $Cu_2S_{0.5}Te_{0.5}$ — thermoelectric efficiency (ZT = 0.25) at 400 °C, which allows us to hope for the possibility of improving the characteristics of samples of this composition to acceptable values for practical thermoelectric devices by selecting the optimal alloying.

Keywords: thermoelectric materials; copper sulfide; crystal structure; conductivity; diffusion; thermal conductivity; Seebeck coefficient; superionic conductors.

Introduction

The current efforts of researchers are aimed at developing fuel cells characterized by high efficiency, low cost and environmental compatibility, which largely depend on the properties of the corresponding catalyst materials (the most important components of the fuel cell) [1]. Currently, the best and most commonly used catalysts for fuel cells are still noble metal nanocomposites (catalysts (the most important components of a fuel cell), especially Pt), if we take into account their comparable catalytic characteristics relative to ORR and much lower cost [1].

Metal chalcogenide-based catalysts, mainly based on Se and S, again attracted considerable attention after Alonso-Vante and Tributsch [2] found that $Ru_2Mo_4Se_8$ has an activity in accelerating the oxygen reduction reaction comparable to the activity of Pt in H_2SO_4 [3, 4]. Many metals forming chalcogenides with S, Se and Te have shown good activity of the oxygen reduction reaction (ORR) [1–4].

Experimental part

The method of synthesis of thermoelectric materials

Due to the high reactivity of tellurium, the synthesis of the required $Cu_{2-x}Te_xS$ samples took place in two stages:

1. First, non-stoichiometric compositions of $Cu_{2-x}S$ were obtained.
2. The second stage of the preparation of $Cu_{2-x}Te_xS$ samples consisted in the introduction of tellurium instead of the copper missing to the stoichiometric composition in such a way that for the metal as a whole. The binary alloy obtained after homogenization was ground in an agate mortar and placed in quartz ampoules filled with argon, pieces of lithium were placed inside the ampoules of the powder so that they did not come into contact with the walls of the ampoule.

The synthesis temperature was reached within three days with a gradual increase in temperature. The furnace was slowly heated to melt lithium and held for several hours until it dissolved in reagents. The final stage of the synthesis of the substance took place at a temperature of 450 °C for three days.

Results and discussion

The results of alloy synthesis $Cu_2S_yTe_{1–y}$

Triple $Cu_2S_yTe_{1–y}$ alloys were synthesized. Strong alloying or substitution is in line with the modern strategy of optimizing the thermoelectric properties of materials [5–8].

Table shows the results of X-ray spectral analysis of the chemical composition of the $Cu_2S_{0.5}Te_{0.5}$ alloy. The chemical composition was determined by averaging measurements at three different points on the surface. The sample was in the form of a fine powder.

The presence of a noticeable amount of oxygen in the sample indicates a significant oxidation of the surface. Taking into account the formation of an oxide film, the chalcogenide composition on the surface corresponds to the chemical formula $Cu_{1.84}S_{0.37}Te_{0.63}$. The lack of copper in the composition compared to the charge composition is caused by the action of oxygen. The excess of tellurium and the lack of tellurium relative to the composition of the charge can be explained by significant evaporation of sulfur during synthesis, which took place in a loosely closed ampoule in the presence of argon.

Table

Results of X-ray spectral analysis of the chemical composition $Cu_2S_{0.5}Te_{0.5}$

Atom %	S	Cu	Se	Fe	O	Te	Sum
$Cu_{1.84}S_{0.37}Te_{0.63}$	9.9	60.1	0	0.94	12.11	16.94	100.00

When replacing tellurium with sulfur in copper telluride, the band gap gradually changes. This leads to a change in both the equilibrium concentration of charge carriers and the values of the the Seebeck coefficient.

Figure 1 shows the results of a study of the Seebeck coefficient of the sample $Cu_2S_{0.5}Te_{0.5}$. In general, with increasing temperature, the thermo-EMF coefficient increases, but there are small steps in the temperature dependence at 540 K, 620 K and 700 K. The α values are significantly higher than in Cu_2Te, but slightly lower than in Cu_2Te.

The thermo-EMF coefficient, as is known, directly depends on the position of the Fermi level and on the scattering factor of charge carriers. In the materials under study, it is possible to determine electrochemically the relative height of the Fermi electron level directly during the experiment on measuring thermo-EMF.

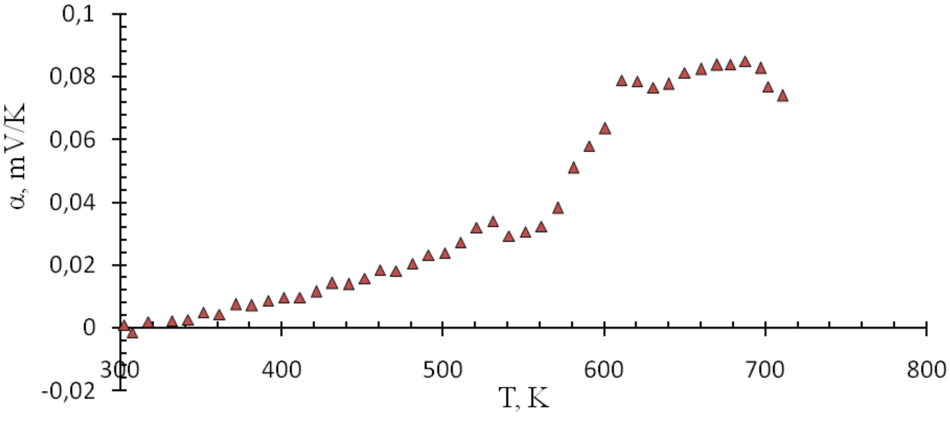

Figure 1. Temperature dependence of the coefficient of electronic thermo-emf of a coarse-grained sample $Cu_2S_{0.5}Te_{0.5}$

Figure 2 shows the temperature dependence of the EMF (E) of the electrochemical cell $Cu/CuBr/Cu_2S_{0.5}Te_{0.5}/Pt$, which essentially shows the movement of the Fermi electron level in the studied phase $Cu_2S_{0.5}Te_{0.5}$ relative to the Fermi level of electrons in the copper electrode with increasing temperature.

The break in the dependence E(T) at 620 K is associated with a phase transition in CuBr, since at (600–620) K it completes the transition to a high-temperature superionic phase. Above 630 K, a linear dependence E(T) is observed, which makes it possible to determine the entropy of copper atoms in a sample by the slope of the graph according to the method described in [9].

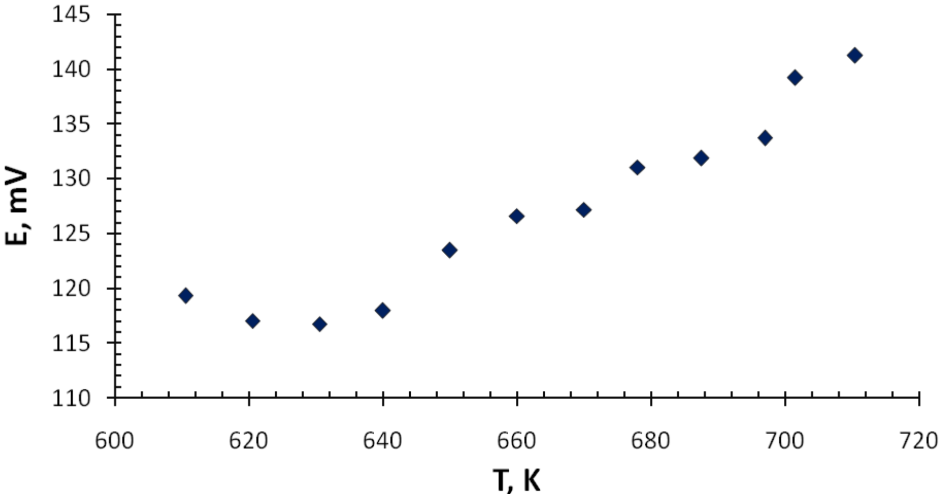

Figure 2. Temperature dependence of the EMF of an electrochemical cell Cu/CuBr/$Cu_2S_{0.5}Te_{0.5}$/Pt

Figure 3 shows the dependence of the coefficient of thermal EMF of the alloy $Cu_2S_{0.5}Te_{0.5}$ on the EMF Cu/CuBr/Cu_2S_0. Figure 3 — Dependence of the thermo-EMF coefficient of coarse-grained $5Te_{0.5}$/Pt. The dependence has a break at 130 mV, which corresponds to a temperature of about 680 K (according to Figure 2). From Figure 1 it can be seen that the temperature dependence of the Seebeck coefficient also has a break at 680 K.

In general, the investigated triple compounds of the $Cu_2S_yTe_{1-y}$ type show the values of the thermal EMF coefficient significantly lower than those of pure copper sulfide and lithium-doped copper sulfide.

Electronic conductivity and thermal EMF of $Cu_2S_{0.5}Te_{0.5.}$

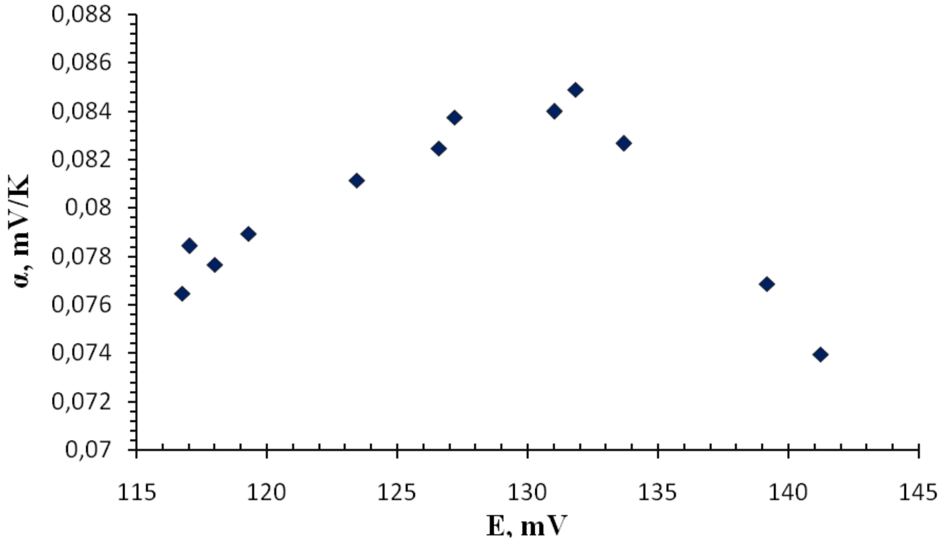

Figure 3. Dependence of the thermo-EMF coefficient of coarse-grained $Cu_2S_{0.5}Te_{0.5}$
from the EMF of an electrochemical cell Cu/ CuBr/$Cu_2S_{0.5}Te_{0.5}$/Pt

Figure 4 shows the temperature dependence of the electron conductivity of coarse-grained $Cu_2S_{0.5}Te_{0.5}$.

In general, the investigated triple compounds of $Cu_2S_yTe_{1-y}$ type show the values of the thermal EMF coefficient significantly lower than those of pure copper sulfide and lithium-doped copper sulfide.

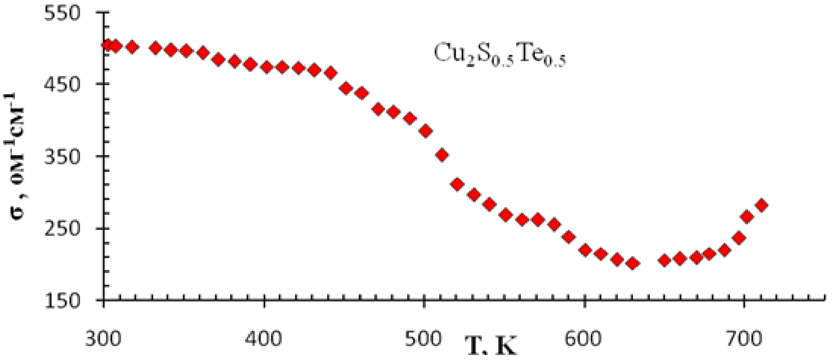

Figure 4. Temperature dependence of the electron conductivity of coarse-grained $Cu_2S_{0,5}Te_{0,5}$

The thermal conductivity of $Cu_2S_yTe_{1-y}$. Figure 5 shows the thermal conductivity results of three alloys of the $Cu_2S_{0,5}Te_{0,5}$ triple system. Low thermal conductivity values were found (from 0.4 to 0.6 W m^{-1} K^{-1}).

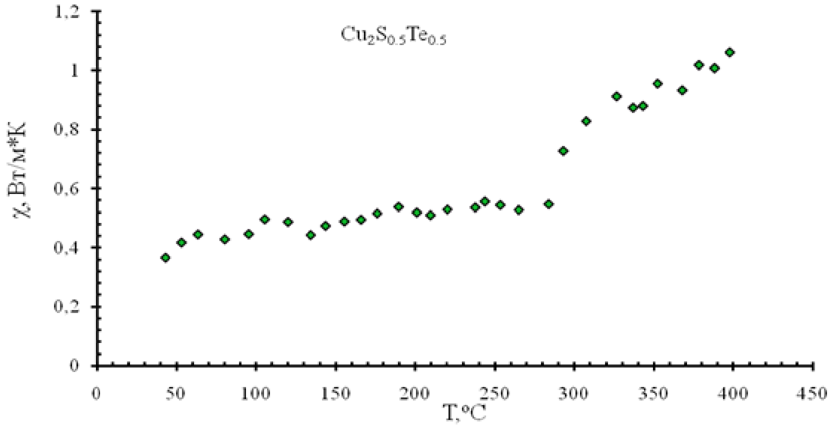

Figure 5. Temperature dependence of the thermal conductivity coefficient of a solid solution $Cu_2S_{0.5}Te_{0.5}$

Thermoelectric efficiency of $Cu_2S_yTe_{1-y}$.

Figure 6 shows the temperature dependence of the thermoelectric efficiency ZT of coarse-grained $Cu_2S_{0.5}Te_{0.5}$. The observed values of thermoelectric efficiency — 0.25 at 400° C allow us to hope for the possibility of improving the characteristics of samples of this composition to acceptable values for practical thermoelectric devices by selecting the optimal alloying.

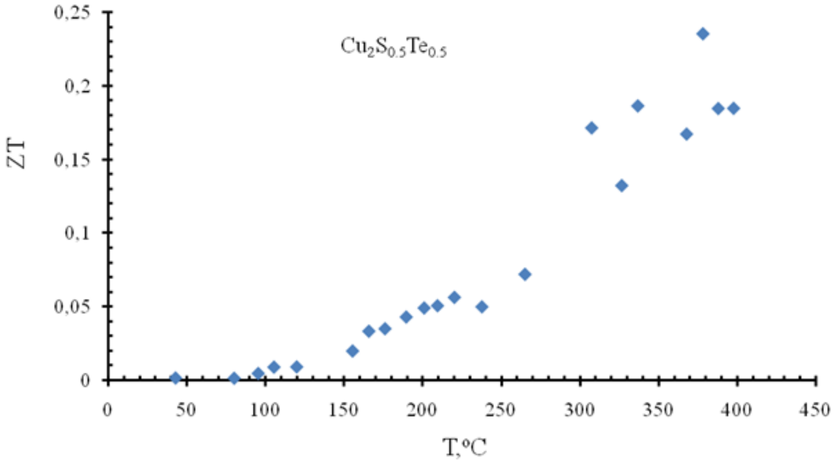

Figure 6. Temperature dependence of the thermoelectric efficiency of a coarse-grained alloy sample $Cu_2S_{0.5}Te_{0.5}$

Conclusion

To optimize the thermoelectric properties of the materials, the substitution of tellurium with nonstoichiometric copper sulfide was used.

The materials obtained are of particular interest for use as a catalyst (the most important components of a fuel cell).

Nanostructuring was used to reduce the thermal conductivity of materials, which has a positive effect on the thermoelectric efficiency of the material. For the studied composition, nanostructured samples showed a decrease in thermal conductivity by (25–30) % and a slight increase in the thermal emf coefficient compared with large-crystal samples. Low thermal conductivity was found in the range (0.3–1.1) W m^{-1} K^{-1} with a conductivity above 1000 $ohms^{-1}cm^{-1}$. However, it was not possible to obtain simultaneously high values of the Seebeck coefficient for the non-stoichiometric composition studied by us. Since the thermoelectric, electrical and thermal properties of chalcogenides are very sensitive to non-stoichiometry of the composition, it is possible that higher indicators of thermoelectric efficiency can be achieved by selecting the optimal degree of non-stoichiometry of the composition [10–12].

Acknowledgments

The Science Committee of the Republic of Kazakhstan, which is part of the Ministry of Science and Higher Education, provided funding for this research (No. AP14871197).

References

1 Kuterbekov, K.A., Nikonov, A.V., Bekmyrza, K.Z., Pavzderin, N.B., Kabyshev, A.M., Kubenova, M.M., Kabdrakhimova, G.D., & Aidarbekov, N. (2022). Classification of Solid Oxide Fuel Cells Review. *Nanomaterials, 12*(7), 1059. https://doi.org/10.3390/nano12071059.

2 Kubenova, M.M., Kuterbekov, K.A., Balapanov, M.K., Ishembetov, R.K., Kabyshev, A.M., & Bekmyrza, K.Z. (2021). Some Thermoelectric Phenomena in Copper Chalcogenides Replaced by Lithium and Sodium Alkaline Metals Review. *Nanomaterials, 11*, 2238. https://doi.org/10.3390/nano11092238.

3 Afroze, S., Reza, M.S., Kuterbekov, K., Kabyshev, A., Kubenova, M.M., Bekmyrza, K.Z., & Azad, A.K. (2023). Emerging and Recycling of Li-Ion Batteries to Aid in Energy Storage, A Review. *Recycling, 8*(3), 48. https://doi.org/10.3390/recycling8030048.

4 Reza, M.S., Afroze, S., Kuterbekov, K., Kabyshev, A., Bekmyrza, K., Taweekun, J., Ja'afar, F., Saifullah, Abu Bakar M., Azad, A.K., Roy, H., & Islam, M.S. (2023). Ex Situ Catalytic Pyrolysis of Invasive Pennisetum purpureum Grass with Activated Carbon for Upgrading Bio-Oil. *Sustainability, 15*, 7628. https://doi.org/10.3390/su15097628.

5 Snyder, J. & Toberer, E.S. (2008). Complex thermoelectric materials. *Nat. Mater., 7*, 105-114.

6 Dresselhaus, M.S., Chen, G., Tang, M.Y., Yang, R.G., Lee, H., Wang, D.Z., Ren, Z.F., Fleurial, J.P., & Gogna, P. (2007). New Directions for Low-Dimensional Thermoelectric Materials. *Advanced Materials, 19*, 1043.

7 Mona, Zebarjadi, Keivan, Esfarjani, Ali, Shakouri, Zhixi, Bian, Je-Hyeong, Bahk, Gehong, Zeng, John, Bowers, Hong, Lu, Joshua, Zide, & Art, Gossard (2009). Effect of Nanoparticles on Electron and Thermoelectric Transport. *Journal of Electronic Materials, 38*, 954.

8 Minnich, A.J., Dresselhaus, M.S., Ren, Z.F., & Chen, G. (2009). Bulk nanostructured thermoelectric materials: current research and future prospects. *Energy & Environmental Science, 2*(5).

9 Larsen, T.H., Sigman, M., Ghezelbash, A., Doty, R.C., & Korgel, B.A. (2003). Solventless Synthesis of Copper Sulfide Nanorods by Thermolysis of a Single Source Thiolate-Derived Precursor. *J. Am. Chem. Soc., 125*(19), 5638-5639.

10 Kuterbekov, K.A., Balapanov, M.K., Kubenova, M.M., Ishembetov, R.Kh., Zeleev, M.Kh., Yakshibaev, R.A., Kabyshev, A.M., Alina, R.A., Bekmyrza, K.Zh., Baikhozhaeva, B.U., Abseitov, E.T., & Taimuratova, L.U. (2022). Chemical diffusion and ionic conductivity in nonstoichiometric nanocrystalline superionic $Na_xCu_{1.75}S$ ($x = 0.1, 0.15, 0.2, 0.25$) materials. *Ionics, 28*, 4311–4319. https://doi.org/10.1007/s11581-022-04651-y.

11 Kuterbekov, K.A., Balapanov, M.Kh., Kubenova, M.M., Palymbetov, R.Sh., Ishembetov, R.Kh., Sakhabayeva, S.M., Kabyshev, A.M., Akhmetgaliev, B.M., Bekmyrza, K.Zh., Abseitov, Ye.T., & Giniyatova, Sh.G. (2022). Thermal properties of nanocrystalline copper sulfides $K_xCu_{1.85}S$ ($0 < x < 0.05$). *Letters on Materials, 12*, 191–196. https://doi.org/10.22226/2410-3535-2022-3-191-196.

12 Omarbekova, G.I., Aimukhanov, A.K., Ilyassov, B.R., Alexeev, A.M., Zeinidenov, A.K., & Zhakanova, A.M. (2023). Effect of the thickness and surface interface of In_2O_3 films on the transport and recombination of charges in a polymer solar cell. *Bulletin of the University of Karaganda-Physics, 2*(110), 17-24.

М.М. Кубенова, К.А. Кутербеков, М.Х. Балапанов, Р.Х. Ишембетов,
Г.Д. Кабдрахимова, Р.А. Алина, Д. Булатова, М. Татай, О. Елибаев

Нанокристалды мыс халькогенидтерінің термоэлектрлік қасиеттерін зерттеу

Зерттеушілердің заманауи күш–жігері катализаторлардың тиісті материалдарының қасиеттеріне, яғни отын элементінің маңызды компоненттеріне байланысты жоғары тиімділікпен, төмен бағамен және экологиялық таза болуымен сипатталатын отын элементтерін дамытуға бағытталған. Металл халькогенидтеріне негізделген, негізінен S сипатындағы катализаторлар H_2SO_4-тегі Pt белсенділігімен салыстырылатын оттегінің тотықсыздану реакциясын жеделдету белсенділігіне ие. Жұмыста ұнтақты материалдарды ықшамдау әдісі қолданылған және көлемді үлгілер алынған. Бөлшектердің орташа мөлшері (50 – 100) нм болатын нанодисперсті ұнтақ фракциялары алынды. Термо-эқк коэффициентінің мәндері (шамамен 0,08 м В/К) $Cu_2S_{0.5}Te_{0.5}$ типті катиондық тор бойынша ақауы аз зерттелетін қорытпа үшін алынған. Түйіршіктер мөлшерінің азаюы барлық зерттелетін үлгілер үшін электронды өткізгіштіктің айтарлықтай төмендеуіне әкелетіні анықталды. Мақалада $Cu_2S_{0.5}Te_{0.5}$ үштік қорытпасының термоэлектрлік қасиеттерін зерттеу нәтижелері келтірілген. Зерттелген құрам үшін жылу өткізгіштіктің 25–30%-ға төмендеуі және ірі кристалды үлгілермен салыстырғанда термо-эқк коэффициентінің шамалы өсуі алынды. 1000 Ом$^{-1}$см$^{-1}$ -ден жоғары өткізгіштік кезінде (0.3 – 1.1) Вт м$^{-1}$ К$^{-1}$ диапазонында төмен жылу өткізгіштік анықталды. Зерттелетін үлгі үшін $Cu_2S_{0.5}Te_{0.5}$– 400 °C температурада термоэлектрлік тиімділік (ZT= 0.25), бұл оңтайлы легирлеуді таңдау арқылы практикалық термоэлектрлік құрылғылар үшін осы құрамның үлгілерінің өнімділігін қолайлы шамаларға дейін жақсарту мүмкіндігіне үміттенуге мүмкіндік береді.

Кілт сөздер: термоэлектрлік материалдар, мыс сульфиді, кристалдық құрылым, өткізгіштік, диффузия, жылу өткізгіштік, Зеебек коэффициенті, суперионды өткізгіштер.

М.М. Кубенова, К.А. Кутербеков, М.Х. Балапанов, Р.Х. Ишембетов,
Г.Д. Кабдрахимова, Р.А. Алина, Д. Булатова, М. Татай, О. Елибаев

Исследование термоэлектрических свойств нанокристаллических халькогенидов меди

Современные усилия исследователей направлены на разработку топливных элементов, характеризующихся высокой эффективностью, низкой стоимостью и экологичностью, которые во многом зависят от свойств соответствующих материалов катализаторов — важнейших компонентов топливного элемента. Катализаторы на основе халькогенидов металлов, преимущественно на основе S, обладают активностью в ускорении реакции восстановления кислорода, сравнимой с активностью Pt в H_2SO_4. В статье использована методика компактирования порошковых материалов и получены объемные образцы. Получены фракции нанодисперсного порошка со средним размером частиц (50–100) нм. Значения коэффициента термо-эдс (порядка 0,08 мВ/К) получены для исследуемого сплава с малой дефектностью по катионной подрешетке типа $Cu_2S_{0.5}Te_{0.5}$. Установлено, что уменьшение размеров зерен приводит к значительному снижению электронной проводимости для всех исследуемых образцов. Авторами представлены результаты исследования термоэлектрических свойств тройного сплава $Cu_2S_{0.5}Te_{0.5}$. Для исследованного состава было получено снижение теплопроводности на 25–30 % и небольшое возрастание коэффициента термо-эдс по сравнению с крупнокристаллическими образцами. Обнаружена низкая теплопроводность в диапазоне 0,3–1,1 Вт м$^{-1}$К$^{-1}$ при проводимости выше 1000 Ом$^{-1}$см$^{-1}$. Для исследуемого образца $Cu_2S_{0.5}Te_{0.5}$ — термоэлектрическая эффективность ZT = 0,25 при 400 °C, что позволяет надеяться на возможность улучшения характеристики образцов этого состава до приемлемых величин для практических термоэлектрических устройств за счет подбора оптимального легирования.

Ключевые слова: термоэлектрические материалы, сульфид меди, кристаллическая структура, проводимость, диффузия, теплопроводность, коэффициент Зеебека, суперионные проводники.

Information about authors

Kubenova, M.M. — PhD, Research teacher, Department of Standardization and Certification, L.N. Gumilyov Eurasian National University, Astana, Kazakhstan. ORCID: https://orcid.org/0000-0003-2012-2702

Kuterbekov, K.A. — Doctor of physical and mathematical sciences, Professor of the International Department of Nuclear Physics, new materials and technologies, L.N. Gumilyov Eurasian National University, Astana, Kazakhstan. ORCID: https://orcid.org/0000-0001-7116-1520

Balapanov, M.Kh. — Doctor of physical and mathematical sciences, Professor of the Department of General Physics, Ufa University of Science and Technology, Ufa, Russia. ORCID: https://orcid.org/0000-0001-788 5-9462

Ishembetov, R.Kh. — Candidate of physical and mathematical sciences, Docent of the Department of General Physics, Ufa University of Science and Technology, Ufa, Russia. ORCID: https://orcid.org/0000-0002-0938-3998

Kabdrakhimova, G.D. — PhD, Associate professor of the International Department of Nuclear Physics, new materials and technologies, L.N. Gumilyov Eurasian National University, Astana, Kazakhstan. ORCID: https://orcid.org/0000-0003-2453-1028

Alina, R.A. — Doctoral student, L.N. Gumilyov Eurasian National University, Astana, Kazakhstan.

Bulatova, D. — Student, L.N. Gumilyov Eurasian National University, Astana, Kazakhstan.

Tatay, M. — Student, L.N. Gumilyov Eurasian National University, Astana, Kazakhstan.

Yelibayev, O. — Student, L.N. Gumilyov Eurasian National University, Astana, Kazakhstan.

Article

Received: 08.10.2023
Accepted: 05.12.2023

UDC 621.785.616

https://doi.org/10.31489/2024PH1/66-72

N.E. Berdimuratov, Ye.Ye. Kambarov, M. Maulet,
S.D. Bolatov, Zh.B. Sagdoldina, D.R. Baizhan*

Sarsen Amanzholov East Kazakhstan University, Ust-Kamenogorsk, Kazakhstan
Corresponding author's e-mail: daryn.baizhan@mail.ru

Electrofriction treatment of plow shares

This paper presents the results of research aimed at developing the technology of plow share hardening by means of electrofriction hardening. It is shown that in electrofriction hardening of plow shares a structure with microhardness gradient is formed along the depth of the hardened zone. After electrofriction hardening the microhardness of plow share increases in 3–3.5 times in comparison with the initial state. The reason for the gradient character of microhardness distribution along the thickness of the modified layer is the ultra-high cooling rate, which causes a high temperature gradient near the surface. On the basis of the results of scanning electron microscopy it is established that at electrofriction hardening of steel 40Kh the hardened surface layer is formed, consisting of two zones: the surface hardened zone with the structure of fine–needle martensite and austenite; the zone of thermal influence (transition layer) with martensite-perlite structure, smoothly passing into the initial ferrite-perlite structure. It is established that the phase composition of steel 40Kh in the initial state consists of α-Fe phase with BCC lattice, and after electrofriction hardening the hardening phases of residual austenite (γ-Fe) and martensite (α'-Fe) are formed. The obtained data allow us to conclude that electrofriction treatment is an effective method of plow share hardening from structural steel 40Kh.

Keywords: electrofriction technology, hardening, plow share, microstructure, microhardness.

Introduction

Increasing the service life of soil tillage machinery working elements is one of the urgent problems of modern agricultural engineering. Analysis of the reliability level of tillage machinery shows that about 40% of the total number of failures is attributed to soil-cutting elements (plow shares, plow bits, bucket teeth of excavators, etc.) [1]. Operational and technological indicators of plows do not always meet the consumer properties declared by the manufacturer. According to [2] the average service life of P-702 chisel-shaped plow shares varies from 5 to 20 ha and the highest intensity of wear of plow shares by weight on sandy soils with stony inclusions is 260–450 g/ha, and on sandy and sandy loam soils without stony inclusions decreases to 100–260 g/ha. Thus, there is a serious scientific and technical problem associated with a low level of consumer properties of tillage tools operated under high impact-abrasive loads. The principal solution of the problem is the use of resource-saving hardening technologies, which will allow to increase the operational characteristics of critical parts of tillage machines. Therefore, the material science direction of new developments for parts of agricultural machines is the most important.

At present in Kazakhstan the following methods of increasing wear resistance of working parts of tillage machines are used: electric arc surfacing with hard-alloy electrodes or sormite and heating with high frequency currents under hardening [3]. One of the methods of hardening and restoration of plow shares, which has a wide application, is electric arc cladding (cladding reinforcement) [4, 5]. At the enterprises of the Karaganda region, the greatest use in repair production was made of cladding, which provides more than 70% of the restoration volume [6]. However, the disadvantages of cladding methods are: lack of hardness gradients, thermal influence, warping of products, reduction of resistance to cracking and destruction. Mikhalchenko A.M. and his co-authors analyzed the works reflecting the issues of heat treatment during hardening and hardening restoration with the use of cladding reinforcement. The analysis allowed to establish that the fact of hardness gain is insignificant, which does not provide a significant increase in the wear resistance of the plow share, so the authors recommend scientific searches to improve the technology [7].

In Kazakhstan, research is being conducted on the development of technology for hardening of soil tillage machine parts. A combined method of hardening of the blade of the working organ has been developed. This method includes electrospark alloying of the hardened surface with a carbide electrode and high-speed boriding of the hardened layer with subsequent re-treatment with electrospark alloying [8]. The method of restoration and hardening of worn parts using welding is known, mainly for hardening of lancet tines of cultivators. To restore the lancet tines, compensating plates (made of steel) of a certain repair size are used, which are welded to the restored part with a continuous seam using electric arc welding [9]. However, in our country there are no studies on strengthening of soil tillage machine working elements with the help of electrofriction technology.

Electrofriction technology is based on the joint fusion of the surfaces of the cast iron electrode and the blade of the tillage tool by introducing the energy of low-voltage electric arcs and cooling with water [10, 11]. The arcs are generated using safe welding voltage and friction of the electrode surfaces against the tool. EFT should provide the creation of a hardness gradient of the blade material, increasing resistance to abrasive wear and self-sharpening ability.

Bogdanovich P.N. and co-authors used the technology of electrofriction hardening as an experimental method for processing of cutting drum blades of forage harvesters. The effectiveness of using high-strength cast iron in the construction of cutting drum blades of forage harvesters is considered. The results of testing the wear resistance of hardened samples showed that the electrofriction method of hardening, depending on the regime of testing, increased the wear resistance of samples in 1.1–1.5 times, the thickness of the hardening zone was 400 μm [12]. It should be noted that for modern conditions of soil cultivation it is necessary to ensure the strength of the material of the product 1500–1800 MPa, and impact toughness should correspond to values not less than 0.8–1.0 MJ/m2 [13]. To reduce the intensity of abrasive wear it is necessary to provide the maximum possible surface hardness of 60–65 HRC. Such values of strength, impact toughness and hardness in the manufacture of parts from steels L53 and 65G (replaceable parts of plow bodies) are not provided by traditional technologies (hardening + tempering) [14].

The purpose of this work is to study the structural-phase state and microhardness of the surface layer of the plow share made of structural steel 40 Kh after electrofriction hardening.

Materials and experimental methodology

In the present work, plow shares made of structural alloy steel 40Kh are chosen as the material for electrofriction technology (EFT). The samples for the study were cut out from the plow shares with the size of 100×30×10 mm and were pre-treated with grinding paper with P100 grit.

Figure 1 shows a schematic diagram of the electrofriction technology setup. The friction of the electrode against the workpiece is accompanied by the formation and breaking of electrical contact between them. Contact between the product and the electrode is carried out by a sublayer of cooling liquid (water), which causes heating up to melting of the contacting surfaces. The treated surface of the product is melted, the melt is alloyed with elements included in the electrode or in the cooling liquid. Periodic breaking of the electrical contact, when the interelectrode gap increases, creates conditions for rapid cooling of the surface of the product doped in the melt. The cooling rate reaches 10^4–10^5 °C/s. A cast iron disk was used as an electrode for EFT. The electrode rotation speed is 165 rpm. The electrode is included in the electric circuit by the anode and isolated from the plant structure. Friction of the modified surface of the product was carried out against the periphery of the electrode with a force of 5 N. EFT treatment of steel 40 Kh was carried out at a current strength of 200 A and voltage of 70 V.

a) schematic representation of EFT; *b*) plow share after electrofriction treatment

Figure 1. EFT hardening of steel products

The microstructure of the investigated samples was studied using Altami MET 5C optical microscope and TESCAN MIRA3 LMH scanning electron microscope. After electrofriction treatment, mechanical treatment (grinding and polishing) was carried out for further studies. Chemical treatment (etching) of the sample surface in 5 % ethyl alcohol based HNO_3 solution was carried out to study the microstructure of the sample on the cross section. X-ray phase analysis of the studied samples was performed on a SHIMADZU XRD–6000 diffractometer (monochromatic Cuα-radiation, wavelength 1.54056 Å) with the following imaging parameters: accelerating voltage 45 kV, beam current 30 mA, scanning step 0.02° in the range of angles 30–85°, signal acquisition time 0.5 s. The analysis of phase composition was carried out using PDF4+ databases and POWDER CELL 2.4 full-profile analysis program. The microhardness of the machined surface was determined on a METOLAB 502 microhardness tester at indenter load P=1N and dwell time at this load 10 s.

Experimental results

In the EFH process, steel and cast iron are subjected to high temperature and pressure generated by frictional forces and electric current. High temperatures can cause the transformation of austenite (the resistant crystalline structure of iron) into more stable phases such as martensite and cementite, but can also promote the formation of residual austenite. With the reverse polarity created by the arc in the EFH process, the electrode is heated more and the surface of the sample is alloyed with the elements that make up the cast iron (electrode). The process of heating and frictional forces leads to phase transformations in the surface layer of the material. These transformations may include recrystallization and martensitic transformation. A characteristic feature of the used EFH technology is the zonality of the formed structures along the thickness of the modified layer, which can be divided into the following zones: the zone of hardening, thermal influence and the base of the treated material.

The results of metallographic study of plow share microstructure after EFH showed that the thickness of the modified layer is ~500 μm (Fig. 2*d*). The structure of the surface layer consists of a hardened layer with austenite-martensite structure (Fig. 2*a*) and after the hardened layer there is a transition layer, which undergoes incomplete hardening, with the structure of martensite and ferrite (Fig. 2*b*). The base of the product (initial structure) is a ferrite-perlite structure (Fig. 2*c*). The hardened layer has the microstructure of needle martensite and has a smooth transition to the heat affected zone. The plates of greater thickness between the martensite needles are residual austenite (Fig. 2*a*). No microcracks are found at the transition boundary to the original structure. It was noted in [5] that the presence of a small amount of residual austenite in the structure of the surface and near-surface layers is a positive factor, since austenitic interlayers with increased ductility along the boundaries of martensitic plates are barriers to the propagation of cracks from the quenched layer into the base metal.

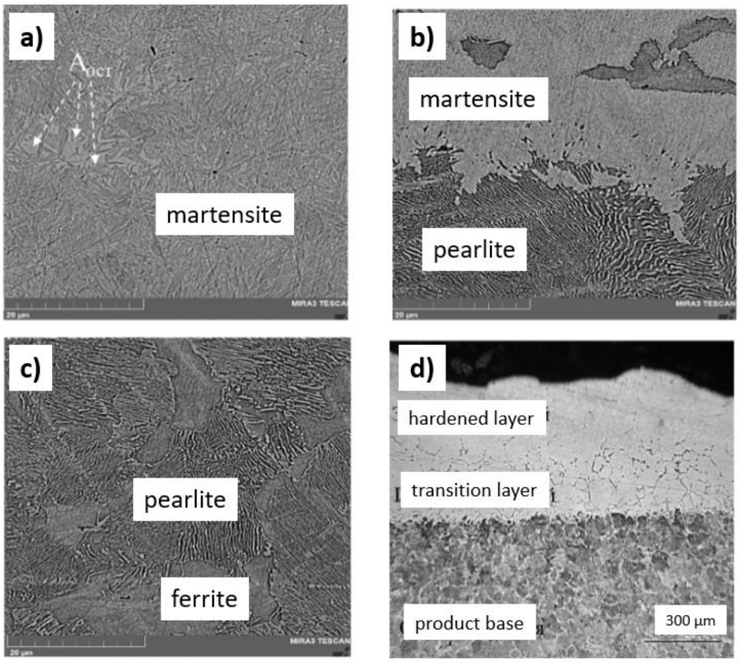

a — hardened layer; *b* — transition layer; *c* — base of the product (untreated layer);
d — general view of the hardened layer (metallographic microscope)

Figure 2. Cross-sectional microstructure of steel 40Kh after EPH

Figure 3 shows diffractograms of steel 40Kh before and after EPH. The phase composition of steel 40 Kh in the initial state consists of α-Fe phase with BCC lattice (Fig. 3b). After EPH of steel 40Kh, residual austenite (γ-Fe) and martensite (α'-Fe) phases appear. Martensite is formed on the steel surface as a result of rapid cooling during the EPH process. The results of X-ray phase analysis are consistent with the results of the study of the microstructure of steel 40Kh after EPH.

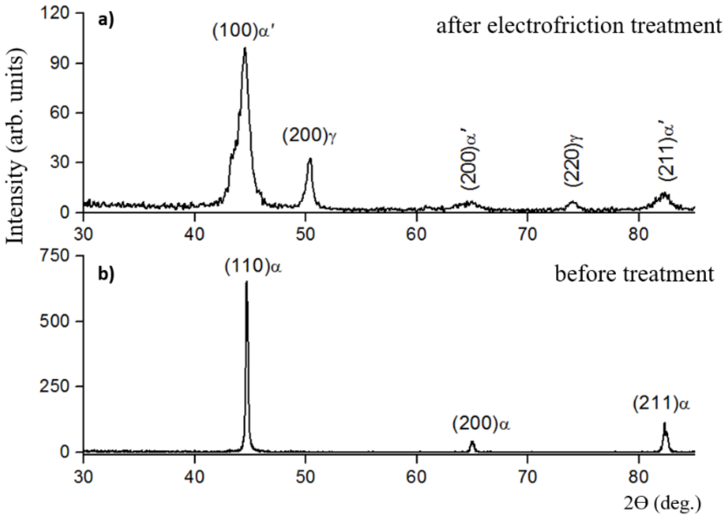

Figure 3. Diffractogram of steel 40Kh before and after electrofriction treatment

It is known that the characteristic properties of steel with martensitic structure are high hardness [15]. Of particular interest is the consideration of hardness distribution curves along the thickness of the modified steel layer after hardening. The study of microhardness distribution along the depth showed the presence in them of a harder surface layer and a less hard layer underlying it, the extent of which is ~550 μm. Figure 4*a* shows that the microhardness in the modification zone decreases smoothly from the surface to the depth of the sample. In the near-surface layers, the microhardness of steel 40 Kh reaches an average value of 960 HV$_{0.1}$ with a smooth transition to the heat affected zone, which has an average microhardness of 813 HV$_{0.1}$. The microhardness of steel 40Kh in the initial state is 252±16 HV$_{0.1}$.

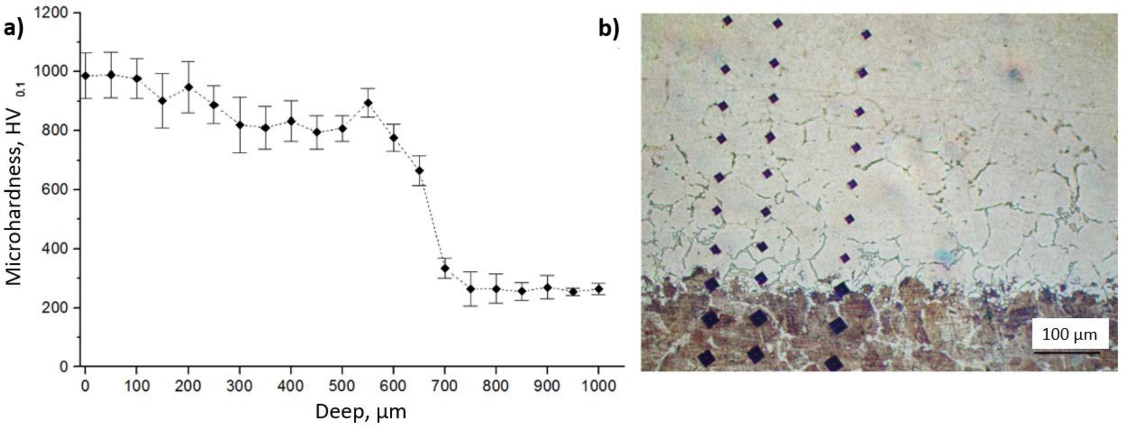

a — distribution of microhardness by thickness of hardened layers; *b* — microstructure of the modified layer

Figure 4. Microhardness of steel 40Kh after EFH

Thus, the obtained data allow us to conclude that electrofriction treatment is an effective method of hardening of plow shares made of steel 40Kh. The hardness of the rapidly hardened layer smoothly decreases from the surface of the modified layer to the boundary with the base. It should be noted that the basis of known hardening methods is the creation of surface layers with a hardness gradient along the cross-section of the treated product.

Conclusion

The influence of electrofriction treatment of structural steel 40Kh on the structure and microhardness of a plow share made of structural steel 40Kh was investigated. It was found that the structure of the cross–section of steel 40 Kh after electrofriction hardening was conditionally divided into 3 zones: hardened layer, heat affected zone and the base of the treated material. The microstructure of the hardened layer of steel 40Kh consisted of needle-like martensitic structure and residual austenite. The heat affected zone of steels contains martensite and highly dispersed pearlite (trostite). The microstructure of the initial state of steel 40Kh consists of ferrite-perlite structure. It is shown that a gradient structure with a regular changing micro-hardness of structural components is formed at the depth of the zone. High hardness of steels after electrofriction treatment is explained by the formation of martensitic structure as a result of ultra-high heating and cooling rates, which are unattainable by traditional heat treatment methods.

Acknowledgements

This research has been funded by the Science Committee of the Ministry of Science and Higher Education of the Republic of Kazakhstan. Grant AP14872211.

References

1 Панов И.М. Технический уровень почвообрабатывающих и посевных машин / И.М. Панов, А.Н. Черепахин // Тракторы и сельскохозяйственные машины. — 2000. — № 9. — С. 10–12.

2 Шило И.Н. Повышение работоспособности деталей рабочих органов сельскохозяйственных машин: моногр. / И.Н. Шило, Г.Ф. Бетеня, Г.И. Анискович. — Минск: БГАТУ, 2010. — № 320.

3 Косатбекова Д.Ш. Разработка и обоснование параметров сошниказернотукотравяной сеялки и повышение ресурса работы его рабочей поверхности / Д.Ш. Косатбекова, С.О. Нукешев // Материалы Междунар. науч.-теор. конф. «Сейфуллинские чтения–17: Современная аграрная наука: цифровая трансформация», посвящ. 30-летию Независимости Республики Казахстан. — 2021. — Т. 1. Ч. 2. — С. 225–228.

4 Singh P. Reduction of abrasive wear via hardfacing of mouldboard ploughshare / P. Singh, S. Singh Chatha // Materials Today: Proceedings. — 2020. — Vol. 33 (3). — P. 1505–1512.

5 Kostencki P. Wear of cultivator coulters reinforced with cemented–carbide plates and hardfacing / P. Kostencki, T. Stawicki, A. Krolicka, P. Sędłak // Wear. — 2019. — Vol. 438–439. — P. 203063.

6 Жаркевич О.М. Анализ методов восстановления деталей наплавкой / О.М. Жаркевич, А.В. Жукова, О.А. Нуржанова // Материалы X Междунар. науч.-техн. конф. «Техника и технологии машиностроения». — Омск, 2021. — С. 122–125.

7 Михальченко А.М. Способы упрочнения и упрочняющего восстановления лемехов плугов с сопутствующей термообработкой / А.М. Михальченко, И.В. Козарез, А.А. Тюрева // Вестн. Брян. гос. с.-х. акад. — 2017. — № 2 (60). — С. 24–27.

8 Шугаев Б.К. Патент на изобретение № 32142. Комбинированный способ упрочнения лезвия рабочего органа / Б.К. Шугаев, С.А. Кадочников. — Опубл. от 08.12.2015 г.

9 Шугубаев Ж.Б. Патент на изобретение № 27615. Способ восстановления рабочих органов почвообрабатывающих машин / Ж.Б. Шугубаев // Бюл. — № 11. — Опубл. 15.11.2013 г.

10 Sagdoldina Zh. Electrofrictional Hardening of the 40Kh and 65G Steels / Zh. Sagdoldina, Yr. Tyurin, N. Berdimuratov, O. Stepanova, N. Magazov, D. Baizhan // Coatings. — 2023. — 13(11). — 1820.

11 Tyurin Y.N. Investigation of the hardness of 65G steel after electrofriction treatment / Y.N. Tyurin, Zh. Sagdoldina, Y.Y. Kambarov, M.N. Magazov // Bulletin D. Serikbayev of EKTU. — 2023. — No. 3. — P. 99–106.

12 Богданович П.Н. Исследование влияния электрофрикционного упрочнения ножей режущего барабана кормоуборочного комбайна на их износостойкость / П.Н. Богданович, М.И. Михайлов, К.М. Михайлов // Вестн. Баранович. гос. ун-та. Сер. Технические науки. — 2016. — Т. 4. — С. 77–84.

13 Машиностроение: энцикл.: [В 40-а т.]. — Машиностроение. —2002. — Т. IV. — Вып. 16.

14 Канаев А.Т. Плазменная закалка лемеха плуга из конструкционной стали 65Г / А.Т. Канаев, А.А. Гуляренко, П.А. Тополянский, Т.Е. Сарсембаева // Горение и плазмохимия. — 2020. — Вып. 18. — С. 87–93.

15 Rakhadilov B.K. Impact of Volume and Surface Heat Treatment on the Structure and Properties of Steel 30HGSA / B.K. Rakhadilov, R.S. Kozhanova, P. Kowalewski, D.R. Baizhan, Zh.B. Sagdoldina, L.G. Zhurerova, G.U. Yerbolatova // Bulletin of the University of Karaganda – Physics. — 2021. — Vol. 4(104). — P. 16–24.

Н.Е. Бердимуратов, Е.Е. Камбаров, М. Маулет,
С.Д. Болатов, Ж.Б. Сагдолдина, Д.Р. Байжан

Соқа түренін электрфрикциялық өңдеу

Мақалада электрфрикциялық қатайту тәсілімен соқа түренін қатайту технологиясын әзірлеуге бағытталған зерттеу нәтижелері баяндалған. Соқа түренін электрфрикциялық өңдеуде қатайтылған аймақтың тереңдігі бойынша микроқаттылық градиентті құрылымда қалыптасатыны көрсетілген. Электрфрикциялық қатайтудан кейін соқаның микроқаттылығы бастапқы күймен салыстырғанда 3-3,5 есе артады. Модификацияланған қабаттың қалыңдығы бойынша микроқаттылықтың таралуының градиенттік сипатының себебі аса жоғары салқындату жылдамдығы болып табылады, бұл бетке жақын температураның жоғары градиентін тудырады. Сканерлеуші электрондық микроскопияның нәтижелері негізінде 40Х болатын электрфрикциялық қатайту кезінде екі аймақтан тұратын қатайтылған беткі қабат түзілетіні анықталды: ұсақ ине тәрізді мартенсит пен аустенит құрылымы бар беткі қатайтылған аймақ; бастапқы феррито-перлит құрылымына тегіс ауысатын мартенсит-перлит құрылымы бар термиялық әсер ету аймақтары (өтпелі қабат). Бастапқы күйдегі 40Х болаттың фазалық құрамы BCC торымен α-Fe фазасынан тұратыны анықталды, ал электрфрикциялық қатайтудан кейін қатайтатын қалдық аустенит (γ-Fe) және мартенсит (α'-Fe) деген фазалар пайда болады. Алынған мәліметтер бойынша электрфрикциялық өңдеу 40Х құрылымдық болаттан жасалған соқаны қатайтудың тиімді әдісі болып табылады деген қорытынды жасауға мүмкіндік береді.

Кілт сөздер: электрфрикциялық технология, беріктендіру, соқа түрені, микроқұрылым, микроқаттылық.

Н.Е. Бердимуратов, Е.Е. Камбаров, М. Маулет,
С.Д. Болатов, Ж.Б. Сагдолдина, Д.Р. Байжан

Электрофрикционная обработка лемеха плуга

В статье изложены результаты исследований, направленные на разработку технологии упрочнения лемеха плуга способом электрофрикционного упрочнения. Показано, что в электрофрикционной обработке лемеха плуга по глубине упрочненной зоны формируется структура с градиентом микротвердости. После электрофрикционного упрочнения микротвердость лемеха плуга увеличивается в 3–3,5 раза по сравнению с исходным состоянием. Причиной градиентного характера распределения микротвердости по толщине модифицированного слоя является сверхвысокая скорость охлаждения, вызывающая высокий градиент температуры вблизи поверхности. На основе результатов сканирующей электронной микроскопии установлено, что при электрофрикционном упрочнении стали 40Х формируется упрочненный поверхностный слой, состоящий из двух зон: поверхностной закаленной зоны со структурой мелкоигольчатого мартенсита и аустенита; зоны термического влияния (переходный слой) с мартенситно-перлитной структурой, плавно переходящей в исходную феррито-перлитную структуру. Установлено, что фазовый состав стали 40Х в исходном состоянии состоит из фазы α–Fe с ОЦК решеткой, а после электрофрикционного упрочнения образуются упрочняющие фазы: остаточный аустенит (γ–Fe) и мартенсит (α’–Fe). Полученные данные позволяют сделать вывод, что электрофрикционная обработка является эффективным способом упрочнения лемеха плуга из конструкционной стали 40Х.

Ключевые слова: электрофрикционная технология, упрочнение, лемех плуга, микроструктура, микротвердость.

References

1 Panov, I.M., & Cherepakhin, A.N. (2000). Tekhnicheskii uroven pochvoobrabatyvaiushchikh i posevnykh mashin [Technical level of tillage and seeding machines]. *Traktory i selskokhoziaistvennye mashiny — Tractors and Agricultural Machines*, 9, 10–12 [in Russian].

2 Shilo, I.N., Betenya, G.F., & Aniskovich, G.I. (2010). Povyshenie rabotosposobnosti detalei rabochikh organov selskokhoziaistvennykh mashin [Improving the serviceability of parts of working bodies of agricultural machines]. Minsk: Belorusskii gosudarstvennyi agrarnyi tekhnicheskii universitet [in Russian].

3 Kosatbekova, D.Sh. & Nukeshev, S.O. (2021). Razrabotka i obosnovanie parametrov soshnikazernotukotravianoi seialki i povyshenie resursa raboty ego rabochei poverkhnosti [Development and justification of the coulter parameters of grain and grass seeders and increase of its working surface resource]. *Materialy Mezhdunarodnoi nauchno-teoreticheskoi konferentsii «Seifullinskie chteniia–17: Sovremennaia agrarnaia nauka: tsifrovaia transformatsiia», posviashchennoi 30-letiiu Nezavisimosti Respubliki Kazakhstan — Proceedings of the international scientific and theoretical conference “Seifullin readings – 17: Modern Agrarian Sci-*

ence: digital transformation", dedicated to the 30th anniversary of Independence of the Republic of Kazakhstan, 1, 2, 225–228 [in Russian].

4 Singh, P. & Singh, Chatha S. (2020). Reduction of abrasive wear via hardfacing of mouldboard ploughshare. *Materials Today: Proceedings, 33*(3), 1505–1512.

5 Kostencki, P., Stawicki, T., Krolicka, A., & Sędłak, P. (2019). Wear of cultivator coulters reinforced with cemented-carbide plates and hardfacing. *Wear,* 438–439, 203063.

6 Zharkevich, O.M., Zhukova, A.V., & Nurzhanova, O.A. (2021). Analiz metodov vosstanovleniia detalei naplavkoi [Analysis of methods of restoration of parts by cladding]. *Materialy X Mezhdunarodnoi nauchno-tekhnicheskoi konferentsii «Tekhnika i tekhnologii mashinostroeniia» — Proceedings of the X International Scientific and Technical Conference "Engineering and Technology of Mechanical Engineering". Omsk,* 122–125 [in Russian].

7 Mikhalchenko, A.M., Kozarez, I.V., & Tyureva, A.A. (2017). Sposoby uprochneniia i uprochniaiushchego vosstanovleniia lemekhov plugov s soputstvuiushchei termoobrabotkoi [Ways of strengthening and reinforcing recovery of ploughshares with concomitant heat treatment]. *Vestnik Brianskoi gosudarstvennoi selskokhoziaistvennoi akademii — Bulletin of Bryansk State Agricultural Academy,* 2(60), 24–27 [in Russian].

8 Shugaev, B.K. & Kadochnikov, S.A. Patent na izobretenie № 32142. Kombinirovannyi sposob uprochneniia lezviia rabochego organa [Patent for invention No. 32142, Combined method of workpiece blade hardening]. Published on 08.12.2015 [in Russian].

9 Shugubaev, J.B. Patent na izobretenie № 27615. Sposob vosstanovleniia rabochikh organov pochvoobrabatyvaiushchikh mashin [Patent for invention No. 27615, Method of restoration of working bodies of soil tillage machines] [in Russian].

10 Sagdoldina, Zh., Tyurin, Yu., Berdimuratov, N., Stepanova, O., Magazov, N., & Baizhan, D. (2023). Electrofrictional Hardening of the 40Kh and 65G Steels. *Coatings, 13*(11), 1820.

11 Tyurin, Y.N., Sagdoldina, Zh., Kambarov, Y.Y, & Magazov, M.N. (2023). Investigation of the hardness of 65G steel after electrofriction treatment. *Bulletin D. Serikbayev of EKTU,* 3, 99–106.

12 Bogdanovich, P.N., Mikhailov, M.I., & Mikhailov, K.M. (2016). Issledovanie vliianiia elektrofriktsionnogo uprochneniia nozhei rezhushchego barabana kormouborochnogo kombaina na ikh iznosostoikost [Investigation of the influence of electrofriction hardening of cutting drum knives of forage harvester on their wear resistance]. *Vestnik Baranovichskogo gosudarstvennogo universiteta. Seriia Tekhnicheskie nauki — Bulletin of Baranovichi State University. Series Technical Sciences, 4,* 77–84 [in Russian].

13 (2002). Mashinostroenie: entsiklopediia: [V 40 tomakh] [Mechanical engineering: encyclopedia: in 40 vol.]. Moscow: Mashinostroenie, IV, 16 [in Russian].

14 Kanaev, A.T., Gulyarenko, A.A., Topolyanskiy, P.A., & Sarsembayeva, T.Ye. (2020). Plazmennaia zakalka lemekha pluga iz konstruktsionnoi stali 65G [Plasma quenching of plow plowshare made of 65G structural steel]. *Gorenie i plazmokhimiia — Combustion and Plasma Chemistry, 18,* 87–93 [in Russian].

15 Rakhadilov, B.K., Kozhanova, R.S., Kowalewski, P., Baizhan, D.R., Sagdoldina, Zh.B., Zhurerova, L.G., & Yerbolatova, G.U. (2021). Impact of Volume and Surface Heat Treatment on the Structure and Properties of Steel 30HGSA. *Bulletin of the University of Karaganda – Physics, 4*(104), 16–24.

Information about authors

Berdimuratov, N.E. — Junior researcher of scientific research center "Surface engineering and tribology", Sarsen Amanzholov East Kazakhstan University, Ust-Kamenogorsk, Kazakhstan; e-mail: nurbol.ber@gmail.com. ORCID ID: https://orcid.org/0009-0000-6880-6439

Kambarov, Ye.Ye. — Researcher of scientific research center "Surface engineering and tribology" Sarsen Amanzholov East Kazakhstan University, Ust-Kamenogorsk, Kazakhstan. e-mail: yedilzhan@mail.ru. ORCID ID: https://orcid.org/0000-0002-0838-6724

Maulet, M. — Senior researcher of scientific research center "Surface engineering and tribology", Sarsen Amanzholov East Kazakhstan University, Ust-Kamenogorsk, Kazakhstan; e-mail: maulet_meruert@mail.ru. ORCID ID: https://orcid.org/0000-0003-1570-0301

Bolatov, S.D. — Engineer of scientific research center "Surface engineering and tribology", Sarsen Amanzholov East Kazakhstan University, Ust-Kamenogorsk, Kazakhstan; e-mail: sanzharbolatov94@gmail.com. ORCID ID: https://orcid.org/0009-0003-3136-0535

Sagdoldina, Zh.B. — PhD, Associate professor, Leading researcher of scientific research center "Surface engineering and tribology" Sarsen Amanzholov East Kazakhstan University, Ust-Kamenogorsk, Kazakhstan; e-mail: sagdoldina@mail.ru. ORCID ID: https://orcid.org/0000-0001-6421-2000

Baizhan, D. — Senior researcher of scientific research center "Surface engineering and tribology", Sarsen Amanzholov East Kazakhstan University, Ust-Kamenogorsk, Kazakhstan; e-mail: daryn.baizhan@mail.ru. ORCID ID: https://orcid.org/0000-0002-9105-3129

Article

Received: 24.10.2023
Accepted: 10.12.2023

UDC 539

https://doi.org/10.31489/2024PH1/73-82

G.S. Bektasova[1], K.M. Issina[1*], G.T. Imanzhanova[1], L.I. Kveglis[1],
N. Kantai[1], A.I. Nedobitkov[2], A.B. Sadibekov[2]

[1]Sarsen Amanzholov East Kazakhstan University, 070020, Ust-Kamenogorsk, Kazakhstan;
[2]D. Serikbaev East Kazakhstan Technical University, Ust-Kamenogorsk, Kazakhstan
[*]Corresponding author's e-mail: gyka1983@mail.ru

Study of the copper structure samples externed to extreme influences

This work is devoted to the study of changes in the crystal structure, chemical and phase composition of copper samples subjected to extreme effects of temperature, pressure and electromagnetic fields. With the help of X-ray diffraction, as well as microanalysis, it was revealed that the plastic deformation of copper wires in the car power supply system leads to the formation of a superconducting Cu_2O phase. This is the reason for the rapid ignition of the car, as it leads to a sharp increase in the magnitude of the electric current and temperature in the plastic deformation zone of copper wires. During explosion welding of copper samples, the Cu_2O phase appears on their surface, which has superconducting properties. This significantly changes the electrophysical properties of copper samples. In metallurgical processes during the smelting of copper products, there is a possibility of the appearance of a superconducting Cu_2O phase. When modifying a copper melt with hardening additives, the superconducting Cu_2O phase makes it possible to obtain fracture-resistant copper products with high electrical conductivity. Plastic deformation of a copper foil 30 mkm thick by a magnetic field generated by a current of 180 kA leads to the formation of a texture and rupture of the foil. This has been detected using X-ray diffraction, as well as optical and scanning electron microscopy.

Keywords: copper samples, ignition zone, plastic deformation, explosion processing, deformation by electromagnetic wave flow.

Introduction

In recent years, with the continuous development of science and technology, the number of new high-power electrical appliances used in people's daily lives is growing. This increases the requirements for the structure and properties of products in the electrical industry.

The formation of copper oxide particles in copper wiring under extreme impacts in copper wire is described in articles [1, 2]. The following works [3–8] are devoted to the study of the current overload of copper conductors, accompanied by a current pulse and plastic deformation. The possibility of high temperature superconductivity in a copper conductor, with the formation of Cu_2O, is discussed in [9]. In the technique [10], a diffractometric method for studying copper conductors with melting was first proposed based on the detection of Cu_2O. The same is reported by the authors of [11].

The purpose of our work is to investigate structural and phase changes in various copper samples subjected to extreme effects of high temperatures, mechanical loads and electromagnetic fields, which make it possible to increase the strength and electrical conductivity of copper products.

To achieve this goal, the process of current overload in the electrical system of cars was investigated. For this, fragments of copper conductors subjected to current overload [3–8] were studied, which made it possible to establish changes in the crystal structure and chemical composition. Similar experiments were carried out to study the surface of a copper cylinder subjected to an explosion, as well as when copper foil was compressed by a magnetic field. The magnetic field has a significant effect on metals: it can set the metal in motion, cause plastic deformation and heat the metal. When a strong pulsed, field interacts with a metal conductor the first interesting effects appear in the range of 0.1–1 MOe.

It is necessary to increase the strength of copper products that are exposed to electromagnetic fields. Near 400 kOe, the diffusion of the magnetic field becomes nonlinear, and the magnetic pressure exceeds the yield strength of most metals [11].

Since copper has rather low yield strength, it is necessary to increase the strength of copper products by introducing hardening additives into it during smelting. Known strengthening additives dramatically reduce the electrical conductivity of copper [12].

Material and methods of research

The sections of the conductors of the electrical system of the car, subjected to current overload and having signs of residual plastic deformation, were studied, since, according to [7, 8], it is these signs that indicate an electric arc process, accompanied by a pulsed field, and causing the car to ignite.

For the study, copper conductors seized from the scene of a car fire were used. Fragments of damaged copper conductors were filled with epoxy resin in a standard holder, which were then ground and polished as shown in Figure 1.

Figure 1. Fragments of copper conductors subjected to current overload and prepared for research

The holder with conductors was examined in an Xpert PRO X-ray diffractometer ($U = 40$ kV, $I = 30$ mA CuKα) and a scanning electron microscope with a microanalyzer.

Figure 2 shows images of fragments of a sample of a copper cylinder torn apart by TNT.

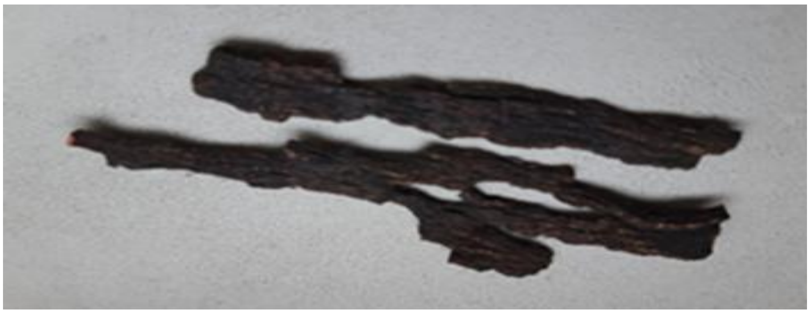

Figure 2. Fragments of a copper cylinder torn apart by TNT

Figures 3 *a*, *b* show fragments of a copper foil sample before and after the magnetic field destruction test. The micrograph (Fig. 3 *a*) shows traces of rolling; this confirms the x-ray diffraction image below.

a *b*

Figure 3. Fragments of a sample of copper foil before (*a*) and after (*b*) the magnetic field destruction test. The micrograph (*a*) shows traces of rolling, which confirms the X-ray diffraction picture

Results and discussions

Figure 4 shows a picture taken in a scanning electron microscope from a section of a copper wire subjected to current overload and removed from a burned-out car. It can be seen how cracks appeared in the plastically deformed section of the copper wire, from which drops of liquid copper were formed. The drop is shown in a separate Figure 5.

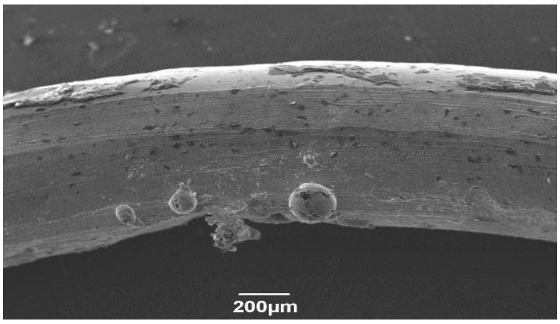

Figure 4. Ball melting on the bends of the deformed conductor [5]

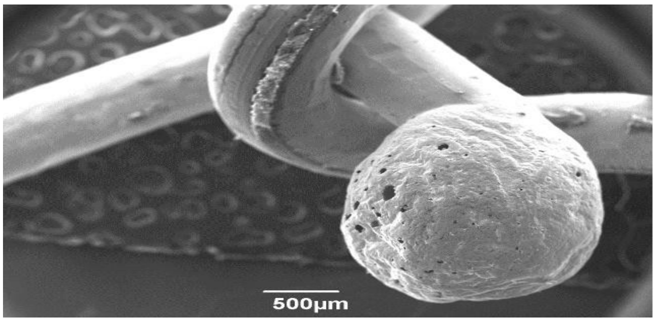

Figure 5. Ball melting of the end of the copper conductor [5]

X-ray fluorescent energy spectra were obtained from such a drop (Fig. 6 and Table 1). The drops contain mainly copper and oxygen (Table 1). The temperature exceeding the boiling point of copper (10830C) arose in the bending zones, that is, in the zones of mechanical load transferred to these wires during plastic deformation [5]. Since the flow of mechanical energy per unit time during plastic deformation in a localized zone was too large, the energy turned into heat. As a result of heating the copper conductor, the insulation ignited, which was intensified due to the electric arc process that arose due to the formation of a superconducting Cu_2O layer in the surface layer of copper wires with an increase in their temperature.

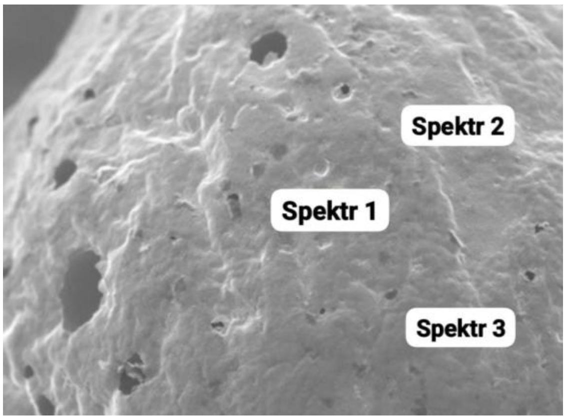

Figure 6. Image of the areas where X-ray spectral analysis was carried out [5]

Table 1

Ball Reflow Spectra

O	Al	Si	Cu	Total
12.24	1.45		86.31	100.00
17.24	3.84		78.93	100.00
4.69	3.06		92.24	100.00
9.22	6.15		84.63	100.00
14.32	1.30	0.82	83.56	100.00
9.38	3.16		87.46	100.00
17.24	6.15	0.82	92.24	
4.69	1.30	0.82	78.93	

X-ray diffraction revealed the presence of a superconducting Cu_2O phase in drops that appeared in the damage zones of copper conductors (Fig. 7*a*).

The presence of the superconducting phase [13] increases the current, which leads to an instantaneous increase in temperature, exceeding the melting point of copper (1083 °C). The X-ray diffraction pattern (Fig. 7*a*) shows the diffraction intensities and angles: 111 Cu, 200 Cu, 220 Cu reflections. We also see a weak reflection of the Cu_2O phase (before 111 Cu). The formation of this phase is associated with the process of car ignition.

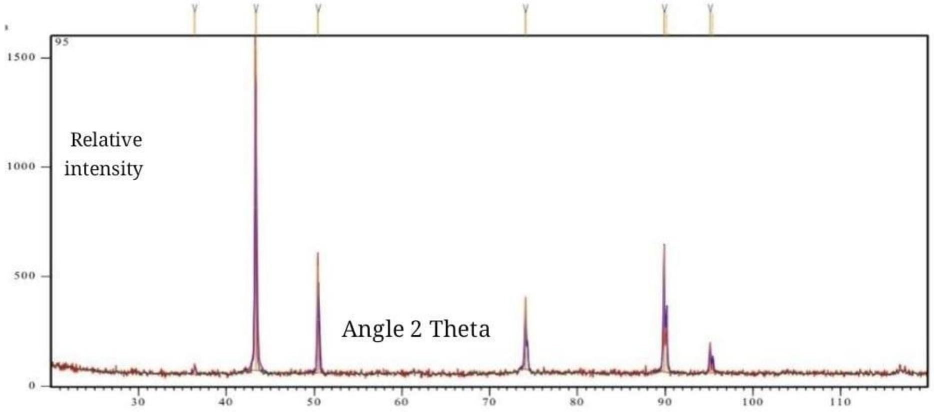

Figure 7 *a*. X-ray diffraction pattern obtained from samples of copper wire subjected to current overload [9]

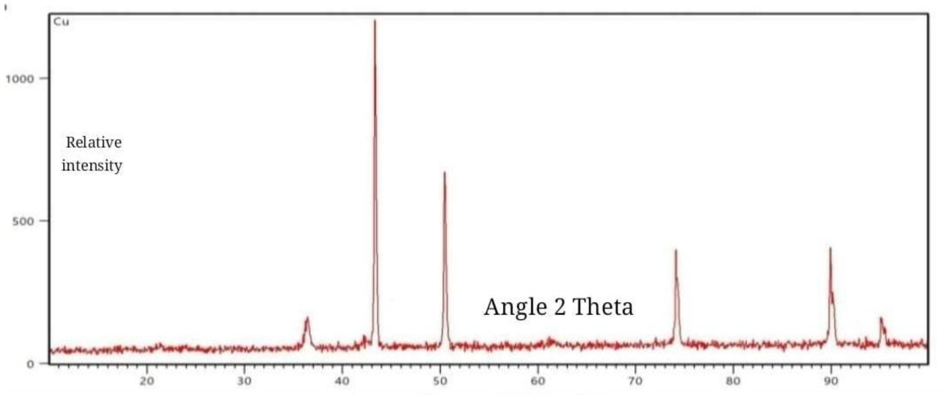

Figure 7 *b*. X-ray diffraction spectrum obtained from a sample subjected to an explosion with TNT

Figure 7 *b* shows an X-ray pattern obtained from a copper sample treated with an explosion, and the interpretation data are given in Table 2.

Table 2

Diffraction spectrum of a copper sample contain the Cu_2O phase

№	HKL	d/n [A]	2θ [°]	I [%]
1	011	3.01864	29.569	5.1
2	110	3.00		0.3
3	111	2.46471	36.424	100
4	111	2.45		100
5	020	2.13450	42.309	35.3
6	121	1.74281	52.461	1.2
7	022	1.50932	61.367	28.6
8	122	1.42300	65.547	0.0
9	031	1.34998	69.584	0. 3
10	131	1.28715	73.518	22.1
11	132	1.14094	84.931	0.2
12	200	2.12		31
13	222	1.23235	77.374	4.8

From a comparison of the X-ray image interpretation table [14], presented in Figure 7 *a* and 7 *b* and the tabulated values of copper Cu (Table 3) and copper dioxide Cu_2O (Table 3), we see that the same processes occur in the samples of copper wire from a burnt car and an exploded copper sample. By analyzing the chemical composition of an exploded copper sample and comparing the chemical composition of copper wire samples after combustion, we can conclude that in both cases copper dioxide is formed.

Table 3

Diffraction spectrum of Cu_2O

d = 2.08603	43.341	2.086	100.0	111	100	2.088	–0.002	3.613
d = 1.80617	50.489	1.806	20.4	200	46	1.808	–0.002	3.612
d = 1.27697	74.202	1.277	83.3	220	20	1.278	–0.001	3.612
d = 1.08980	89.954	1.090	31.5	311	17	1.090	0.000	3.615
d = 1.04357	95.146	1.044	11.9	222	5	1.044	0.000	3.617

The exploded sample was examined using a JEOL 683 scanning electron microscope with a microanalyzer. A micrograph and an energy dispersive spectrum are shown in Figure 8.

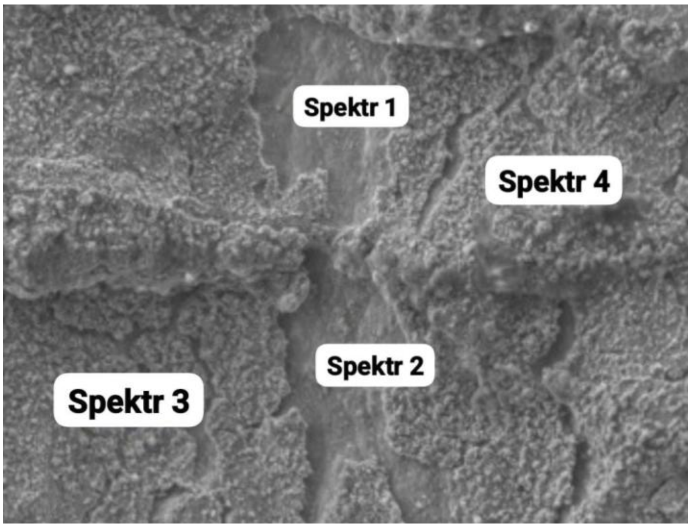

Figure 8. Scanning electron microscopy energy dispersive analysis

Table 4

Energy-dispersive spectrum obtained from the surface subjected to an explosion

O	Al	Cu	Total
1.51	0.30	98.19	100.00
3.39	0.58	96.03	100.00
12.88	0.63	86.49	100.00
15.20	0.60	84.20	100.00
8.25	0.53	91.23	100.00
6.80	0.15	6.91	
15.20	0.63	98.19	
1.51	0.30	84.20	

Table 4 shows that the sample subjected to the explosion contains copper, oxygen and a small admixture of aluminum. During explosion welding, the effect of pressure on metal conductors can lead to an increase in the internal energy of the latter to values that significantly exceed the chemical binding energy in solids. Obviously, at such levels of energy impact, the properties of metals (the behavior of atoms and ions in the lattice), as well as the transport properties of electrons, can differ significantly from those that occur under normal conditions. The change in the binding energy in solids is the result of solid-state synthesis.

It is known that a feature of solid-phase synthesis is the high values of the diffusion coefficients of atoms or ions of the components in the solid phase. Unlike ordinary diffusion, which is determined by the concentration gradients of the components, this type of diffusion is called “deformational atomic mixing” or “ballistic diffusion”. A variety of assumptions have been made regarding the mechanism of this process, but there is still no consensus on the mechanism of deformation atomic mixing [15]. Thus, the external pressure gradient leads to the appearance of new phases.

Samples of copper foil subjected to magnetic field pressure as a result of the passage of a high frequency current were examined for structural changes. The X-ray diffraction interpretation spectrum obtained from a section of a copper foil sample compressed by an electromagnetic wave (Fig. 3 b).

Using X-ray diffraction had studied of areas the torn sample. It was shown that the lattice parameter of copper can change both upward and downward. The lattice parameter of copper can vary depending on the localization of deformation, which clearly exceeded the yield strength of copper. As a result of the impact of an electromagnetic wave, as a stream of charged particles, the copper foil broke. The dependence of the energy flux of the current magnetic field on the magnitude of the alternating current is given by the expression [16]:

$$W_M = \frac{LI^2}{2},$$

W = current magnetic field energy; L = inductance; I = current in conductor.

Using X-ray diffraction and optical microscopy (Fig. 3*a*), it was found that compression of a copper foil 30 mkm thick by a magnetic field created by a current of 180 kA leads to its plastic deformation and the formation of texture [17].

Thus, studies of changes in the crystal structure, chemical and phase composition of copper samples subjected to extreme effects of temperature, pressure and electromagnetic fields have shown the possibility of mechanochemical reactions that change the crystal lattice of the material of copper samples and the appearance of new phases.

With the help of X-ray diffraction, as well as microanalysis, it was revealed that the plastic deformation of copper wires in the car power supply system leads to the formation of a superconducting Cu_2O phase. This is the reason for the rapid ignition of the car, as it leads to a sharp increase in the magnitude of the electric current and temperature in the plastic deformation zone of copper wires. Plastic deformation of a copper foil 30 mkm thick by a magnetic field generated by a current of 180 kA leads to the formation of a texture and rupture of the foil. This has been detected using X-ray diffraction, as well as optical and scanning electron microscopy.

During explosion welding of copper samples, the Cu_2O phase appears on their surface, which has superconducting properties. This significantly changes the electrophysical properties of copper samples. In metallurgical processes during the smelting of copper products, there is a possibility of the appearance of a superconducting Cu_2O phase. When modifying a copper melt with hardening additives, the superconducting Cu_2O phase makes it possible to obtain fracture-resistant copper products with high electrical conductivity. The electrical resistivity of pure copper is $1.7\cdot 10^{-2}$ Ohm*mm^2/m. When modified, it can increase up to 35 %, which significantly worsens the properties of electrical copper. Due to the fact that Cu_2O is formed in the reaction mixture during the smelting of copper products, the electrical resistance of the material is significantly reduced.

Conclusions

1. During plastic deformation of copper wires located in the power supply system of the car and subjected to current overload, the formation of the superconducting Cu_2O phase occurs at a high speed, which leads to ignition of the insulation and ignition of the car.
2. During explosion welding of copper samples, the Cu_2O phase appears on their surface, which has superconducting properties.
3. Using X-ray diffraction and optical microscopy, we found that compression of a copper foil 30 mkm thick by a magnetic field created by a current of 180 kA leads to its plastic deformation, texture formation and rupture.
4. It was found that in copper samples under conditions of extreme energy exposure, a superconducting Cu_2O phase can form, which affects the electrical properties of copper samples.

Acknowledgments

The authors thank the staff of the M.A. Lavrent'ev Institute of Hydrodynamics, Russian Academy of Sciences, for kindly providing the samples.

References

1 Логинов Ю.Н. Взаимодействие частицы оксида меди с медью в процессе волочения / Ю.Н. Логинов, С.Л. Демаков, А.Г. Илларионов, М.А. Иванова // Металлы. — 2012. — № 6. — С. 36–44.

2 Ditenberg I.A. Microstructural peculiarities of copper and mechanisms of its hardening after mechanical activation and torsion in Bridgman anvils / I.A. Ditenberg, K.I. Denisov, A.N. Tyumentsev, M.A. Korchagin, A.V. Korznikov // Physical mesomechanics. — 2013. — 16(6). — 81–87.

3 Nedobitkov A.I. Study of microhardness of a copper conductor subjected to current overload in vehicle electric mains / A.I. Nedobitkov // Fire and Explosion Safety. — 2020. — Vol. 29, No. 2. — P. 17–25. DOI: 10.18322/PVB.2020.29.02.17-25.

4 Nedobitkov A.I. Peculiarities of current overload in the car electric network / A.I. Nedobitkov // Fire and Explosion Safety. — 2019. — Vol. 28, No. 4. — P. 42–50. DOI: 10.18322/PVB.2019.28.04.42-50.

5 Nedobitkov A.I. On physical basis of local current overload in vehicle electric mains / A.I. Nedobitkov, B.M. Abdeev // Fire and Explosion Safety. — 2019. — Vol. 28, No. 6. — P. 18–28. DOI: 10.18322/PVB.2019.28.06.18-28.

6 Nedobitkov A.I. Inelastic Stretching of a Single-Wire Copper Conductor under Unlimited Local Strains at Positive Temperature. Zhurnal Tekhnicheskoi Fiziki / B.M. Abdeev // Technical Physics. — 2021. — Vol. 91, No. 6. — P. 948–955. DOI: 10.1134/S1063784221060128.

7 Чешко И.Д. Механизм формирования следов протекания сверхтоков по медному проводнику / И.Д. Чешко, А.Ю. Мокряк, С.В. Скодтаев // Вестн. СПб. ун-та ГПС МЧС России. — 2015. — № 1. — С. 41–46. — [Электронный ресурс]. — Режим доступа: https://vestnik.igps.ru/wp-content/uploads/V71/7.pdf

8 Cheshko I.D. Classification of emergency fire-hazardous operations of electric networks of cars and the scheme of identifying their trails after the fire / S.V. Skodtayev, T.D. Teplyakova // Problems of Technosphere Risk Management. — 2019. — 1(49). — P. 107–115.

9 Недобитков Ю.А. О возможности высокотемпературной сверхпроводимости в медном проводнике / Ю.А. Недобитков // Материалы XVII Междунар. науч. конф. «ǴYLYM JÁNE BILIM». — Астана: Изд-во ЕНУ им. Л.Н. Гумилева, 2022. — Т. 12. — С. 6457–6461.

10 Митричев Л.С. Исследование медных проводников в зонах короткого замыкания и термического воздействия: метод. рекомендации / Л.С. Митричев, А.И. Колмаков, Б.В. Степанов. — М.: ВНИИ МВД СССР, 1986. — 43 с.

11 Taubkin I.S. Methodological resources for investigating the failure status of electrical wiring with copper conductors as the cause of fire / I.S. Taubkin, A.R. Saklantiy // Theory and Practice of Forensic Science. — 2018. — 13(3). — P. 38–46. DOI: 10.30764/1819-2785-2018-13-3-38-46.

12 Мамонтов А.А. Обработка меди давлением / А.А. Мамонтов // Решетновские чтения – 2022: XXVI Междунар. науч.-практ. конф. — 2022.

13 Бабкин В.Г. Особенности формирования структуры и свойств дисперсно-упрочненных сплавов электротехнического назначения на основе меди / В.Г. Бабкин, А.И. Трунова, А.А. Ковалева // Металлы. — 2021. — № 3. — С. 68–74.

14 Gnezdilov V.P. Magnetoelectricity in the ferrimagnetic $Cu_2O\,SeO_3$: symmetry analysis and Raman scattering study / K.V. Lamonova, Yu.G. Pashkevich, P. Lemmens, H. Berger, F. Bussy, S.L. Gnatchenko // Low Temperature Physics. — 2010. — Vol. 36. — P. 550–557. doi:10.1063/1.3455808.

15 Горелик С.С. Рентгенографический и электронно-оптический анализ / С.С. Горелик. — М.: Изд-во МИСИС, 1994.

16 Болдырев В.В. Механохимия и механическая активация твёрдых веществ / В.В. Болдырев // Успехи химии. — 2006. — Т. 75, № 3. — С. 203–216.

17 Кнопфель Г. Сверхсильные импульсные магнитные поля / Г. Кнопфель. — М.: Мир, 1972.

Г.С. Бектасова, К.М. Исина, Г.Т. Иманжанова, Л.И. Квеглис,
Н. Кантай, А.И. Недобитков, А.Б. Садибеков

Экстремалды әсерлерге ұшыраған мыс үлгілерінің құрылымын зерттеу

Мақала температураның, қысымның және электрмагниттік өрістердің экстремалды әсеріне ұшыраған мыс үлгілерінің кристалдық құрылымының, химиялық және фазалық құрамының өзгеруін зерттеуге арналған. Рентген сәулелерінің дифракциясының, сонымен қатар микроталдау анықтағандай, автомобильдің электрмен жабдықтау жүйесіндегі мыс сымдарының пластикалық деформациясы асқын өткізгіш Cu_2O фазасының пайда болуына әкелетіні айқындалды. Бұл мыс үлгілерінің пластикалық деформация аймағында электр тогының шамасы мен температураның күрт жоғарылауына әкеліп соғатындықтан, автокөліктің жылдам тұтануына себепкер болады. Мыс үлгілерін жарылыс дәнекерлеу кезінде олардың бетінде асқын өткізгіштік қасиеті бар Cu_2O фазасы пайда болады. Бұл мыс үлгілерінің электрфизикалық қасиеттерін айтарлықтай өзгертеді. Металлургиялық үрдістерде мыс өнімдерін балқыту кезінде асқын өткізгіш Cu_2O фазасының пайда болу мүмкіндігі бар. Мыс балқымасын қатайтатын қоспалармен өзгерткен кезде, Cu2O асқын өткізгіш фазасы жоғары электр өткізгіштігі бар сынуға төзімді мыс өнімдерін алуға мүмкіндік береді. Қалыңдығы 30 мкм мыс фольгасының 180 кА тогы әсерінен пайда болған магнит өрісінің пластикалық деформациясы фольга құрылымының түзілуіне және жарылуына әкеледі. Бұл рентгендік дифракция, сондай-ақ оптикалық және электронды микроскопия көмегімен анықталды.

Кілт сөздер: мыс үлгілері, тұтану аймағы, пластикалық деформация, жарылыспен өңдеу, электрмагниттік толқын ағынының деформациясы.

Г.С. Бектасова, К.М. Исина, Г.Т. Иманжанова, Л.И. Квеглис,
Н. Кантай, А.И. Недобитков, А.Б. Садибеков

Исследование структуры медных образцов, подвергнутых экстремальным воздействиям

Статья посвящена исследованию изменений кристаллической структуры, химического и фазового состава медных образцов, подвергнутых экстремальным воздействиям температуры, давления и электромагнитных полей. С помощью дифракции рентгеновских лучей, а также микроанализа выявлено, что пластическая деформация медных проводов, находящихся в системе электропитания автомобиля, приводит к образованию сверхпроводящей фазы Cu_2O. Это является причиной быстрого возгорания автомобиля, поскольку приводит к резкому возрастанию величины электрического тока и температуры в зоне пластической деформации медных проводов. При сварке взрывом медных образцов на их поверхности возникает фаза Cu_2O, обладающая сверхпроводящими свойствами. Это существенно изменяет электрофизические свойства медных образцов. В металлургических процессах при выплавке изделий из меди существует возможность появления сверхпроводящей фазы Cu_2O. При модифицировании медного расплава упрочняющими добавками сверхпроводящая фаза Cu_2O позволяет получать стойкие к разрушению изделия из меди с высокой электропроводностью. Пластическая деформация медной фольги толщиной 30 мкм магнитным полем, созданным током 180 кА, приводит к формированию текстуры и разрыву фольги. Это обнаружено с помощью дифракции рентгеновских лучей, а также оптической и растровой электронной микроскопии.

Ключевые слова: медные образцы, зона возгорания, пластическая деформация, обработка взрывом, деформация потоком электромагнитных волн.

References

1 Loginov, Y.N., Demakov, S.L., Illarionov, A.G., & Ivanova, M.A. (2012). Vzaimodeistvie chastitsy oksida medi s mediu v protsesse volocheniia [Interaction of a particle of copper oxide with copper in the process of drawing]. *Metally — Metals*, 6, 36–44 [in Russian].

2 Ditenberg, I.A., Denisov, K.I., Tyumentsev, A.N., Korchagin, M.A., & Korznikov, A.V. (2013). Microstructural peculiarities of copper and mechanisms of its hardening after mechanical activation and torsion in Bridgman anvils. *Physical mesomechanics*, *16*(6), 81–87.

3 Nedobitkov, A.I. (2020). Study of microhardness of a copper conductor subject to current overload in vehicle electric mains. *Fire and Explosion Safety, 29*(2), 17–25. DOI: 10.18322/PVB.2020.29.02.17–25.

4 Nedobitkov, A.I. (2019). Peculiarities of current overload in the car electric network. *Fire and Explosion Safety, 28*(4), 42–50. DOI: 10.18322/PVB.2019.28.04.42–50.

5 Nedobitkov, A.I. & Abdeev, B.M. (2019). On physical basis of local current overload in vehicle electric mains. *Fire and Explosion Safety, 28*(6), 18–28. DOI: 10.18322/PVB.2019.28.06.18–28.

6 Nedobitkov, A.I. & Abdeev, B.M. (2021). Inelastic Stretching of a Single-Wire Copper Conductor under Unlimited Local Strains at Positive Temperature. *Technical Physics*, *91*(6), 948–955. DOI: 10.1134/S1063784221060128.

7 Cheshko, I.D., Mokryak, A.Yu., & Skodtaev, S.V. (2015). Mekhanizm formirovaniia sledov protekaniia sverkhtokov po mednomu provodniku [Formation mechanism of excess currents passage traces in copper conductors]. *Vestnik Sankt-Peterburgskogo universiteta GPS MChS Rossii — Bulletin of St. Petersburg University State Fire Service Emergency Situations Ministry of Russia*, 1, 41–46. Retrieved from https://vestnik.igps.ru/wp-content/uploads/V71/7 [in Russian].

8 Cheshko, I.D., Skodtayev, S.V., & Teplyakova, T.D. (2019). Classification of emergency fire-hazardous operations of electric networks of cars and the scheme of identifying their trails after the fire. *Problems of Technosphere Risk Management, 1*(49), 107–115.

9 Nedobitkov, Yu.A. (2022). O vozmozhnosti vysokotemperaturnoi sverkhprovodimosti v mednom provodnike [On the possibility of high-temperature superconductivity in a copper conductor]. *Materialy XVII Mezhdunarodnoi nauchnoi konferentsii «ǴYLYM JÁNE BILIM» — Proceedings of the XVII International scientific conference «SCIENCE AND EDUCATION»*. Astana: Izdatelstvo Evrasiiskogo natsionalnogo universiteta, 12, 6457–6461 [in Russian].

10 Mitrichev, L.S., Kolmakov, A.I., & Stepanov, B.V. (1986). Issledovanie mednykh provodnikov v zonakh korotkogo zamykaniia i termicheskogo vozdeistviia: metod, rekomendatsii [Investigation of copper conductors in short circuit and thermal impact zones: method, recommendations]. Moscow: Vserossiiskii nauchno-issledovatelskii institut Ministerstva vnutrennikh del USSR [in Russian].

11 Taubkin, I.S. & Saklantiy, A.R. (2018). Methodological resources for investigating the failure status of electrical wiring with copper conductors as the cause of fire. *Theory and Practice of Forensic Science, 13*(3), 38–46. DOI: 10.30764/1819-2785-2018-13-3-38-46.

12 Mamontov, A.A. (2022). Obrabotka medi davleniem [Processing of copper by pressure]. *Reshetnovskie chteniia — Reshetnov Readings* [in Russian].

13 Babkin, V.G., Trunova, A.I., & Kovaleva, A.A. (2021). Osobennosti formirovaniia struktury i svoistv dispersnouprochennykh splavov elektrotekhnicheskogo naznacheniia na osnove medi [Features of the formation of the structure and properties of dispersion-strengthened alloys for electrical purposes based on copper*]*. *Metally — Metals*, 3, 68–74 [in Russian].

14 Gnezdilov, V.P., Lamonova, K.V., Pashkevich, Yu.G., Lemmens, P., Berger, H., Bussy, F., & Gnatchenko S.L. (2010). Magnetoelectricity in the ferrimagnetic Cu_2O SeO_3: symmetry analysis and Raman scattering study. *Low Temperature Physics,* 36, 550–557. doi:10.1063/1.3455808

15 Gorelik, S.S. (1994). *Rentgenograficheskii i elektronno-opticheskii analiz [X-ray and electron-optical analysis]*. Moscow: Izdatelstvo MISIS [in Russian].

16 Boldyrev, V.V. (2006). Mekhanokhimiia i mekhanicheskaia aktivatsiia tverdykh veshchestv [Mechanochemistry and mechanical activation of solids]. *Uspekhi khimii — Advances in Chemistry, 75* (3), 203–216 [in Russian].

17 Knopfel, G. (1972). *Sverkhsilnye impulsnye magnitnye polia [Superstrong impulse magnetic fields]*. Moscow: Mir [in Russian].

Information about authors

Bektasova, G.S. — Associate professor of the Department of Physics and Technology, Sarsen Amanzholov East Kazakhstan University, Ust-Kamenogorsk, Kazakhstan; e-mail: bektasovags@mail.ru, ORCID 0000-0002-6746-4964

Issina, K.M. — 5th year student “Nuclear Physics”, Sarsen Amanzholov East Kazakhstan University, Ust-Kamenogorsk, Kazakhstan; e-mail: gyka1983@mail.ru

Imanzhanova, G.T. — Senior lecturer, Sarsen Amanzholov East Kazakhstan University, Ust-Kamenogorsk, Kazakhstan; e-mail: kuba_6164@mail.ru

Kvenglis, L.I. — Professor of the Department of Physics and Technology, Sarsen Amanzholov East Kazakhstan University, Ust-Kamenogorsk, Kazakhstan; e-mail: kveglis@list.ru. ORCID: 0000-0002-6850-354X

Kantai, N. — Engineer of the national laboratory, Sarsen Amanzholov East Kazakhstan University, Ust-Kamenogorsk, Kazakhstan; e-mail: nurgan85@mail.ru

Nedobitkov, A.I. — Cand. Sci. (Eng.), Senior Research Center of Excellence of the D. Serikbayev East Kazakhstan Technical University, Ust-Kamenogorsk, Kazakhstan; e-mail: a.nedobitkov@mail.ru. ORCID: 0000-0003-4605-9668

Sadibekov, A.B. — Research engineer, D. Serikbayev East Kazakhstan Technical University, Ust-Kamenogorsk, Kazakhstan; e-mail: ajdarsadibekov@gmail.com, ORCID: 0000-0002-2932-7029

Article

Received: 10.10.2023
Accepted: 15.12.2023

UDC 621.3.01

https://doi.org/10.31489/2024PH1/83-91

S. Katsyv[1], V. Kukharchuk[1], V. Madyarov[1], V. Kucheruk[2*], P. Kulakov[2], M. Hribov[3]

[1]*Vinnytsia National Technical University, Vinnytsia, Ukraine;*
[2]*Uman National University of Horticulture, Uman, Ukraine;*
[3]*National Academy of Internal Affairs, Kyiv, Ukraine*
[*]*Corresponding author's e-mail: vladimir.kucheruk@gmail.com*

Application of non-Euclidean metric in the electric power industry for reduction of measurement uncertainty

The paper proposes the use of the non-Euclidean metric to reduce the uncertainty that occurs when measuring voltage for the tasks of ongoing continuous control of electric power consumption in large, branched high-voltage electric networks. The problem is that for continuous control of electric power consumption, it is necessary to install the active and reactive power measuring equipment in each node of the electric network (at each substation) and to ensure the transmission of measurement information to dispatching control centers. For countries with large electric networks, long distances between electric grid nodes and dispatch control centers, this requires huge capital costs. Therefore, it is advisable to place equipment for measuring electric power and voltage only in individual nodes of the electrical network, and then calculate the parameters of the remaining nodes based on Kirchhoff's laws. But at the same time, there is a significant measurement uncertainty, because the complex value of the voltage is usually not measured, only the modulus of the voltage values is used for the calculation. The use of non-Euclidean metrics provides the reduction of the input data uncertainty, which are necessary to control the consumption of electric power in each node of the electric network.

Keywords: non-Euclidean metric, high-voltage electric network, electric power, measurement uncertainty, measurement information.

Introduction

In order to ensure continuous monitoring of electric power consumption, it is necessary to install equipment for measuring active and reactive power at each node of the electric network (at each substation) and to ensure their connection with dispatching control centers. For countries with large electric networks, large distances between power grid nodes and control centers, this approach requires large capital expenditures, so it makes sense to place measuring equipment only in individual nodes, and then reproduce (identify) all unknown network mode parameters according to Kirchhoff's laws. Devices for measuring complex power values in the power grid (its active and reactive components) are simple in principle and relatively cheap, since the phase shift angle is determined between the current and voltage measured on the same power supply line. As for devices for measuring complex voltage values on substation buses, the difficulty in this case is that the phase shift angle must be determined between the voltages of different substations. Such measuring equipment requires significant capital investments, which complicates the implementation of such measuring procedures. In practice, in most cases, it is possible to receive only voltage modulus in network nodes from telemetric measuring devices. It follows that the input data of the task of reproducing the modes of electrical networks have significant uncertainty. Therefore, it is important to develop new mathematical models and methods that allow to reduce the level of measurement results uncertainty [1].

Non-Euclidean geometry is a relatively new and powerful mathematical apparatus, which is currently used for analysis and calculations in the field of automation and robotics [2–4], in physics [5, 6], medicine [7, 8], information technologies [9–11], the educational process [12], and other fields of science. Recently, non-standard methods of analyzing processes in electric circuits and networks have been actively developed [13, 14]. Non-Euclidean geometry in the theory of electric circuits is a non-standard method of analysis, it is used for the analysis of multi-port electric circuits [15, 16], its application in electromechanics [17, 18] is promising, as well as for calculating load modes, determining the parameters of load mode regulators of power electric circuits [19, 20].

The purpose of the work is to create the method of using a non-Euclidean metric to reduce the uncertainty of voltage measurement for tasks of controlling electricity consumption in large, branched high-voltage electrical networks.

Non-Euclidean modulus of the voltage vector

Consider the proposed method of reducing the uncertainty of input measured data, which is associated with the practical impossibility of measuring the phase shift angle between the voltages of different substations.

The space of complex electrotechnical parameters can be represented as a two-dimensional linear metric space with the Euclidean metric. The modulus of the voltage vector at any node of the network in this space has the form:

$$U=\sqrt{U_a^2+U_p^2}\,, \tag{1}$$

where U_a — active component of the voltage vector, U_p — reactive component of the voltage vector.

In order to emphasize the dependence of this value on the selected space metric, let's call it the Euclidean modulus of the voltage vector. This modulus in the any network node significantly depends on the network parameters, the voltages of the power sources and the currents in the network coils.

But in such a two-dimensional linear metric space, the metric does not necessarily have to be Euclidean — it should only correspond to the axioms of the metric:

$$\rho(x,y)=0\Leftrightarrow x=y, \tag{2}$$

$$\rho(x,y)=\rho(y,x), \tag{3}$$

$$\rho(x,z)\le\rho(x,y)+\rho(y,z), \tag{4}$$

where $\rho(x,y)$ — the distance in this space between the points *x* and *y*.

Let's try to find the certain generalizing parameter that characterizes the voltage at any network node, and at the same time depends much less than the Euclidean modulus of the voltage vector on the network parameters, the voltages of the power sources and the currents in the network coils.

One of the directions of the search for such a generalizing parameter is the use of a metric different from the Euclidean metric in the space of complex electrotechnical parameters. Quite often, various non-Euclidean metrics are used to solve different tasks [2–12]. These can be linear non-Euclidean metrics for which $\rho(x,y)$ is a linear function, quadratic non-Euclidean metrics for which $\rho(x,y)$ is a quadratic function, etc [8]. A detailed comparative analysis of these metrics is the subject of a separate study and is beyond the scope of this paper. We only note that to achieve our local goal it is quite sufficient to use a linear non-Euclidean metric for which

$$\rho(x,y)=\beta\,|\,y_1-x_1\,|+|\,y_2-x_2\,|, \tag{5}$$

where β — the reduction factor, that is a positive real number.

Let's verify what the expression (5) confirms to the axioms of the metric. For the first axiom we can write:

$$x=y\Rightarrow\rho(x,y)=\beta\,|\,x_1-x_1\,|+|\,x_2-x_2\,|=0. \tag{6}$$

The second axiom has the form:

$$\beta\,|\,y_1-x_1\,|+|\,y_2-x_2\,|=\beta\,|\,x_1-y_1\,|+|\,x_2-y_2\,|. \tag{7}$$

The validity of expressions (6) and (7) is obvious. Correspondence of (5) to the third axiom is not so obvious, so let's prove that

$$\beta\,|\,x_1-z_1\,|+|\,x_2-z_2\,|\le\beta\,|\,x_1-y_1\,|+|\,x_2-y_2\,|+\beta\,|\,y_1-z_1\,|+|\,y_2-z_2\,|. \tag{8}$$

If the coordinates of the vectors *x*, *y*, *z* satisfy the condition $(x_1\ge y_1\ge z_1)\wedge(x_2\ge y_2\ge z_2)$, then expression (8) will take the form

$$\beta(x_1-z_1)+(x_2-z_2)\le\beta(x_1-y_1)+(x_2-y_2)+\beta(y_1-z_1)+(y_2-z_2). \tag{9}$$

After carrying out the transformation of expression (9), we get

$$\beta x_1-\beta z_1+x_2-z_2\le\beta x_1-\beta y_1+x_2-y_2+\beta y_1-\beta z_1+y_2-z_2. \tag{10}$$

After reducing the identical terms of expression (10), we have

$$\beta x_1 - \beta z_1 + x_2 - z_2 = \beta x_1 - \beta z_1 + x_2 - z_2 \tag{11}$$

which had to be proved.

If the coordinates of the vectors x, y, z satisfy the condition $\left(x_1 \le y_1 \le z_1\right) \wedge \left(x_2 \le y_2 \le z_2\right)$, expression (8) will take the form

$$\beta\left(-x_1 + z_1\right) + \left(-x_2 + z_2\right) \le \beta\left(-x_1 + y_1\right) + \left(-x_2 + y_2\right) + \beta\left(-y_1 + z_1\right) + \left(-y_2 + z_2\right). \tag{12}$$

After opening the parentheses and reducing the identical terms, we get

$$-\beta x_1 + \beta z_1 - x_2 + z_2 = -\beta x_1 + \beta z_1 - x_2 + z_2\,, \tag{13}$$

which had to be proved.

In a similar way, the correspondence of expression (5) to the third axiom of the metric is proved for other ratios of coordinates of vectors x, y, z.

Let's consider how the modulus of the voltage vector in any node of the network will look with the use of such a metric, and what properties it will have. By analogy with the usual Euclidean modulus of the voltage vector, it is possible to write

$$U = \beta\,|U_a| + |U_p|. \tag{14}$$

Let's call this value the linear non-Euclidean modulus of the voltage vector. To determine the properties of this value, consider the equivalent circuit of the electrical network section (Fig.).

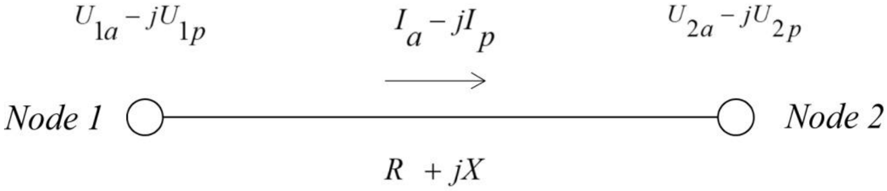

Figure. Equivalent circuit of the electrical network section

It should be noted that installation of telemetry equipment at individual nodes of the electrical network and subsequent determination of all unknown regime parameters according to Kirchhoff's laws has a high cost in networks of 110-35 kV, since these networks contain hundreds of nodes. The number of nodes in 330–750 kV networks is much smaller, and equipping all nodes with telemetry devices is much cheaper [16].

The following notations are used in Figure: $U_{1a} - jU_{1p}$ — complex voltage of the power supply (U_{1a}, U_{1p} — active and reactive components, respectively); $U_{2a} - jU_{2p}$ – complex voltage of the load node (U_{2a}, U_{2p} — active and reactive components, respectively); $I_a - jI_p$ — complex section current (I_a, I_p — active and reactive components, respectively); $R + jX$ — complex resistance of the section (note that in 110–35 kV networks this resistance has an active and inductive components).

Let's denote the linear non-Euclidean modulus of the voltage vectors of the first and second nodes, respectively

$$U_1^{\#} = \beta\,|U_{1a}| + |U_{1p}| \tag{15}$$

and

$$U_2^{\#} = \beta\,|U_{2a}| + |U_{2p}|. \tag{16}$$

Let's find how they depend on network parameters and currents. According to Ohm's law, it can be written

$$\begin{aligned} U_{2a} - jU_{2p} &= U_{1a} - jU_{1p} - \sqrt{3}\left(I_a - jI_p\right)\left(R + jX\right) = \\ &= U_{1a} - \sqrt{3}I_aR - \sqrt{3}I_pX - jU_{1p} - j\sqrt{3}I_aX + j\sqrt{3}I_pR = \\ &= U_{1a} - \sqrt{3}\left(I_aR + I_pX\right) - j\left(U_{1p} + \sqrt{3}\left(I_aX - I_pR\right)\right). \end{aligned} \tag{17}$$

It follows from (17)

$$U_{2a} = U_{1a} - \sqrt{3}\left(I_aR + I_pX\right), \tag{18}$$

$$U_{2p} = U_{1p} + \sqrt{3}\left(I_a X - I_p R\right). \tag{19}$$

So

$$U_1^{\#} = \beta\,|U_{1a}| + |U_{1p}|, \tag{20}$$

$$U_2^{\#} = \beta\,|U_{2a}| + |U_{2p}| = \beta\,|U_{1a} - \sqrt{3}\left(I_a R + I_p X\right) + |U_{1p} + \sqrt{3}\left(I_a X - I_p R\right)|. \tag{21}$$

By analogy with the voltage loss in the section (Fig.), which is defined as

$$\Delta U = \sqrt{U_{1a}^2 + U_{1p}^2} - \sqrt{U_{2a}^2 + U_{2p}^2}, \tag{22}$$

let's introduce the concept of linear non-Euclidean voltage loss, which is defined as

$$\begin{aligned} \Delta U^{\#} &= U_1^{\#} - U_2^{\#} = \beta\,|U_{1a}| + |U_{1p}| - \beta\,|U_{2a}| - |U_{2p}| = \\ &= \beta\,|U_{1a}| + |U_{1p}| - \beta\,|U_{1a} - \sqrt{3}\left(I_a R + I_p X\right)| - |U_{1p} + \sqrt{3}\left(I_a X - I_p R\right)|. \end{aligned} \tag{23}$$

In expression (23), let's reveal the sign of the absolute value, taking into account the fact that for networks of 110–35 kV with an inductive load, U_{1a}, U_{1p}, U_{2a}, U_{2p}, I_a, I_p — positive real numbers. In addition, the ratios are valid for the same conditions

$$U_{1a} >> \sqrt{3}\left(I_a R + I_p X\right), \tag{24}$$

$$I_a X > I_p R. \tag{25}$$

As a result, we get

$$\begin{aligned} \Delta U^{\#} &= \beta\,|U_{1a}| + |U_{1p}| - \beta\,|U_{1a} - \sqrt{3}\left(I_a R + I_p X\right)| - |U_{1p} + \sqrt{3}\left(I_a X - I_p R\right)| = \\ &= \beta U_{1a} + U_{1p} - \beta U_{1a} + \sqrt{3}\beta I_a R + \sqrt{3}\beta I_p X - U_{1p} - \sqrt{3} I_a X + \sqrt{3} I_p R = \\ &= \sqrt{3}\left(\beta I_a R + \beta I_p X + I_p R - I_a X\right). \end{aligned} \tag{26}$$

It is obvious that depending on the parameters of the network, parameters of the mode and the reduction factor β, the linear non-Euclidean voltage loss $\Delta U^{\#}$ (unlike traditional voltage loss) can be equal to 0, and also take a positive or negative value.

It is quite clear that in order to solve the problem of reproducing all the unknown parameters of the network mode, we will be primarily interested in the cases of zero linear non-Euclidean voltage loss, i.e. the condition $U_1^{\#} = U_2^{\#}$. Therefore, let's formulate and prove the corresponding theorem, namely:

Theorem.

For networks of 110–35 kV with an inductive load, the linear non-Euclidean voltage loss in the section is 0 if and only if the condition $\frac{R_0}{X_0} = \frac{1 - \beta\,\mathrm{tg}\,\varphi}{\beta + \mathrm{tg}\,\varphi}$ is fulfilled, where R_0 — resistivity of the section, X_0 — inductive resistivity of the section, φ — phase shift angle between voltage and current, β — reduction factor.

Proof.

Let's solve the equation

$$\Delta U^{\#} = \sqrt{3}\left(\beta I_a R + \beta I_p X + I_p R - I_a X\right) = 0. \tag{27}$$

If I — current modulus, then $I_a = I\cos\varphi$ and $I_p = I\sin\varphi$, in addition, $R = R_0 L$, $X = X_0 L$, where L — section length. Taking these ratios into account, equation (27) can be written in the form

$$\sqrt{3} I\left(\beta R_0 L\cos\varphi + \beta X_0 L\sin\varphi + R_0 L\sin\varphi - X_0 L\cos\varphi\right) = 0. \tag{28}$$

Dividing the left and right sides of equation (28) by $\sqrt{3} IL\cos\varphi$, we get

$$\beta R_0 + \beta X_0\,\mathrm{tg}\,\varphi + R_0\,\mathrm{tg}\,\varphi - X_0 = R_0\left(\beta + \mathrm{tg}\,\varphi\right) - X_0\left(1 - \beta\,\mathrm{tg}\,\varphi\right) = 0. \tag{29}$$

It follows from equation (29)

$$R_0\left(\beta + \mathrm{tg}\,\varphi\right) = X_0\left(1 - \beta\,\mathrm{tg}\,\varphi\right) \tag{30}$$

and

$$\frac{R_0}{X_0}=\frac{1-\beta\,\mathrm{tg}\,\varphi}{\beta+\mathrm{tg}\,\varphi}, \tag{31}$$

which proves the theorem for all cases except those for which $I=0$, or $\cos\varphi=0$, which we exclude from consideration as not occurring in practice.

Condition $\frac{R_0}{X_0}=\frac{1-\beta\,\mathrm{tg}\,\varphi}{\beta+\mathrm{tg}\,\varphi}$ can be recorded in other forms. It is obvious that there are identities:

$$\frac{R_0}{X_0}=\frac{1-\beta\,\mathrm{tg}\,\varphi}{\beta+\mathrm{tg}\,\varphi}\Leftrightarrow \mathrm{tg}\,\varphi=\frac{X_0-\beta R_0}{\beta X_0+R_0}\Leftrightarrow \beta=\frac{X_0-R_0\,\mathrm{tg}\,\varphi}{X_0\,\mathrm{tg}\,\varphi+R_0}. \tag{32}$$

Therefore, if one of the conditions (32) is fulfilled for any 110–35 kV section with an inductive load, the equation $U_1^{\#}=U_2^{\#}$ is valid, that is, the linear non-Euclidean modulus of the voltage vector at the beginning of the section is equal to the linear non-Euclidean modulus of the voltage vector at the end of the section.

Estimation of the limits of use of the linear non-Euclidean modulus of the voltage vector

Let's analyze the conditions (32) of the theorem proved above from the point of view of its use to reduce the uncertainty of measurements. It is obvious that resistivity of the section R_0 and inductive resistivity of the section X_0 are constant and independent quantities. Phase shift angle between voltage and current φ although constantly changing (within narrow limits), it is also an independent quantity. So it is the only quantity that can be influenced by the researcher to ensure the condition $U_1^{\#}=U_2^{\#}$, is the reduction factor β. Table 1 shows the values β, which ensure the validity of the theorem depending on the values R_0, X_0 and $\cos\varphi$. They are designed for overhead lines for a range of cross-sections from 50 to 240 mm^2 and $\cos\varphi$ from 0.85 to 0.99. As follows from Table 1, in these ranges, β can take values from 0.887 to 2.141. From the above, we state that by choosing the appropriate value β for each line of a certain section and with a certain value of the power factor, it is possible to ensure the fulfillment of condition $U_1^{\#}=U_2^{\#}$.

Table 1

Dependence of the reduction factor β on the values R_0, X_0 and power factor cosφ

Cross-section, mm^2	50	70	95	120	150	185	240
R_0, Ohm/km	0.603	0.428	0.31	0.25	0.199	0.158	0.122
X_0, Ohm/km	0.452	0.441	0.43	0.423	0.417	0.41	0.401
cosφ							
0.85	0.089	0.251	0.413	0.523	0.642	0.757	0.878
0.86	0.108	0.271	0.435	0.548	0.67	0.788	0.913
0.87	0.128	0.293	0.459	0.574	0.699	0.821	0.95
0.88	0.149	0.315	0.485	0.602	0.73	0.856	0.99
0.89	0.171	0.339	0.511	0.632	0.764	0.894	1.034
0.90	0.195	0.364	0.54	0.664	0.8	0.935	1.081
0.91	0.219	0.391	0.571	0.698	0.839	0.98	1.134
0.92	0.245	0.42	0.604	0.736	0.882	1.03	1.192
0.93	0.273	0.451	0.641	0.777	0.93	1.086	1.258
0.94	0.304	0.486	0.681	0.823	0.984	1.149	1.333
0.95	0.338	0.524	0.727	0.876	1.046	1.223	1.422
0.96	0.376	0.568	0.78	0.938	1.12	1.311	1.529
0.97	0.42	0.62	0.843	1.012	1.21	1.42	1.665
0.98	0.474	0.684	0.924	1.108	1.328	1.566	1.849
0.99	0.549	0.774	1.039	1.248	1.504	1.79	2.141

Let's consider the cases when conditions (32) are not fulfilled. Inequalities follow from equations (27) and (32):

$$\beta > \frac{X_0 - R_0 \operatorname{tg}\varphi}{X_0 \operatorname{tg}\varphi + R_0} \Rightarrow \Delta U^{\#} > 0, \tag{33}$$

$$\beta < \frac{X_0 - R_0 \operatorname{tg}\varphi}{X_0 \operatorname{tg}\varphi + R_0} \Rightarrow \Delta U^{\#} < 0. \tag{34}$$

Let's perform the comparative analysis of the relative losses of conventional and non-Euclidean voltage for one of the widespread cross-sections of 120 mm^2 at the value of $\cos\varphi = 0.92$, quite typical for a 110 kV network. Voltage losses are determined at the current modulus value of 100 A and the section length of $L = 30$ km. Let's calculate the non-Euclidean voltage loss for different values of the reduction factor β. For simplification, let's take $U_1 = U_{1a} = 115$ kV, $U_{1p} = 0$. We will calculate the relative losses according to the formulas

$$\frac{\Delta U}{U_1} = 1 - \sqrt{\left(1 - \frac{\sqrt{3}IL\left(R_0\cos\varphi + X_0\sin\varphi\right)}{U_1}\right)^2 + \left(\frac{\sqrt{3}IL\left(X_0\cos\varphi - R_0\sin\varphi\right)}{U_1}\right)^2}, \tag{35}$$

$$\frac{\Delta U^{\#}}{U_1^{\#}} = \frac{\sqrt{3}IL\left(\beta R_0\cos\varphi + \beta X_0\sin\varphi + R_0\sin\varphi - X_0\cos\varphi\right)}{U_1^{\#}}. \tag{36}$$

The results of the calculations are shown in Table 2.

Table 2

Conventional and non-Euclidean voltage loss in the section AC-120 at cosφ = 0.92, *I* = 100 A, *L* = 30 km and different reduction factors β

ΔU,%	$\Delta U^{\#}$,%	
1.78	$\beta = 0.600$	–0.24
	$\beta = 0.700$	–0.06
	$\beta = 0.736$	0
	$\beta = 0.800$	0.11
	$\beta = 0.9$	0.29

Let's analyze the results given in Tables 1 and 2. It is obvious that even if the researcher inaccurately predicts cosφ in the section, and accordingly inaccurately determines the reduction factors β, then the value of $\Delta U^{\#}$ in this case will be 6–15 times less than the value of ΔU. This makes it reasonable to use the linear non-Euclidean modulus of the voltage vector $U^{\#}$ when reproducing the modes of electrical networks. To do this, it is necessary to calculate the network mode at average statistical loads, determine the values of the reduction factor β that provide for each section $\Delta U^{\#} = 0$, and then determine the value of $U^{\#}$ in each node. If we assume that the values of cosφ in the sections under current loads remain unchanged, then it can be assumed that the values of $U^{\#}$ in each node under current loads will also not change, and after receiving from the telemetry devices the voltage values in the nodes, it will be possible to calculate the active and reactive components of node voltage. Since in networks of 110-35 kV, the values of cosφ fluctuate in a rather narrow range, the uncertainty of measuring the active and reactive components of the node voltage is quite acceptable for the task of reproducing the modes of electrical networks.

The method of reproducing the modes of electric networks using the linear non-Euclidean modulus of the voltage vector $U^{\#}$ was implemented in the software complex "Analytical system of reproducing electricity consumption", which was implemented in the divisions of the energy supply company "Vinnytsiaoblenergo", the city of Vinnytsia, Ukraine. In the process of operating the developed software complex, both company specialists and developers continuously assessed the uncertainty of network mode reproduction.

In the conditions of providing the software complex with telemetric information at 70% of the maximum level, it was established that due to the use of the non-Euclidean modulus of the voltage vector, the standard deviation of the modes integral indicators decreased by almost 50% compared to traditional methods. This practically proves the expediency of using non-Euclidean metrics in power industry.

Conclusions

To ensure continuous current control of electric power consumption, the optimal solution is to place sensors of active and reactive power in each node of the electric network and transfer measurement information to dispatching control centers, which for large networks requires huge capital costs. Therefore, it is advisable to install such sensors only in individual nodes, followed by reproducing of all unknown parameters of the network mode based on Kirchhoff's laws.

Measuring complex values of voltage on substation buses requires determining the phase shift angle between the voltages of different substations, which is an extremely difficult task, requires significant capital investments, and in most cases leads to the impracticality of such measurements. In order to solve this problem, it is proposed to receive from telemetry devices only modulus of voltages in the network nodes, which means that the input data for the task of reproducing the electrical networks modes have the significant uncertainty. In order to reduce this uncertainty, the expediency of using not the usual quadratic Euclidean metric, but a linear non-Euclidean metric to determine the node voltage modulus has been theoretically proven and practically confirmed.

Based on the calculations and practical studies, it was established that the uncertainty of reproducing network mode parameters according to Kirchhoff's laws, in the presence of the necessary telemetry information for the “Analytical system of reproducing electricity consumption” software complex, is significantly smaller when using a linear non-Euclidean modulus of the voltage vector than when using the usual voltage vector modulus.

References

1 Vasilevskyi, O. Kulakov, P., Kompanets, D., Lysenko, O.M., Prysyazhnyuk, V., & Waldemar, Wojcik, et al. (2018). A new approach to assessing the dynamic uncertainty of measuring devices. *Proceedings of SPIE — The International Society for Optical Engineering*, 257–268. https://doi.org/10.1117/12.2501578.

2 Lukyanenko, Anton, & Soudbakhsh, Damoon (2023). Probabilistic motion planning for non-Euclidean and multi-vehicle problems. *Robotics and Autonomous Systems, 168*, 104487, ISSN 0921-8890. https://doi.org/10.1016/j.robot.2023.104487.

3 Wen, Y., & Zhang, W. (2022). A Minimax Model for Generalized Penetration Distance Between Convex Sets by Directed Hausdorff Distance. *IEEE Robotics and Automation Letters, 7*(3), 6123–6130. doi: 10.1109/LRA.2022.3166111.

4 Santina, C.D., & Albu-Schaeffer, A. (2021). Exciting Efficient Oscillations in Nonlinear Mechanical Systems Through Eigenmanifold Stabilization. *IEEE Control Systems Letters*, *5*(6), 1916–1921. doi: 10.1109/LCSYS.2020.3048228.

5 Efrati, E., Sharon, E., & Kupferman, R. (2009). Buckling transition and boundary layer in non-Euclidean plates. *Physical Review E, 80*(1), 016602. https://doi.org/10.1103/PhysRevE.80.016602.

6 Klein, Y, Venkataramani, S, & Sharon, E. (2011). Experimental study of shape transitions and energy scaling in thin non-Euclidean plates. *Phys Rev Lett., 106*(11), 118303. doi: 10.1103/PhysRevLett.106.118303. Epub 2011 Mar 14. PMID: 21469903.

7 Amritha, Abdul Salam, Manjunatha, Mahadevappa, Asha, Das, & Madhu, S. Nair (2022). RDD-Net: retinal disease diagnosis network: a computer-aided diagnosis technique using graph learning and feature descriptors. *Vis. Comput. 39*, 10, 4657–4670. https://doi.org/10.1007/s00371-022-02615-x.

8 Ambellan, F., Zachow, S., & Tycowicz, C.V. (2021). Rigid motion invariant statistical shape modeling based on discrete fundamental forms: Data from the osteoarthritis initiative and the Alzheimer's disease neuroimaging initiative. *Med Image Anal., 73*, 102178. doi: 10.1016/j.media.2021.102178. Epub 2021 Jul 15. PMID: 34343840.

9 Combettes P.L. & Pesquet, J.-C. (2021). Fixed Point Strategies in Data Science. *IEEE Transactions on Signal Processing, 69*, 3878–3905. doi: 10.1109/TSP.2021.3069677.

10 Egghe, L. (2005). The power of power laws and an interpretation of Lotkaian informetric systems as self-similar fractals. *Journal of the American Society for Information Science and Technology, 56*(7), 669–675.

11 Chaczko, Z. & Resconi, G. (2012). Application of Morphotronic Theory to Parallel Robots. In: Moreno-Díaz, R., Pichler, F., Quesada-Arencibia, A. (eds). Computer Aided Systems Theory — EUROCAST 2011. EUROCAST 2011. *Lecture Notes in Computer Science, 6928*. Springer, Berlin, Heidelberg. https://doi.org/10.1007/978-3-642-27579-1_20.

12 Kuz'mich, V.I. & Kuz'mich, V.I. (2020). Elements of non-Euclidean geometry in the formation of the concept of rectilinear placement of points in schoolchildren. *Journal of Physics: Conference Series, Volume 1840, XII International Conference on Mathematics, Science and Technology Education (ICon-MaSTEd 2020) 15–17 October, Kryvyi Rih, Ukraine.* DOI 10.1088/1742-6596/1840/1/012004.

13 Katsyv, S. (2022). Non-standard analysis in electrical engineering. Transient analysis in second-order electrical circuits with violation of switching laws. *Bulletin of the University of Karaganda-Physics,* 4(108), 56–64. DOI 10.31489/2022PH4/56-64.

14 Katsyv, S. (2023). Nonstandard analysis in electrical engineering. The analysis of the direct current circles with ideal reactive elements. *Bulletin of the University of Karaganda-Physics,* 1(109), 31–41. DOI 10.31489/2023PH1/31-41.

15 Penin, A. (2016). Projective Geometry Invariants of Human Body and Multi-port Electrical Circuits. In: Sontea, V., Tiginyanu, I. (Ed.). *3rd International Conference on Nanotechnologies and Biomedical Engineering. IFMBE Proceedings, 55*. Springer, Singapore. https://doi.org/10.1007/978-981-287-736-9_81.

16 Penin, A. (2020). Operating Regimes of an Active Multi-port. In: *Analysis of Electrical Circuits with Variable Load Regime Parameters. Power Systems.* Springer, Cham. https://doi.org/10.1007/978-3-030-35366-7_6.

17 Kucheruk, V.Yu. (2019). Computer-measuring system of the induction motor’s dynamical torque-speed characteristics. *Bulletin of the University of Karaganda-Physics,* 2(94), 92–100. DOI: 10.31489/2019Ph2/92-100.

18 Hraniak, V.F., Kukharchuk, V.V., Kucheruk, V.Y., & Khassenov, A.K. (2018). Using instantaneous cross-correlation coefficients of vibration signals for technical condition monitoring in rotating electric power machines. *Bulletin of the University of Karaganda-Physics, 1*(89), 72–80.

19 Penin, A. (2014). Non-Euclidean geometrical transformation groups in the electric circuit theory with stabilization and regulation of load voltages. *International Journal of Circuits, Systems and Signal Processing, 8,* 182–194.

20 Penin, A. (2011). About the definition of parameters and regimes of active two-port networks with variable loads on the basis of projective geometry. *WSEAS Transactions on Circuits and Systems, 10*(5), 157–172.

С. Кацыв, В. Кухарчук, В. Мадьяров, В. Кучерук, П. Кулаков, М. Грибов

Өлшеу қателігін азайту үшін электр энергетикасында евклидтік емес көрсеткіштерді қолдану

Мақалада ірі, тармақталған жоғары вольтты электр желілерінде электр энергиясын тұтынуды үздіксіз бақылау есептерінде кернеуді өлшеу кезінде туындайтын белгісіздікті азайту үшін евклидтік емес метриканы пайдалану ұсынылған. Мәселе мынада, электр энергиясын тұтынуды үздіксіз бақылау үшін электр желісінің әрбір торабында (әрбір қосалқы станцияда) белсенді және реактивті қуатты өлшеу құралдарын орнату және диспетчерлік басқару орталықтарына өлшеу ақпаратын беруді қамтамасыз ету қажет. Ірі электр желілері бар, электр тораптары мен диспетчерлік орталықтар арасындағы үлкен қашықтық бар елдер үшін бұл үлкен күрделі шығындарды талап етеді. Сондықтан электр қуаты мен кернеуді өлшеуге арналған жабдықты тек электр желісінің жеке тораптарына орналастырған жөн, содан кейін Кирхгоф заңдары негізінде қалған тораптың параметрлерін есептеген жөн. Бірақ сонымен бірге өлшеудің айтарлықтай белгісіздігі бар, өйткені күрделі кернеу мәні әдетте өлшенбейді және есептеу үшін тек кернеу мәндерінің модулі қолданылады. Евклидтік емес көрсеткіштерді пайдалану электр желісінің әрбір торабында электр энергиясын тұтынуды бақылау үшін қажетті кіріс деректерінің белгісіздігін төмендетуді қамтамасыз етеді.

Кілт сөздер: евклидтік емес метрика, жоғары вольтты электр желісі, электр қуаты, өлшеу белгісіздігі, өлшеу ақпараты.

С. Кацыв, В.В. Кухарчук, В. Мадьяров, В. Кучерук, П. Кулаков, М. Грибов

Применение неевклидовой метрики в электроэнергетике для уменьшения погрешности измерения

В статье предложено использовать неевклидову метрику для уменьшения неопределенности, которая возникает при измерении напряжения в задачах непрерывного контроля потребления электроэнергии в крупных, разветвленных высоковольтных электрических сетях. Проблема заключается в том, что для непрерывного контроля потребления электроэнергии необходимо в каждом узле электрической сети (на каждой подстанции) установить средства измерения активной и реактивной мощности и обеспечить передачу измерительной информации в диспетчерские центры управления. Для стран с крупными электрическими сетями, большими расстояниями между узлами электросетей и диспетчерскими центрами это требует огромных капитальных затрат. Поэтому оборудование для измерения электрической мощности и напряжения целесообразно размещать только в отдельных узлах электрической сети, а затем рассчитывать параметры остальных узлов на основе законов Кирхгофа. Однако в то же время существует значительная неопределенность измерения, поскольку комплексное значение напряжения обычно не измеряется, а для расчета применяется только модуль значений напряжения. Использование неевклидовых метрик обеспечивает снижение неопределенности входных данных, необходимых для контроля потребления электроэнергии в каждом узле электрической сети.

Ключевые слова: неевклидова метрика, высоковольтная электрическая сеть, электрическая мощность, неопределенность измерений, измерительная информация.

Information about authors

Katsyv, S.S. — Candidate of technical sciences, Associate professor of the Department of Computerized Electromechanical Systems and Complexes, Vinnytsia National Technical University, Ukraine; e-mail: katsyvsam@ukr.net ORCID: 0000-0003-1375-5229

Kukharchuk, V.V. — Doctor of technical sciences, Professor of the Department of Computerized Electromechanical Systems and Complexes, Vinnytsia National Technical University, Ukraine; e-mail: BKuch@ukr.net ORCID: 0000-0001-9920-2726

Madyarov, V.G. — Candidate of technical sciences, Professor of the Department of Computerized Electromechanical Systems and Complexes, Vinnytsia National Technical University, Ukraine; e-mail: madiarov@vntu.edu.ua ORCID: 0000-0001-5116-6017

Kucheruk, V.Yu. — Professor, Doctor of science (Engineering), Professor of the Department of Information Technologies, Uman National University of Horticulture, Ukraine, e-mail: vladimir.kucheruk@gmail.com, https://orcid.org/0000-0002-6422-7779

Kulakov, P.I. — Doctor of technical sciences, Professor of the Department of Information Technologies, Uman National University of Horticulture, Ukraine, e-mail: kulakovpi@gmail.com ORCID: 0000-0002-0167-2218

Hribov, M.L. — Doctor of Law, Professor of the Department of Investigative Activities of the National Academy of Internal Affairs, Ukraine; e-mail: griboff007@gmail.com ORCID: 0000-0003-2437-5598

Article

Received: 05.09.2023
Accepted: 30.11.2023

UDC 621.548.9

https://doi.org/10.31489/2024PH1/92-98

N.K. Tanasheva[1, 2], A.R. Bakhtybekova[1, 2*], N.N. Shuyushbayeva[3],
A.N. Dyusembaeva[1], M.A. Burkov[1, 2], S.A. Nurkenov[4]

[1]*Karaganda Buketov University, Karaganda, Kazakhstan;*
[2]*Scientific Center "Alternative Energy", Karaganda, Kazakhstan;*
[3]*Sh .Ualikhanov Kokshetau University, Kokshetau, Kazakhstan;*
[4]*Astana International University, Astana, Kazakhstan*
[*]*Corresponding author's e-mail: asem.alibekova@inbox.ru*

Experimental study of aerodynamic coefficients of a combined blade

Magnus wind turbines have a number of advantages in the form of electricity generation at low wind values, ranging from 3-4 m/s. However, at high speeds around the existing blades of wind turbines, there is a phenomenon of separation of vortices, which entails the destruction of the structure, as well as an increase in drag. Based on this, an urgent issue is the regulation of the flow around cylindrical bodies, along with a decrease in drag force. The novelty of the work is the elimination of vortices, as well as their control, by adding a fixed blade to the cylinder. Authors of the article for this purpose created a mock-up of the cylinder blade with a fixed blade. A number of experimental studies were carried out to determine the aerodynamic forces and coefficients depending on the angle of inclination with respect to the incoming flow at U = 5 m/s. It was found that at an angle of inclination of 0° and 180°, the combined blade has a maximum lifting force of 2.7 N and 2.75 N, respectively. It is determined that at these angles, the drag force is the lowest and is 1.26 N and 1.08 N.

Keywords: Wind turbine, Magnus, combined blade, cylinder, lifting force, drag force, flow velocity, tilt angle.

Introduction

It is well known that the tasks of studying transversely streamlined cylindrical bodies are relevant for wide industries ranging from thermal power engineering and aerodynamics to cosmonautics. However, despite all the simplicity of geometric visualization, the flow around a round rotating cylinder is complex, and largely depends on the flow mode.

The classical aerodynamic problem of the flow around the cylinder modules is the object of the study of aerohydrogas dynamics. Of these, the study of the flow around a rotating vertical cylinder is of great interest.

Many scientists and researchers in the field of aerodynamics have devoted their work to studying the flow pattern around the cylinderat high Reynolds numbers [3–5].

In the study [6], the authors experimentally and numerically investigated the flow characteristics around a rotating circular cylinder, the diameter of which is 20 mm. Parameters such as the time-averaged velocity, turbulence intensity, drag coefficient and flow structure at the Reynolds number $5900 \leq Re \leq 11800$ and the rotation coefficient $0 \leq \alpha \leq 0.525$ were investigated. Using the SST turbulence model, a numerical simulation of the flow was carried out. The authors found that due to the rotational movement of the cylinder, a change in profiles is observed the average and fluctuation velocities, and the area of velocity reduction has become smaller due to arise in the Reynolds number. It is established that symmetry of the flow breaking is observed with an increase in the rotation coefficient.

The authors of the work [7] investigated the problem of the flow around a round cylinder, with a constant angular velocity, fixed in a homogeneous flow. An interesting result is that, as the rotation speed increases, the vortex loss is suppressed. It is also determined that rotation weakens the secondary instability and rises the critical Reynolds number for the occurrence of this instability.

At high Reynolds numbers starting from $5\ 10^4$, with the transverse flow around the cylinders with an increase in the flow velocity, the separation of vortices is observed, and the formation of a trace behind the cylinder, the so-called Pocket track. Mechanical vibrations caused by the disruption of vortices can lead to vibration, acoustic noise and, if the frequency of the separation of vortices coincides with the natural frequency of the structure, to its destruction.

Based on this, the task of regulating the flow of cylindrical bodies, along with reducing the drag force, is relevant.

The purpose of this work is experimental study of aerodynamic coefficients of a combined blade in the form of a cylinder and a fixed plate, depending on the angle of inclination relative to the incoming flow.

Research objectives:

– creation of a laboratory layout of a combined blade;

– study of the influence of the angle of inclination on the values of aerodynamic forces;

– investigation of the influence of the angle of inclination on the values of the aerodynamic coefficients of lift and drag force.

The use of the plate as a means of preventing the formation and separation of the boundary layer behind the rotating cylinder is a novelty of the work. The studied object of research is a combined blade that can be used as the power element of Magnus wind turbines, with a vertical axis of rotation.

Experimental methodology

The authors of the work created a combined blade in the form of a cylinder with a fixed blade with a vertical axis of rotation to solve the problem of separation of the boundary layer as well as its prevention.

Aerodynamic experiments were completed in the laboratory “Aerodynamic Measurements” at the scientific center “Alternative Energy” at the E.A. Buketov Karaganda University. The object under study is installed in the working area of the T-1-M wind tunnel (Fig. 1).

Figure 1. Experimental layout of a cylinder with a fixed blade

As can be seen from Figure 1, the experimental layout consists of a cylinder and a fixed blade attached to disc-shaped bases on both sides, fixed between them. To start the cylinders in rotational motion, an electric drive is used, fixed on the upper part of the base.

The geometric dimensions of the sample are given in Table below.

Table

Parameters	Values
Cylinder diameter	4 cm
Cylinder length	9 cm
Width of the fixed blade	3 cm
Fixed blade length	10.5 cm

Figure 2 shows the layout of the fixed blade relative to the flow.

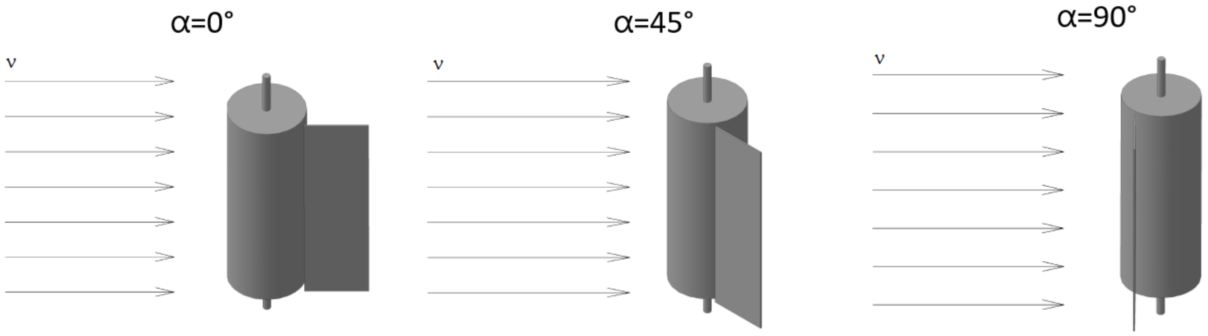

Figure 2. Location of the stationary blade of the rotating cylinder

Results and Discussion

When the flow velocity changes from 3 to 15 m/s, the angle of inclination of the fixed blade on the aerodynamic forces of the entire blade layout is studied.

In the course of experimental studies, graphs of the dependence of aerodynamic forces and their coefficients depending on the angle were obtained (Fig. 3–6).

Figure 3 below shows the results of measurements of the drag force depending on the angle of inclination at a wind speed of 5 m/s.

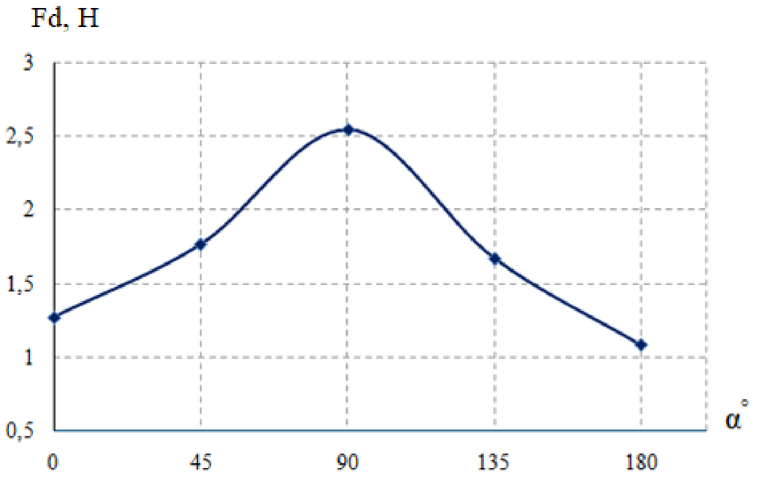

Figure 3. The results of measurements of the drag force from the angle of inclination at a flow rate of 5 m/s

As can be seen from the graph, the minimum value of the drag force of 1.25 N is observed at an angle of 0 degrees, after which, with an increase in the angle of inclination to 90 degrees, the force value increases to 2.5 N, which is the maximum value of the drag force.

As can be seen from the graph, the minimum value of the drag force of 1.25 N is observed at an angle of 0 degrees, after which, with an increase in the angle of inclination to 90 degrees, the force value increases to 2.5 N, which is the maximum value of the drag force. The reason for this is an increase in the mid-section of the entire blade in relation to the flow, which subsequently slows down the flow by forming pressure on the front part. In the future, with an increase in the angle to 180 degrees, there is a monotonous decrease in the value of the drag force to a minimum of 1.1 N. The explanation for this is the favorable flow around the blade without obstacles.

Figure 4 below shows the results of measurements of the lifting force values depending on the pitch of the fixed blade at a speed of 5 m/s.

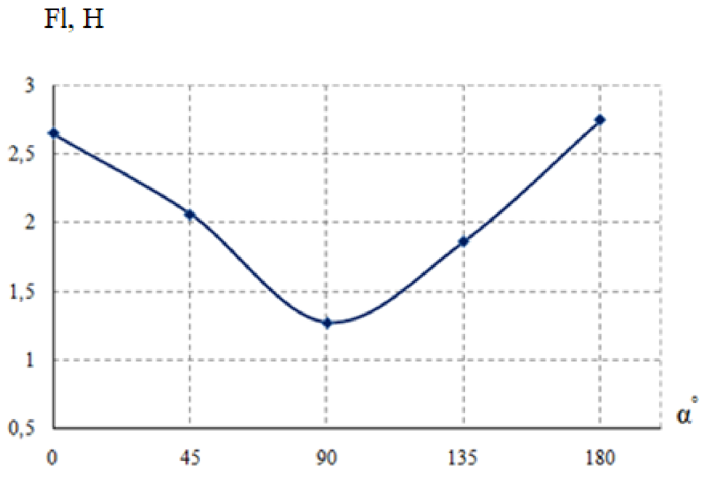

Figure 4. The results of lifting force measurements depending on the angle of inclination at a flow rate of 5 m/s

As can be seen from Figure 4, the value of the maximum lifting force of 2.7 N is observed at a speed of 0 degrees, after which it decreases linearly with an increase in the angle of inclination to 90 degrees.

According to the Kutta-Joukowski theorem [8] (the lifting force theorem of a body), where the lifting force is equal to the product of the density and velocity of the liquid, the circulation of the flow velocity and the length of the blade, which occurs at right angles against the direction of circulation, i.e. with non-symmetrical flow with an increase in the mid-section of the combined blade relative to the flow, there will be an increase in lifting force with an increase in the angle of attack to a critical value (90°). As can be seen from graphs 4 and 5, after 90° there is a sharp decrease in lifting force, due to the occurrence of flow disruption with an increase in the force of frontal resistance.

The calculated aerodynamic coefficients depending on the angle of inclination at different flow rates are shown in Figures 5 and 6. The aerodynamic coefficients are calculated using the formulas in the work [9].

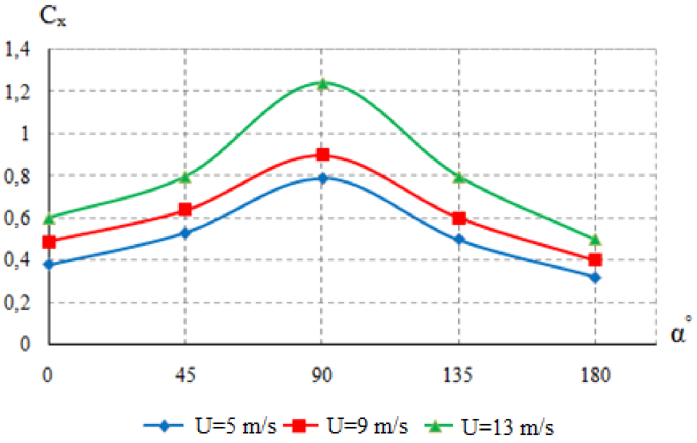

Figure 5. Change in the drag coefficient a depending on the angle of inclination at different flow rates

From Figure 5, it is established that with an increase in the angle of inclination to 90 degrees, there is an increase in the drag coefficient to 1.2 at 13 m/s, subsequently, with an increase in the angle to 180, there is a decrease in the coefficient value of 0.5.

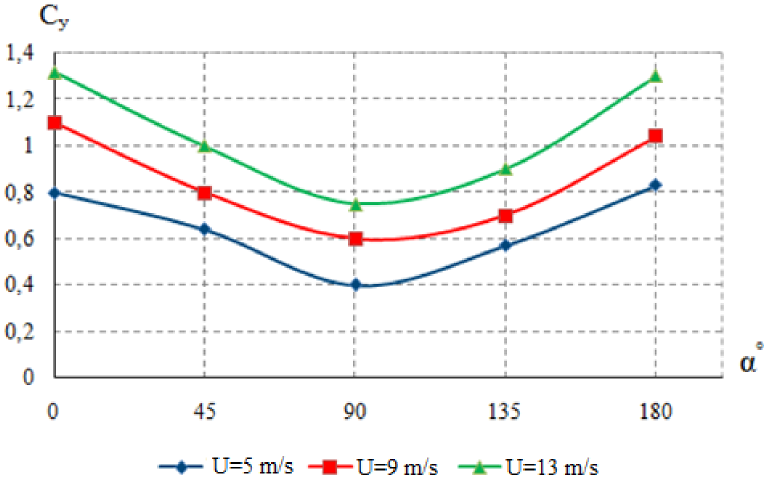

Figure 6. Change in the lift coefficient a depending on the angle of inclination at different flow rates

From Figure 6, it is determined with an increase in the angle of inclination from 0 to 90 degrees, there is a decrease in the coefficient of lift from 1.3 to 0.75 at 13 m/s, subsequently, with an increase in the angle from 90 to 180, there is an increase in the coefficient value to 1.32. The nature of the changes in the dependency lines presented in Graphs 5 and 6 do not contradict the previous experimental [10] and numerical [11] results.

Conclusions

In the course of conducting experimental studies, the authors of the work obtained the following results:

– A model of a combined blade with a diameter of 4 cm and a length of 9 cm of the cylinder, and a fixed blade with a length of 10.5 cm and a width of 3 cm has been developed and created;

– The graph of the dependence of the drag force on the angle of inclination of the fixed blade to the flow is obtained, during which the maximum drag is 2.5 N at an angle of 90 °;

– From the lifting force measurement results, it is determined that the maximum values of 2.7 N and 2.75 N are obtained at tilt angles of 0 ° and 180 °;

– From the calculated results of drag force values, it is determined that at an angle of 90 ° and U = 13 m/s, the maximum value is 1.2;

– It was determined that the maximum values of the lift coefficients 1.32 and 1.3 were obtained at an angle of 90 ° and U = 13 m/s;

– The drop in the value of the lifting force after increasing the angle of attack from 90 to 180 is a consequence of the occurrence of the physical phenomenon of disruption of vortices, which is also the reason for the increase in the drag force;

– It is determined that the angles of inclination of 0 ° and 180 ° are favorable angles for the location of a fixed blade, followed by obtaining maximum lift and minimum drag force.

The experimental results obtained by the authors will be useful in developing a layout of a wind turbine with a vertical axis of rotation containing combined blades.

Acknowledgments

The work was carried out with the financial support of the Science Committee of the Ministry of Science and Higher Education of the Republic of Kazakhstan (IRN AP14870066 “Development and creation of an energy-efficient combined vertical-axial wind power plant using a gearless low-speed electric generator”).

References

1 Ran, Y., Deng, Z., Yu, H., Chen, W., & Gao, D. (2023). Review of passive control of flow past a circular cylinder. *Journal of Visualization, 26*(1), 1–44.

2 Tanasheva, N.K., Bakhtybekova, A.R., Minkov, L.L., Bolegenova, S.A., Shuyushbaeva, N.N., Tleubergenova, A.Z., & Toktarbaev, B.A. (2021). Influence of a rough surface on the aerodynamic characteristics of a rotating cylinder. *Bulletin of the University of Karaganda–Physics,* (3), 52.

3 Wu, C., Kinnas, S.A., Li, Z., & Wu, Y. (2019). A conservative viscous vorticity method for unsteady unidirectional and oscillatory flow past a circular cylinder. *Ocean Engineering, 191*, 106504.

4 Zhao, M., & Taheri, E. (2022). Control of flow past a circular cylinder using a rotating control rod. *Journal of Marine Science and Engineering, 10*(5), 608.

5 Tanasheva, N.K., Bakhtybekova, A.R., Shuyushbayeva, N.N., Tussupbekova, A.K., & Tleubergenova, A.Z. (2022). Calculation of the Aerodynamic Characteristics of a Wind-Power Plant with Blades in the Form of Rotating Cylinders. *Technical Physics Letters, 48(*2), 51–54.

6 Ezadi, Yazdi, M.J., Rad, A.S., & Khoshnevis, A.B. (2019). Features of the flow over a rotating circular cylinder at different spin ratios and Reynolds numbers: Experimental and numerical study. *The European Physical Journal Plus*, *134*, 1–21.

7 El Akoury, R., Braza, M., Perrin, R., Harran, G., & Hoarau, Y. (2008). The three-dimensional transition in the flow around a rotating cylinder. *Journal of Fluid Mechanics, 607,* 1–11.

8 Limacher, E.J., & Wood, D.H. (2021). An impulse-based derivation of the Kutta–Joukowsky equation for wind turbine thrust. *Wind Energy Science*, *6*(1), 191–201.

9 Tanasheva, N.K., Sakipova, S.E., Minkov, L.L., Bakhtybekova, A.R., Shuyushbaeva, N.N., & Burkov, M.A. (2021). Study of aerodynamic characteristics of a cylindrical blade with deflector. *Eurasian Physical Technical Journal, 18*(3 (37)), 48–52.

10 Yao, J., Lou, W., Shen, G., Guo, Y., & Xing, Y. (2019). Influence of inflow turbulence on the flow characteristics around a circular cylinder. *Applied Sciences, 9* (17), 3595.

11 Catalano, P., Wang, M., Iaccarino, G., & Moin, P. (2003). Numerical simulation of the flow around a circular cylinder at high Reynolds numbers. *International journal of heat and fluid flow*, *24*(4), 463–469.

Н.К. Танашева, А.Р. Бахтыбекова, Н.Н. Шуюшбаева,
А.Н. Дюсембаева, М.А. Бурков, С.А. Нуркенов

Құрамалы қалақшаның аэродинамикалық сипаттамаларын зерттеу

Магнус эффектісіне негізделген жел энергетикалық қондырғысы 3-4 м/с–тан басталатын жел жылдамдығының төмен мәндерінде электр энергиясын өндіру түрінде бірқатар артықшылықтарға ие және желдің бағытын аз талап етеді. Алайда, жел энергетикалық қондырғыларында, яғни цилиндрлердің қолданыстағы қалақтарының айналасында үлкен жылдамдықта құйындылардың үзілуінен күрделі физикалық құбылыс пайда болады, бұл қондырғының құрылымын бұзуға, сондай-ақ маңдайлық кедергі күшінің жоғарылауына әкеледі, осылайша қондырғының тиімділігін төмендетеді. Ауа ағынының көлденең бағытына қарай ағатын цилиндрлер айналмалы қозғалысқа келтірілгенде цилиндрлердің бетінде ілеспелі ағын пайда болады. Осыдан цилиндрлік денелердің айналуын реттеу, сонымен қатар маңдайлық кедергі күшінің төмендеуі және көтеру күшінің жоғарылауы (Магнус күші) өзекті мәселе болып саналады. Жұмыстың ғылыми-зерттеу жаңалығы — цилиндрге бекітілген қалақшаны қосу арқылы құйындыларды жою, сонымен қатар оларды басқару. Осы мақсатта жұмыс авторлары қозғалмайтын қалақшасы бар цилиндр түріндегі қалақ үлгісін жасады. Т-1-М аэродинамикалық құбырын қолдана отырып, U=5 м/с-та көтерілу ағынына қатысты көлбеу бұрышқа тәуелді аэродинамикалық күштер мен коэффициенттерді анықтау үшін бірқатар эксперименттік зерттеулер жүргізілді. 0° және 180° көлбеу бұрышында құрамалы қалақшаның (бекітілген қалақшасы бар цилиндр) сәйкесінше 2,7 Н және 2,75 Н максималды көтеру күші бар екені анықталды. Бұл бұрыштарда кедергі күші ең аз және 1,26 Н мен 1,08 Н құрайтыны айқындалды.

Кілт сөздер: жел энергетикалық қондырғы, Магнус, құрамалы қалақша, цилиндр, көтеру күші, маңдайлық кедергі күші, ағын жылдамдығы, көлбеу бұрышы.

Н.К. Танашева, А.Р. Бахтыбекова, Н.Н. Шуюшбаева,
А.Н. Дюсембаева, М.А. Бурков, С.А. Нуркенов

Исследования аэродинамических характеристик комбинированной лопасти

Ветроэнергетические установки на основе эффекта Магнуса обладают целым рядом преимуществ в виде выработки электроэнергии при низких значениях ветрах, начиная от 3–4 м/с, и менее требовательны к направлению ветра. Однако при больших скоростях вокруг существующих лопастей ветроэнергетических установок-цилиндров возникает сложное физическое явление — отрыв вихрей, которое влечет собою разрушение конструкции самой установки, а также рост лобового сопротивления, снижая тем самым эффективность работы установки. Исходя из этого, актуальным вопросом является регулирование обтекания цилиндрических тел, наряду с уменьшением силы лобового сопротивления и увеличением подъемной силы (силы Магнуса). Новизной работы является устранение вихрей, а также управление ими путем добавления неподвижной лопасти к цилиндру. Авторы работы для этой цели создали макет лопасти в виде цилиндра с неподвижной лопастью. Провели ряд экспериментальных исследований по определению аэродинамических сил и коэффициентов в зависимости от угла наклона по отношению к набегающему потоку при U = 5 м/с, используя аэродинамическую трубу Т–1–М. Установлено, что при углах наклона 0 и 180° комбинированная лопасть (цилиндр с неподвижной лопастью) обладает максимальным значением подъемной силы 2,7 и 2,75 Н соответственно. Определено, что при данных углах сила лобового сопротивления самая минимальная и составляет 1,26 и 1,08 Н.

Ключевые слова: ветроэнергетическая установка, Магнус, комбинированная лопасть, цилиндр, подъемная сила, сила лобового сопротивления, скорость потока, угол наклона.

Information about authors

Tanasheva, N.K. — PhD doctor, Associate professor of the Karaganda Buketov University, Karaganda, Kazakhstan; e-mail: nazgulya_tans@mail.ru; ORCID ID https://orcid.org/0000-0003-4273-0960

Bakhtybekova, A.R. (corresponding author) — PhD 3rd year doctoral student, Karaganda Buketov University, Karaganda, Kazakhstan; e-mail: asem.alibekova@inbox.ru; ORCID https://orcid.org/0000-0002-2018-8966

Shuyushbayeva, N.N. — PhD doctor, Associate professor, Sh. Ualikhanov Kokshetau University, Kokshetau, Kazakhstan; e-mail: nn_shuish@mail.ru; ORCID https://orcid.org/0000-0001-7166-6449

Dyusembaeva, A.N. — PhD, doctor, Karaganda Buketov University, Karaganda, Kazakhstan; e-mail: aikabesoba88@mail.ru; ORCID ID https://orcid.org/0000-0001-6627-7262

Burkov, M.A. — PhD 1st year doctoral student, Karaganda Buketov University, Karaganda, Kazakhstan, e-mail: mail-verification-2012@mail.ru

Nurkenov, S.A. — PhD, Astana International University, Astana, Kazakhstan; e-mail: S.Nurkenov@gmail.com, ORCID https://orcid.org/0000-0001-7116-1520

Article

Received: 25.09.2023
Accepted: 05.12.2023

UDC 537.291

https://doi.org/10.31489/2024PH1/99-105

I.F. Spivak-Lavrov[1], S.U. Sharipov[1*], A.B. Seiten[1], A.A. Trubitsyn[2]

[1]*K. Zhubanov Aktobe Regional University, Aktobe, Kazakhstan;*
[2]*Ryazan State Radio Engineering University, Ryazan, Russia*
[*]*Corresponding author's e-mail: sharipov_samat@mail.ru*

Edge field of deflectorplates with expanding screens

Deflector plates consist of two parallel conductive plates that create a deflecting electric field. They can be used to control the flow of charged particles — electrons or ions. The effect of the edge field of deflector plates leads to a change in the velocity of charged particles in the longitudinal and transverse directions, consequently of which their real trajectories change, deviating from ideal ones, which violates the space-time resolution of corpuscular optical devices in which they are used. Apart from that, the electric field at the input to the plates of deflector can vary over time, which must also be taken into account when the deflector diverts the beam of charged particles. Thus, in many cases, the use of deflector plates with open ends is inappropriate, since uncontrolled scattering fields are formed. In this article, we can consider the field of deflector plates with expanded screens at the output, so that deflecting beams of charged particles can be used at the output of deflector plates. Using the methods of the theory of complex variable functions, analytical expressions for the edge field of deflector plates with grounded screens were obtained. Firstly, by grounding the screens and shielding the plates from the deflection field, we can localize the edge electric field and reduce the uncontrolled scattering fields, and secondly, such a field can be accurately calculated analytically.

Keywords: deflector plates, grounded screens, edge field, boundary problem of electrostatics, electron beam control.

Introduction

Deflector plates are two parallel plates that create a deflecting electric field. In their effect on charged particle beams, they are similar to the field of a plate capacitor and used for controlling electron beams in electron beam lithography [1–3], as well as in various electron beam instruments [4–6], and nowadays they have become a significant element in the ultrafast electron microscopy UEM [7–10], where they are used for deflections of the electron beam along the aperture when scanning the sample. All of these apps, a highly important role is played by the spatial and temporal resolution of the electron beam. It is not possible to achieve an increase in the resolution of the scanning beam without taking into account the effect of the edge field of deflection plates on the deflection of the beam of charged particles.

The impact of the edge field leads to a change in the electron velocity in both the transverse and longitudinal directions, hence of which their real trajectory deviates from the ideal one and this leads to a violation of the space-time resolution of KOS. Moreover, the electric field at the entrance to the deflector plates usually depends on time. Therefore, it is necessary to calculate the dynamic properties of the electron beam after its deflection by the deflector.

The influence of edge fields in electromagnetic sectors was first studied in the works [11–13], nevertheless, the results obtained in these works are difficult to apply to parallel deflector plates because unlike electromagnetic sectors the curvature of the electron trajectory in the deflector plates is not a constant value. Besides that, in deflector plates, as already noted, electric fields usually change over time, which also requires additional research.

Note that using the methods of the theory of functions of a complex variable, approximate mathematical formulas were obtained for the edge field of a plate and cylindrical capacitor with open ends [14, 15]. At that moment, it seemed to us that we were the first to consider the edge field of a plate and cylindrical capacitor in this approximation. But when we got acquainted with the work [16], we found in it a reference to the work of Maxwell [17], who obtained formulas for a plate capacitor at the end of the 19th century. So, we have priority only for the approximate description of the cylindrical capacitor field. By the way, in the review work on beautiful fields [16], 3D graphs of the edge fields of plate and cylindrical capacitors are also given. It should also be noted that in [14, 15] an original method of integrating the equations of motion is also proposed, in which the electric potential and the force function are used as independent variables, and new schemes of energy analyzers are calculated using this method [18]. An approximate account of the impact of the edge field on electron beams was made in [19, 20], but these studies cannot be considered exhaustive.

Experimental

Consider the case when expanding grounded screens are located at the outlet of the deflector plates. This case is shown in Figure 1, where the grounded screens form an angle $\alpha\pi$ with the reflex plates in the plane $z = x + iy$. In this figure, deflector plates with potential $\pm\frac{V}{2}$ are represented by thick lines, screens with potential V_0 are thin.

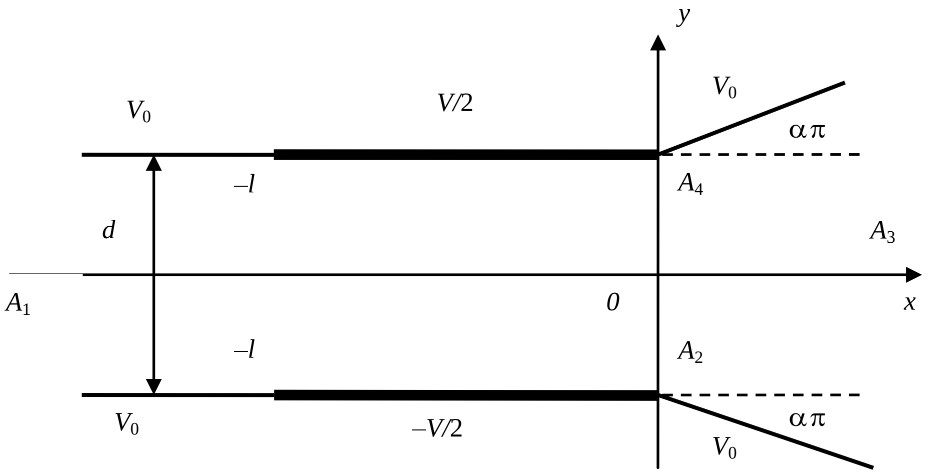

Figure 1. Schematic representation of deflector plates with divergent screens

The mapping of the quadrilateral $A_1 A_2 A_3 A_4$ with two vertices A_1 and A_3 at infinity, shown in Figure 1, to the upper half-plane $w = u + iv$ is carried out by the following conformal Schwarz-Christoffel transformation [21]:

$$z = C\int_{-1}^{w} \frac{(w^2-1)^{\alpha}\,dw}{w^{2\alpha}} + C_1 . \tag{1}$$

Here the following correspondence of the vertices of the quadrilateral to the points of the real axis of the *w*-plane is performed: A_1 – $-\infty$, A_2 – -1, A_3 – 0, A_4 –$+1$. The boundary value problem in the *w*-plane is shown in Figure 2.

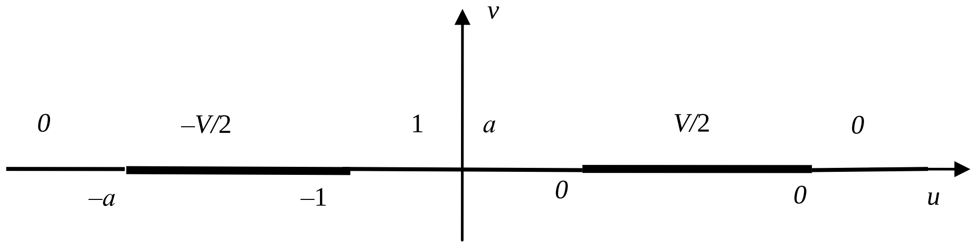

(2)

Figure 2. Boundary value problem in the w -plane

Same as in works [22–24], we will consider that the potential of the screens $V_0 = 0$, and the distance between the conductive plates is equal d . For the distribution of the potential in the *w*-plane, we obtain the following expression:

$$\varphi(u,v) = \frac{V}{2\pi}\left(\operatorname{arctg}\frac{u+1}{v} - \operatorname{arctg}\frac{u+a}{v}\right) + \frac{V}{2\pi}\left(\operatorname{arctg}\frac{u-1}{v} - \operatorname{arctg}\frac{u-a}{v}\right). \tag{3}$$

The value $a > 1$ depends on the type of transformation (1), that is, on the value of the angle α and on the length of the deflector plates l.

Results and Discussion

The integral in (1) for rational α is expressed in elementary functions and reduces to the integral of the binomial differential. So, for $\alpha = 0$ we come to the case considered in [22–24], and for $\alpha = 1$ we get, as in the case of deflector plates without screens:

$$z = \frac{d}{2\pi}\left(e^{w} + w + 1\right) + \frac{l}{2}; \tag{4}$$

at $\alpha = 1/2$:

$$z = -\frac{d}{\pi}\left[\ln\left(w + \sqrt{w^2 - 1}\right) - \frac{\sqrt{w^2 - 1}}{w}\right] + i\frac{d}{2}; \tag{5}$$

at $\alpha = 1/4$:

$$z = \frac{2d}{\pi}\left[\sqrt[4]{w^2 - 1} + \frac{1}{4}\ln\left(\frac{\sqrt[4]{w^2 - 1} - 1}{\sqrt[4]{w^2 - 1} + 1}\right) - \frac{1}{2}\operatorname{arctg}\sqrt[4]{w^2 - 1}\right]. \tag{6}$$

Differentiating both parts (1) we find partial derivatives:

$$\frac{dz}{dw} = \frac{\partial x}{\partial u} + i\frac{\partial y}{\partial u} = \frac{\partial y}{\partial v} - i\frac{\partial x}{\partial v} = C\frac{(w^2 - 1)^{\alpha}}{w^{1+2\alpha}}. \tag{7}$$

Now we find the inverse partial derivatives $\dfrac{\partial u}{\partial x}$ and $\dfrac{\partial u}{\partial y}$, as well as $\dfrac{\partial v}{\partial x}$ and $\dfrac{\partial v}{\partial y}$:

$$\frac{\partial u}{\partial x} = \frac{\dfrac{\partial y}{\partial v}}{\dfrac{\partial x}{\partial u}\dfrac{\partial y}{\partial v} - \dfrac{\partial x}{\partial v}\dfrac{\partial y}{\partial u}}, \quad \frac{\partial u}{\partial y} = \frac{\dfrac{\partial x}{\partial v}}{\dfrac{\partial y}{\partial u}\dfrac{\partial x}{\partial v} - \dfrac{\partial x}{\partial u}\dfrac{\partial y}{\partial v}}, \tag{8}$$

$$\frac{\partial v}{\partial x} = \frac{\dfrac{\partial y}{\partial u}}{\dfrac{\partial y}{\partial u}\dfrac{\partial x}{\partial v} - \dfrac{\partial x}{\partial u}\dfrac{\partial y}{\partial v}}, \quad \frac{\partial v}{\partial y} = \frac{\dfrac{\partial x}{\partial u}}{\dfrac{\partial x}{\partial u}\dfrac{\partial y}{\partial v} - \dfrac{\partial y}{\partial u}\dfrac{\partial x}{\partial v}}. \tag{9}$$

To find the field of deflector plates with divergent screens, we write down the following expressions for the derivatives of the potential:

$$\frac{\partial \varphi}{\partial x} = \frac{\partial \varphi}{\partial u}\frac{\partial u}{\partial x} + \frac{\partial \varphi}{\partial v}\frac{\partial v}{\partial x}, \quad \frac{\partial \varphi}{\partial y} = \frac{\partial \varphi}{\partial u}\frac{\partial u}{\partial y} + \frac{\partial \varphi}{\partial v}\frac{\partial v}{\partial y}. \tag{10}$$

To create a picture of the electric field lines the differential equation can be numerically integrated:

$$\frac{dx}{dy} = \frac{\dfrac{\partial \varphi}{\partial x}}{\dfrac{\partial \varphi}{\partial y}}. \tag{11}$$

Thus, we have built a mathematical model for calculating potentials, as well as for calculating potential derivatives. It can be used to study the dynamics of charged particle beams in deflector plates with expanding screens.

Conclusion

The work considers the edge field of deflector plates with expanding screens. The complexity of the problem is due to the fact that it is impossible to explicitly determine the electrostatic potential as a function of the geometric coordinates of the corpuscular optical system. Therefore, various mathematical techniques are used to overcome this difficulty. Analytical expressions for the potential, taking into account the type of the edge field, are obtained using methods of the theory of functions of a complex variable. The potential distribution in the upper half-plane is also considered. This made it possible to investigate the nature of the edge field of deflector plates with expanding screens. It is shown that the use of grounded shields leads to the localization of the marginal electric field near the edge of the deflector plates. As a result, the use of grounded screens localizes the edge electric field near the edge of the deflector plates, in an area characteristic dimensions of which are of the order of the distance between the plates *d*. Localization of the edge field also reduces the influence of uncontrolled scattering fields, which increases the accuracy of numerical calculations and their correspondence to the real physical situation.

The results obtained in this work can also be used to describe the edge field of magnets with magnetic screens.

Acknowledgments

The work was carried out within the framework of a project with grant funding from the Committee of Science of the Ministry of Science and Higher Education of the Republic of Kazakhstan (IRN AP09258546).

References

1 Ogasawara M. Development of a fast beamblanking system / M. Ogasawara H. Sunaoshii, R. Yoshikawa // Part of the SPIE Conference on Photomask and X-Ray Mask Technolociy V, Kawasaki. — Japan. — 1998. — P. 79–85.

2 Mulder E. Spot movement due to signal transients in multiple deflector blankers in electron beam lithography machines / E. Mulder, P. Kruit // Microelectron. Eng. — 1998. — 41. — P. 159–162.

3 Auzelyte V. The beam blanking system for microlithography at Lund Nuclear Microprobe / V. Auzelyte, M. Elfman, P. Kristiansson, K. Malmqvist, L. Wallman, C. Nilsson, J. Pallon, A. Shariff, M. Wegdén // Nucl. Instrum. Methods Phys. Res., Sect. B. — M., 2004. — 219. — P. 485–489.

4 Thong J.T.L. High repetition rate electron beam chopping system for electron beam testing at microwave frequencies / J.T.L. Thong, B.C. Breton, W.C. Nixon // J. Vac. Sci. Technol., B. — 1990. — 8. — 2048.

5 Winkler D. Flexible picosecond probing of integrated circuits with chopped electron beams / D. Winkler, R. Schmitt, M. Brunner, B. Lischke // IBM J. Res. Dev. — 1990. — 34. — 189–203.

6 Winkler D. A phase-shift technique for high-speed e-beam testing with picosecond time resolution / D. Winkler, R. Schmitt, M. Brunner, B. Lischke // Scanning. — 1989. — 11. — 100–103.

7 Moerland R.J. Time-resolved cathode luminescence microscopy with subnanosecond beam blanking for direct evaluation of the local density of states / R.J. Moerland, I.G.C. Weppelman, M.W.H. Garming, P. Kruit, J.P. Hoogenboom // Opt. Express. — 2016. 24. — 24760.

8 Weppelman I.G.C. Concept and design of a beam blanker with integrated photoconductive switch for ultrafast electron microscopy / I.G.C. Weppelman, R.J. Moerland, J.P. Hoogenboom, P. Kruit // Ultramicroscopy. — 2018. — 184. — 8–17.

9 Verhoeven W. High quality ultrafast transmission electron microscopy using resonant microwave cavities / W. Verhoeven, V.R. Jfm, E.R. Kieft, M. Pha, O.J. Luiten // Ultramicroscopy. — 2018. — 188. — 85–89.

10 Meuret S. Complementary cathodoluminescence lifetime imaging configurations in a scanning electron microscope / S. Meuret, M. Sola Garcia, T. Coenen, E. Kieft, H. Zeijlemaker, M. Latzel, S. Christiansen, S.Y. Woo, Y.H. Ra, Z. Mi, A. Polman // Ultramicroscopy. — 2019. — 197. — 28–38.

11 Wollnik H. The influence of magnetic and electric fringing fields on the trajectories of charged particles / H. Wollnik, H. Ewald // Nuclear Instruments & Methods. — 1965. — 36. — 93–104.

12 Matsuda H. Third order transfer matrices of the fringing field of an inhomogeneous magnet / H. Matsuda, H. Wollnik // Nuclear Instruments & Methods. — 1970. — 77. — 283–292.

13 Matsuda H. The influence of a toroidal electric fringing field on the trajectories of charged particles in a third order approximation / H. Matsuda // Nuclear Instruments & Methods. — 1971. — 77. — 40–54.

14 Doskeyev G.A. Influence of the fringe field on moving of the charged particles in flat and cylindrical capacitors / G.A. Doskeyev, O.A. Edenova, I.F. Spivak-Lavrov // Nucl. Instrum. Methods Phys. Res., Sect. A. — 2011. — 645. — 163–167.

15 Baisanov O.A. Investigation of the influence of edge fields on the motion of charged particles in flat and cylindrical capacitors / O.A.Baisanov, G.A. Doskeyev, A.O. Edenova, I.F. Spivak-Lavrov // Applied Physics. — 2012. — 2. — 67–72.

16 Metodiev E.M. Fringe electric fields of flat and cylindrical deflectors in electrostatic charged particle storage rings / E.M. Metodiev, K.L. Huang, Y.K. Semertzidis, W.M. Morse // Phys.rev.st Accel. beams. — 2014. — 17.

17 Maxwell J.C. A Treatise on Electricity and Magnetism / J.C. Maxwell. — Clarendon, Oxford. — 1873. — Vol. 1.

18 Spivak-Lavrov I.F. Analytical Methods for The Calculation and Simulation of New Schemes of Static and Time-of-Flight Mass Spectrometers / I.F.Spivak-Lavrov // Advances in Imaging and Electron Physics. — 2016. — 193. — 45–128. Burlington: Academic Press.

19 Souto C.L. Fringe field effects on electrostatic deflection of electrons by a pair of charged plates / C.L. Souto, C.G. Carll, J. Wang // J. Electrostat. — 2018. — 94. — 73–79.

20 Weppelman I.G.C. Pulse length, energy spread, and temporal evolution of electron pulses generated with an ultrafast beam blanker / I.G.C. Weppelman, R.J. Moerland, L. Zhang, E. Kieft, P. Kruit, J.P. Hoogenboom // StructDyn. — 2019. — 6. — 024102.

21 Lavrentiev M.A. Methods of the theory of functions of a complex variable / M.A. Lavrentiev, B.V. Shabat. — Moscow: Nauka, 1976.

22 Спивак-Лавров И.Ф. Краевое поле дефлекторных пластин с заземленными экранами / И.Ф. Спивак-Лавров, Д.Б. Джеткергенов, С.У. Шарипов // Вестн. Актюбин. регион. гос. ун-та им. К. Жубанова. Физико-математические науки. — 2019. — № 4(58). — С. 27–36.

23 Spivak-Lavrov I.F. Edge Fields of Flat Capasitor with Two Earthed Screens / I.F. Spivak-Lavrov, S.U. Sharipov // AIP Conference Proceedings. — 2022. — 2467. — 060039-1–060039-7; 010001. doi.org/10.1063/12.0010068.

24 Spivak-Lavrov I.F. Fringe fields of deflector plates with two earthed screens / I.F. Spivak-Lavrov, S.U. Sharipov, B.O. Sarsembaev // Nuclear Inst. and Methods in Physics Research, A V. — 2023. — 1051. — 1–4. doi.org/10.1016/j.nima.2023.168161.

И.Ф. Спивак-Лавров, С.У. Шарипов, А.Б. Сейтен, А.А. Трубицын

Кеңейтілген экрандары бар дефлекторлық пластиналардың шеткі өрісі

Дефлекторлық пластиналар — бұл екі параллель өткізгіш пластиналар, олардың көмегімен ауытқитын электр өрісі жасалады. Олар қозғалған бөлшектердің, яғни электрондардың немесе иондардың ағындарын басқару үшін қолданылады. Дефлекторлық пластиналардың шеткі өрісінің әсері зарядталған бөлшектердің жылдамдығының көлденең де, бойлық та өзгеруіне әкеледі, нәтижесінде олардың нақты траекториялары идеалдан ауытқып өзгереді, бұл олар қолданылатын корпускулалық-оптикалық құрылғылардың кеңістіктік-уақыттық ажыратымдылығын бұзады. Сонымен қатар, дефлектор пластиналарының кіреберісіндегі электр өрісі уақыт өте келе өзгеруі мүмкін, сондықтан дефлектормен зарядталған бөлшектер шоғының ауытқыған кезінде ескерілуі қажет. Осылайша, көптеген жағдайларда ашық ұштары бар дефлекторлық пластиналарды қолдану мақсатты емес, өйткені бұл ретте бақыланбайтын шашырау өрістері пайда болады. Мақалада дефлекторлық пластиналардың кеңейтілген экранға шығу кезіндегі өрісі, яғни дефлекторлық пластиналардан шыққан зарядталған бөлшектердің шоғын қолдануға болатындығы қарастырылған. Кешенді айнымалы функциялар теориясының әдістерін қолдана отырып, жерге тұйықталған экрандары бар дефлекторлық пластиналардың шеткі өрісі үшін аналитикалық өрнектер алынды. Біріншіден, экрандарды жерге тұйықтау және плиталардың ауытқу өрісін қорғау арқылы біз шеткі электр өрісін локализациялаймыз және бақыланбайтын шашырау өрістерін басамыз, екіншіден, мұндай өрісті аналитикалық түрде дәл есептеуге болады.

Кілт сөздер: дефлекторлық пластиналар, жерге тұйықталған экрандар, шеткі өріс, электрстатиканың шекаралық есептері, электронды шоқпен басқару.

И.Ф. Спивак-Лавров, С.У. Шарипов, А.Б. Сейтен, А.А. Трубицын

Краевое поле дефлекторных пластин с расширяющимися экранами

Дефлекторные пластины представляют собой две параллельные проводящие пластины, с помощью которых создается отклоняющееся электрическое поле. Используются они для управления потоками заряженных частиц — электронов или ионов. Влияние краевого поля дефлекторных пластин приводит к изменению скорости заряженных частиц как в поперечном, так и в продольном направлении, в результате чего изменяются их реальные траектории, отклоняясь от идеальных, что нарушает пространственно-временное разрешение корпускулярно-оптических устройств, в которых они используются. Кроме того, электрическое поле на входе в пластины дефлектора может изменяться во времени, поэтому этот факт необходимо учитывать при отклонении пучка заряженных частиц дефлектором. Таким образом, во многих ситуациях применение дефлекторных пластин с открытыми торцами оказывается нецелесообразным, так как возникают неконтролируемые поля рассеяния. В настоящей работе мы рассмотрели поле дефлекторных пластин с расширяющимися на выходе экранами, для того чтобы на выходе из дефлекторных пластин можно было использовать расходящийся пучок заряженных частиц. С помощью методов теории функций комплексной переменной получены аналитические выражения для краевого поля дефлекторных пластин с заземленными экранами. Во-первых, заземляя экраны и экранируя отклоняющее поле пластин, мы локализуем краевое электрическое поле и подавляем неконтролируемые поля рассеяния, а во-вторых, такое поле может быть точно рассчитано аналитически.

Ключевые слова: дефлекторные пластины, заземленные экраны, краевое поле, граничная задача электростатики, управление электронным пучком.

References

1 Ogasawara, M., Sunaoshii, H., & Yoshikawa, R. (1998). Development of a fast beamblanking system. *Part of the SPIE Conference on Photomask and X-Ray Mask Technolociy V, Kawasaki*, 79–85. Japan.

2 Mulder, E. & Kruit, P. (1998). Spot movement due to signal transients in multiple deflector blankers in electron beam lithography machines. *Microelectron. Eng., 41*, 159–162.

3 Auzelyte, V., Elfman, M., Kristiansson, P., Malmqvist, K., Wallman, L., Nilsson, C., Pallon, J., Shariff, A., & Wegdén, M. (2004). The beam blanking system for microlithography at Lund Nuclear Microprobe. *Nucl. Instrum. Methods Phys. Res., Sect. B*, 219, 485–489.

4 Thong, J.T.L., Breton, B.C., & Nixon, W.C. (1990). High repetition rate electron beam chopping system for electron beam testing at microwave frequencies. *J. Vac. Sci. Technol., B*, 8, 2048.

5 Winkler, D., Schmitt, R., Brunner, M., & Lischke B. (1990). Flexible picosecond probing of integrated circuits with chopped electron beams. *IBM J. Res. Dev., 34*, 189–203.

6 Winkler, D., Schmitt, R., Brunner, M., & Lischke, B. (1989). A phase-shift technique for high-speed e-beam testing with picosecond time resolution. *Scanning*, 11, 100–103.

7 Moerland, R.J., Weppelman, I.G.C., Garming, M.W.H., Kruit, P., & Hoogenboom, J.P. (2016). Time-resolved cathode luminescence microscopy with subnanosecond beam blanking for direct evaluation of the local density of states. *Opt. Express, 24*, 24760.

8 Weppelman, I.G.C., Moerland, R.J., Hoogenboom, J.P., & Kruit, P. (2018). Concept and design of a beam blanker with integrated photoconductive switch for ultrafast electron microscopy. *Ultramicroscopy*, 184, 8–17.

9 Verhoeven, W., Jfm, V.R., Kieft, E.R., Pha, M., & Luiten, O.J. (2018). High quality ultrafast transmission electron microscopy using resonant microwave cavities. *Ultramicroscopy*, 188, 85–89.

10 Meuret, S., Sola Garcia, M., Coenen, T., Kieft, E., Zeijlemaker, H., Latzel, M., Christiansen, S., Woo, S.Y., Ra, Y.H., Mi, Z., & Polman, A. (2019). Complementary cathodoluminescence lifetime imaging configurations in a scanning electron microscope. *Ultramicroscopy*, 197, 28–38.

11 Wollnik, H. & Ewald, H. (1965). The influence of magnetic and electric fringing fields on the trajectories of charged particles. *Nuclear Instruments & Methods*, 36, 93–104.

12 Matsuda, H. & Wollnik, H. (1970). Third order transfer matrices of the fringing field of an inhomogeneous magnet. *Nuclear Instruments & Methods*, 77, 283–292.

13 Matsuda, H. (1971). The influence of a toroidal electric fringing field on the trajectories of charged particles in a third order approximation. *Nuclear Instruments & Methods*, 77, 40–54.

14 Doskeyev, G.A., Edenova, O.A., & Spivak-Lavrov, I.F. (2011). Influence of the fringe field on moving of the charged particles in flat and cylindrical capacitors. *Nucl. Instrum. Methods Phys. Res., Sect. A*, 645, 163–167.

15 Baisanov, O.A., Doskeyev, G.A., Edenova, A.O., & Spivak-Lavrov, I.F. (2012). Investigation of the influence of edge fields on the motion of charged particles in flat and cylindrical capacitors. *Applied Physics*, 2, 67–72. Moscow.

16 Metodiev, E.M., Huang, K.L., Semertzidis, Y.K., & Morse, W.M. (2014). Fringe electric fields of flat and cylindrical deflectors in electrostatic charged particle storage rings. *Phys.rev.st Accel. beams*, 17.

17 Maxwell, J.C. (1873). A Treatise on Electricity and Magnetism. Vol. 1. Clarendon, Oxford.

18 Spivak-Lavrov, I.F. (2016). Analytical Methods for The Calculation and Simulation of New Schemes of Static and Time-of-Flight Mass Spectrometers. *Advances in Imaging and Electron Physics, 193*, 45–128. Burlington: Academic Press.

19 Souto, C.L., Carll, C.G., & Wang, J. (2018). Fringe field effects on electrostatic deflection of electrons by a pair of charged plates. *J. Electrostat*., 94, 73–79.

20 Weppelman, I.G.C., Moerland, R.J., Zhang, L., Kieft, E., Kruit, P., & Hoogenboom, J.P. (2019). Pulse length, energy spread, and temporal evolution of electron pulses generated with an ultrafast beam blanker. *StructDyn*, 6, 024102.

21 Lavrentiev, M.A. & Shabat, B.V. (1976). Methods of the theory of functions of a complex variable. 716 p. Moscow: Nauka.

22 Spivak-Lavrov, I.F., Zhetkergenov, D.B., & Sharipov, S.U. (2019). Kraevoe pole deflektornykh plastin s zazemlennymi ekranami [Edge field of deflector plates with grounded screens]. *Vestnik Aktiubinskogo regionalnogo gosudarstvennogo universiteta imeni K. Zhubanova. Fiziko-matematicheskie nauki — Bulletin of Aktobe Regional State University named after K. Zhubanov. Physical and mathematical sciences*, 4(58), 27–36 [in Russian].

22 Spivak-Lavrov, I.F. & Sharipov, S.U. (2022). Edge Fields of Flat Capasitor with Two Earthed Screens. *AIP Conference Proceedings*, 2467, 060039-1–060039-7; 010001; doi.org/10.1063/12.0010068.

23 Spivak-Lavrov, I.F., Sharipov, S.U., & Sarsembaev, B.O. (2023). Fringe fields of deflector plates with two earthed screens. *Nuclear Inst. and Methods in Physics Research*, A V, 1051, 1–4. doi.org/10.1016/j.nima.2023.168161.

Information about authors

Spivak-Lavrov, I.F. — Doctor of physical and mathematical sciences, Professor, K. Zhubanov Aktobe Regional University, Kazakhstan; e-mail: spivakif@rambler.ru, ORCID ID: https://orcid.org/0000-0001-6235-3897

Sharipov, S.U. — Senior lecturer, K. Zhubanov Aktobe Regional University, Kazakhstan; e-mail: sharipov_samat@mail.ru, ORCID ID: https://orcid.org/0000-0003-4350-2361

Seiten, A.B. — 2nd year PhD student, K. Zhubanov Aktobe Regional University, Kazakhstan; e-mail: aizhanat_bolatovna@mail.ru, ORCID ID: https://orcid.org/0009-0001-5530-1658

Trubitsyn, A.A. — Doctor of physical and mathematical sciences, Professor, Ryazan State Radio Engineering University, Ryazan, Russia; e-mail: assur@bk.ru, ORCID ID: https://orcid.org/0000-0002-9337-8947